NEOCORTICAL CIRCUIT MECHANISMS OF SENSORIMOTOR PROCESSING

By

Luis Enrique Martinetti

A DISSERTATION

Submitted to
Michigan State University
in partial fulfillment of the requirements
for the degree of

Neuroscience – Doctor of Philosophy

2024

ABSTRACT

Sensorimotor processing is a dynamic process by which the central nervous system combines sensory inputs with motor commands to generate appropriate actions, a process underlying almost every aspect of normal behavior. In the somatosensory (touch) system, two major pathways carry sensory information from the periphery into the neocortex, with sensorimotor interactions happening at every level mediated by the motor cortex. Although much is known about sensorimotor interactions along the ascending sensory pathways, not much is known about sensorimotor interactions at the level of the neocortex. Using the mouse vibrissae (whisker) system, we aimed to understand the synaptic and cellular mechanisms governing sensorimotor interactions between the whisker representation of the primary somatosensory (vS1) and motor (vM1) cortices.

Long-range interactions between cortical areas play a central role in cognitive function, but the dynamic regulation of these synapses (i.e., short-term synaptic plasticity) and their impact on a postsynaptic target neuron is unclear. In Chapter 2, we use optogenetic and electrophysiological strategies in vitro to study the long-range pathways connecting vM1 and vS1. We found that short-term synaptic facilitation was strong in both directions, as compared to other intracortical connections. This facilitation was dependent on the presynaptic calcium sensor synaptotagmin-7 and altered by several optogenetic approaches. Furthermore, the properties of the connections linking vS1 with secondary somatosensory cortex (vS2) resemble those from vS1 to vM1. These results reveal a synaptic mechanism by which intracortical projections may mediate specific changes in cellular excitability with repetitive activity.

Moreover, previous literature has shown that vM1 can alter sensory processing in the ventral posteromedial nucleus (VPm) of the thalamus via the recruitment of corticothalamic (CT) neurons in layer 6 (L6) of vS1. Indeed, L6a CT neurons can modulate thalamic activity to shape sensory throughput into the cortex. However, direct influence of M1 on the two main classes of L6a CT cells in S1 has been understudied, likely due to technical challenges in their identification. Using retrograde tracing, in vitro recordings, and optogenetic control strategies in mice, we investigated the synaptic effects of vM1 input on the two main classes of L6a CT neurons. Our results reveal selective engagement by vM1 of CT neurons projecting to both the VPm and posteromedial (POm) nuclei in the thalamus ("Dual" CT neurons). These neurons exhibited spiking activity exclusively when held at a depolarized membrane potential simulating an "active state". This selective engagement is possibly due to the differences in intrinsic membrane physiology making these Dual CT neurons more excitable, in addition to receiving stronger direct excitation from vM1. These findings provide new insights into the complex synaptic and circuit mechanisms underpinning neocortical sensorimotor interactions.

To all those who give everything for their children. In particular, my extraordinary mother, Lorena Aguirre Orpinel, whose resilience and sacrifices have paved the path to my achievements.

ACKNOWLEDGEMENTS

I would like to express my deep gratitude to my academic advisor, Dr. Shane R. Crandall, for the opportunity to pursue my doctoral research in his lab. His rigorous and thoughtful approach to science initially attracted me, and this was confirmed by the extensive and rich scientific discussions, the freedom to explore my questions, and the focus on meticulous detail that he encouraged. I also want to thank Dawn Autio, who became my dear friend and is someone I will always look up to. I appreciate all her support, conversations about gardening, biking, and everything in general! I also want to thank Dr. Suryadeep Dash, who became both my friend and mentor. I will always miss having lunch in the BPS gardens in the summer while having great conversations. It was an honor and pleasure to work with such great scientists.

I want to thank Dr. Gina Leinninger for her tremendous support and mentorship since the beginning. I greatly value her down-to-earth approach and vibrant personality, which brightens the day of every student she interacts with (student polls indicate). Although she was not my academic advisor, she became my mentor by looking out for me at every step of my degree, and beyond by helping me start my professional career. I also want to thank my other committee members, Drs. Charles Lee Cox, Daniel Vogt, and Hongbing Wang for offering constructive and thoughtful feedback on my project. I truly was advised by a great group of scientists.

I have had the pleasure and am deeply grateful to work with great people in the neuroscience program, including Eleri Thomas, Julie Delgado, Dr. AJ Robison, and the neuroscience students who made my time at MSU memorable. From the start, Eleri and Julie have been incredibly supportive in every aspect of my degree, for which I am truly grateful. I also cherish their friendship and hope to keep it in the future. I want to thank AJ for his tremendous support during my degree and the strong representation he gives to the graduate students.

I want to thank my friends from Ciudad Juarez and El Paso for their unwavering support and genuine care throughout this entire time. I also want to thank the friends that I have made in Lansing, who come from all around and I have learned so much from. Particularly, I want to thank my friends Zac Fernandez and Samantha Caico, who I have gone through multiple life milestones with, for their loving support and friendship.

I want to thank my mom Lorena, my sisters Aracely and Silvana, and my nieces Aurora and Regina, for their unconditional love and support throughout my entire career. I want to thank my greatest friend and twin brother, Luis Bernardo for the natural friendship, love, and support over the years. We have shared each other's significant life and educational milestones, and I am deeply grateful to have someone who understands and supports me on my life path. I am happy to have had him and his beautiful dogs, Apollo and Amber, as my support system during my doctoral studies.

Lastly, I want to thank my loving partner, best friend, and lab partner, Kelly Bonekamp, for being such a positive influence on my career and life since we met. I want to thank her for her support throughout the entirety of my studies, for teaching me patience, and for being one of the most loving and noblest people I have met. I will forever be thankful to her for constantly teaching me new things about electrophysiology, for making the long days of recording together be something to look forward to, and for the never-ending discussions about nature and science that keep me fascinated. Finally, I want to thank her for bringing our furry companions Lulu and Rosie into my life, I feel very fulfilled.

TABLE OF CONTENTS

LIST OF ABBREVIATIONS

AAV	:	adeno-associated virus
ACSF	:	artificial cerebrospinal fluid
Ai14	:	cre-dependent tdTomato reporter mouse
AP	:	action potential
APV	:	2-amino-5-phosphonovaleric acid / NMDAr antagonist
CC	:	corticocortical / intracortical
ChR2	:	Channelrhodopsin-2
CT	:	corticothalamic
CTB	:	choleratoxin subunit-b
DNQX	:	6,7-dinitroquinoxaline-2,3-dione / AMPAr antagonist
Dual CT	:	corticothalamic cell projecting to VPm and POm (see below)
E/I	:	Excitation / Inhibition ratio
EPSC	:	excitatory post-synaptic current
EPSP	:	excitatory post-synaptic potential
EYFP	:	enhanced yellow-fluorescent protein
IPSC	:	inhibitory post-synaptic current
IPSP	:	inhibitory post-synaptic potential
KO	:	genetic knock-out
L1-6	:	layers 1, 2/3, 4, 5, and 6
L6aL	:	lower section of layer 6a
L6aU	:	upper section of layer 6a
LED	:	light-emitting diode

ms : milliseconds

mV : millivolts

pA : picoamps

POm : posteromedial nucleus of the thalamus

PrV : principal trigeminal nucleus

PV : parvalbumin-expressing

RMP : resting membrane potential

RS : regular spiking

SOM : somatostatin-expressing

SpV : spinal trigeminal nucleus

Syt7 : Synaptotagmin-7

TC : thalamocortical

tdT : tdTomato fluorescent protein

TRN : thalamic reticular nucleus

TTX : tetrodotoxin

VIP : vasoactive intestinal peptide-expressing

vM1 : vibrissa representation of the motor cortex

VPm : ventral posteromedial nucleus of the thalamus

vS1 : vibrissa representation of the primary somatosensory cortex

vS2 : vibrissa representation of the secondary somatosensory cortex

ZI : zona incerta

CHAPTER 1: INTRODUCTION

1.1 – Why is sensorimotor processing important?

The importance of sensorimotor processing cannot be overstated, as it underlies nearly every aspect of normal behavior and survival. Sensorimotor processing is a dynamic process by which the central nervous system combines sensory inputs with motor commands to generate appropriate actions, a process fundamental to interacting with the world (Petersen 2019). This intricate process ensures that organisms can respond adaptively to their environment, allowing for the coordination of complex movements, from manipulating objects with precision to navigating through diverse terrains (Alcock 2009; Dallos and Oertel 2008). Such capabilities are not only essential for daily activities and exploring new environments but are also essential for avoiding danger and securing resources, directly impacting an organism's survival. In essence, efficient sensorimotor processing is what creates seamless and effective engagement with the ever-changing demands of the external world, making it a cornerstone of both routine behavior and evolutionary success (von der Emde and Warrant 2016).

In this dissertation, I dedicated myself to advancing our understanding of the intricate synaptic and circuit mechanisms underpinning neocortical sensorimotor processing using the mouse somatosensory system.

1.2 – The mouse whisker system is a model to study sensorimotor interactions

Historically, mice have served as an essential model in scientific research, attributed to their shared genetics with humans, ease of breeding, and the straightforward monitoring of their behaviors in controlled environments (Clarke, 2002). This utility is highlighted in sensory neuroscience, where mice are invaluable for studying the somatosensory system. Mice use their whiskers to actively sense the environment by moving them back and forth in a rhythmic motion (although also used for passive tactile sensation; Kerekes et al. 2017), called “whisking”. This motor control of a whisker is generally thought to enhance the selective gathering of sensory information. Sensory signals from the whiskers are relayed to higher brain centers, channeled through parallel pathways to the brainstem and thalamus, and ultimately to the somatosensory and motor cortices for sensory perception (Petersen 2014).

Sensory and motor systems coordinate closely across multiple levels along the ascending lemniscal and paralemniscal sensory pathways (discussed in further detail in this chapter). This coordination begins at the whisker follicle, proceeds through the trigeminal ganglia, then to trigeminal nuclei in the brainstem, moves to the contralateral thalamus, and ends in the primary vibrissa/whisker representation of the somatosensory cortex (vS1), facilitating highly coordinated sampling and processing of sensory information (Kleinfeld et al., 2006; Diamond et al., 2008). Each of these sensory processing levels are connected to motor areas in nested loops (sensorimotor loops) all throughout the ascending sensory pathways, with certain differences between the lemniscal and lemniscal portions (Kleinfeld et al. 1999). Ultimately, this coordination is a consequence of the highly cooperative nature of sensory and motor systems, allowing for a prompt and appropriate behavioral response to any given sensory input.

A large gap in knowledge lies in our understanding of sensorimotor processing at the level of the neocortex since it has been understudied, perhaps due to its highly complicated circuitry. Understanding sensorimotor processing at subcortical levels provides insight into how sensory and motor circuits interact at the level of the cortex. Therefore, in this chapter I will describe some of our knowledge about sensorimotor processing along the lemniscal and paralemniscal pathways, ultimately leading to cortex.

Ascending somatosensory pathways. Mice utilize their whiskers to explore their surroundings and can extract two main types of environmental features: specific features like texture, and spatial location in reference to the rodent’s head. The whiskers serve as the primary sensory organs and are innervated by collaterals of pseudounipolar neurons whose cell bodies are located in the trigeminal ganglion (Olszewski 1950; Zucker and Welker 1969; Vincent 1913). These neurons convert the mechanical energy of the whisker follicle into action potentials, and their projection to the trigeminal complex in the brainstem gives rise to the lemniscal and paralemniscal pathways. These ascending pathways are often referred to as the "whisker-to-barrel pathways" because of their unique anatomical circuit characteristics at each level (Staiger and Petersen 2021). Areas that are part of these pathways have a somatotopic representation (a map) of the mouse's whisker pad, where separate microcircuits represent and process information from each whisker in a one-to-one ratio.

The lemniscal pathway. The lemniscal pathway, also known as the 'what' pathway, first appears in highly organized projections from the trigeminal ganglion (TG) targeting multiple “barrelettes” from the principal trigeminal nucleus with large axons ending in clustered terminals (PrV; Vincent 1913; Dörfl 1982; Rice et al. 1986; Chiaia et al. 1991; Williams et al. 1994). This pathway is thought to transmit detailed sensory information that represents specific features of touched objects, such as shape and texture from the whiskers, with high temporal and spatial fidelity (Ma 1991; Diamond et al. 2008; Sosnik et al. 2001). Barrelettes in the PrV primarily project to the representation of the same whisker in “barreloids” in the ventral posteromedial nucleus of the thalamus (VPm;

Rhoades et al. 1987; Chiaia et al. 1991; Williams et al. 1994; Friedberg et al. 1999; Sosnik et al. 2001). Fibers from neurons in the VPm barreloids then project to the respective whisker representation “barrels” in the vibrissa representation of the primary somatosensory cortex (vS1; Woolsey and Van der Loos 1970; Welker 1971; Killackey 1973; Jensen and Killackey 1987) This orderly structure facilitates a detailed and topographic transfer of sensory information, enabling each whisker's touch to be precisely mapped within the brain and allowing for highly detailed sensory processing at all levels (Diamond et al., 2008).

The paralemniscal pathway. In parallel to the lemniscal pathway, the paralemniscal pathway, also known as the 'where' pathway, also begins at the projections from TG neurons synapsing onto the oralis, interpolaris, and caudalis areas of the spinal trigeminal nucleus of the brainstem with axons of smaller diameter and diffuse connectivity (SpV; Torvik 1956; Clarke and Bowsher 1962; Chiaia et al. 1991; Williams et al. 1994; Veinante et al. 2000). The SpV caudalis and interpolaris also possess a topographic map of the whiskers “barrelettes” (Ma and Woolsey 1984), but not the oralis section although it also receives sensory input from the whiskers (Belford and Killackey 1979b; Belford and Killackey 1979a). Instead, this pathway primarily characterized by more diffuse projections from TG neurons lacking a clear one-to-one correspondence, enabling neurons to integrate signals from multiple whiskers. This pathway is thought to primarily convey spatial information, such as angle deflection of the whisker, by transducing specific features about the whiskers' movement (Furuta et al., 2006). Neurons from the barrelettes in SpV primarily project to the whisker representation in the posteromedial nucleus of the thalamus (POm), but also to the VPm to a lesser extent (Lund and Webster

1967; Erzurumlu and Killackey 1980; Bruce et al. 1987; Veinante et al. 2000). Neurons from POm then send projections to the areas between the barrels (septa) in vS1 and also directly to vS2 (Koralek et al. 1988; El-Boustani et al. 2020). These pathways exemplify the dual facets of sensory processing in parallel – the lemniscal pathway, with its precise spatial mapping, is generally thought to be crucial for detailed sensory discrimination and spatial processing (Armstrong-James and Fox 1987; Diamond 1995; Simons 1995; Moore et al. 2015; Severson et al. 2017). Although we know less about the paralemniscal pathway, it is generally thought that it likely plays a role in temporal coding processing, providing signals that can be used for contextual awareness in the cortex (Ahissar et al. 2000). In essence, the paralemniscal pathway perhaps forms and communicates a “tactile” image of the surrounding environment, integrating a wider range of sensory inputs to provide a comprehensive sense of space.

In order for this sensory information to result in complex behaviors, it makes sense to have motor influences, or sensorimotor loops (Kleinfeld et al., 1999), integrated at all stages of the sensory pathways to rapidly transform sensory input into behavioral output. In the next section, I will discuss the sensorimotor loops present along the ascending lemniscal and paralemniscal pathways. Although these loops are not the focus of this dissertation, it is important how sensorimotor processing occurs at all stages of processing and they will be further discussed next.

Sensorimotor processing in the brainstem. In the ascending somatosensory pathways, sensorimotor loops are created through regions that process sensory information and their projections to motor areas. These motor areas are capable of initiating or regulating whisker movement (Kleinfeld et al. 1999). These sensorimotor loops start at the hindbrain and re-occur along the lemniscal and paralemniscal pathways, eventually leading up to the cortex and involving multiple forebrain structures.

The earliest and most compact form of sensorimotor loops happens in the hindbrain, which includes the pathways between the vibrissa, TG, trigeminal nuclei (both PrV and SpV), who then contact the lateral facial nucleus (LFN) that possesses motor neurons that control whisker movement by contacting the papillary muscles around each vibrissa (Arvidsson 1982; Dörfl 1982; Dörfl 1985; Arvidsson and Rice 1991). Interestingly, studies have shown that feedback from the motor cortex (discussed in further detail in this chapter) targets motor neurons in the LFN (Klein and Rhoades 1985; Herfst and Brecht 2008) and central pattern generators in the intermediate reticular formation of the brainstem (Carvell et al. 1991; Carvell et al. 1996; Matyas et al. 2010; Sreenivasan et al. 2015), possibly driving rhythmic whisker protraction through the engagement of various excitatory and inhibitory premotor neurons in the hindbrain sensorimotor loop (Moore et al. 2013). Furthermore, the involvement of the motor cortex is a recurrent situation along all sensorimotor loops, possibly providing contextual input for accurate sensory processing.

Sensorimotor processing in the thalamus – Forebrain sensorimotor loop. The next step in the ascending somatosensory pathways is the thalamus. While there exist distinct pre- and post- thalamic areas dedicated to all sensory modalities, a common feature shared by all senses is the relay of information through the thalamus (olfaction is highly debated, but see Courtiol and Wilson, 2014, 2015).

The sensorimotor loop involving the thalamus in the ascending somatosensory pathways is the forebrain loop and is perhaps the most complex, as it involves many areas (Kleinfeld et al. 1999). This sensorimotor loop is formed by the sensory projections from TG contacting the vibrissa to PrV and SpV, who project to the VPm and POm. Both VPm and POm receive input from both brainstem nuclei, but the VPm receives stronger input from PrV whereas the POm receives most of its sensory input from SpV (Sosnik et al. 2001).The forebrain loop also includes thalamocortical projections from VPm and POm into both vS1 and vS2, in addition to the whisker representation of the motor cortex (vM1), which is considered to be at the top of the hierarchy (Petersen 2019). This section will not delve into sensorimotor processing within the cortex, as that topic will be addressed subsequently. Instead, the discussion will concentrate on the role of the thalamus in the context of sensorimotor integration within the sub-cortical sections of the forebrain loop.

On the descending part of this sensorimotor loop lie the corticothalamic (CT) pathways which are generally considered as feedback loops from the cortex that modulate/alter the responses of neurons in the thalamus receiving ascending sensory inputs (Deschênes et al. 1998). These CT projections descend from pyramidal neurons in layers 5 and 6 of vS1 and vM1, providing reciprocal connections to the thalamic nuclei that they are targeted by, in addition to the TN, FN, and central pattern generators in the reticular formation (Jones and Wise 1977; Donoghue et al. 1979; Donoghue and Kitai 1981; Hoogland et al. 1987; Koralek et al. 1988; Sreenivasan et al. 2015; Kleinfeld et al. 1999; Deschenes et al. 1996).

Motor influences in the forebrain sensorimotor loop. Regarding functionality, research indicates that the VPm barreloids receive sensory inputs from the PrV, which convey precise tactile information crucial for spatial processing (Armstrong-James and Fox 1987; Sosnik et al. 2001; Pierret et al. 2000; Ahissar et al. 2000; Ghazanfar and

Nicolelis 1997; Ghazanfar et al. 2000; Nicolelis and Chapin 1994). This is manifested as encoding the spatial location of the activated whisker. The integration of information from various sources allows the VPm to communicate a comprehensive sensory input to the cortex. Although most of the cortical feedback the VPm receives comes from vS1 (Deschênes et al. 1998), studies have suggested that the sparse projections from vM1 to the head region of the VPm barrelettes is involved in processing information about whisker motion (Urbain and Deschênes 2007), due to vM1 being involved in initiation and modulation of rhythmic whisking (Carvell et al. 1996). Furthermore, indirect motor modulation has been shown in the VPm where the motor cortex can alter the receptive field properties of relay neurons, putatively via the recruitment of corticothalamic neurons present in layer 6 of the barrel cortex (Lee et al., 2008), which chapter 3 focuses on.

The posteromedial nucleus of the thalamus (POm), primarily engaged in the paralemniscal pathway , receives inputs from both PrV and SpV, but receives the bulk of its sensory inputs from the latter (Erzurumlu and Killackey, 1980; Bruce et al., 1987; Veinante et al. 2000; Trageser and Keller, 2004). It is hypothesized that the paralemniscal inputs to the POm are involved in processing temporal information that matches the spatial processing routed through the VPm (Ahissar et al. 2000; Sosnik et al. 2001). This is represented as the correlation of spike counts and latency in the POm (Ahissar et al. 1997; Ahissar 1998).

The POm seems to have a bigger role in sensorimotor processing in the thalamus as its activity depends on the activity of motor cortex (Diamond et al. 1992; Kleinfeld et al. 1999). It has been proposed that the strong excitatory influence from motor cortex to POm, in addition to the disinhibitory mechanism through the zona incerta (ZI) makes the paralemniscal pathway communicate sensory information contingent upon motor instructions controlling the whiskers (Lavallée et al., 2005; Urbain and Deschênes, 2007b). Indeed, studies have reported that the inputs POm receives from the brainstem are under the inhibitory control of the ZI (Trageser and Keller 2004). The dependence of POm activity in cortical activity is presented as direct excitation from vS1 (Diamond et al. 1992), in addition to the disinhibition of ZI by vM1 (through the recruitment of intra-incertal inhibitory neurons; Urbain and Deschênes 2007).

Furthermore, it is important to note the tremendous inhibitory role that the thalamic reticular nucleus (TRN) has in controlling the excitation over both the VPm and POm through reciprocally connected circuits (Sherman and Guillery, 1996; Huntsman et al., 1999; Pinault, 2004; Wang et al., 2011). The TRN acts as an interface between thalamocortical (TC) and corticothalamic (CT) projections, where associated axon fibers target the same zone within the TRN (Jones, 1975; Guillery and Harting, 2003). The intricate engagement of TRN circuits by both thalamocortical (TC) and corticothalamic (CT) pathways facilitates complex sensory processing in the thalamus , such as surround suppression. In this process, input from a single whisker can suppress the activity of surrounding neurons in the thalamus, enhancing the transfer of information as seen in the visual system (Jones et al., 2012).

1.3 – Sensorimotor processing in the neocortex

The reciprocally connected vS1 and vM1 cortical areas sit at the top of the forebrain sensorimotor loop (Kleinfeld et al. 1999), whose communication is thought to be critically important for facilitation of sensory perception and sensorimotor coordination (Goodale and Milner 1992; Mesulam 1998; Yamashita et al. 2013). It is important to note that much of our knowledge about sensory systems is derived from research concentrating on the visual system. Further research has confirmed that the organizational and functional principles governing one sensory system usually apply to others as well.

In the vibrissal representation of the somatosensory cortex (vS1) of mice, each column is defined by discrete cytoarchitectonic units in L4 called barrels representing individual whiskers on the mouse's snout (Woolsey and Van der Loos, 1970). An important anatomical and functional feature of the neocortex is its organization into columns that contain vertically organized microcircuits (Douglas and Martin, 2004; Oberlaender et al., 2012; Narayanan et al., 2017), with high interconnectivity amongst functionally related areas (e.g., vS1 and vM1). Although vS1 is perhaps one of the most important areas for sensory computations, it relies on the local and long-range connections to integrate sensory information from the periphery as well as motor signals from vM1, essential computations for adaptive behavior (Bastos et al., 2012; Petersen, 2019).

Functional organization of the neocortex. A key organizational feature of the neocortex is its abundant interconnectivity amongst functionally related areas. Early studies categorized cortical areas as "lower" or "higher" order based on their distinct laminar projection patterns and the specific layers where the originating neurons are located (Rockland and Pandya 1979). Primary sensory areas, such as vS1, receive substantial sensory inputs from the thalamus and are thought to process basic features of sensory input (Felleman and Van Essen 1991). Primary sensory areas are classified as lower order due to their projections, which mainly originate from and target superficial layers. In contrast, secondary sensory and motor areas, such as vS2 and vM1, receive substantial sensory inputs from lower order areas and are thought to process more complex features of the sensory inputs (Felleman and Van Essen 1991). Secondary sensory areas are classified as higher order due to their projections originate from and target L1 and deep layers (Rockland and Pandya 1979; Veinante and Deschênes 2003).

Due to this organization, the cortex has been proposed to be arranged hierarchically, with “lower areas” communicating receptive field properties to “higher areas” via corticocortical feedforward projections (Felleman and Van Essen 1991; Rockland and Pandya 1979). In turn, higher cortical areas send feedback projections that influence the responsiveness of their target neurons according to ongoing behavior and context to satisfy momentary demands (Felleman and Van Essen, 1991; Gilbert and Sigman, 2007; Gilbert and Li, 2013; Kwon et al., 2016; Briggs, 2020).

To understand how sensory information is processed in the cortex, we first need to understand its highly complicated organization. As briefly mentioned, the cortex is divided into columns, which are vertically organized microcircuits that respond to the same sensory input (e.g., one whisker barrel is one column; Simons 1978). The cortex is also layered, which can often be easily distinguished by their distinct anatomical appearance under bright -field microscopy. It is currently recognized that vS1 has the following layers: layers 1, 2/3 (called this due to its lack of visible distinguishing anatomical markers in rodents; Luo et al., 2017), 4, 5, and 6 (Petersen, 2019), with subdivisions in layers 5 and 6 (L5a and b, L6a and b). Most layers are a heterogenous mix of both of excitatory and inhibitory neurons, except L1, which has only interneurons (Schuman et al., 2019). The morphological and physiological heterogeneity among both excitatory and inhibitory neuronal populations has complicated the study of cortical processing (Gouwens et al. 2019; Gouwens et al. 2020).

The stereotyped flow of sensory information in cortex is as follows: L4 (also known as the thalamo-recipient layer; (Castro-Alamancos and Connors, 1997) receives strong and reliable thalamic inputs from their respective VPm barreloids (Gil et al., 1999; Gabernet et al., 2005) and communicates it to the superficial L2/3 (Douglas and Martin 2004; Gilbert and Wiesel 1983; Feldmeyer 2012). L2/3 pyramidal neurons send/receive inputs to/from other cortical areas (feedforward and feedback projections, respectively; (Yamashita et al. 2018; Rockland and Pandya 1979), and are proposed to process whisker information in an “associative” manner, perchance serving as a memory function (Constantinople and Bruno 2011). Information is then relayed to deep layers 5 and 6, who are recognized as the output layers of the cortex (Zhang and Deschênes, 1997, 1998; Veinante and Deschênes, 2003; Pluta et al., 2019; Egger et al., 2020), but also receive direct inputs from thalamus (Constantinople and Bruno 2013). Importantly for this dissertation, L5 and L6 also send/receive inputs to other cortical areas and the thalamus, and they have distinct functions like sensory discrimination, coincidence detection, and fine-tuning of cortical coding (Bastos et al., 2012; Pluta et al., 2019; Egger et al., 2020; Qi et al., 2022). Although this is the recognized canonical flow, this is an overgeneralization due to the high interconnectivity among layers, serving distinct functions in sensory processing (DeNardo et al., 2015), not essential for this dissertation.

Cellular and synaptic physiology. Historically, cortical excitatory neurons have been typically characterized by the morphological organization of their dendritic tree, exhibiting three main types: pyramidal, star pyramidal, and stellate cells (Narayanan et al. 2015; Staiger et al. 2004). It has recently become more obvious that differences in long-range projections, laminar location, gene expression patterns, and membrane physiology are functionally relevant features to characterize excitatory cortical neurons (Economo et al. 2018; Gouwens et al. 2019). Furthermore, it is widely recognized that the activity of cortical neurons depends on their intrinsic membrane properties dictating its excitability, in addition to the synaptic inputs they receive (Llinás 1988). For example, two pyramidal neurons who receive the same input might react dramatically differently due to having different membrane excitability, possibly dictated by differences in membrane resistance, rheobase currents, and/or threshold potentials.

Building on the understanding of the intrinsic and extrinsic characteristics that define cortical excitatory neuron functionality, attention turns to the mechanisms of cortical communication. The intricate morphological and physiological properties of these neurons lay the groundwork for understanding the cortical network's communication strategies (e.g., integration of long-range inputs). Specifically, an idea in the field is that the cortex uses two principal methods for intracortical communication (Sherman and Guillery 2011): direct long-range glutamatergic projections (Rockland and Pandya 1979; Mason and Larkman 1990; Petreanu et al. 2007) and cortico-thalamo-cortical pathways, also known as trans-thalamic pathways (Guillery 1995; Shumikhina and Molotchnikoff 1999; Soares et al. 2004; Theyel et al. 2010; Sherman and Guillery 2011).

The transthalamic model proposes a hierarchical structure including various cortical areas and thalamic nuclei (Shepherd and Yamawaki 2021; Mo and Sherman 2019). This model highlights the diverse outputs from the cortex to the thalamus, including transthalamic pathways, emphasizing the complex network of connections that facilitate communication across different cortical regions. A recent idea in transthalamic architecture suggests that it plays a significant role in consciousness-related behaviors as suggested by Shepherd and Yamawaki (Shepherd and Yamawaki 2021). Within this framework, layer 5 pyramidal neurons projecting to the pyramidal tract are thought to be crucial for integrating apical and basal inputs via active dendritic processes, supporting the idea of coincidence detection (Larkum et al. 1999; Larkum et al. 2009; Larkum 2013; Llinás and Ribary 2006; Takahashi et al. 2020). Although the transthalamic model is an interesting idea, this dissertation focuses on studying direct, intracortical communication.

In parallel to the transthalamic pathways, the intracortical/corticocortical pathways are more direct and travel through either the white matter tracts or deep layers (Rocco and Brumberg 2007). Cortical sensory areas process information in a hierarchical fashion (Felleman and Van Essen 1991), where primary sensory areas (e.g., vS1) process thalamocortical information and send it in to secondary sensory (e.g., vS2) or motor (vM1) areas in a feedforward fashion for further processing and association . Interestingly, every higher cortical area sends a reciprocal feedback input (Rockland and Pandya 1979; Felleman and Van Essen 1991), suggested to provide excitatory glutamatergic inputs to manipulate the excitability of cells in primary sensory areas to alter how they process sensory information (Gilbert and Li 2013; Bastos et al. 2012; Gilbert and Sigman 2007).

One persistent idea in the field is that feedforward pathways have “driver-like” activity, whereas feedback pathways have “modulating-type” activity (De Pasquale and Sherman 2011; Sherman and Guillery 2011). The drivers vs. modulators idea was initially proposed for pathways targeting core thalamic relay cells with drivers being sensory afferents and modulators being of cortical origin (Crick and Koch 1998; Sherman and

Guillery 1996; Sherman and Guillery 1998), but has now developed to include direct intracortical connections (Sherman and Guillery 2011), and it characterizes glutamatergic pathways by certain anatomical and functional properties.

Anatomically, driver pathways have thick axons with large, dense terminal arborization in post-synaptic perisomatic dendrites that possess fast- ionotropic glutamatergic receptors (Sherman and Guillery 2011). Modulating pathways have thin axons with small, sparse terminal arborization on post-synaptic apical dendrites that possess both ionotropic and metabotropic receptors (Sherman and Guillery 2011). Physiologically, driving synapses exhibit short-term depression, defined as a strong excitatory post-synaptic potential (EPSP) to the initial stimulus in a train of activity and it decreases with subsequent stimuli (Fioravante and Regehr 2011). Modulating synapses exhibit short-term facilitation defined as a weak initial EPSP with increasing strength in subsequent stimuli (Covic and Sherman 2011). The difference in the dynamic nature of driver and modulator synapses allows them to perform distinct computations for information processing (Silver 2010). For example, driver inputs efficiently communicate sensory information with initial strong inputs, thought to be those communicating receptive field properties (i.e., afferent sensory information; Sherman and Guillery 1998). Conversely, modulating inputs generate graded potentials in the post-synaptic neurons with repetitive activity, perhaps altering the responses of targeted neurons to “driver” inputs (Sherman and Guillery 1998; Sherman and Guillery 2011; Covic and Sherman 2011; De Pasquale and Sherman 2011). Interestingly, no behavioral correlates have been attributed to short-term facilitation in the neocortex, which is a topic in which much current research focuses on (Jackman and Regehr 2017), including chapter 2 in this dissertation.

A large gap in knowledge lies in our understanding of the dynamic nature of long-range intracortical synapses and how they process sensory information, particularly in the integration of sensory input to generate a motor/behavioral response. It is thought that different long-range cortical pathways from primary sensory cortices are vital for the specialized processing of sensory information. These parallel cortical streams are believed to support distinct facets of sensory perception and sensorimotor coordination, perhaps depending on their target (Goodale and Milner 1992; Mesulam 1998; Yamashita et al. 2013). However, the cellular and network mechanisms that underpin sensorimotor processing remain largely elusive. Therefore, this dissertation focuses on understanding the cellular and synaptic mechanisms governing the activity between the reciprocally connected vS1 and vM1, thought to be the highest level in sensorimotor processing (Kleinfeld et al. 1999)

The reciprocally connected vS1 and vM1. In Chapter 2, we performed a full characterization of the synaptic communication between vS1 and vM1. The vS1 – vM1 feedforward pathway is distinct from other cortical sensory pathways and is thought to encode object detection and location (by their main sensors, the whiskers; Chen et al., 2013; Yamashita et al., 2013). Literature shows that the sensory signals created by whisker contacts are quickly communicated (millisecond timescale) from vS1 to vM1, thought to convey the detection and location of an object (Yamashita et al. 2013; Matyas et al. 2010). Although there is no general consensus for the function of vM1, studies have shown that activating it causes rhythmic whisking (Carvell et al. 1996), particularly by controlling the protraction of the whiskers (Matyas et al. 2010). Furthermore, it is important to understand the dynamic nature of these pathways in the context of whisking.

One elegant study showed that vS1 communicates two kinds of whisker stimuli differentially (Yamashita et al. 2013). During exploratory behavior (i.e., repetitive whisking), vM1-projecting pyramidal neurons from L2/3 seem to be transiently active in the initial part of a whisking bout, whereas those L2/3 neurons that project to vS2 exhibit a sustained activity pattern. Interestingly, during quiet wakefulness (i.e., not actively exploring), vM1- projecting L2/3 neurons are transiently active (short period) to a passive unexpected stimulus, whereas those neurons projecting to vS2 lacked a significant increase in activity. These results suggest that the vS1 – vS2 pathway is important for communicating information regarding the quality of object features over time, as seen by the strong responsiveness of these neurons across time during repetitive whisker touch (Yamashita et al. 2013; Chen et al. 2013). Furthermore, it is hypothesized that the vS1 – vM1 pathway communicates stimulus onset, thus important for prompting vM1 to initiate whisking for exploratory behavior (Matyas et al. 2010; Yamashita et al. 2013; Chen et al. 2013; Ferezou et al. 2007).

In contrast, the vM1 – vS1 feedback pathway provides diffuse projections throughout almost layers of vS1 (except L4). It has been proposed that vS1 and vM1 do not process information in a hierarchical fashion, due to the nature of their functions (sensory vs motor; Sherman and Guillery 2011). It is time to re-evaluate this notion because these reciprocally connected pathways follow the same anatomical rules of hierarchical organization (Rockland and Pandya 1979; Felleman and Van Essen 1991) where vS1 targets superficial layers of vM1, whereas vM1 preferentially diffusely targets superficial layers 1 & 2/3, and also deep layer 5 and 6 (White and DeAmicis 1977; Fabri and Burton 1991; Aroniadou and Keller 1993; Miyashita et al. 1994; Izraeli and Porter

1995; Veinante and Deschênes 2003; Zhang and Deschênes 1997). Albeit the feedback projection is not as strong as the vS1 – vM1 pathway, the inputs that vM1 provides to vS1 are strong enough to alter neuronal responsiveness, perhaps during vibrissa-dependent tasks, according to ongoing behavior and context to satisfy momentary demands (Felleman and Van Essen 1991; Gilbert and Sigman 2007; Briggs 2020; Kwon et al. 2016; Petreanu et al. 2012; Gilbert and Li 2013). This modulation of activity happens through a variety of cellular, synaptic, and circuit mechanisms. For example, it has been suggested that this feedback pathway can release L2/3 pyramidal neuron dendrites from inhibition by somatostatin-expressing (SOM) interneurons, via a di-synaptic feedforward inhibitory circuit (i.e., inhibition of inhibition) by activating vasointestinal peptide-expressing (VIP) interneurons, who suppress SOM interneurons (Lee et al. 2013; Pi et al. 2013; Yang et al. 2016; Yu et al. 2019). The effects of vM1 feedback have been extensively studied in superficial layers of vS1, whereas much less is known about its effects in deep layers.

Feedback influence onto deep layers has been thought to communicate context-dependent modulatory signals based on the motor plan (repetitive, rhythmic whisking; Carvell et al. 1996), encoding for complex cognitive functions like coincidence detection and predictive coding (Bastos et al. 2012; Kleinfeld et al. 1999; Kleinfeld et al. 2006). Layer 6 (L6) is especially interesting due to its ability to link intracortical and thalamocortical inputs (Constantinople and Bruno 2013; Crandall et al. 2017; Egger et al. 2020), control the flow of information into the cortex (Crandall et al. 2015), as well as controlling the gain of sensory inputs across the cortical column directly through the activity of corticothalamic cells (CT) or the recruitment of translaminar interneurons (Olsen et al. 2012; Bortone et al. 2014; Simons and Carvell 1989; Bruno and Simons 2002; Lee et al. 2008; Kinnischtzke et al. 2014; Kinnischtzke et al. 2016; Kim et al. 2014; Frandolig et al. 2019).

Furthermore, the nature of the synaptic dynamic properties of the vS1 – vM1 pathways (i.e., either transient or repetitive activity) suggest an involvement in communicating specific features of self-generated whisker movements in real time (i.e., the motor plan). Therefore, it is essential to study the synaptic, cellular and circuit mechanisms that govern the communication between long-range cortical pathways, involved in sensorimotor processing. In Chapter 2, we performed a comprehensive study by examining the connectivity of the reciprocally connected vS1 and vM1.

Motor cortex can modulate thalamic processing through L6 corticothalamic cells of vS1. L6 of vS1 is the least studied layer, yet it has major significant roles like gating the flow of sensory information in the thalamus via their topographically aligned corticothalamic (CT) projections (Temereanca and Simons, 2004), and within the cortex. CT neurons represent the most numerous type of neurons in L6 (~60%; Usrey and Sherman, 2023), and can directly modulate sensory flow in the thalamus (Crandall et al., 2015; Pauzin and Krieger, 2018; Ansorge et al., 2020; Born et al., 2021), and in cortex via the recruitment of L6 trans-laminar parvalbumin-expressing interneurons (Olsen et al., 2012; Bortone et al., 2014; Frandolig et al., 2019; Pauzin et al., 2019). Interestingly, many studies have reported that most L6 CT neurons are silent during behavioral tasks, and do not respond to afferent sensory inputs (Tsumoto and Suda, 1980; Landry and Dykes, 1985; Sirota et al., 2005; Briggs and Usrey, 2009; Kwegyir-Afful and Simons, 2009; Vélez-Fort et al., 2014), although some receive sensory inputs (Crandall et al., 2017). One question that arises is: when are CT neurons active, and who engages their activity?

There has been a recent increase in studies trying to understand the functional impact of L6 CT neuron activity *in vivo* and have provided various invaluable insights. Relevant to this dissertation, a study performed in our laboratory (Dash et al., 2022) established that a proportion of L6 CT cells are highly active when mice are actively whisking or modulated during motor behaviors, possibly via the inputs from vM1. Indeed, vM1 send the densest and strongest projections to L6a (Deschênes et al., 1998; Zhang and Deschênes, 1998; Kinnischtzke et al., 2014, 2016; Whilden et al., 2021; Martinetti & Bonekamp et al., 2022), its activity is highly elevated during whisking (Carvell et al., 1996), and can influence sensory throughput in the thalamus via the recruitment of L6 CT neurons in vS1 (Lee et al. 2008) and reviewed by Briggs and Usrey (2008). This literature provides insights to the functional relevance of this pathway in active sensation, but we know much less about the synaptic mechanisms that guide these observed behaviors, perhaps due to the neuronal heterogeneity in L6a (Briggs, 2010; Thomson, 2010). In chapter 3, the overarching goal is to understand the synaptic mechanisms governing the recruitment of L6a CT circuits.

L6a can be subdivided into two sections along its vertical axis, characterized by the presence of distinct CT circuits (Bourassa et al., 1995; Chevée et al., 2018; Frandolig et al., 2019; Whilden et al., 2021). By performing a thorough characterization of the anatomical layout of CT circuits in L6a of vS1, we show that CT neurons that only project to the VPm represent most of the CT population (~84%) in the upper section of L6a (L6a$_U$), whereas those who project to both the VPm and POm represent most (~70%) of the CT population in the lower section of L6a (L6a$_L$). L6a$_U$ CT (VPm CT neurons in chapter 3) neurons have been shown to be responsive to afferent sensory input coming directly from the thalamus (Vélez-Fort et al., 2014, 2018; Whilden et al., 2021), whereas no sensory inputs have been observed directly in L6aL CT neurons (Dual CT neurons in chapter 3). Interestingly, in this dissertation I show that vM1 preferentially targets Dual CT neurons in L6a$_{\mathrm{L}}$ and provides weak inputs to VPm CT neurons in L6a$_{\mathrm{U}}$. These results suggest that CT circuits in L6a of vS1 have perhaps distinct functions in processing sensory and motor inputs. It is plausible that L6aU circuits are more involved in gating sensory flow into and within vS1 (Olsen et al., 2012; Bortone et al., 2014; Kim et al., 2014; Crandall et al., 2017; Frandolig et al., 2019; Whilden et al., 2021), whereas L6aL are more involved in the output of the cortex with a strong motor influence (Dash et al., 2022). Furthermore, in chapter 4 I report preliminary experiments focusing on accessing L6a CT circuits separately to study the specific influence that L6aU and L6aL have in the somatosensory thalamus.

Furthermore, intracortical pathways within vM1 and vS1 feature diffuse projections, making it difficult to study with conventional electrophysiological techniques (i.e., electrical stimulation; Rocco and Brumberg 2007). For example, if collected in the right configuration, the corticothalamic pathway from vS1 to the somatosensory thalamus (Vpm and POm) can be isolated and studied using electrical stimulation due to the high density of clustered axons, making an easy target for electrical stimulation (Agmon and Connors 1991). Therefore, many studies have tried to study cortical long-range connections using optogenetics, a technique that allows the spatiotemporal control of pathways to study circuits (Yizhar et al. 2011). In the next section, I will introduce optogenetic techniques and how they have allowed us to study cortical communication.

1.4 – Optogenetic technology to study intracortical and corticothalamic pathways

“Optogenetics” involves the genetic introduction of light-sensitive proteins into specific neurons, enabling precise control over neuronal activity within intact, living neural circuits (Boyden et al. 2005; Nagel et al. 2003; Nagel et al. 2005). This neuronal control is through the expression of light-sensitive cation channels (Channelrhodopsins) that insert into neuronal membranes (Deisseroth et al. 2006; Mattis et al. 2011). The expression of these channels is driven by various methods, mostly involving genetics and viral strategies. Once these channels are functional, an experimenter can shine high powered LED light over them either in vitro or in vivo. The light will cause a change in conformation of the protein, which opens the pore of the channel and allows for cations to rush across the cell membrane, depolarizing the neuron and likely bringing it to action potential threshold (Boyden et al. 2005; Nagel et al. 2003; Nagel et al. 2005). Conversely, certain types of opsins suppress neuronal activity by enabling the influx of chloride ions or the efflux of protons, thus hyperpolarizing the cell membrane (Madisen et al. 2012). Optogenetics can thus be used to activate or suppress a very selective population of cells to determine how they affect their postsynaptic targets.

Conventional electrophysiological stimulation methods (i.e. electrical stimulation, glutamate uncaging) have been instrumental in providing key neuroscience data for decades. However, certain areas of the brain are more amenable to these approaches than others. For example, electrical stimulation of an axon tract can be a powerful way to drive afferent pathways to study their physiology in vivo or in vitro. Axons that are unidirectional and made up of all the same type of axon can be studied this way easily; stimulation of these axons will drive action potential firing in most if not all of the axons (e.g., the corticothalamic pathway; Agmon and Connors 1991), causing neurotransmitter release at their axon terminals. However, if the axons of the pathway you want to stimulate are not organized in this way, it will be impossible to know which axons you are stimulating, because you are just injecting direct current into the extracellular space. Optogenetics brings an advantage, as it can be expressed in a very specific pathway of interest (Gradinaru et al. 2010). Additionally, the stimulus (i.e. light) does not endogenously activate any pathway in the slice and will only activate the specific pathway, so that its effects on its target regions can be studied properly .

To express these Channelrhodopsin (ChR2) in neuronal membranes, there are a few major approaches. First, ChR2 expression can be driven via a Cre/lox system, which will express ChR2 only in a very specific set of neurons, where ChR2 genetic material is incorporated based on the co-expression of both Cre-recombinase and lox-p sites (Jackman et al. 2014; Yizhar et al. 2011; Madisen et al. 2012). Also, ChR2 can also be packaged into viruses that can be injected constitutively; these viruses will express in and surrounding the injection site of the virus after days to weeks of protein expression time.

Cre/lox driven optogenetics expression is driven in two ways, either by breeding specific transgenic mice together, or injecting viruses that will encode ChR2 if Cre-recombinase is present in the injection site. First is to use a Cre-driver mouse line to label the cells of interest with Cre-recombinase, and cross this mouse where ChR2 genetic material is flanked by lox-pp sites (Madisen et al. 2012). This will drive ChR2 expression wherever there is Cre-recombinase. If there is not a Cre-driver mouse line that will label your cells of interest, there are also viruses you can inject that will express these channels in a spatially restricted manner (Mattis et al. 2011).

Optogenetics has been immensely helpful in neuroscience research over the last 20 years, but every method comes with its pitfalls. The kinetics of the ChR2 protein have limits, such that when they are activated repetitively at a high frequency, the protein may not have time to fully recover from stimulation by the time the next stimulation comes, therefore the channel is not as functional (Nagel et al. 2005; Boyden et al. 2005; Lin 2011). This means it drives less current through the channel pore with each repetitive stimulation, causing an artificial short-term depression phenotype.

Understanding the pitfalls of using optogenetics to study synaptic properties is important, because short-term synaptic dynamics control the strength of specific synapses across the dimension of time (Fioravante and Regehr 2011; Abbott and Regehr 2004; Jackman and Regehr 2017). This is very realistic because neurons are not static and are constantly communicating with each other at various frequencies. The strength of a synapse will play a large role in determining if this will cause a cell to reach action potential threshold, and thus if the strength increases over time, it can shift from subthreshold to suprathreshold responses only by varying time. Alternatively, if the strength decreases over time, it can shift responses to subthreshold (Jackman and Regehr 2017; Fioravante and Regehr 2011; Silver 2010). These short-term patterns of activity add another dimension to neuronal communication that will be crucial to understanding behaviors relevant to this time scale (i.e. repetitive whisking in a mouse; Hass and Glickfeld 2016). Furthermore, it has been described that different viral serotypes can influence the rate of strength change over time of these synapses (Jackman et al. 2014). Each serotype has its own tropisms, rate of selectivity, and receptors used so this will all determine how the virus will express (Yizhar et al. 2011).

Furthermore, in chapter 2 we characterize many more aspects to consider if using it to study circuits, particularly in the acute brain slice preparation (Martinetti & Bonekamp et al. 2022).

Understanding the nuances and intricacies of how to use these tools properly is crucial to accurate data collection and interpretation. Optogenetics is a relatively new tool, only about 20 years old. This means there will undoubtedly be pitfalls and caveats with using these techniques, which need to be addressed. Many of these technical limitations arise when trying to stimulate them beyond their capability, meaning each identical stimulation will not cause the same response due to the factor of time and the rate of stimulation (Glasgow et al. 2019; Cho et al. 2019; Klapoetke et al. 2014). Thus, special considerations need to be in place when using optogenetics to study circuits, especially when studying how repetitive stimulation influences circuit activity. Other considerations that need to be made when using this tool *in vitro* include: concentration of divalent cations, such as calcium and magnesium, light power and power densitiy, spot size, viral serotype, and fusion protein (Asrican et al. 2013; Martinetti & Bonekamp et al. 2022).

Since the invention of optogenetics, many researchers have been continuously improving the tools and offering more and more variations to probe neural circuits in new ways (Yizhar et al. 2011). One of these improvements have been creating opsins with varied kinetic properties. Some opsins, such as Chronos (Klapoetke et al. 2014; Yizhar et al. 2011), are meant to have very fast kinetics, which would allow for the channel to recover fully before the next stimulation and could therefore be used for higher frequency stimulation of circuits. However, these improvements may come with their own pitfalls, for example Chronos has very low conductance, so even if the channel is opening with proper kinetics, the overall number of ions moving through will be very low.

1.5 – Goals of this dissertation

Understanding the mechanisms of cortical circuits is essential not only for probing models of brain disorders and creating therapies, as noted by Staiger and Petersen (2021), but also for enhancing our knowledge of sensorimotor processing. While considerable insights have been gained about sensorimotor functions in sub-cortical areas (Kleinfeld et al. 1999; Petersen 2019), our understanding of cortical sensorimotor processing remains limited. Despite detailed studies on the anatomical organization, the functional properties of long-range cortical synapses and their role in integrating sensory information are less understood. This has been perhaps due to the complicated nature of cortical anatomy and physiology, but studying the cortex has become more attainable with the recent advance of genetic techniques (i.e., optogenetics).

Due to the dynamic nature of sensorimotor behavior (i.e., repetitive whisking), studies focusing on the reciprocally connected vS1 – vM1 pathway have done so by assessing the short-term synaptic dynamics of these pathways (reviewed next). As noted by Yamashita (Yamashita et al. 2013), vS1 communicates different information to higher sensory areas, exhibiting two types of activity (passive and active touch). While sensory information derived from active touch gets relayed to both vS1 and vM1, only sensory information derived from passive touch is communicated to vM1. This suggests a mechanism that allows vS1 to communicate unexpected inputs to vM1 so it can initiate active whisking (Chen et al. 2013; Yamashita et al. 2013). Studies focusing on understanding the synaptic mechanisms of the cortical feedforward connectivity suggest that the vS1 – vM1 feedforward pathway exhibits short-term depression (Covic and

Sherman 2011; Rocco-Donovan et al. 2011; Petrof et al. 2015; Naskar et al. 2021), which was expected from this “feedforward driving” pathway (Sherman and Guillery 2011). Furthermore, these studies also suggest that cortical feedback pathway between vM – vS1 also exhibits short-term depressing synapses, which is contrary to the common belief that “feedback modulating” synapses exhibit short-term facilitation (Sherman and Guillery 2011; Zolnik et al. 2020). This discrepancy can perhaps be caused due to improper use of optogenetic methods to study cortical long-range interactions.

These conflicting reports point to a need to study long-range intracortical synapses rigorously in order to start understanding the dynamic nature of sensorimotor processing in the cortex. Therefore, chapter 2 in this dissertation focuses on assessing the synaptic properties and post-synaptic effects of the reciprocally connected pathways between vS1 and vM1 (Martinetti & Bonekamp et al. 2022). My central hypothesis is that **the vM1 – vS1 feedback pathway exhibits short-term facilitation and can alter the excitability, and thus responsiveness of excitatory cells in L2/3 and L6.** To examine this hypothesis, I used a combination of survival *in vivo* stereotaxic surgeries, electrophysiological, histological, and optogenetic methods. These techniques allowed me to complete the following goals:

1) **Examine the synaptic and cellular mechanisms that govern dynamic communication between the reciprocally connected vS1 – vM1 pathways (Chapter 2).**

<u>Hypotheses</u>: 1) the vS1 – vM1 feedforward pathway exhibits short-term depression, whereas the vM1 – vS1 feedback projection exhibits short-term facilitation. 2) The short-term facilitation observed in the feedback pathway is functionally relevant by altering the

excitability in targeted neurons.

2) **Understand the cellular and network mechanisms by which vM1 feedback modulates these distinct L6 corticothalamic circuits (Chapter 3).**

Hypotheses: 1) vM1 preferentially targets CT neurons located in the lower part of L6a in vS1. 2) L6a CT circuits are separated along the vertical depth of L6a.

BIBLIOGRAPHY

Abbott LF, Regehr WG (2004) Synaptic Computation. Nature Available at: https://doi.org/10.1038/nature03010.

Agmon A, Connors BW (1991) Thalamocortical responses of mouse somatosensory (barrel) cortex in vitro. Neuroscience 41:365–379.

Ahissar E, Haidarliu S, Zacksenhouse M (1997) Decoding temporally encoded sensory input by cortical oscillations and thalamic phase comparators. Proc Natl Acad Sci USA 94:11633–11638.

Ahissar E, Sosnik R, Haidarliu S (2000) Transformation from temporal to rate coding in a somatosensory thalamocortical pathway. Nature 406:302–306.

Ahissar E (1998) Temporal-code to rate-code conversion by neuronal phase-locked loops. Neural Comput 10:597–650.

Alcock J (2009) Animal Behavior: An Evolutionary Approach, Ninth Edition, 9th ed. Sunderland, Mass: Sinauer Associates is an imprint of Oxford University Press.

Ansorge J, Humanes-Valera D, Pauzin FP, Schwarz MK, Krieger P (2020) Cortical layer 6 control of sensory responses in higher-order thalamus. J Physiol (Lond) 598:3973–4001.

Armstrong-James M, Fox K (1987) Spatiotemporal convergence and divergence in the rat S1 “barrel” cortex. J Comp Neurol 263:265–281.

Aroniadou VA, Keller A (1993) The patterns and synaptic properties of horizontal intracortical connections in the rat motor cortex. J Neurophysiol 70:1553–1569.

Arvidsson J, Rice FL (1991) Central projections of primary sensory neurons innervating different parts of the vibrissae follicles and intervibrissal skin on the mystacial pad of the rat. J Comp Neurol 309:1–16.

Arvidsson J (1982) Somatotopic organization of vibrissae afferents in the trigeminal sensory nuclei of the rat studied by transganglionic transport of HRP. J Comp Neurol 211:84–92.

Asrican B et al. (2013) Next-generation transgenic mice for optogenetic analysis of neural circuits. Front Neural Circuits 7:160.

Bastos AM, Usrey WM, Adams RA, Mangun GR, Fries P, Friston KJ (2012) Canonical microcircuits for predictive coding. Neuron 76:695–711.

Belford GR, Killackey HP (1979a) Vibrissae representation in subcortical trigeminal centers of the neonatal rat. J Comp Neurol 183:305–321.

Belford GR, Killackey HP (1979b) The development of vibrissae representation in subcortical trigeminal centers of the neonatal rat. J Comp Neurol 188:63–74.

Born G, Schneider-Soupiadis FA, Erisken S, Vaiceliunaite A, Lao CL, Mobarhan MH, Spacek MA, Einevoll GT, Busse L (2021) Corticothalamic feedback sculpts visual spatial integration in mouse thalamus. Nat Neurosci 24:1711–1720.

Bortone DS, Olsen SR, Scanziani M (2014) Translaminar inhibitory cells recruited by layer 6 corticothalamic neurons suppress visual cortex. Neuron 82:474–485.

Bourassa J, Pinault D, Deschênes M (1995) Corticothalamic projections from the cortical barrel field to the somatosensory thalamus in rats: a single-fibre study using biocytin as an anterograde tracer. Eur J Neurosci 7:19–30.

Boyden ES, Zhang F, Bamberg E, Nagel G, Deisseroth K (2005) Millisecond-timescale, genetically targeted optical control of neural activity. Nat Neurosci 8:1263–1268.

Briggs F, Usrey WM (2009) Parallel processing in the corticogeniculate pathway of the macaque monkey. Neuron 62:135–146.

Briggs F (2010) Organizing principles of cortical layer 6. Front Neural Circuits 4:3.

Briggs F (2020) Role of feedback connections in central visual processing. Annu Rev Vis Sci 6:313–334.

Bruce LL, McHaffie JG, Stein BE (1987) The organization of trigeminotectal and trigeminothalamic neurons in rodents: a double-labeling study with fluorescent dyes. J Comp Neurol 262:315–330.

Bruno RM, Simons DJ (2002) Feedforward mechanisms of excitatory and inhibitory cortical receptive fields. J Neurosci 22:10966–10975.

Carvell GE, Miller SA, Simons DJ (1996) The relationship of vibrissal motor cortex unit activity to whisking in the awake rat. Somatosens Mot Res 13:115–127.

Carvell GE, Simons DJ, Lichtenstein SH, Bryant P (1991) Electromyographic activity of mystacial pad musculature during whisking behavior in the rat. Somatosens Mot Res 8:159–164.

Castro-Alamancos MA, Connors BW (1997) Thalamocortical synapses. Prog Neurobiol 51:581–606.

Chen JL, Carta S, Soldado-Magraner J, Schneider BL, Helmchen F (2013) Behaviour-dependent recruitment of long-range projection neurons in somatosensory cortex. Nature 499:336–340.

Chevée M, Robertson JDJ, Cannon GH, Brown SP, Goff LA (2018) Variation in activity state, axonal projection, and position define the transcriptional identity of individual neocortical projection neurons. Cell Rep 22:441–455.

Chiaia NL, Rhoades RW, Bennett-Clarke CA, Fish SE, Killackey HP (1991) Thalamic processing of vibrissal information in the rat. I. Afferent input to the medial ventral posterior and posterior nuclei. J Comp Neurol 314:201–216.

Cho YK, Park D, Yang A, Chen F, Chuong AS, Klapoetke NC, Boyden ES (2019) Multidimensional screening yields channelrhodopsin variants having improved photocurrent and order-of-magnitude reductions in calcium and proton currents. J Biol Chem 294:3806–3821.

Clarke T (2002) Mice make medical history. Nature.

Clarke WB, Bowsher D (1962) Terminal distribution of primary afferent trigeminal fibers in the rat. Exp Neurol 6:372–383.

Constantinople CM, Bruno RM (2011) Effects and mechanisms of wakefulness on local cortical networks. Neuron 69:1061–1068.

Constantinople CM, Bruno RM (2013) Deep cortical layers are activated directly by thalamus. Science 340:1591–1594.

Courtiol E, Wilson DA (2014) Thalamic olfaction: characterizing odor processing in the mediodorsal thalamus of the rat. J Neurophysiol 111:1274–1285.

Courtiol E, Wilson DA (2015) The olfactory thalamus: unanswered questions about the role of the mediodorsal thalamic nucleus in olfaction. Front Neural Circuits 9:49.

Covic EN, Sherman SM (2011) Synaptic properties of connections between the primary and secondary auditory cortices in mice. Cereb Cortex 21:2425–2441.

Crandall SR, Cruikshank SJ, Connors BW (2015) A corticothalamic switch: controlling the thalamus with dynamic synapses. Neuron 86:768–782.

Crandall SR, Patrick SL, Cruikshank SJ, Connors BW (2017) Infrabarrels Are Layer 6 Circuit Modules in the Barrel Cortex that Link Long-Range Inputs and Outputs. Cell Rep 21:3065–3078.

Crick F, Koch C (1998) Constraints on cortical and thalamic projections: the no-strong-loops hypothesis. Nature 391:245–250.

Dallos P, Oertel D (2008) The senses a comprehensive Reference. Elsevier.

Dash S, Autio DM, Crandall SR (2022) State-dependent modulation of activity in distinct layer 6 corticothalamic neurons in barrel cortex of awake mice. J Neurosci 42:6551–6565.

DeNardo LA, Berns DS, DeLoach K, Luo L (2015) Connectivity of mouse somatosensory and prefrontal cortex examined with trans-synaptic tracing. Nat Neurosci 18:1687–1697.

Deschenes M, Bourassa J, Parent A (1996) Striatal and cortical projections of single neurons from the central lateral thalamic nucleus in the rat. Neuroscience 72:679–687.

De Pasquale R, Sherman SM (2011) Synaptic properties of corticocortical connections between the primary and secondary visual cortical areas in the mouse. J Neurosci 31:16494–16506.

Deschênes M, Veinante P, Zhang ZW (1998) The organization of corticothalamic projections: reciprocity versus parity. Brain Res Brain Res Rev 28:286–308.

Diamond ME, Armstrong-James M, Budway MJ, Ebner FF (1992) Somatic sensory responses in the rostral sector of the posterior group (POm) and in the ventral posterior medial nucleus (VPM) of the rat thalamus: dependence on the barrel field cortex. J Comp Neurol 319:66–84.

Diamond ME, von Heimendahl M, Knutsen PM, Kleinfeld D, Ahissar E (2008) “Where” and “what” in the whisker sensorimotor system. Nat Rev Neurosci 9:601–612.

Diamond ME (1995) Somatosensory thalamus of the rat. In: The barrel cortex of rodents (Jones EG, Diamond IT, eds), pp 189–219 Cerebral Cortex. Boston, MA: Springer US.

Donoghue JP, Kerman KL, Ebner FF (1979) Evidence for two organizational plans within the somatic sensory-motor cortex of the rat. J Comp Neurol 183:647–663.

Donoghue JP, Kitai ST (1981) A collateral pathway to the neostriatum from corticofugal neurons of the rat sensory-motor cortex: an intracellular HRP study. J Comp Neurol 201:1–13.

Dörfl J (1982) The musculature of the mystacial vibrissae of the white mouse. J Anat 135:147–154.

Dörfl J (1985) The innervation of the mystacial region of the white mouse: A topographical study. J Anat 142:173–184.

Douglas RJ, Martin KAC (2004) Neuronal circuits of the neocortex. Annu Rev Neurosci 27:419–451.

Economo MN, Viswanathan S, Tasic B, Bas E, Winnubst J, Menon V, Graybuck LT, Nguyen TN, Smith KA, Yao Z, Wang L, Gerfen CR, Chandrashekar J, Zeng H, Looger LL, Svoboda K (2018) Distinct descending motor cortex pathways and their roles in movement. Nature 563:79–84.

Egger R, Narayanan RT, Guest JM, Bast A, Udvary D, Messore LF, Das S, de Kock CPJ, Oberlaender M (2020) Cortical output is gated by horizontally projecting neurons in the deep layers. Neuron 105:122-137.e8.

El-Boustani S, Sermet BS, Foustoukos G, Oram TB, Yizhar O, Petersen CCH (2020) Anatomically and functionally distinct thalamocortical inputs to primary and secondary mouse whisker somatosensory cortices. Nat Commun 11:3342.

Erzurumlu RS, Killackey HP (1980) Diencephalic projections of the subnucleus interpolaris of the brainstem trigeminal complex in the rat. Neuroscience 5:1891–1901.

Fabri M, Burton H (1991) Topography of connections between primary somatosensory cortex and posterior complex in rat: a multiple fluorescent tracer study. Brain Res 538:351–357.

Feldmeyer D (2012) Excitatory neuronal connectivity in the barrel cortex. Front Neuroanat 6:24.

Felleman DJ, Van Essen DC (1991) Distributed hierarchical processing in the primate cerebral cortex. Cereb Cortex 1:1–47.

Ferezou I, Haiss F, Gentet LJ, Aronoff R, Weber B, Petersen CCH (2007) Spatiotemporal dynamics of cortical sensorimotor integration in behaving mice. Neuron 56:907–923.

Fioravante D, Regehr WG (2011) Short-term forms of presynaptic plasticity. Curr Opin Neurobiol 21:269–274.

Frandolig JE, Matney CJ, Lee K, Kim J, Chevée M, Kim S-J, Bickert AA, Brown SP (2019) The synaptic organization of layer 6 circuits reveals inhibition as a major output of a neocortical sublamina. Cell Rep 28:3131-3143.e5.

Friedberg MH, Lee SM, Ebner FF (1999) Modulation of receptive field properties of thalamic somatosensory neurons by the depth of anesthesia. J Neurophysiol 81:2243–2252.

Furuta T, Nakamura K, Deschenes M (2006) Angular tuning bias of vibrissa-responsive cells in the paralemniscal pathway. J Neurosci 26:10548–10557.

Gabernet L, Jadhav SP, Feldman DE, Carandini M, Scanziani M (2005) Somatosensory integration controlled by dynamic thalamocortical feed-forward inhibition. Neuron 48:315–327.

Ghazanfar AA, Nicolelis MA (1997) Nonlinear processing of tactile information in the thalamocortical loop. J Neurophysiol 78:506–510.

Ghazanfar AA, Stambaugh CR, Nicolelis MA (2000) Encoding of tactile stimulus location by somatosensory thalamocortical ensembles. J Neurosci 20:3761–3775.

Gilbert CD, Li W (2013) Top-down influences on visual processing. Nat Rev Neurosci 14:350–363.

Gilbert CD, Sigman M (2007) Brain states: top-down influences in sensory processing. Neuron 54:677–696.

Gilbert CD, Wiesel TN (1983) Functional organization of the visual cortex. In: Proceedings of the 9th meeting of the international neurobiology society, pp 209–218 Progress in brain research. Elsevier.

Gil Z, Connors BW, Amitai Y (1999) Efficacy of thalamocortical and intracortical synaptic connections: quanta, innervation, and reliability. Neuron 23:385–397.

Glasgow SD, McPhedrain R, Madranges JF, Kennedy TE, Ruthazer ES (2019) Approaches and limitations in the investigation of synaptic transmission and plasticity. Front Synaptic Neurosci 11:20.

Goodale MA, Milner AD (1992) Separate visual pathways for perception and action. Trends Neurosci 15:20–25.

Gouwens NW et al. (2019) Classification of electrophysiological and morphological neuron types in the mouse visual cortex. Nat Neurosci 22:1182–1195.

Gouwens NW et al. (2020) Integrated morphoelectric and transcriptomic classification of cortical gabaergic cells. Cell 183:935-953.e19.

Gradinaru V, Zhang F, Ramakrishnan C, Mattis J, Prakash R, Diester I, Goshen I, Thompson KR, Deisseroth K (2010) Molecular and cellular approaches for diversifying and extending optogenetics. Cell 141:154–165.

Guillery RW, Harting JK (2003) Structure and connections of the thalamic reticular nucleus: Advancing views over half a century. J Comp Neurol 463:360–371.

Guillery RW (1995) Anatomical evidence concerning the role of the thalamus in corticocortical communication: a brief review. J Anat 187 (Pt 3):583–592.

Hass CA, Glickfeld LL (2016) High-fidelity optical excitation of cortico-cortical projections at physiological frequencies. J Neurophysiol 116:2056–2066.

Herfst LJ, Brecht M (2008) Whisker movements evoked by stimulation of single motor neurons in the facial nucleus of the rat. J Neurophysiol 99:2821–2832.

Hoogland PV, Welker E, Van der Loos H (1987) Organization of the projections from barrel cortex to thalamus in mice studied with Phaseolus vulgaris-leucoagglutinin and HRP. Exp Brain Res 68:73–87.

Huntsman MM, Porcello DM, Homanics GE, DeLorey TM, Huguenard JR (1999) Reciprocal inhibitory connections and network synchrony in the mammalian thalamus. Science 283:541–543.

Izraeli R, Porter LL (1995) Vibrissal motor cortex in the rat: connections with the barrel field. Exp Brain Res 104:41–54.

Jackman SL, Beneduce BM, Drew IR, Regehr WG (2014) Achieving high-frequency optical control of synaptic transmission. J Neurosci 34:7704–7714.

Jackman SL, Regehr WG (2017) The mechanisms and functions of synaptic facilitation. Neuron 94:447–464.

Jensen KF, Killackey HP (1987) Terminal arbors of axons projecting to the somatosensory cortex of the adult rat. I. The normal morphology of specific thalamocortical afferents. J Neurosci 7:3529–3543.

Jones EG, Wise SP (1977) Size, laminar and columnar distribution of efferent cells in the sensory-motor cortex of monkeys. J Comp Neurol 175:391–438.

Jones EG (1975) Some aspects of the organization of the thalamic reticular complex. J Comp Neurol 162:285–308.

Jones HE, Andolina IM, Ahmed B, Shipp SD, Clements JTC, Grieve KL, Cudeiro J, Salt TE, Sillito AM (2012) Differential feedback modulation of center and surround mechanisms in parvocellular cells in the visual thalamus. J Neurosci 32:15946–15951.

Kerekes P, Daret A, Shulz DE, Ego-Stengel V (2017) Bilateral Discrimination of Tactile Patterns without Whisking in Freely Running Rats. J Neurosci 37:7567–7579.

Killackey HP (1973) Anatomical evidence for cortical subdivisions based on vertically discrete thalamic projections from the ventral posterior nucleus to cortical barrels in the rat. Brain Res 51:326–331.

Kim J, Matney CJ, Blankenship A, Hestrin S, Brown SP (2014) Layer 6 corticothalamic neurons activate a cortical output layer, layer 5a. J Neurosci 34:9656–9664.

Kinnischtzke AK, Fanselow EE, Simons DJ (2016) Target-specific M1 inputs to infragranular S1 pyramidal neurons. J Neurophysiol 116:1261–1274.

Kinnischtzke AK, Simons DJ, Fanselow EE (2014) Motor cortex broadly engages excitatory and inhibitory neurons in somatosensory barrel cortex. Cereb Cortex 24:2237–2248.

Klapoetke NC et al. (2014) Independent optical excitation of distinct neural populations. Nat Methods 11:338–346.

Kleinfeld D, Ahissar E, Diamond ME (2006) Active sensation: insights from the rodent vibrissa sensorimotor system. Curr Opin Neurobiol 16:435–444.

Klein BG, Rhoades RW (1985) Representation of whisker follicle intrinsic musculature in the facial motor nucleus of the rat. J Comp Neurol 232:55–69.

Kleinfeld D, Berg RW, O'Connor SM (1999) Invited Review Anatomical loops and their electrical dynamics in relation to whisking by rat. Somatosens Mot Res 16:69–88.

Koralek KA, Jensen KF, Killackey HP (1988) Evidence for two complementary patterns of thalamic input to the rat somatosensory cortex. Brain Res 463:346–351.

Kwegyir-Afful EE, Simons DJ (2009) Subthreshold receptive field properties distinguish different classes of corticothalamic neurons in the somatosensory system. J Neurosci 29:964–972.

Kwon SE, Yang H, Minamisawa G, O’Connor DH (2016) Sensory and decision-related activity propagate in a cortical feedback loop during touch perception. Nat Neurosci 19:1243–1249.

Landry P, Dykes RW (1985) Identification of two populations of corticothalamic neurons in cat primary somatosensory cortex. Exp Brain Res 60:289–298.

Larkum ME, Nevian T, Sandler M, Polsky A, Schiller J (2009) Synaptic integration in tuft dendrites of layer 5 pyramidal neurons: a new unifying principle. Science 325:756–760.

Larkum ME, Zhu JJ, Sakmann B (1999) A new cellular mechanism for coupling inputs arriving at different cortical layers. Nature 398:338–341.

Larkum M (2013) A cellular mechanism for cortical associations: an organizing principle for the cerebral cortex. Trends Neurosci 36:141–151.

Lavallée P, Urbain N, Dufresne C, Bokor H, Acsády L, Deschênes M (2005) Feedforward inhibitory control of sensory information in higher-order thalamic nuclei. J Neurosci 25:7489–7498.

Lee S, Carvell GE, Simons DJ (2008) Motor modulation of afferent somatosensory circuits. Nat Neurosci 11:1430–1438.

Lee S, Kruglikov I, Huang ZJ, Fishell G, Rudy B (2013) A disinhibitory circuit mediates motor integration in the somatosensory cortex. Nat Neurosci 16:1662–1670.

Lin JY (2011) A user’s guide to channelrhodopsin variants: features, limitations and future developments. Exp Physiol 96:19–25.

Llinás R, Ribary URS (2006) Consciousness and the brain. Ann N Y Acad Sci 929:166–175.

Llinás RR (1988) The intrinsic electrophysiological properties of mammalian neurons: insights into central nervous system function. Science 242:1654–1664.

Lund RD, Webster KE (1967) Thalamic afferents from the spinal cord and trigeminal nuclei. An experimental anatomical study in the rat. J Comp Neurol 130:313–328.

Luo H, Hasegawa K, Liu M, Song W-J (2017) Comparison of the Upper Marginal Neurons of Cortical Layer 2 with Layer 2/3 Pyramidal Neurons in Mouse Temporal Cortex. Front Neuroanat 11:115.

Madisen L et al. (2012) A toolbox of Cre-dependent optogenetic transgenic mice for light-induced activation and silencing. Nat Neurosci 15:793–802.

Martinetti LE, Bonekamp KE, Autio DM, Kim H-H, Crandall SR (2022) Short-Term Facilitation of Long-Range Corticocortical Synapses Revealed by Selective Optical Stimulation. Cereb Cortex 32:1932–1949.

Mason A, Larkman A (1990) Correlations between morphology and electrophysiology of pyramidal neurons in slices of rat visual cortex. II. Electrophysiology. J Neurosci 10:1415–1428.

Mattis J, Tye KM, Ferenczi EA, Ramakrishnan C, O'Shea DJ, Prakash R, Gunaydin LA, Hyun M, Fenno LE, Gradinaru V, Yizhar O, Deisseroth K (2011) Principles for applying optogenetic tools derived from direct comparative analysis of microbial opsins. Nat Methods 9:159–172.

Matyas F, Sreenivasan V, Marbach F, Wacongne C, Barsy B, Mateo C, Aronoff R, Petersen CCH (2010) Motor control by sensory cortex. Science 330:1240–1243.

Ma PM, Woolsey TA (1984) Cytoarchitectonic correlates of the vibrissae in the medullary trigeminal complex of the mouse. Brain Res 306:374–379.

Mesulam MM (1998) From sensation to cognition. Brain 121 (Pt 6):1013–1052.

Miyashita E, Keller A, Asanuma H (1994) Input-output organization of the rat vibrissal motor cortex. Exp Brain Res 99:223–232.

Mo C, Sherman SM (2019) A Sensorimotor Pathway via Higher-Order Thalamus. J Neurosci 39:692–704.

Moore JD, Deschênes M, Furuta T, Huber D, Smear MC, Demers M, Kleinfeld D (2013) Hierarchy of orofacial rhythms revealed through whisking and breathing. Nature 497:205–210.

Moore JD, Mercer Lindsay N, Deschênes M, Kleinfeld D (2015) Vibrissa Self-Motion and Touch Are Reliably Encoded along the Same Somatosensory Pathway from Brainstem through Thalamus. PLoS Biol 13:e1002253.

Nagel G, Brauner M, Liewald JF, Adeishvili N, Bamberg E, Gottschalk A (2005) Light activation of channelrhodopsin-2 in excitable cells of Caenorhabditis elegans triggers rapid behavioral responses. Curr Biol 15:2279–2284.

Nagel G, Szellas T, Huhn W, Kateriya S, Adeishvili N, Berthold P, Ollig D, Hegemann P, Bamberg E (2003) Channelrhodopsin-2, a directly light-gated cation-selective membrane channel. Proc Natl Acad Sci USA 100:13940–13945.

Narayanan RT, Egger R, Johnson AS, Mansvelder HD, Sakmann B, de Kock CPJ, Oberlaender M (2015) Beyond Columnar Organization: Cell Type- and Target Layer-Specific Principles of Horizontal Axon Projection Patterns in Rat Vibrissal Cortex. Cereb Cortex 25:4450–4468.

Narayanan RT, Udvary D, Oberlaender M (2017) Cell Type-Specific Structural Organization of the Six Layers in Rat Barrel Cortex. Front Neuroanat 11:91.

Naskar S, Qi J, Pereira F, Gerfen CR, Lee S (2021) Cell-type-specific recruitment of GABAergic interneurons in the primary somatosensory cortex by long-range inputs. Cell Rep 34:108774.

Nicolelis MA, Chapin JK (1994) Spatiotemporal structure of somatosensory responses of many-neuron ensembles in the rat ventral posterior medial nucleus of the thalamus. J Neurosci 14:3511–3532.

Oberlaender M, de Kock CPJ, Bruno RM, Ramirez A, Meyer HS, Dercksen VJ, Helmstaedter M, Sakmann B (2012) Cell type-specific three-dimensional structure of thalamocortical circuits in a column of rat vibrissal cortex. Cereb Cortex 22:2375–2391.

Olsen SR, Bortone DS, Adesnik H, Scanziani M (2012) Gain control by layer six in cortical circuits of vision. Nature 483:47–52.

Olszewski J (1950) On the anatomical and functional organization of the spinal trigeminal nucleus. J Comp Neurol 92:401–413.

Pauzin FP, Krieger P (2018) A corticothalamic circuit for refining tactile encoding. Cell Rep 23:1314–1325.

Pauzin FP, Schwarz N, Krieger P (2019) Activation of corticothalamic layer 6 cells decreases angular tuning in mouse barrel cortex. Front Neural Circuits 13:67.

Petersen CCH (2014) Cortical control of whisker movement. Annu Rev Neurosci 37:183–203.

Petersen CCH (2019) Sensorimotor processing in the rodent barrel cortex. Nat Rev Neurosci 20:533–546.

Petreanu L, Gutnisky DA, Huber D, Xu N, O’Connor DH, Tian L, Looger L, Svoboda K (2012) Activity in motor-sensory projections reveals distributed coding in somatosensation. Nature 489:299–303.

Petreanu L, Huber D, Sobczyk A, Svoboda K (2007) Channelrhodopsin-2-assisted circuit mapping of long-range callosal projections. Nat Neurosci 10:663–668.

Petrof I, Viaene AN, Sherman SM (2015) Properties of the primary somatosensory cortex projection to the primary motor cortex in the mouse. J Neurophysiol 113:2400–2407.

Pierret T, Lavallée P, Deschênes M (2000) Parallel streams for the relay of vibrissal information through thalamic barreloids. J Neurosci 20:7455–7462.

Pinault D (2004) The thalamic reticular nucleus: structure, function and concept. Brain Res Brain Res Rev 46:1–31.

Pi H-J, Hangya B, Kvitsiani D, Sanders JI, Huang ZJ, Kepecs A (2013) Cortical interneurons that specialize in disinhibitory control. Nature 503:521–524.

Pluta SR, Telian GI, Naka A, Adesnik H (2019) Superficial Layers Suppress the Deep Layers to Fine-tune Cortical Coding. J Neurosci 39:2052–2064.

Qi J, Ye C, Naskar S, Inácio AR, Lee S (2022) Posteromedial thalamic nucleus activity significantly contributes to perceptual discrimination. PLoS Biol 20:e3001896.

Rhoades RW, Belford GR, Killackey HP (1987) Receptive-field properties of rat ventral posterior medial neurons before and after selective kainic acid lesions of the trigeminal brain stem complex. J Neurophysiol 57:1577–1600.

Rice FL, Mance A, Munger BL (1986) A comparative light microscopic analysis of the sensory innervation of the mystacial pad. I. Innervation of vibrissal follicle-sinus complexes. J Comp Neurol 252:154–174.

Rocco-Donovan M, Ramos RL, Giraldo S, Brumberg JC (2011) Characteristics of synaptic connections between rodent primary somatosensory and motor cortices. Somatosens Mot Res 28:63–72.

Rocco MM, Brumberg JC (2007) The sensorimotor slice. J Neurosci Methods 162:139–147.

Rockland KS, Pandya DN (1979) Laminar origins and terminations of cortical connections of the occipital lobe in the rhesus monkey. Brain Res 179:3–20.

Schuman B, Machold RP, Hashikawa Y, Fuzik J, Fishell GJ, Rudy B (2019) Four unique interneuron populations reside in neocortical layer 1. J Neurosci 39:125–139.

Severson KS, Xu D, Van de Loo M, Bai L, Ginty DD, O'Connor DH (2017) Active Touch and Self-Motion Encoding by Merkel Cell-Associated Afferents. Neuron 94:666-676.e9.

Shepherd GMG, Yamawaki N (2021) Untangling the cortico-thalamo-cortical loop: cellular pieces of a knotty circuit puzzle. Nat Rev Neurosci 22:389–406.

Sherman SM, Guillery RW (1996) Functional organization of thalamocortical relays. J Neurophysiol 76:1367–1395.

Sherman SM, Guillery RW (1998) On the actions that one nerve cell can have on another: distinguishing “drivers” from “modulators”. Proc Natl Acad Sci USA 95:7121–7126.

Sherman SM, Guillery RW (2011) Distinct functions for direct and transthalamic corticocortical connections. J Neurophysiol 106:1068–1077.

Shumikhina S, Molotchnikoff S (1999) Pulvinar participates in synchronizing neural assemblies in the visual cortex, in cats. Neurosci Lett 272:135–139.

Silver RA (2010) Neuronal arithmetic. Nat Rev Neurosci 11:474–489.

Simons DJ, Carvell GE (1989) Thalamocortical response transformation in the rat vibrissa/barrel system. J Neurophysiol 61:311–330.

Simons DJ (1978) Response properties of vibrissa units in rat SI somatosensory neocortex. J Neurophysiol 41:798–820.

Simons DJ (1995) Neuronal integration in the somatosensory whisker/barrel cortex. In: The barrel cortex of rodents (Jones EG, Diamond IT, eds), pp 263–297 Cerebral Cortex. Boston, MA: Springer US.

Sirota MG, Swadlow HA, Beloozerova IN (2005) Three channels of corticothalamic communication during locomotion. J Neurosci 25:5915–5925.

Soares JGM, Diogo ACM, Fiorani M, Souza APB, Gattass R (2004) Effects of inactivation of the lateral pulvinar on response properties of second visual area cells in Cebus monkeys. Clin Exp Pharmacol Physiol 31:580–590.

Sosnik R, Haidarliu S, Ahissar E (2001) Temporal frequency of whisker movement. I. Representations in brain stem and thalamus. J Neurophysiol 86:339–353.

Sreenivasan V, Karmakar K, Rijli FM, Petersen CCH (2015) Parallel pathways from motor and somatosensory cortex for controlling whisker movements in mice. Eur J Neurosci 41:354–367.

Staiger JF, Flagmeyer I, Schubert D, Zilles K, Kötter R, Luhmann HJ (2004) Functional diversity of layer IV spiny neurons in rat somatosensory cortex: quantitative morphology of electrophysiologically characterized and biocytin labeled cells. Cereb Cortex 14:690–701.

Staiger JF, Petersen CCH (2021) Neuronal circuits in barrel cortex for whisker sensory perception. Physiol Rev 101:353–415.

Takahashi N, Ebner C, Sigl-Glöckner J, Moberg S, Nierwetberg S, Larkum ME (2020) Active dendritic currents gate descending cortical outputs in perception. Nat Neurosci 23:1277–1285.

Temereanca S, Simons DJ (2004) Functional topography of corticothalamic feedback enhances thalamic spatial response tuning in the somatosensory whisker/barrel system. Neuron 41:639–651.

Theyel BB, Llano DA, Sherman SM (2010) The corticothalamocortical circuit drives higher-order cortex in the mouse. Nat Neurosci 13:84–88.

Thomson AM (2010) Neocortical layer 6, a review. Front Neuroanat 4:13.

Torvik A (1956) Afferent connections to the sensory trigeminal nuclei, the nucleus of the solitary tract and adjacent structures; an experimental study in the rat. J Comp Neurol 106:51–141.

Trageser JC, Keller A (2004) Reducing the uncertainty: gating of peripheral inputs by zona incerta. J Neurosci 24:8911–8915.

Tsumoto T, Suda K (1980) Three groups of cortico-geniculate neurons and their distribution in binocular and monocular segments of cat striate cortex. J Comp Neurol 193:223–236.

Urbain N, Deschênes M (2007a) A new thalamic pathway of vibrissal information modulated by the motor cortex. J Neurosci 27:12407–12412.

Urbain N, Deschênes M (2007b) Motor cortex gates vibrissal responses in a thalamocortical projection pathway. Neuron 56:714–725.

Usrey WM, Sherman SM eds. (2023) The cerebral cortex and thalamus. Oxford University PressNew York.

Veinante P, Deschênes M (2003) Single-cell study of motor cortex projections to the barrel field in rats. J Comp Neurol 464:98–103.

Veinante P, Jacquin MF, Deschênes M (2000) Thalamic projections from the whisker-sensitive regions of the spinal trigeminal complex in the rat. Journal of Comparative Neurology.

Vélez-Fort M, Bracey EF, Keshavarzi S, Rousseau CV, Cossell L, Lenzi SC, Strom M, Margrie TW (2018) A Circuit for Integration of Head- and Visual-Motion Signals in Layer 6 of Mouse Primary Visual Cortex. Neuron 98:179-191.e6.

Vélez-Fort M, Rousseau CV, Niedworok CJ, Wickersham IR, Rancz EA, Brown APY, Strom M, Margrie TW (2014) The stimulus selectivity and connectivity of layer six principal cells reveals cortical microcircuits underlying visual processing. Neuron 83:1431–1443.

Vincent SB (1913) The tactile hair of the white rat. J Comp Neurol 23:1–34.

von der Emde G, Warrant E eds. (2016) The ecology of animal senses. Cham: Springer International Publishing.

Wang X, Sommer FT, Hirsch JA (2011) Inhibitory circuits for visual processing in thalamus. Curr Opin Neurobiol 21:726–733.

Welker C (1971) Microelectrode delineation of fine grain somatotopic organization of (SmI) cerebral neocortex in albino rat. Brain Res 26:259–275.

Whilden CM, Chevée M, An SY, Brown SP (2021) The synaptic inputs and thalamic projections of two classes of layer 6 corticothalamic neurons in primary somatosensory cortex of the mouse. J Comp Neurol 529:3751–3771.

White EL, DeAmicis RA (1977) Afferent and efferent projections of the region in mouse SmL cortex which contains the posteromedial barrel subfield. J Comp Neurol 175:455–482.

Williams MN, Zahm DS, Jacquin MF (1994) Differential foci and synaptic organization of the principal and spinal trigeminal projections to the thalamus in the rat. Eur J of Neuroscience 6:429–453.

Woolsey TA, Van der Loos H (1970) The structural organization of layer IV in the somatosensory region (SI) of mouse cerebral cortex. The description of a cortical field composed of discrete cytoarchitectonic units. Brain Res 17:205–242.

Yamashita T, Pala A, Pedrido L, Kremer Y, Welker E, Petersen CCH (2013) Membrane potential dynamics of neocortical projection neurons driving target-specific signals. Neuron 80:1477–1490.

Yamashita T, Vavladeli A, Pala A, Galan K, Crochet S, Petersen SSA, Petersen CCH (2018) Diverse Long-Range Axonal Projections of Excitatory Layer 2/3 Neurons in Mouse Barrel Cortex. Front Neuroanat 12:33.

Yang GR, Murray JD, Wang X-J (2016) A dendritic disinhibitory circuit mechanism for pathway-specific gating. Nat Commun 7:12815.

Yizhar O, Fenno LE, Davidson TJ, Mogri M, Deisseroth K (2011) Optogenetics in neural systems. Neuron 71:9–34.

Yu J, Hu H, Agmon A, Svoboda K (2019) Recruitment of GABAergic Interneurons in the Barrel Cortex during Active Tactile Behavior. Neuron 104:412-427.e4.

Zhang ZW, Deschênes M (1997) Intracortical axonal projections of lamina VI cells of the primary somatosensory cortex in the rat: a single-cell labeling study. J Neurosci 17:6365–6379.

Zhang ZW, Deschênes M (1998) Projections to layer VI of the posteromedial barrel field in the rat: a reappraisal of the role of corticothalamic pathways. Cereb Cortex 8:428–436.

Zolnik TA, Ledderose J, Toumazou M, Trimbuch T, Oram T, Rosenmund C, Eickholt BJ, Sachdev RNS, Larkum ME (2020) Layer 6b Is Driven by Intracortical Long-Range Projection Neurons. Cell Rep 30:3492-3505.e5.

Zucker E, Welker WI (1969) Coding of somatic sensory input by vibrissae neurons in the rat’s trigeminal ganglion. Brain Res 12:138–156.

CHAPTER 2: SHORT-TERM FACILITATION OF LONG-RANGE CORTICOCORTICAL SYNAPSES REVEALED BY SELECTIVE OPTICAL STIMULATION

This chapter was adapted from L. E. Martinetti, K. E. Bonekamp, D. M. Autio, H.-H. Kim, S. R. Crandall, Short-Term Facilitation of Long-Range Corticocortical Synapses Revealed by Selective Optical Stimulation, Cerebral Cortex, 2022, 32, 1932–1949, by permission of Oxford University Press under license #5756681311681.

L. E. Martinetti and K. E. Bonekamp contributed equally to this work.

2.1 – Abstract

Short-term plasticity regulates the strength of central synapses as a function of previous activity. In the neocortex, direct synaptic interactions between areas play a central role in cognitive function, but the activity-dependent regulation of these long-range corticocortical connections and their impact on a postsynaptic target neuron is unclear. Here, we use an optogenetic strategy to study the connections between mouse primary somatosensory and motor cortex. We found that short-term facilitation was strong in both corticocortical synapses, resulting in far more sustained responses than local intra-cortical and thalamocortical connections. A major difference between pathways was that the synaptic strength and magnitude of facilitation were distinct for individual excitatory cells located across all cortical layers and specific subtypes of GABAergic neurons. Facilitation was dependent on the presynaptic calcium sensor synaptotagmin-7 and altered by several optogenetic approaches. Current-clamp recordings revealed that during repetitive activation, the short-term dynamics of corticocortical synapses enhanced the excitability of layer 2/3 pyramidal neurons, increasing the probability of spiking with activity. Furthermore, the properties of the connections linking primary with secondary somatosensory cortex resemble those between somatosensory-motor areas. These short-term changes in transmission properties suggest long-range corticocortical

synapses are specialized for conveying information over relatively extended periods.

2.2 – Introduction

The strength of a synapse depends on its recent history of activity, and the rules governing these use-dependent changes can vary widely from one synapse to another (Zucker and Regehr 2002). For example, repetitive activation leads to increased transmitter release (facilitation) from some synapses and decreases from others (depression), while many synapses respond with neither or both. These diverse forms of synaptic plasticity lend flexibility to neural circuits (Abbott and Regehr 2004), allowing communication to be regulated dynamically and selectively.

Communication within the neocortex is essential for sensation, motor control, and cognitive function. It contains three general excitatory connections: local intracortical synapses and long-range synapses from other cortical areas and the thalamus. Although the properties of thalamocortical and local cortical synapses are relatively well understood (Gil et al. 1999; Reyes and Sakmann 1999; Hempel et al. 2000; Feldmeyer et al. 2002; Bruno and Sakmann 2006), the effect of a signal transmitted from one cortical area to another is less clear. Obviously, understanding the properties of these synapses is essential to understanding corticocortical (CC) information processing and could provide insight into cortex-dependent processes such as attention, prediction, and awareness (Engel et al. 2001; Bastos et al. 2012; Gilbert and Li 2013).

Addressing this critical issue has been technically challenging, mainly because long-range CC synaptic pathways are not amenable to study using conventional electrophysiological approaches. For example, CC projections can be diffuse and reciprocal (Veinante and Deschenes 2003), making it difficult to access and accurately measure their synapses' relative contribution *in vivo*. Furthermore, in isolated brain preparations, electrical stimulation of CC inputs is problematic due to the proximity of these axons to non-targeted cells/axons (Dong et al. 2004; Covic and Sherman 2011; Rocco-Donovan et al. 2011; Petrof et al. 2015).

Optogenetic strategies overcome many of these problems (Petreanu et al. 2007; Cruikshank et al. 2010; Collins et al. 2018), but there are several difficulties in using these approaches to study synapses (Jackman et al. 2014). In most studies using opsins, the emphasis has been on isolating monosynaptic CC responses during perfusion of sodium and potassium channel blockers (Petreanu et al. 2009; Mao et al. 2011; Hooks et al. 2013; Yang et al. 2013; D'Souza et al. 2016; Young et al. 2021). This approach helps determine anatomical connections, but it can distort short-term dynamics (Cruikshank et al. 2010). In other studies, the characterization of synapses was limited (Kinnischtzke et al. 2014; Petrof *et al.* 2015; Zolnik et al. 2020; Naskar et al. 2021), and they did not address the pitfalls associated with using opsins to study synapses, such as artificial depression (Zhang and Oertner 2007; Jackman et al. 2014).

Here we apply an optogenetic strategy that overcomes these difficulties to investigate the connections between mouse vibrissal primary sensory (vS1) and motor cortex (vM1) (White and DeAmicis 1977; Porter and White 1983), two areas essential for active sensation, motor execution, and sensorimotor integration (Kleinfeld et al. 2006; Diamond et al. 2008). Contrasting with most excitatory synapses in the neocortex, we find that monosynaptic CC responses underwent short-term facilitation and that this synaptic adjustment plays a critical role in controlling the excitability of pyramidal cells. Therefore, long-range CC synapses appear specialized for carrying signals over sustained periods.

2.3 – Materials and Methods

Animals. All procedures were carried out in accordance with the National Institutes of Health (NIH) Guidelines for the Care and Use of Laboratory Animals and approved by the Michigan State University Institutional Animal Care and Use Committee (IACUC). We used the following mouse lines in this study: Crl: CD1 (ICR) (Charles River: 022), Ai14 (Jackson Labs: 007908) (Madisen et al. 2010), *PV-Cre* (Jackson Labs: 008069) (Hippenmeyer et al. 2005), *SOM-IRES-Cre* (Jackson Labs: 013044) (Taniguchi et al. 2011), *VIP-IRES-Cre* (Jackson Labs: 010908) (Taniguchi et al. 2011), *Scnn1a-Tg3-Cre* (Jackson Labs: 009613) (Madisen et al. 2010), *Syt7* knockout (Jackson Labs: 004950) (Chakrabarti et al. 2003), *Ntsr1-Cre* (MMRRC: 017266-UCD) (Gong et al. 2007), *Rbp4-Cre* (MMRRC: 031125-UCD) (Gong et al. 2007), and *5HT3a-EGFP* (MMRRC: 000273-UNC). The *Ntsr1-Cre*, *Rbp4-Cre*, *Scnn1a-Tg3-Cre*, *Syt7* knockout, and *5HT3a-EGFP* mouse lines had ICR genetic backgrounds. All mice, except for ICR, *Syt7* knockout, and *5HT3a-EGFP* mice, were bred by crossing homozygous or heterozygous Cre mice with homozygous Ai14 reporter mice, resulting in experimental mice that were heterozygous for the indicated genes. Animals were group-housed with same-sex littermates in a dedicated animal care facility maintained on a 12:12 hour light-dark cycle. Food and water were available *ad libitum*. We used both male and female mice in this study.

Stereotaxic virus injections. For all functional experiments characterizing the properties of CC synapses, we used an adeno-associated virus (AAV2) that encoded genes for hChR2 (H134R)-EYFP fusion proteins (rAAV2/hSyn-hChR2[H134R]-eYFP-WPREpA, AV4384, University of North Carolina Viral Vector Core). For the AAV serotype experiments, we also used the following AAV vectors obtained from Addgene: pAAV1-

hSyn-hChR2(H134R)-EYFP, pAAV5-hSyn-hChR2(H134R)-EYFP, and pAAV9-hSyn-hChR2(H134R)-EYFP (Addgene plasmid # 26973). For the fusion protein experiment, we used AAV2/hSyn-hChR2(H134R)-mCherry (AV4385, University of North Carolina Viral Vector Core). Retrograde-Cre experiments were carried out similarly, with injections of AAVretro-Ef1a-mCherry-IRES-Cre (Addgene plasmid # 55632) into vS1 followed by an AAV injection in vM1 that drove Cre-dependent expression of ChR2 (pAAV1-hSyn-hChR2(H134R)-EYFP, Addgene plasmid # 26973). We performed dual-optogenetic experiments with injections of rAAV2/hSyn-hChR2[H134R]-eYFP-WPREpA (AV4384, University of North Carolina Viral Vector Core) into vS1 followed by injecting AAV2/hsyn-Flex-ChrimsonR-tdT (AV6555, University of North Carolina Viral Vector Core) into vM1 1-week after of a PV-Cre mouse. We achieved selective optical control of local excitatory neurons and axons/terminals by injecting a Cre-dependent AAV2 in Cre-driver mice (Scnn1a-Tg3-Cre and Rbp4-Cre) (rAAV2/EF1a-DIO-hChR2(H134R)-eYFP, AV4378, University of North Carolina Viral Vector Core).

For all surgeries, the virus was injected unilaterally into vS1 or vM1 of mice in vivo, as previously described (Crandall et al. 2015; Crandall et al. 2017). Injections were normally performed on mice ~3 weeks old (Mean injection age: 22.2 ± 0.7 days, range 17-42 days). Briefly, mice were anesthetized with a Ketamine-Dexdomitor mixture diluted in sterile saline (KetaVed, 70 mg/kg; Dexdomitor, 0.25 mg/kg; intraperitoneally). Once deeply anesthetized, mice were placed into a digital stereotaxic frame with an integrated warming base that maintained core body temperature (Stoelting). A thin layer of ophthalmic ointment was applied to the eyes to prevent drying (Patterson Veterinary Artificial Tears). Next, an incision was made over the skull by scalpel or fine surgical scissors, the scalp and periosteum overlying the skull deflected, and a small craniotomy made over the target site. A small volume of the virus was then pressure-ejected via a glass micropipette attached to a Picospritzer pressure system (0.1-0.2 μl per injection site over 5-10 min; titer = 3.1-3.5 x 1012 viral genomes/ml). In some experiments, we used a virus-retrobead or saline-retrobead mixture (red RetroBeads, Lumafluor, Cat# R180). When comparing different AAV serotypes, we kept titer levels consistent by diluting each viral preparation to the same titer (3.1 x 1012 viral genomes/ml) just before intracranial injection. Following injection, the pipette was held in place for an additional 5-10 min before being slowly advanced or withdrawn from the brain. After surgery, the scalp was closed with a surgical adhesive (GLUture), and animals were given Antisedan (2.5 mg/kg) to reverse the effects of Dexdomitor. Mice were allowed to recover on a heating pad for 1 hr before returning to their home cage. Most experiments were performed ~3 weeks after the virus injections to allow sufficient expression (Mean expression time: 20.4 ± 0.3, range 11-25 days). Coordinates from bregma for vS1 were 3.4 mm lateral, 0.8 mm posterior, 0.40, and 1.0 mm depth. Coordinates for vM1 were 1.25 mm lateral, 0.9 and 1.3 mm anterior, 0.40, and 1.0 mm depth. Coordinates for VPm were 1.8 mm lateral, 0.75 mm posterior, 3.05 mm depth.

In vitro slice preparation. After allowing ~3 weeks for ChR2-EYFP expression (Mean experimental age: 44.0 ± 3.3 days, Median age: 41 days, range 30-259 days), acute coronal brain slices (300 μm thick) containing vM1 and vS1 were prepared for in vitro recording, as described previously (Crandall et al. 2010; Crandall et al. 2017). In four mice, acute thalamocortical brain slices (300 μm thick) containing VPm and vS1 were prepared, as described previously (Agmon and Connors 1991; Crandall et al. 2017).

Briefly, animals were anesthetized with isoflurane before being decapitated. Brains were removed and placed in a cold (~4° C) oxygenated (95% O2, 5% CO2) slicing solution containing (in mM) 3 KCl, 1.25 NaH2PO4, 10 MgSO4, 0.5 CaCl2, 26 NaHCO3, 10 glucose, and 234 sucrose. Brain slices were cut using a vibrating tissue slicer (Leica, VT1200S) and then transferred to a holding chamber with warm (32° C) oxygenated artificial cerebrospinal fluid (ACSF) containing (in mM): 126 NaCl, 3 KCl, 1.25 NaH2PO4, 2 MgSO4, 2 CaCl2, 26 NaHCO3, and 10 glucose. Slices were maintained at 32° C for 20 min and then at room temperature for a minimum of 40 min before recording. Slices containing the injection site were always collected for imaging to confirm injection site accuracy and assess tissue health. We only considered mice in which there were no signs of tissue damage or off-target injections.

*In Vitro Electrophysiological Recordings and Data Acquisitio*n. Individual brain slices (300 μm) were transferred to a submersion-type recording chamber and bathed continually (2.5 - 3.0 ml/min) with warm (32 ± 1°C) oxygenated ACSF containing (in mM): 126 NaCl, 3 KCl, 1.25 NaH2PO4, 1 MgSO4, 1.2 CaCl2, 26 NaHCO3, and 10 glucose. Neurons were visualized using infrared differential interference contrast optics (IR-DIC) with a Zeiss Axio Examiner.A1 microscope equipped with a 40x water immersion objective (Zeiss, W Plan-Apo 40x/1.0NA) and video camera (Olympus, XM10-IR). Whole-cell recordings were obtained using patch pipettes with tip resistances of 4-6 MΩ when filled with a potassium-based internal solution containing (in mM): 130 K-gluconate, 4 KCl, 2 NaCl, 10 HEPES, 0.2 EGTA, 4 ATP-Mg, 0.3 GTP-Tris, and 14 phosphocreatine-K (pH 7.25, 290 mOsm). Voltages were corrected for a -14 mV liquid junction potential. The average reversal potential for GABAA receptor-mediated inhibitory responses was -91 mV when measured in excitatory cortical cells (n = 3 cells). The calculated reversal potential was -95 mV. Neurobiotin (0.25%, w/v; Vector Laboratories) was added to the internal solution to inject into neurons during whole-cell recordings for subsequent identification in a subset of experiments.

Electrophysiological data were acquired and digitized at 20 kHz using Molecular Devices hardware and software (MultiClamp 700B amplifier, Digidata 1550B4, pClamp 11). Signals were low-pass filtered at 10 kHz (current-clamp) or 3 kHz (voltage-clamp) prior to digitizing. During recordings, the pipette capacitances were neutralized, and series resistances (typically 10-25 MΩ) were compensated online (100% for current-clamp and 70-80% for voltage-clamp). Series resistances were continually monitored and adjusted during experiments to ensure sufficient compensation. The local field potential (LFP) was monitored with a patch-style pipette (~0.6 MΩ) filled with 3 M NaCl, and signals were band-pass filtered between 0.1 Hz – 4 kHz. The LFP pipette was placed in L1 for recordings in vS1 and L2/3 for recordings in vM1. Cell attached recordings were obtained using patch-style pipettes filled with a potassium-based internal solution (see above), and signals were high pass filtered (100 Hz). All pharmacological agents were bath-applied at least 10 min before subsequent experimental tests. Pharmacological agents included Tetrodotoxin citrate (TTX, Tocris, Cat# 1069), 4-Aminopyridine (4-AP, Sigma, Cat# A78403), DL-AP5 (Sigma, Cat# A5282), DNQX (Sigma, Cat# D0540), Picrotoxin (Sigma, Cat# P1675), and CGP 55845 hydrochloride (Tocris, Cat# 1248).

Photostimulation. ChR2 was optically excited using a high-power white light-emitting diode (LED) (Mightex, LCS-5500-03-22) driven by a LED controller (Mightex, BLS-1000-2). For the two-color photostimulation experiments (Figure 2.13), ChR2 and

Chrimson were excited using a high-power blue (455 nm; LCS-0455-03-22) and red (625 nm; LCS-0625-03-22) LED, respectively, combined by a multi-wavelength beam combiner (Mightex, LCS-BC25-0495). LED on/off times were fast (< 50 µs) and of constant amplitude and duration when verified with a fast photodiode (Thorlabs, DET36A). The light was collimated and reflected through a single-edge dichroic beam-splitter (Semrock, FF660-FDi02) and a high-magnification water immersion objective (Zeiss, W Plan-Apo 40x/1.0 NA), resulting in an estimated spot diameter of ~1500 µm and maximum white LED power at the focal plane of ~32 mW (~18 mW/mm2). Stimuli were delivered as 0.5 ms flashes and were directed at ChR2-expressing axons/terminals by centering the light over the recorded cell. The LED intensity was typically adjusted to evoke a 200 pA EPSC in the recorded neuron when held in voltage-clamp at -94 mV, near the reversal potential for inhibition (see Table S1 for the LED intensities needed for each cell type). This intensity was always subthreshold for the recorded cell (~3 mV; Table S1). For the over terminal stimulation experiments (Figure 2.6), ChR2 was excited using a high-power white LED (Mightex, BLS-GCS-6500-65-A0510) attached to a Digital Mirror Device (DMD) based pattern illuminator (Mightex, Polygon 400). The pattern illuminator was used to briefly illuminate a small spot (0.5-ms flashes; 150 µm diameter) centered over the soma (Max LED power across all mirrors ~44.3; Max LED power when illuminating a 150 µm diameter spot ~4.9 mW or 276 mW/mm2). For these experiments, the LED light was reflected through the same water immersion objective as mentioned above.

Live slice imaging. Before recording, all live brain slices (300 µm) were imaged using a Zeiss Axio Examiner.A1 microscope equipped with a 2.5x objective (Zeiss, EC

Plan-Neofluar) and Olympus XM10IR camera and cellSens software. Brightfield and fluorescence images were obtained to confirm the accuracy of the injection, tissue health at the injection site, and the overall expression in axons/terminals in the target region. During imaging, live slices were kept in a submersion recording chamber and continually bathed with oxygenated ACSF (at room temperature).

Immunohistochemistry and tissue processing for neurobiotin. All tissue for immunohistochemistry was prepared from acute coronal brain slices, as described previously (Crandall et al. 2017) (Mean age of genotype pairs: 97.8 ± 9.3 days, range 73-116 days). Briefly, acute brain slices (300 µm) containing vS1 or vM1 were fixed by immersion overnight at 4°C in a vial containing 4% paraformaldehyde in 0.1 M phosphate buffer (PB) solution. Slices were then transferred to a 30% sucrose in 0.1 M PB solution until re-sectioned (4°C; 2-3 days). Tissue was re-sectioned at 60 µm using a freezing microtome (Leica, SM2010 R). Next, sections were immunostained for Syt7, as described previously (Jackman et al. 2016; Turecek et al. 2017). Briefly, sections were washed 2 times in 0.1 M phosphate buffer followed by 3 times in 0.1 M phosphate buffer with 0.9% NaCl, pH 7.4 (PBS) (5 min per wash). After washing, sections were pre-incubated for 1 hour at room temperature with a blocking solution (0.1% Tween, 0.25% Triton X-100, 10% normal goat serum in PBS), then incubated with primary antibody for 24 hours with rotation at 4°C. Following primary incubation, sections were washed 5 times in PBS (5 min per wash), pre-incubated for 45 min in blocking solution (same as above), incubated with secondary antibody for 2 hours at room temperature, then washed 3 times in PBS (10 min per wash) and 2 times in PB (5 min per wash). Sections were mounted and cover-slipped using Vectashield with DAPI (Vector Laboratories H-1500). The primary antibody was rabbit polyclonal anti-synaptotagmin 7 (1:200, Synaptic Systems, Cat# 105-173), and the secondary antibody goat anti-rabbit IgG (H+L) cross-adsorbed secondary antibody Alexa Fluor 568 (1:500, Thermo Fisher Scientific, Cat# A-11011). Antibodies were stored and prepared as recommended by the manufacturer and did not undergo repeated freeze/thaw cycles. For experiments comparing genotypes (WT and Syt7 KO), all tissue was prepared, stained, and processed in parallel. For each staining run, no primary and no secondary controls were conducted. Images were taken using a Zeiss Axio Imager.D2 fluorescence microscope equipped with appropriate filter sets and a high-resolution monochrome digital camera (Zeiss, AxioCam) and Zen software. For each genotype pair, images were collected from identical anatomical locations, using the same microscope settings, and processed identically in Fiji: ImageJ.

Slices containing cells injected with neurobiotin were transferred to 4% paraformaldehyde in 0.1 M PB solution overnight at 4°C (18 – 24 hr). The next day, slices were changed to 30% sucrose in 0.1 M PB until re-sectioned (4°C; 2 – 3 days). Individual brain slices were re-sectioned at 100-150 µm using a freezing microtome (Leica SM2010 R). Floating sections were washed twice in 0.1 M PB followed by three washes in 0.1 M PBS, pH 7.4 (5 min per wash). After washing, sections were incubated for 1 hr at room temperature in a blocking solution containing 0.1% Tween, 0.25% Triton X-100, and 10% normal goat serum in PBS. Sections were then incubated using Streptavidin/Biotin Blocking Kit (Vector Labs, SP-2002), 30 minutes in streptavidin solution, followed by 30 minutes in biotin solution with a brief rinse of PBS after each. Sections were then incubated with Alexa Fluor 568-conjugated streptavidin (Thermo-Fisher Scientific, S11226, 1:5000, 2µg/µl) solution in blocking solution for 3 hrs with rotation at room temperature. Following incubation, sections were washed 3 times in PBS, then 2 times in 0.1 M PB solution (10 min per wash), mounted, and cover-slipped using Vectashield Vibrance with DAPI (Vector Laboratories, H1800). Confocal image stacks of labeled neurons were taken using an Olympus FluoView 1000 filter-based Laser Scanning Confocal Microscope with an Olympus 40x Oil UPLFLN O (NA 1.3) objective and updated Version 4.2 software (laser excitation 543nm).

Electrophysiological data analysis. Analysis of electrophysiological data was performed in Molecular Devices Clampfit 11 and Microsoft Excel. Synaptic responses to optical stimulation were measured from postsynaptic neurons recorded in whole-cell voltage-clamp. The amplitude of an evoked EPSC was measured relative to a baseline before the stimulus (0.5-10 ms depending on the frequency of the stimulation). The EPSC peak was measured over the 10 ms immediately after stimulus onset or over the 4.5 ms immediately after stimulus onset for all layer comparisons. Reported values were based on average responses to 3–20 stimuli (typically 10). Values for the fiber volley and opsin potential were based on average responses to ~200 stimuli, and their peaks were measured over the 10 ms immediately after stimulus onset. The field postsynaptic potential (fPSP) slope was measured over a 0.5 ms region immediately after the peak negativity. Intrinsic physiological properties were measured using previously described methods (Crandall et al., 2017). Regular-spiking (RS) neurons were identified using established physiological criteria, including their spike-frequency adaptation, growing afterhyperpolarization (AHP) during spike trains, and relatively long spike half-widths (McCormick et al. 1985).

Layer comparisons using Cre-driver mouse lines. Previous work has shown that the Cre-driver mouse lines used in this study are selective for excitatory cells of distinct layers (L4: Scnn1a-Tg3-Cre; L5: Rbp4-Cre; L6: Ntsr1-Cre) (Olsen et al. 2012; Kim et al. 2014; Adesnik 2018). Live slices prepared from Cre mice crossed with a tdTomato (tdT) reporter (Ai14) confirmed that Cre-expressing cells were mostly confined to their respective layers and that the subpial distances for the layers were in agreement with previous reports. Layers were identified by drawing horizontal lines where the density of tdTomato-expressing cells decreased (Frandolig et al. 2019). Depth measurements for cells are reported as absolute distance or normalized distance from the top of their respective layer. Whole-cell recordings further confirmed that all tdTomato positive cells had intrinsic physiological properties consistent with excitatory cortical cells (McCormick et al. 1985; Crandall et al. 2017). No Cre expression was observed in vM1 of the Scnn1-Cre mouse, consistent with the idea that the agranular cortex lacks spiny stellate cells (Harris and Shepherd 2015). A Cre-driver mouse line was not used for L2/3 recordings. However, all L2/3 cells were confirmed post hoc to be located within the superficial layers of the cortex (average recorded depth from pia: vS1 L2/3 cells, 190.5 ± 3.9 µm, range: 120-310 µm; vM1 L2/3 cells: 238.0 ± 5.4 µm, range: 135-361 µm). To control for variability in ChR2 expression in different slices and mice, we sequentially recorded from an identified L2/3 RS cell and an excitatory neuron (tdTomato-positive and tdTomato-negative) in a separate layer of the same column. For synaptic strength comparisons, brief flashes of the same intensity were delivered over the recorded soma.

Experimental design and statistical analysis. No formal method for randomization was used in this study. Experiments and data analyses were performed blind to the conditions of the Syt7 experiments. For all other studies, the experimenters were not blind to experimental groups. No statistical methods were used to predetermine sample size, but our sample sizes are similar to those reported in previous studies (Crandall et al. 2015; Crandall et al. 2017). Statistical comparisons were performed in OriginPro 2019. The Shapiro-Wilk test was first applied to determine whether the data had been drawn from a normally distributed population, in which case parametric tests were used. If the assumption of normality was not valid, non-parametric tests were used. Significance was assessed using the appropriate parametric (Paired t-test or Two-sample t-test) or non-parametric test (Wilcoxon paired signed-rank test or Mann-Whitney U test) as indicated in the Results. A two-way analysis of variance (ANOVA) was used to compare short-term synaptic dynamics across 20 Hz trains. A one-way ANOVA was used for multiple comparisons. All tests were two-tailed. Data are represented as mean ± SEM, and statistical significance was defined as $p < 0.05$.

2.4 – Results

Optical control of cc synaptic transmission. Here we applied optogenetic control strategies to examine the connections between vS1 and vM1 (Crandall et al. 2015; Crandall et al. 2017). We identified vM1 and vS1 using viral-mediated anterograde tracing and the presence of large L4 barrels, respectively. vM1 was defined as a narrow region in the posteromedial part of the frontal cortex that reciprocally connected with vS1, consistent with previous studies (Hoffer et al. 2003; Ferezou et al. 2007; Mao et al. 2011). Next, we injected an adeno-associated virus (AAV2) carrying genes for a channelrhodopsin-2/enhanced yellow fluorescent protein construct (ChR2-EYFP) in vS1 or vM1 of mice in vivo. Three weeks after vS1 injections, there was robust ChR2-EFYP expression in vS1 axons/terminals within vM1 (Figure 1A). vS1 terminal arbors formed a narrow band ascending from the white matter within vM1 and concentrated in layer 1 (L1) and L2/3, consistent with a previous report (Mao et al. 2011). Similarly, three weeks after vM1 injections, there was intense ChR2-EYFP expression in vM1 axons/terminals within vS1 (Figure 1B). vM1 terminal arbors covered a large expanse of vS1 and concentrated in L1 and L5/6, precisely where they are known to terminate (Veinante and Deschenes 2003).

Previous studies suggest that ChR2 desensitization impairs axons' ability to follow during repetitive stimulation (Olsen et al. 2012; Hass and Glickfeld 2016), resulting in artificial synaptic depression. To determine the efficacy of ChR2 for activating CC pathways, we stimulated vM1 and vS1 axons/terminals with 20 Hz optical trains (10 pulses, 0.5 ms flashes, 1500 µm diameter spot) and measured effects on the extracellular, pharmacologically isolated fiber volley (Hass and Glickfeld 2016). Fiber volley amplitude directly relates to the number of axons recruited by stimulation (Andersen et al. 1977). We found that optical stimulation evoked remarkably consistent fiber volley waveforms with modest amplitude decay (8.2 ± 3.8%) and minimal latency shift within trains (0.35 ± 0.05 ms; Figure 2.11, E-G). Thus, 20 Hz optical stimulation of CC pathways is reliable under our conditions and can be used to study these synaptic connections.

Long-range cc synapses express short-term facilitation. We first examined the pathway linking vS1 to vM1. We used voltage-clamp recordings to measure optically evoked excitatory postsynaptic currents (EPSCs) from excitatory regular-spiking (RS) neurons in L2/3 of vM1 (Figure 2.1C). Here the RS cells were identified using previously described physiological criteria (see Methods). We used brief, low-intensity LED stimuli to avoid mixed mono- and polysynaptic excitatory activity, keeping the initial synaptic current ~200 pA when measured near the inhibitory reversal potential (-94 mV; see Methods). This intensity evoked subthreshold potentials for all cells tested (~3 mV).

For all L2/3 RS cells recorded near ChR2-expressing vS1 arbors within vM1, brief LED flashes evoked fast EPSCs with onset latencies averaging 2.34 ± 0.04 ms. These onsets are consistent with the timing of neurotransmission at fast synapses (Sabatini and Regehr 1999) and indicate that cells did not express ChR2. We next used paired-pulse stimulation to assess short-term plasticity (Zucker and Regehr 2002). Pairs of closely spaced optical flashes resulted in facilitation for interstimulus intervals of 50-200 ms and a peak enhancement of ~1.5-fold (Figure 2.1C). However, we observed intense short-term depression for interstimulus intervals of 10-20 ms, consistent with reports that ChR2 does not reliably evoke spikes above 25 Hz (Lin et al. 2009). Since presynaptic neurons often discharge several action potentials in vivo, we also assessed synaptic dynamics using trains of flashes. Consistent with paired-pulse stimulation, all responses underwent facilitation during 5-20 Hz optical trains (Figure 2.1D).

We next examined the reciprocal pathway linking vM1 to vS1 (Figure 2.1E). Again, we recorded from L2/3 RS cells, which receive direct input from vM1 on their apical dendrites in L1 (Petreanu et al. 2009). For most cells located near ChR2-expressing vM1 axons/terminals in L1, brief photostimulation evoked clear synaptic responses with short onset latencies (1.79 ± 0.03 ms). When we used paired-pulse stimulation, cells responded with an increase in synaptic strength for short interstimulus intervals of 50-500 ms and a peak enhancement of ~2-fold (Figure 2.1E). Furthermore, all responses evoked by 2-20 Hz optical trains exhibited facilitation (Figure 2.1F).

The short onset latencies of the CC responses suggest they are likely mediated by fast ionotropic glutamate receptors. Indeed, the combined application of the selective NMDA and AMPA kainate-type glutamate receptor antagonists APV and DNQX (50 and 20 µM, respectively) eliminated the responses in all cells tested (6/6 cells from 4 mice). Responses were also abolished after blocking sodium channels with tetrodotoxin (TTX: 1 µM) but returned with the subsequent addition of the potassium channel blocker 4-aminopyridine (4AP: 1 mM; 5/5 cells from 2 mice). The latter finding confirms that the light-evoked responses were both action potential-dependent and monosynaptic (Petreanu et al. 2009; Cruikshank et al. 2010).

To rule out the possibility that the observed facilitation reflects the superposition of long-range and local inputs, we compared the responses evoked under control conditions with those recorded on trials that we reduced the likelihood of postsynaptic firing. We suppressed the responsiveness of local excitatory cells either optogenetically by activating cortical parvalbumin (PV)-expressing interneurons that conditionally expressed the red-shifted opsin ChrimsonR (Klapoetke et al. 2014) or pharmacologically by blocking nonlinearities in the synaptic conductances associated with NMDA receptors (APV: 50 µM) (Larkum et al. 2009). We found that silencing local excitatory cells during the activation of long-range projections did not affect the observed facilitation, indicating that local inputs do not confound the CC responses.

To determine if our light stimulation method, which includes over-terminal illumination, significantly blunted short-term facilitation, we compared responses evoked by our approach and over-axon stimulation, which produces more physiological responses (Jackman et al. 2014). We found that the two stimulation methods produced similar dynamics during 20 Hz trains (Figure 2.14), suggesting that our stimulation method offers a reasonable strategy for assessing the short-term plasticity of CC synapses.

Altogether, these results established that reciprocal CC connections between vS1 and vM1 give rise to facilitating synapses capable of fast sustained excitatory transmission during brief periods of elevated presynaptic activity, contrasting with several previous reports (Lee et al. 2013; Kinnischtzke et al. 2014; Petrof et al. 2015; Naskar et al. 2021).

The temporal dynamics of long-range and local intracortical excitation. The finding that long-range CC responses underwent short-term facilitation is somewhat surprising and intriguing given a key feature of most local excitatory–to–excitatory connections within the cortex is short-term depression (Gil et al. 1999; Reyes and Sakmann 1999; Feldmeyer et al. 2002). To better understand how different excitatory–to–excitatory connections within the neocortex are differentially affected by activity, we compared evoked responses at three general classes of excitatory synapses. At long-range CC synapses, 20 Hz optical stimulation resulted in paired-pulse facilitation (vS1-vM1 L2/3: 1.42 ± 0.08; vM1-vS1 L2/3: 1.80 ± 0.06; Figure 2.2A). This facilitation contrasts sharply with long-range subcortical inputs to the cortex from the thalamus, such as core sensory thalamocortical synapses (VPm-vS1 L4/L6), that exhibited robust paired-pulse depression when tested under identical conditions (0.71 ± 0.02; Figure 2.2A) (Gabernet et al. 2005; Cruikshank et al. 2010). Conversely, local connections between pairs of excitatory cells in vS1 or vM1 were more stable at 20 Hz, depressing only slightly across the tested population (0.98 ± 0.14; Figure 2.2B). Optical stimulation of local ChR2-expressing cortical cells (0.94 ± 0.05) or axons/terminals without parent somata evoked similar paired-pulse ratios (0.95 ± 0.05; Figure 2.2B). These data demonstrate that the synaptic dynamics of three common types of glutamatergic synapses in the neocortex are dramatically different ($p < 0.0001$, Two-way ANOVA, stim. 2-10; Figure 2.2C), suggesting that they might serve dynamically distinct roles in neocortical operations.

Remarkably, local and long-range CC input to excitatory cells displayed different synaptic properties, suggesting that local and long-distance synaptic terminals of the same pyramidal neurons could exhibit different release properties. To test this hypothesis, we next injected AAVretro-Cre into vS1 to gain retrograde access to vS1-projecting(P) neurons in vM1 and then a Cre-dependent AAV-DIO-ChR2-EYFP into the ipsilateral vM1 to optically control the activity of these cells (Figure 2.2D) (Tervo et al. 2016). After allowing for expression, we observed ChR2-EYFP expression in vS1P neurons in vM1. We next recorded non-expressing cells in vM1 to study the dynamics of vS1P inputs onto local excitatory neurons. In contrast to our finding for long-range vM1-vS1 synapses, we found that local vS1P-evoked EPSCs depressed ($p < 0.0001$, Two-way ANOVA, stim. 2-10; Figure 2.2E). These findings imply that the presynaptic properties of CC projection neurons can differ according to whether the target cortical neuron is in their local circuit or a distant cortical area.

Short-term plasticity of CC input as a function of cortical layer. Given the stark laminar differences in the spatial arrangement of vS1 and vM1 projections (Figure 2.1), and previous details about long-range CC connectivity (Petreanu et al. 2009; Mao et al. 2011; Kinnischtzke et al. 2014), we wondered if the short-term dynamics of these synapses depended on cortical layer. To investigate this, we compared the responses in excitatory cells located across the vertical depth of the cortex using layer-specific Cre-recombinase driver mouse lines crossed with a tdTomato (tdT) reporter (see Methods and Table S2). To control for variability in ChR2 expression in different slices and mice, we sequentially recorded from an identified L2/3 RS cell and an excitatory neuron (tdT-positive and negative) in a separate layer of the same column.

In vM1, excitatory vS1 currents were strongest in L2/3 and increased 50-70% during 20 Hz trains, whereas currents in L5/6 cells were significantly weaker, initially facilitated (10-15%), and then depressed with repetitive stimulation (Figure 2.3A-C). In contrast, in vS1, excitatory vM1 currents were strongest in L6, and responses approximately doubled during 20 Hz trains in L2/3 and L6, whereas short-term plasticity was highly heterogeneous across L5 connections (Figure 2.3D-F). Together, these results indicate that many long-range CC synapses undergo short-term facilitation, with absolute strength and dynamics differing with layer.

Properties of excitatory cc synapses onto different L2/3 interneuron subtypes. Long-range CC connections in vS1 and other cortical areas also target GABAergic inhibitory interneurons (Dong et al. 2004; Lee et al. 2013; Yang et al. 2013; Kinnischtzke et al. 2014; Zhang et al. 2014; Naskar et al. 2021). To compare CC responses among different subtypes of L2/3 interneurons, we measured optically evoked CC responses from an identified interneuron and a neighboring RS excitatory cell. To target different L2/3 interneuron subtypes, we crossed three well-established Cre-driver mouse lines with tdT reporter mice (Ai14) to label PV-, somatostatin (SOM)-, or vasoactive intestinal peptide (VIP)-expressing interneurons (see Methods).

Figures 2.4A and 2.4E show optically evoked CC responses from an interneuron and neighboring RS cell. We found that EPSCs recorded from PV cells had the largest amplitudes and showed slightly less facilitation at 20 Hz than RS cells for both pathways (EPSC peak normalized to RS: vM1 PV cells, 13.3 ± 5.8, median = 4.9; vS1 PV cells, 6.1 ± 1.4, median = 4.8; Figure 2.4B, F). EPSCs from SOM cells had much smaller amplitudes for both CC pathways but displayed dramatic short-term facilitation at 20 Hz (EPSC peak normalized to RS: vM1 SOM cells, 0.17 ± 0.03, median = 0.18; vS1 SOM cells, 0.66 ± 0.11, median = 0.55; Figure 2.4C, G). In contrast to those of PV and SOM cells, the EPSCs of VIP cells were significantly weaker in the vS1-vM1 pathway, whereas the EPSC amplitudes were statistically similar to RS cells in the vM1-vS1 pathway (EPSC peak normalized to RS: vM1 VIP cells, 0.14 ± 0.06, median = 0.10; vS1 VIP cells, 0.89 ± 0.28, median = 0.64; Figure 2.4D, H). Furthermore, the excitatory currents in VIP cells initially facilitated (10-45%) and then depressed with repetitive stimulation for both pathways (Figure 2.4D, H). Despite similar EPSC amplitudes, vM1 stimuli always evoked action potentials in the VIP cell (8/8 pairs) but rarely in the RS cell (1/8 pairs). Altogether, these data suggest that long-range CC synapse strength and dynamics depend on the postsynaptic interneuron subtype and pathway.

Experimental strategies that affect CC responses. Our results establish that facilitation is the predominant communication mode for conveying information between vS1 and vM1. To understand why our data differ from those previously reported, we first compared the effect of AAV serotype on optically evoked short-term synaptic plasticity (Jackman et al. 2014). Here, we injected mice with an identical vector to our previous work using AAV2 but with a different viral serotype (AAV1, AAV5, and AAV9; same titer). All three vectors produced robust ChR2-EYFP expression, similar to levels observed using AAV2 (Figure 2.16A). When we drove ChR2 expression by AAV5, responses evoked by optical trains exhibited less facilitation for the vS1-vM1 synapse but not for the vM1-vS1 synapse (Figure 2.5A-B). However, when using AAV1 to express ChR2, facilitation was weaker for the vM1-vS1 synapse but not for the vS1-vM1 synapse (Figure 2.5A-B). Responses were not different from those obtained using AAV2-ChR2 when using AAV9-ChR2. When we examined the effects of different fluorescent fusion proteins on optically evoked responses, we also found that currents evoked by ChR2-mCherry exhibited significantly less facilitation than ChR2-EYFP (Figure 2.5C), perhaps due to the overall poor surface expression observed with ChR2-mCherry. These results indicate that using AAV1 and AAV5 produce only modest facilitation in a pathway-dependent manner and that mCherry tagging of ChR2 caused adverse effects.

We also encountered several cells intermingled with ChR2-EYFP expressing axons/terminals that were light-sensitive when using AAV1, AAV5, and AAV9 (Figure 2.16C-E). However, we rarely encountered ChR2 expressing cells when using AAV2. These observations suggest that retrograde spread within the cortex is more frequent with some AAV serotypes.

Given direct excitation of ChR2-expressing terminals with light can cause artificial depression (Zhang and Oertner 2007; Jackman et al. 2014), we next wondered if the power density of over-terminal illumination affects the magnitude of facilitation at CC synapses. Our approach was to stimulate using brief wide-field illumination (1500 µm diameter spot) and low light power density to minimize complications that may arise due to direct stimulation of presynaptic terminals. To assess the impact of a more focused over-terminal illumination, we compared optical responses evoked by the same total light power but with light-spots of different diameters (1500 µm or 150 µm) (Figure 2.6A). We found that restricting the excitation light to the distal ends of ChR2-expressing axons caused the amplitude of facilitation to decrease significantly during repetitive stimulation (Figure 2.6B-C). We also found that pulse duration disrupted paired-pulse facilitation in a pathway-dependent manner (Figure 2.17A-B).

We next examined the Ca2+-dependence of optically evoked EPSCs and facilitation. It is well established that Ca2+ ions play a crucial role in short-term plasticity (Zucker 1999), and thus far, we have conducted our studies in the presence of 1.2 mM Ca2+, which is around physiological conditions (Somjen 2002). However, many studies are performed in the presence of 2.0 mM external Ca2+. We found that increasing Ca2+ caused a significant increase in EPSC amplitude and reduced paired-pulse facilitation for both synapses. To test further the impact of Ca2+, we measured how EPSC trains evoked with repetitive optical stimulation changed with external Ca2+. Increasing the concentration of Ca2+ to 2.0 mM significantly reduced the magnitude of facilitation observed during 20 Hz trains (Figure 2.6D and 2.5E).

Our findings indicate that both light stimulation technique and external Ca2+ levels can strongly affect the magnitude of facilitation at CC synapses, suggesting that combining these two experimental approaches could convert facilitating responses to depression. To test this hypothesis, we compared CC responses evoked by our standard approach to those triggered by focused stimulation of the distal ends of ChR2-expressing axons while in the presence of 2.0 mM Ca2+ (Figure 2.6F). Under control conditions, the responses underwent strong short-term facilitation, whereas subsequent changes to the light and external Ca2+ levels led to synaptic currents that depressed (Figure 2.6G-H). Overall, these results reveal how different AAV serotypes, fluorescent fusion proteins, methods of light stimulation, and Ca2+ concentrations can influence the short-term synaptic plasticity of CC synapses and perhaps the reliability of synaptically driven circuit activity.

Synaptotagmin-7 mediates facilitation at long-range cc synapses. Recent work has shown that the slow presynaptic Ca2+ sensor, synaptotagmin 7 (Syt7), plays critical roles in synaptic transmission, especially in short-term facilitation at many central synapses (Jackman et al. 2016). Therefore, we tested whether Syt7 could mediate facilitation at CC synapses. Immunohistochemistry revealed a Syt7 pattern in the hippocampus and thalamus similar to a previous report (Jackman et al. 2016). In the neocortex, we observed that Syt7 was present in vM1 and vS1 of wildtype (WT) mice but was absent in Syt7 knockout (KO) animals (Figure 2.7A-B). In WT mice, Syt7 labeling was prominent in L1, where CC synapses are dense and are known to contact the dendrites of pyramidal cells (Cauller et al. 1998; Petreanu et al. 2009; Mao et al. 2011), suggesting a possible expression of Syt7 in long-range CC terminals.

We next examined the functional role of Syt7 in facilitation at both CC synapses by performing similar optogenetic experiments in Syt7 KO mice and age-matched WT littermates. In WT mice, pairs of closely spaced optical stimuli and 5-20 Hz trains of flashes resulted in synaptic facilitation (Figure 2.7C-F). In Syt7 KO mice, facilitation was eliminated (Figure 2.7C-F). The loss of facilitation in Syt7 KO mice cannot be accounted for by the inability of ChR2 to drive presynaptic axons because optical stimulation evoked fiber volleys comparable to that of WT animals (Figure 2.18D-E). Nor can it be explained by differences in intrinsic properties between WT and KO cortical cells. Altogether, these data indicate that Syt7 mediates short-term facilitation at CC synapses linking vS1 and vM1.

Role of short-term dynamics in the direct modulation of L2/3 excitability. Having determined the short-term dynamics of CC synapses, we next examined how these inputs might control the excitability of L2/3 pyramidal neurons. The short-term plasticity of excitatory CC synapses suggests that they may influence L2/3 processing by directly increasing the overall excitation and spike probability of pyramidal neurons with repetitive activity. To test this idea, we recorded in current-clamp from L2/3 RS neurons and performed optical stimulation with 20 Hz trains (Figure 2.8A-B). During repetitive stimulation, the membrane potential of L2/3 vM1 and vS1 cells depolarized progressively, reaching its peak towards the ends of the trains. The overall magnitude of facilitation observed with the excitatory postsynaptic potentials (EPSPs) was consistent with the dynamics of the previously recorded EPSCs (Figure 2.8A-B). To determine the impact of CC input on L2/3 excitability, we next monitored the spiking behavior in response to 20 Hz trains while holding the cell at a depolarized membrane potential (-74 mV) (Figure 2.8C). Under these conditions, trains of optical stimuli reliably drove spiking in L2/3 RS cells. For both vM1 and vS1 neurons, the probability of spike discharge was lowest after the first stimulus and gradually increased following subsequent stimuli so that the maximal spiking probability occurred at the end of the train (Figure 2.8D). Together, these data indicate that direct CC effects on L2/3 excitability are regulated dynamically, mainly generating enhancement during brief periods of sustained activity.

In general, the short-term synaptic dynamics of the CC evoked excitatory responses appeared to parallel the CC modulation of L2/3 excitability. To test the causal relationship between short-term facilitation and the changes in excitability, we performed similar current-clamp experiments in Syt7 KO and WT animals. In Syt7 KO mice, the facilitating CC-evoked EPSPs were abolished (Figure 2.8E-F). This loss of facilitating CC-evoked excitatory responses eliminated the late enhancement in L2/3 excitability (Figure 2.8G-H). These data indicate that the short-term dynamics of inputs to L2/3 cells can account for the CC-triggered late enhancement of their excitability.

Long-range projections from vS1 to vS2 have similar synaptic properties. To determine whether other CC projections might share the same short-term plasticity described for the connections between vS1 and vM1, we examined the vibrissal secondary somatosensory cortex (vS2) and its inputs from vS1. We found that the short-term plasticity of vS1 synapses in L2/3 of vS2 was very similar to that of the vS1-vM1 CC system (Figure 2.9). These data suggest that short-term facilitation might be a general feature of long-range CC connectivity.

2.5 – Discussion

Here we show that the synaptic properties of CC connections between vS1 and vM1 are dramatically different from other major excitatory connections of the neocortex. In contrast to local intracortical and core TC synapses, repetitive activation of many long-range CC synapses leads to short-term facilitation. Similar observations were made with a pathway linking cortical areas within the same sensory modality (vS1 to vS2), suggesting these properties may be a conserved feature of long-range corticocortical projections and not a unique feature of those between motor and sensory areas. A key difference between these pathways was that the synaptic dynamics were distinct for individual excitatory cells located across all cortical layers and specific subtypes of GABAergic neurons. We also found that the slow Ca2+ sensor Syt7 plays an important role in regulating facilitation at these synapses. A series of experiments further demonstrate that the overall excitation and spiking probability of L2/3 pyramidal neurons increases during repetitive stimulation of CC axons. This influence on pyramidal cell excitability depended on the distinct form of short-term plasticity at the CC synapse. Lastly, we identify several potential pitfalls of using optogenetic tools to study CC circuits that influence synaptic responses.

Short-term plasticity lasts from tens of milliseconds to minutes and is likely critical for information processing and cortical circuit function (Abbott et al. 1997; Tsodyks and Markram 1997; Abbott and Regehr 2004). Although the strength and dynamics of synapses targeting cortical neurons can vary widely (Stratford et al. 1996; Markram et al. 1998; Reyes et al. 1998; Gil et al. 1999; Beierlein et al. 2003; Brown and Hestrin 2009), these distinct properties may provide clues to their function and the type of information they convey. For example, core TC synapses are strong, reliable, and show robust short-term depression (Gil et al. 1999; Gabernet et al. 2005), perhaps reflecting the fidelity of the information they carry into the neocortex. On the other hand, the excitatory synapses between neighboring pyramidal cells within the cortex are typically weaker, less reliable, and show modest depression (Gil et al. 1999; Feldmeyer et al. 2002; Feldmeyer et al. 2006) (however see (Reyes and Sakmann 1999; Jouhanneau et al. 2015)). These synaptic features are likely important for how intracortical recurrent circuits distribute and combine information (Douglas et al. 1995; Lien and Scanziani 2013; Cossell et al. 2015; Cohen-Kashi Malina et al. 2016).

In contrast to TC and local CC excitatory synapses, most long-range CC connections displayed robust synaptic facilitation during repeated optical stimulation. This form of short-term plasticity is observed throughout the nervous system at synapses with a low probability of release (Jackman and Regehr 2017). However, this facilitation should not be confused with kinetic sluggishness since CC connections showed a strong ionotropic glutamate component in their response, suggesting an ability to carry rapid signals over sustained periods. The capacity to temporarily enhance their strength with activity suggests that CC synapses could efficiently convey information about ongoing local network activity to other cortical areas (Zagha et al. 2013). Short-term facilitation may also provide greater flexibility and control over target areas since their synaptic strength is activity-dependent, producing graded changes in excitation depending on the level of presynaptic spiking (Figure 2.12).

In vM1, vS1 responses were several times stronger and showed greater short-term facilitation in L2/3 than in other layers. The signals vM1 receives from vS1 are distinct from those conveyed to other cortical areas and likely encode object detection and location (Chen et al. 2013; Yamashita et al. 2013). L2/3 cells also supply a large fraction of the local excitatory drive to infragranular neurons that control motor output (Kaneko et al. 1994; Weiler et al. 2008; Hooks et al. 2011). Thus, these cells appear well-positioned to directly link sensory input and control of movement (Weiler et al. 2008; Mao et al. 2011; Sreenivasan et al. 2016). The facilitation patterns in the vS1 pathway suggest that L2/3 vM1 cells may be most excited during repeated spiking in vS1, such as those reported during repetitive sensory sampling or other active vibrissa-based behavioral tasks (Krupa et al. 2004; O'Connor et al. 2010; Vijayan et al. 2010).

We found that vM1 projections also engaged excitatory vS1 neurons with mostly facilitating synapses. The facilitation was particularly robust and sustained in L2/3 and L6, layers essential for associative interactions and modulating thalamocortical activities, respectively (Olsen et al. 2012; Lee et al. 2013; Crandall et al. 2015). Although the two layers had similar facilitation, L6 responses were 3-4 times stronger, consistent with previous reports of a prominent input to this layer (Lee et al. 2008; Kinnischtzke et al. 2016; Zolnik et al. 2020). In addition, several studies have shown that vM1 activity correlates with various aspects of whisking (Carvell et al. 1996; Hill et al. 2011; Friedman et al. 2012; Castro-Alamancos 2013), and work by Petreanu et al. (2012) has demonstrated that vS1-targeting vM1 projection neurons increase their activity during vibrissa-dependent tasks, with some showing persistent-like activity. Thus, the distinctive short-term dynamics of vM1 synapses may be a specialization tailored to inform vS1 neurons of behaviorally relevant features related to self-generated vibrissa movements over time.

In L5 of vS1, vM1 responses were relatively weak and showed different forms of synaptic plasticity, with approximately half of the inputs displaying depression. The disparate dynamics of these inputs imply at least two types of excitatory connections within L5, whose dynamic properties may be determined by the pre or postsynaptic cell type. The relatively weak responses could be due, in part, to the fact that many vM1 inputs target the apical tuft dendrites of L5 pyramidal neurons (Cauller et al. 1998; Petreanu et al. 2009), which make currents recorded at the soma prone to space-clamp errors and cable attenuation (Williams and Mitchell 2008). This issue suggests that distal vM1 inputs are underrepresented in the current study. Nonetheless, motor-related signals are very effective in modulating the activity of these neurons because they have powerful dendritic nonlinearities that help them actively integrate basal and apical tuft inputs when strong temporal correlations exist during active sensation and sensory perception (Xu et al. 2012; Larkum 2013; Manita et al. 2015; Takahashi et al. 2020).

CC synapse strength and dynamics also depend on the postsynaptic L2/3 interneuron subtype and pathway. For example, both vM1 and vS1 PV interneurons had the largest evoked currents of all cell types and displayed modest facilitation. In contrast, responses in vM1 and vS1 SOM cells were much weaker than neighboring RS cells but showed robust short-term facilitation. A different group of inhibitory interneurons, the VIP cells, had pathway-dependent strengths that depressed late in trains. VIP cells in vM1 had significantly weaker vS1-evoked responses than neighboring RS cells, whereas VIP interneurons in vS1 received similar amplitude vM1-evoked EPSCs. Although the latter finding is inconsistent with previous reports of vM1 synaptic currents being strongest in VIP cells (Lee et al. 2013; Naskar et al. 2021), we did find that these interneurons were very responsive to vM1 input, routinely firing action potentials. Thus, our data suggest that the greater propensity of VIP cells to spike in response to vM1 stimulation is due to differences in intrinsic membrane properties rather than synaptic strength (Figure 2.15). This mechanism is consistent with the idea that VIP interneurons are responsible for vM1-driven disinhibition of pyramidal neurons in vS1 (Lee et al. 2013).

ChR2 is widely used to stimulate axonal pathways to study neural circuits. However, we have identified several pitfalls associated with using optogenetic tools to study long-range CC connectivity. First, we found that some AAV serotypes used to express ChR2 can alter the short-term plasticity of CC synapses. Specifically, AAV1 and AAV5 impaired the magnitude of facilitation in a synapse-dependent manner, similar to observations in other systems (Jackman et al. 2014). Second, we observed AAV1, AAV5, and AAV9 transduce CC axon terminals more efficiently than AAV2, producing sparse but robust retrograde expression of ChR2 in cortical neurons that could potentially cause complications when interrogating these circuits. Third, we found that using the ChR2-mCherry fusion protein caused significant deficits in optically evoked synaptic plasticity, which may have been due to the aggregation of ChR2-mCherry in expressing neurons, a reported problem when mCherry is expressed within some fusions (Asrican et al. 2013). Altogether, these AAV-induced changes to synaptic plasticity and the influence of mCherry tags on optogenetic probe expression and function could explain some of the discrepancies between the current study and previous work reporting depression (Lee et al. 2013; Kinnischtzke et al. 2014; Petrof et al. 2015; Zolnik et al. 2020; Naskar et al. 2021). However, in our hands, neither AAV serotype nor ChR2-mCherry alone caused short-term depression at CC synapses.

In addition to the optogenetic tool used, our data reveal that stimulation strategy and experimental conditions influence CC responses. Specifically, we show that the power density of over-terminal stimulation, light duration, and raising the concentration of extracellular Ca2+ decreased the magnitude of facilitation, likely because ChR2-induced presynaptic terminal depolarization and increased Ca2+ influx result in a greater release probability (Zucker 1999; Zhang and Oertner 2007; Jackman et al. 2014). Although the power density used in previous studies is difficult to determine, the longer pulse durations (3-10 ms) and 2.0 mM extracellular Ca2+ concentration certainly contributed to the previously reported depressing CC responses (Lee et al. 2013; Kinnischtzke et al. 2014; Petrof et al. 2015; Zolnik et al. 2020; Naskar et al. 2021).

Here, we used a low power density, large light stimulation field to minimize complications that may arise due to direct stimulation of presynaptic terminals (Zhang and Oertner 2007; Jackman et al. 2014). Although this approach excites terminals, it probably stimulated CC axons away from their terminations as well. Axon stimulation is a more reliable way of activating presynaptic inputs in other pathways (Jackman et al. 2014) and is likely why robust facilitation was observed in this study. Consistent with this hypothesis, we found good agreement in the short-term plasticity evoked by our approach and over-axon stimulation. Although it is preferable to use over-axon stimulation, we found evoked synaptic responses using this method were considerably weak (<100 pA), probably due to the spatially diffuse nature of CC projections (Veinante and Deschenes 2003). The overall weaker evoked responses could complicate the study of synaptically driven circuit activity (i.e., disynaptic feedforward inhibition). Although the present approach appears to offer a reasonable strategy for studying the contributions of short-term plasticity to CC circuits, desensitization of ChR2 in presynaptic axons/terminals is still likely impacting some axons' ability to follow during stimulation (Figure 2.11). Thus, CC synapses are probably more capable of maintaining sustained transmission than indicated by the data shown here.

One approach to overcome this problem and more reliably recruit axons during repetitive stimulation could be to employ opsins with kinetics faster than ChR2, such as Chronos (Klapoetke et al. 2014; Hass and Glickfeld 2016). However, not all faster opsins may be suitable. For example, Naskar et al. (2021) recently used ChETA, an engineered variant of ChR2 with fast kinetics (Gunaydin et al. 2010), to stimulate vM1-vS1 projections, and reported significant short-term depression. Thus, assessing the fidelity of optogenetic activation in a given pathway is still critical when using any opsin.

Our data begin to unravel how synaptic dynamics may contribute to long-range CC influences. Obviously, synaptic dynamics are not the only factor determining the net CC influence on target areas. Previous work has emphasized crucial roles for topographic alignment, interareal synchrony, network state, synapse distribution, disinhibition, as well as active membrane properties of pyramidal cells (Hoffer et al. 2003; Petreanu et al. 2009; Xu et al. 2012; Larkum 2013; Lee et al. 2013; Zagha et al. 2013; Bastos et al. 2014; Manita et al. 2015). Furthermore, trans-thalamic pathways have been proposed to contribute to CC communication (Sherman and Guillery 2011). The current work complements these elegant studies, and, together, they indicate the dynamic state of CC synapses has an essential role in ongoing cortical functioning.

Acknowledgements. This work was supported by NIH grants K99-NS096108 (to S.R.C), R00-NS096108 (to S.R.C), R00-NS096108-S1 (to S.R.C and L.E.M). We thank Barry Connors (Brown University), Scott Cruikshank (The University of Alabama at Birmingham), and Suryadeep Dash (Crandall Lab) for helpful discussions and comments on the manuscript. We thank Barry Connors for generously providing the Ntsr1-Cre , Rbp4-Cre ,and 5HT3a-EGFP mice. We thank Charles Lee Cox (Michigan State University) for imaging support. We also thank the Michigan State University Center for Advanced Microscopy for confocal imaging support.

BIBLIOGRAPHY

Abbott LF, Regehr WG. 2004. Synaptic computation. Nature. 431:796-803.

Abbott LF, Varela JA, Sen K, Nelson SB. 1997. Synaptic depression and cortical gain control. Science. 275:220-224.

Adesnik H. 2018. Layer-specific excitation/inhibition balances during neuronal synchronization in the visual cortex. J Physiol. 596:1639-1657.

Agmon A, Connors BW. 1991. Thalamocortical responses of mouse somatosensory (barrel) cortex in vitro. Neuroscience. 41:365-379.

Andersen P, Sundberg SH, Sveen O, Wigstrom H. 1977. Specific long-lasting potentiation of synaptic transmission in hippocampal slices. Nature. 266:736-737.

Asrican B, Augustine GJ, Berglund K, Chen S, Chow N, Deisseroth K, Feng G, Gloss B, Hira R, Hoffmann C, Kasai H, Katarya M, Kim J, Kudolo J, Lee LM, Lo SQ, Mancuso J, Matsuzaki M, Nakajima R, Qiu L, Tan G, Tang Y, Ting JT, Tsuda S, Wen L, Zhang X, Zhao S. 2013. Next-generation transgenic mice for optogenetic analysis of neural circuits. Frontiers in neural circuits. 7:160.

Bastos AM, Usrey WM, Adams RA, Mangun GR, Fries P, Friston KJ. 2012. Canonical microcircuits for predictive coding. Neuron. 76:695-711.

Bastos AM, Vezoli J, Bosman CA, Schoffelen JM, Oostenveld R, Dowdall JR, De Weerd P, Kennedy H, Fries P. 2014. Visual Areas Exert Feedforward and Feedback Influences through Distinct Frequency Channels. Neuron.

Beierlein M, Gibson JR, Connors BW. 2003. Two dynamically distinct inhibitory networks in layer 4 of the neocortex. J Neurophysiol. 90:2987-3000.

Brown SP, Hestrin S. 2009. Intracortical circuits of pyramidal neurons reflect their long-range axonal targets. Nature. 457:1133-1136.

Bruno RM, Sakmann B. 2006. Cortex is driven by weak but synchronously active thalamocortical synapses. Science. 312:1622-1627.

Carvell GE, Miller SA, Simons DJ. 1996. The relationship of vibrissal motor cortex unit activity to whisking in the awake rat. Somatosens Mot Res. 13:115-127.

Castro-Alamancos MA. 2013. The motor cortex: a network tuned to 7-14 Hz. Frontiers in neural circuits. 7:21.

Cauller LJ, Clancy B, Connors BW. 1998. Backward cortical projections to primary somatosensory cortex in rats extend long horizontal axons in layer I. J Comp Neurol. 390:297-310.

Chakrabarti S, Kobayashi KS, Flavell RA, Marks CB, Miyake K, Liston DR, Fowler KT, Gorelick FS, Andrews NW. 2003. Impaired membrane resealing and autoimmune myositis in synaptotagmin VII-deficient mice. J Cell Biol. 162:543-549.

Chen JL, Carta S, Soldado-Magraner J, Schneider BL, Helmchen F. 2013. Behaviour-dependent recruitment of long-range projection neurons in somatosensory cortex. Nature. 499:336-340.

Cohen-Kashi Malina K, Mohar B, Rappaport AN, Lampl I. 2016. Local and thalamic origins of correlated ongoing and sensory-evoked cortical activities. Nature communications. 7:12740.

Collins DP, Anastasiades PG, Marlin JJ, Carter AG. 2018. Reciprocal Circuits Linking the Prefrontal Cortex with Dorsal and Ventral Thalamic Nuclei. Neuron. 98:366-379 e364.

Cossell L, Iacaruso MF, Muir DR, Houlton R, Sader EN, Ko H, Hofer SB, Mrsic-Flogel TD. 2015. Functional organization of excitatory synaptic strength in primary visual cortex. Nature. 518:399-403.

Covic EN, Sherman SM. 2011. Synaptic properties of connections between the primary and secondary auditory cortices in mice. Cerebral cortex. 21:2425-2441.

Crandall SR, Cruikshank SJ, Connors BW. 2015. A corticothalamic switch: controlling the thalamus with dynamic synapses. Neuron. 86:768-782.

Crandall SR, Govindaiah G, Cox CL. 2010. Low-threshold Ca2+ current amplifies distal dendritic signaling in thalamic reticular neurons. J Neurosci. 30:15419-15429.

Crandall SR, Patrick SL, Cruikshank SJ, Connors BW. 2017. Infrabarrels Are Layer 6 Circuit Modules in the Barrel Cortex that Link Long-Range Inputs and Outputs. Cell reports. 21:3065-3078.

Cruikshank SJ, Urabe H, Nurmikko AV, Connors BW. 2010. Pathway-specific feedforward circuits between thalamus and neocortex revealed by selective optical stimulation of axons. Neuron. 65:230-245.

D'Souza RD, Meier AM, Bista P, Wang Q, Burkhalter A. 2016. Recruitment of inhibition and excitation across mouse visual cortex depends on the hierarchy of interconnecting areas. eLife. 5.

Diamond ME, von Heimendahl M, Knutsen PM, Kleinfeld D, Ahissar E. 2008. 'Where' and 'what' in the whisker sensorimotor system. Nat Rev Neurosci. 9:601-612.

Dong H, Shao Z, Nerbonne JM, Burkhalter A. 2004. Differential depression of inhibitory synaptic responses in feedforward and feedback circuits between different areas of mouse visual cortex. J Comp Neurol. 475:361-373.

Douglas RJ, Koch C, Mahowald M, Martin KA, Suarez HH. 1995. Recurrent excitation in neocortical circuits. Science. 269:981-985.

Engel AK, Fries P, Singer W. 2001. Dynamic predictions: oscillations and synchrony in top-down processing. Nat Rev Neurosci. 2:704-716.

Feldmeyer D, Lubke J, Sakmann B. 2006. Efficacy and connectivity of intracolumnar pairs of layer 2/3 pyramidal cells in the barrel cortex of juvenile rats. J Physiol. 575:583-602.

Feldmeyer D, Lubke J, Silver RA, Sakmann B. 2002. Synaptic connections between layer 4 spiny neurone-layer 2/3 pyramidal cell pairs in juvenile rat barrel cortex: physiology and anatomy of interlaminar signalling within a cortical column. J Physiol. 538:803-822.

Ferezou I, Haiss F, Gentet LJ, Aronoff R, Weber B, Petersen CC. 2007. Spatiotemporal dynamics of cortical sensorimotor integration in behaving mice. Neuron. 56:907-923.

Frandolig JE, Matney CJ, Lee K, Kim J, Chevee M, Kim SJ, Bickert AA, Brown SP. 2019. The Synaptic Organization of Layer 6 Circuits Reveals Inhibition as a Major Output of a Neocortical Sublamina. Cell reports. 28:3131-3143 e3135.

Friedman WA, Zeigler HP, Keller A. 2012. Vibrissae motor cortex unit activity during whisking. J Neurophysiol. 107:551-563.

Gabernet L, Jadhav SP, Feldman DE, Carandini M, Scanziani M. 2005. Somatosensory integration controlled by dynamic thalamocortical feed-forward inhibition. Neuron. 48:315-327.

Gil Z, Connors BW, Amitai Y. 1999. Efficacy of thalamocortical and intracortical synaptic connections: quanta, innervation, and reliability. Neuron. 23:385-397.

Gilbert CD, Li W. 2013. Top-down influences on visual processing. Nat Rev Neurosci. 14:350-363.

Gong S, Doughty M, Harbaugh CR, Cummins A, Hatten ME, Heintz N, Gerfen CR. 2007. Targeting Cre recombinase to specific neuron populations with bacterial artificial chromosome constructs. J Neurosci. 27:9817-9823.

Gunaydin LA, Yizhar O, Berndt A, Sohal VS, Deisseroth K, Hegemann P. 2010. Ultrafast optogenetic control. Nat Neurosci. 13:387-392.

Harris KD, Shepherd GM. 2015. The neocortical circuit: themes and variations. Nat Neurosci. 18:170-181.

Hass CA, Glickfeld LL. 2016. High-fidelity optical excitation of cortico-cortical projections at physiological frequencies. J Neurophysiol. 116:2056-2066.

Hempel CM, Hartman KH, Wang XJ, Turrigiano GG, Nelson SB. 2000. Multiple forms of short-term plasticity at excitatory synapses in rat medial prefrontal cortex. J Neurophysiol. 83:3031-3041.

Hill DN, Curtis JC, Moore JD, Kleinfeld D. 2011. Primary motor cortex reports efferent control of vibrissa motion on multiple timescales. Neuron. 72:344-356.

Hippenmeyer S, Vrieseling E, Sigrist M, Portmann T, Laengle C, Ladle DR, Arber S. 2005. A developmental switch in the response of DRG neurons to ETS transcription factor signaling. PLoS Biol. 3:e159.

Hoffer ZS, Hoover JE, Alloway KD. 2003. Sensorimotor corticocortical projections from rat barrel cortex have an anisotropic organization that facilitates integration of inputs from whiskers in the same row. J Comp Neurol. 466:525-544.

Hooks BM, Hires SA, Zhang YX, Huber D, Petreanu L, Svoboda K, Shepherd GM. 2011. Laminar analysis of excitatory local circuits in vibrissal motor and sensory cortical areas. PLoS Biol. 9:e1000572.

Hooks BM, Mao T, Gutnisky DA, Yamawaki N, Svoboda K, Shepherd GM. 2013. Organization of cortical and thalamic input to pyramidal neurons in mouse motor cortex. J Neurosci. 33:748-760.

Jackman SL, Beneduce BM, Drew IR, Regehr WG. 2014. Achieving high-frequency optical control of synaptic transmission. J Neurosci. 34:7704-7714.

Jackman SL, Regehr WG. 2017. The Mechanisms and Functions of Synaptic Facilitation. Neuron. 94:447-464.

Jackman SL, Turecek J, Belinsky JE, Regehr WG. 2016. The calcium sensor synaptotagmin 7 is required for synaptic facilitation. Nature. 529:88-91.

Jouhanneau JS, Kremkow J, Dorrn AL, Poulet JF. 2015. In Vivo Monosynaptic Excitatory Transmission between Layer 2 Cortical Pyramidal Neurons. Cell reports. 13:2098-2106.

Kaneko T, Caria MA, Asanuma H. 1994. Information-Processing within the Motor Cortex .2. Intracortical Connections between Neurons Receiving Somatosensory Cortical Input and Motor Output Neurons of the Cortex. J Comp Neurol. 345:172-184.

Kim J, Matney CJ, Blankenship A, Hestrin S, Brown SP. 2014. Layer 6 corticothalamic neurons activate a cortical output layer, layer 5a. J Neurosci. 34:9656-9664.

Kinnischtzke AK, Fanselow EE, Simons DJ. 2016. Target-specific M1 inputs to infragranular S1 pyramidal neurons. J Neurophysiol. 116:1261-1274.

Kinnischtzke AK, Simons DJ, Fanselow EE. 2014. Motor cortex broadly engages excitatory and inhibitory neurons in somatosensory barrel cortex. Cerebral cortex. 24:2237-2248.

Klapoetke NC, Murata Y, Kim SS, Pulver SR, Birdsey-Benson A, Cho YK, Morimoto TK, Chuong AS, Carpenter EJ, Tian Z, Wang J, Xie Y, Yan Z, Zhang Y, Chow BY, Surek B, Melkonian M, Jayaraman V, Constantine-Paton M, Wong GK, Boyden ES. 2014. Independent optical excitation of distinct neural populations. Nat Methods. 11:338-346.

Kleinfeld D, Ahissar E, Diamond ME. 2006. Active sensation: insights from the rodent vibrissa sensorimotor system. Curr Opin Neurobiol. 16:435-444.

Krupa DJ, Wiest MC, Shuler MG, Laubach M, Nicolelis MA. 2004. Layer-specific somatosensory cortical activation during active tactile discrimination. Science. 304:1989-1992.

Larkum M. 2013. A cellular mechanism for cortical associations: an organizing principle for the cerebral cortex. Trends Neurosci. 36:141-151.

Larkum ME, Nevian T, Sandler M, Polsky A, Schiller J. 2009. Synaptic integration in tuft dendrites of layer 5 pyramidal neurons: a new unifying principle. Science. 325:756-760.

Lee S, Carvell GE, Simons DJ. 2008. Motor modulation of afferent somatosensory circuits. Nat Neurosci. 11:1430-1438.

Lee S, Kruglikov I, Huang ZJ, Fishell G, Rudy B. 2013. A disinhibitory circuit mediates motor integration in the somatosensory cortex. Nat Neurosci. 16:1662-1670.

Lien AD, Scanziani M. 2013. Tuned thalamic excitation is amplified by visual cortical circuits. Nat Neurosci. 16:1315-1323.

Lin JY, Lin MZ, Steinbach P, Tsien RY. 2009. Characterization of engineered channelrhodopsin variants with improved properties and kinetics. Biophys J. 96:1803-1814.

Madisen L, Zwingman TA, Sunkin SM, Oh SW, Zariwala HA, Gu H, Ng LL, Palmiter RD, Hawrylycz MJ, Jones AR, Lein ES, Zeng H. 2010. A robust and high-throughput Cre reporting and characterization system for the whole mouse brain. Nat Neurosci. 13:133-140.

Manita S, Suzuki T, Homma C, Matsumoto T, Odagawa M, Yamada K, Ota K, Matsubara C, Inutsuka A, Sato M, Ohkura M, Yamanaka A, Yanagawa Y, Nakai J, Hayashi Y, Larkum ME, Murayama M. 2015. A Top-Down Cortical Circuit for Accurate Sensory Perception. Neuron. 86:1304-1316.

Mao T, Kusefoglu D, Hooks BM, Huber D, Petreanu L, Svoboda K. 2011. Long-range neuronal circuits underlying the interaction between sensory and motor cortex. Neuron. 72:111-123.

Markram H, Wang Y, Tsodyks M. 1998. Differential signaling via the same axon of neocortical pyramidal neurons. Proc Natl Acad Sci USA. 95:5323-5328.

McCormick DA, Connors BW, Lighthall JW, Prince DA. 1985. Comparative electrophysiology of pyramidal and sparsely spiny stellate neurons of the neocortex. J Neurophysiol. 54:782-806.

Naskar S, Qi J, Pereira F, Gerfen CR, Lee S. 2021. Cell-type-specific recruitment of GABAergic interneurons in the primary somatosensory cortex by long-range inputs. Cell reports. 34:108774.

O'Connor DH, Peron SP, Huber D, Svoboda K. 2010. Neural activity in barrel cortex underlying vibrissa-based object localization in mice. Neuron. 67:1048-1061.

Olsen SR, Bortone DS, Adesnik H, Scanziani M. 2012. Gain control by layer six in cortical circuits of vision. Nature. 483:47-52.

Petreanu L, Huber D, Sobczyk A, Svoboda K. 2007. Channelrhodopsin-2-assisted circuit mapping of long-range callosal projections. Nat Neurosci. 10:663-668.

Petreanu L, Mao T, Sternson SM, Svoboda K. 2009. The subcellular organization of neocortical excitatory connections. Nature. 457:1142-1145.

Petrof I, Viaene AN, Sherman SM. 2015. Properties of the primary somatosensory cortex projection to the primary motor cortex in the mouse. J Neurophysiol. 113:2400-2407.

Porter LL, White EL. 1983. Afferent and efferent pathways of the vibrissal region of primary motor cortex in the mouse. J Comp Neurol. 214:279-289.

Reyes A, Lujan R, Rozov A, Burnashev N, Somogyi P, Sakmann B. 1998. Target-cell-specific facilitation and depression in neocortical circuits. Nat Neurosci. 1:279-285.

Reyes A, Sakmann B. 1999. Developmental switch in the short-term modification of unitary EPSPs evoked in layer 2/3 and layer 5 pyramidal neurons of rat neocortex. J Neurosci. 19:3827-3835.

Rocco-Donovan M, Ramos RL, Giraldo S, Brumberg JC. 2011. Characteristics of synaptic connections between rodent primary somatosensory and motor cortices. Somatosens Mot Res. 28:63-72.

Sabatini BL, Regehr WG. 1999. Timing of synaptic transmission. Annu Rev Physiol. 61:521-542.

Sherman SM, Guillery RW. 2011. Distinct functions for direct and transthalamic corticocortical connections. J Neurophysiol. 106:1068-1077.

Somjen GG. 2002. Ion regulation in the brain: implications for pathophysiology. Neuroscientist. 8:254-267.

Sreenivasan V, Esmaeili V, Kiritani T, Galan K, Crochet S, Petersen CC. 2016. Movement Initiation Signals in Mouse Whisker Motor Cortex. Neuron. 92:1368-1382.

Stratford KJ, Tarczy-Hornoch K, Martin KA, Bannister NJ, Jack JJ. 1996. Excitatory synaptic inputs to spiny stellate cells in cat visual cortex. Nature. 382:258-261.

Takahashi N, Ebner C, Sigl-Glockner J, Moberg S, Nierwetberg S, Larkum ME. 2020. Active dendritic currents gate descending cortical outputs in perception. Nat Neurosci. 23:1277-1285.

Taniguchi H, He M, Wu P, Kim S, Paik R, Sugino K, Kvitsiani D, Fu Y, Lu J, Lin Y, Miyoshi G, Shima Y, Fishell G, Nelson SB, Huang ZJ. 2011. A resource of Cre driver lines for genetic targeting of GABAergic neurons in cerebral cortex. Neuron. 71:995-1013.

Tervo DG, Hwang BY, Viswanathan S, Gaj T, Lavzin M, Ritola KD, Lindo S, Michael S, Kuleshova E, Ojala D, Huang CC, Gerfen CR, Schiller J, Dudman JT, Hantman AW, Looger LL, Schaffer DV, Karpova AY. 2016. A Designer AAV Variant Permits Efficient Retrograde Access to Projection Neurons. Neuron. 92:372-382.

Tsodyks MV, Markram H. 1997. The neural code between neocortical pyramidal neurons depends on neurotransmitter release probability. Proc Natl Acad Sci USA. 94:719-723.

Turecek J, Jackman SL, Regehr WG. 2017. Synaptotagmin 7 confers frequency invariance onto specialized depressing synapses. Nature. 551:503-506.

Veinante P, Deschenes M. 2003. Single-cell study of motor cortex projections to the barrel field in rats. J Comp Neurol. 464:98-103.

Vijayan S, Hale GJ, Moore CI, Brown EN, Wilson M. 2010. Activity in the barrel cortex during active behavior and sleep. J Neurophysiol. 103:2074-2084.

Weiler N, Wood L, Yu J, Solla SA, Shepherd GM. 2008. Top-down laminar organization of the excitatory network in motor cortex. Nat Neurosci. 11:360-366.

White EL, DeAmicis RA. 1977. Afferent and efferent projections of the region in mouse SmL cortex which contains the posteromedial barrel subfield. J Comp Neurol. 175:455-482.

Williams SR, Mitchell SJ. 2008. Direct measurement of somatic voltage clamp errors in central neurons. Nat Neurosci. 11:790-798.

Xu NL, Harnett MT, Williams SR, Huber D, O'Connor DH, Svoboda K, Magee JC. 2012. Nonlinear dendritic integration of sensory and motor input during an active sensing task. Nature. 492:247-251.

Yamashita T, Pala A, Pedrido L, Kremer Y, Welker E, Petersen CC. 2013. Membrane potential dynamics of neocortical projection neurons driving target-specific signals. Neuron. 80:1477-1490.

Yang W, Carrasquillo Y, Hooks BM, Nerbonne JM, Burkhalter A. 2013. Distinct balance of excitation and inhibition in an interareal feedforward and feedback circuit of mouse visual cortex. J Neurosci. 33:17373-17384.

Young H, Belbut B, Baeta M, Petreanu L. 2021. Laminar-specific cortico-cortical loops in mouse visual cortex. eLife. 10.

Zagha E, Casale AE, Sachdev RN, McGinley MJ, McCormick DA. 2013. Motor cortex feedback influences sensory processing by modulating network state. Neuron. 79:567-578.

Zhang S, Xu M, Kamigaki T, Hoang Do JP, Chang WC, Jenvay S, Miyamichi K, Luo L, Dan Y. 2014. Selective attention. Long-range and local circuits for top-down modulation of visual cortex processing. Science. 345:660-665.

Zhang YP, Oertner TG. 2007. Optical induction of synaptic plasticity using a light-sensitive channel. Nat Methods. 4:139-141.

Zolnik TA, Ledderose J, Toumazou M, Trimbuch T, Oram T, Rosenmund C, Eickholt BJ, Sachdev RNS, Larkum ME. 2020. Layer 6b Is Driven by Intracortical Long-Range Projection Neurons. Cell reports. 30:3492-3505 e3495.

Zucker RS. 1999. Calcium- and activity-dependent synaptic plasticity. Curr Opin Neurobiol. 9:305-313.

Zucker RS, Regehr WG. 2002. Short-term synaptic plasticity. Annu Rev Physiol. 64:355-405.

APPENDIX A: CHAPTER 2 FIGURES AND TABLES

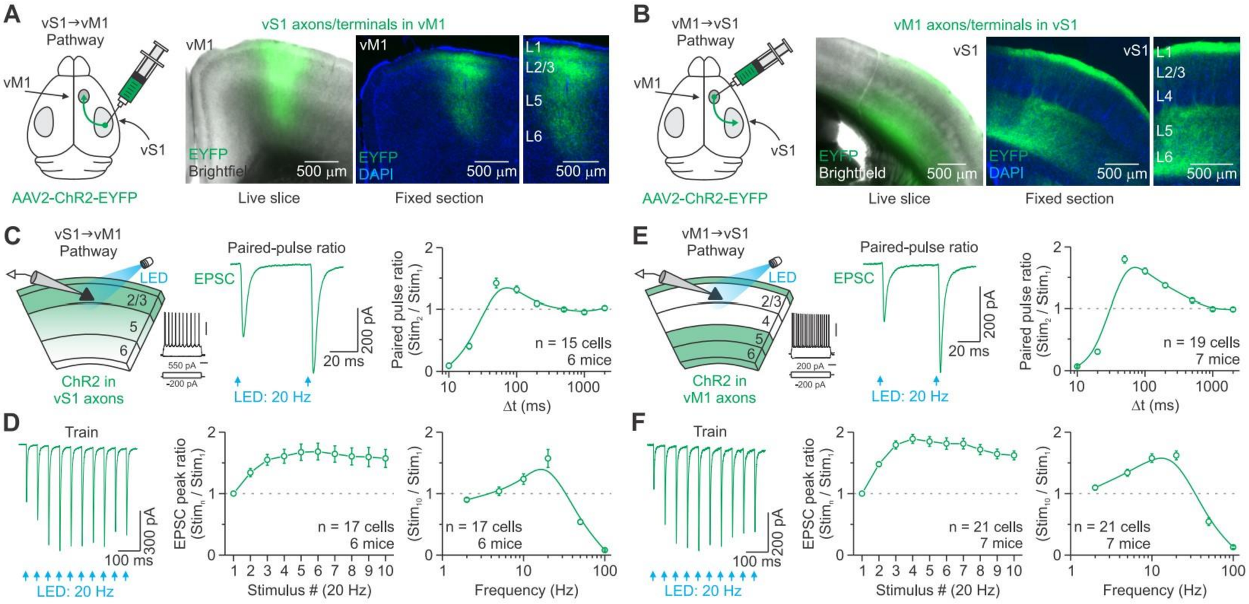

Figure 2.1. Optical stimulation of vS1 and vM1 CC projections evoked facilitating synaptic excitation in L2/3 neurons. (A-B) Left: Schematic showing virus injected into vS1 (A) or vM1 (B) of mice *in vivo*. Middle: Live slice (300 μm) image showing an overlay of EYFP with brightfield. Right: Low- and high-magnification fluorescence image of a 60-μm-thick section from the same live slice. EYFP-labeled vS1 axons terminate densely in superficial layers of vM1 (A), whereas EYFP-labeled vM1 axons terminate densely in L1 and L5/6 of vS1 (B). Sections were counterstained with DAPI. (C) Left: Recording schematic showing photostimulation of ChR2-expressing vS1 terminal arbors (green) and a whole-cell recording from an excitatory L2/3 cell in vM1. Responses of a non-expressing L2/3 RS cell to intracellular current steps (scale bars, 40 mV/200 ms). Middle: vS1-vM1 EPSCs evoked in the same neuron (shown in C, left) by a pair of optical stimuli at 20 Hz (blue arrow, 0.5 ms) (average of 10 trials). Right: Population data showing the average peak paired-pulse ratio at different interstimulus intervals (Δt). (D) Left: vS1-vM1 EPSCs evoked in the same cell (shown in C) by a 20 Hz train of optical stimuli (average of 10 trials). EPSCs increased 60-70% from the first to the fourth pulse. Middle and Right: EPSC amplitudes plotted as a function of stimulus number within 20 Hz trains (normalized to first responses) and the peak responses to the tenth stimulus as a function of stimulus frequency (normalized to first responses). (E) Left: Recording schematic for the vM1-vS1 CC pathway. Responses of a non-expressing L2/3 RS cell to intracellular current steps (scale bars, 40 mV/200 ms). Middle: vM1-vS1 EPSCs evoked in the same neuron (shown in E, left) by a pair of optical stimuli at 20 Hz (blue arrows, 0.5 ms) (average of 16 trials). Right: Population data showing the average peak paired-pulse ratio at different interstimulus intervals (Δt). (F) Left: vM1-vS1 EPSCs evoked in the same neuron (shown in E) by a 20 Hz train of optical stimuli (average of 17 trials). EPSCs nearly doubled from the first to the fourth pulse. Middle and Right: EPSC amplitudes plotted as a function of stimulus number within 20 Hz trains (normalized to first responses) and the peak

Figure 2.1 (cont'd)

responses to the tenth stimulus as a function of stimulus frequency (normalized to first responses). The light intensity for each cell was set to obtain an initial 200 pA EPSC when held near the inhibitory reversal potential (-94 mV, see Methods). Values are represented as mean ± SEM.

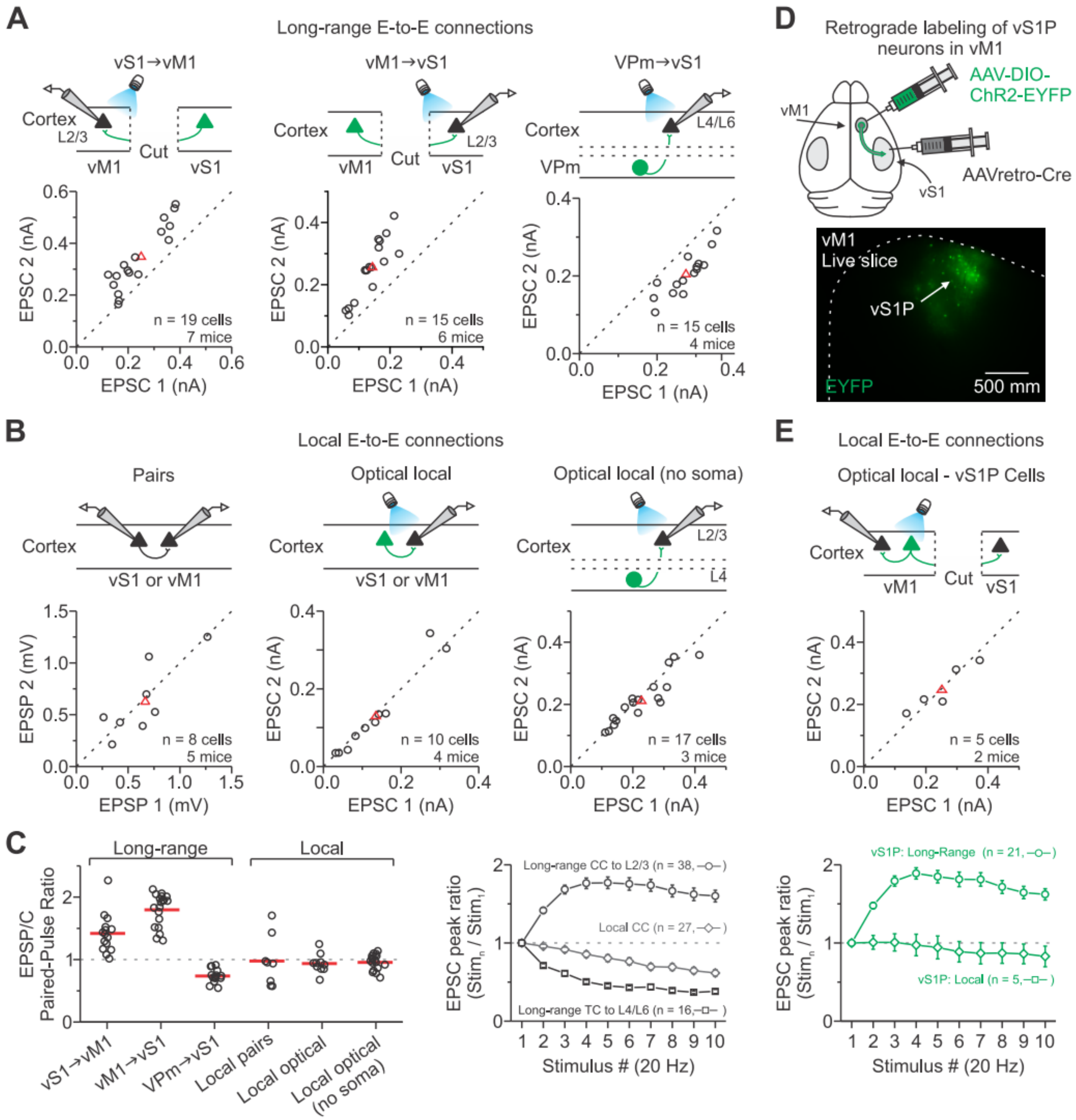

Figure 2.2. Synaptic responses during repetitive activation are more sustained for long-range CC than other excitatory cortical connections. (A) Long-range excitatory-to-excitatory (E-to-E) connections. A comparison of the first and second EPSC amplitude evoked by a pair of optical stimuli (20 Hz) directed at long-range CC or TC axons in the cortex: vM1-vS1L2/3, vS1-vM1L2/3, and VPm-vS1L4/L6. (B) Local E-to-E connections. A comparison of the first and second EPSP/C amplitude evoked by a pair of stimuli for local excitatory connections in the cortex: pairs of excitatory cells (20-60 Hz), photostimulation of local excitatory neurons/axons that conditionally expressed ChR2 in Rbp4-Cre or Scnn1a-Cre-Tg3 mice (10-20 Hz), and photostimulation of L4 to L2/3 axons/terminals (without parent somata) that conditionally expressed ChR2 using

Figure 2.2 (cont'd)

Scnn1a-Cre-Tg3 mice (20 Hz). To isolate axons/terminals from parent somata, a cut was made between L4 and L2/3. (C) Left: Summary graph of paired-pulse ratios for the long-range and local excitatory cortical connections. Paired-pulse ratios were significantly larger for both long-range CC connections than all other excitatory connections ($p < 0.0001$, One-way ANOVA with Bonferroni's post-hoc test). Right: Summary graph shows EPSC amplitudes plotted as a function of stimulus number within 20 Hz trains. Synaptic dynamics were significantly different, with responses to long-range CC inputs exhibiting short-term facilitation ($n = 38$ cells, 13 mice), local connections displaying weak depression ($n = 27$ cells, 7 mice), and long-range thalamocortical inputs showing strong depression ($n = 16$ cells, 4 mice) ($p < 0.00001$, Two-way ANOVA, stim. 2-10). (D) Top: Schematic showing AAVretro-Cre injected into the vS1 and Cre-dependent AAV-DIO-ChR2 injected into ipsilateral vM1 of mice in vivo. Bottom: Live slice (300 µm) image of vM1 showing EYFP fluorescence indicating the location of ChR2-EYFP. (E) Top: A comparison of the first and second EPSC amplitude evoked by a pair of optical stimuli (20 Hz) directed at ChR2-expressing vS1P cells in vM1 ($p = 0.93$, Paired t-test). Bottom: Summary graph shows EPSC amplitudes plotted as a function of stimulus number within 20 Hz trains for local and long-range targets of vS1P cells in vM1 (Local: $n = 5$ cells, 2 mice; Long-range: 21 cells, 7 mice; $p < 0.00001$, Two-way ANOVA, stim. 2-10). Red triangles and lines represent means. Long-range CC data from Figure 2.1. Values are represented as mean ± SEM.

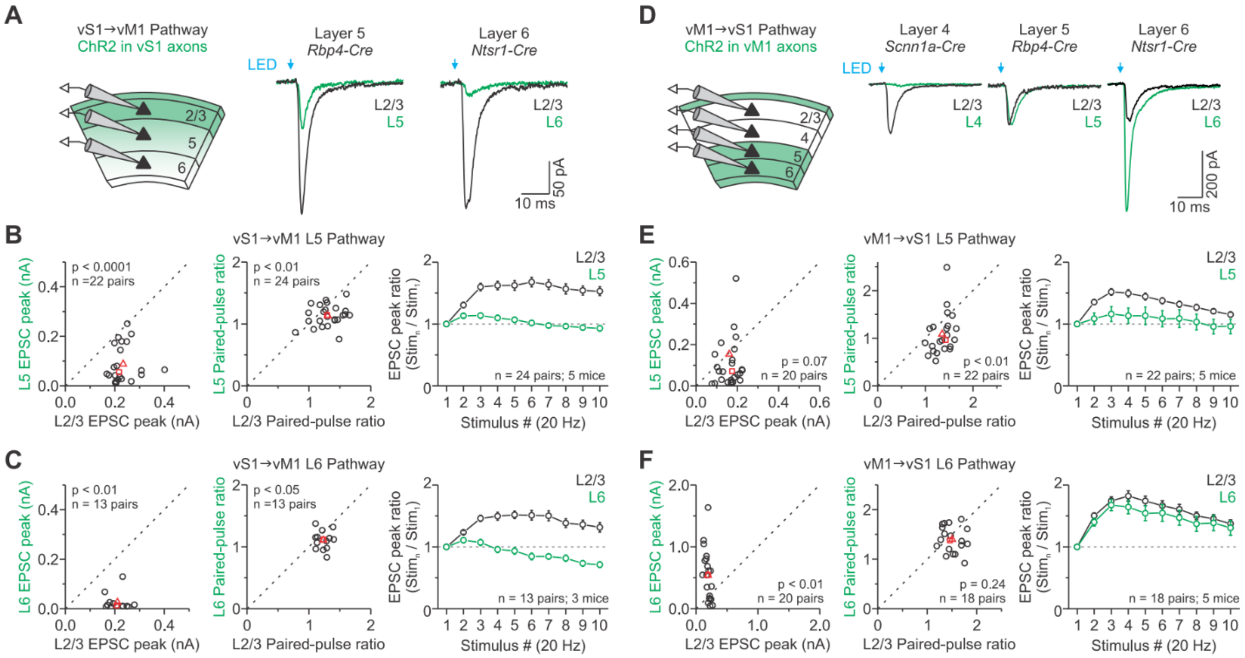

Figure 2.3. Comparison of ChR2-evoked CC responses across layers. (A) Left: Recording schematic for the vS1-vM1 pathway. We sequentially recorded an excitatory L2/3 cell and an excitatory neuron in a separate layer of the same column. Layers were determined using layer-specific Cre-driver mouse lines crossed with a tdTomato reporter (see Methods). Right: Representative single EPSCs evoked optically for pairs of excitatory cells recorded in different layers of vM1 (average of 6-11 trials). (B-C) A comparison of the average vS1-vM1 optically evoked EPSC amplitude (left), paired-pulse ratio at 20 Hz (middle), and EPSC amplitudes plotted as a function of stimulus number within 20 Hz trains for each L2/3-L5 (B) and L2/3-L6 cell pair (C). Red triangles and squares represent means and median, respectively. n displayed on the plot. L5 and L6 responses were significantly lower ($p < 0.01$, Wilcoxon paired signed-rank test), displayed lower paired-pulse ratios ($p < 0.0001$, Paired t-test), and underwent less facilitation during 20 Hz trains than those in L2/3 ($p < 0.0001$, Two-way ANOVA, stim. 2-10). (D) Left: The same experimental approach described in (A) for the vM1-vS1 pathway. Right: Representative single EPSCs evoked for pairs of excitatory cells in different layers of vS1 (average of 5-11 trials). (E-F) A comparison of the average vM1-vS1 optically evoked EPSC amplitude (left), paired-pulse ratio at 20 Hz (middle), and EPSC amplitudes plotted as a function of stimulus number within 20 Hz trains for each L2/3-L5 (E) and L2/3-L6 cell pair (F). Red triangles and squares represent means and median, respectively. n displayed on the plot. EPSCs were stronger in L6 ($p < 0.01$, Paired t-test), weaker in L4 ($n = 7$ pairs, 3 mice, data not shown, $p < 0.03$, Wilcoxon paired signed-rank test), and similar in L5 as compared to those in L2/3 ($p = 0.07$, Wilcoxon paired signed-rank test). L5 responses underwent less facilitation than those in L2/3 (PPR: $p < 0.01$, Mann-Whitney U test; Train: $p < 0.0001$, Two-way ANOVA, stim. 2-10), whereas L6 responses displayed similar paired-pulse facilitation ($p = 0.24$, Paired t-test) but facilitated less than L2/3 during 20 Hz trains ($p < 0.01$, Two-way ANOVA, stim. 2-10). L4 responses were too weak to test dynamics. For single EPSCs, cells were tested at the light intensity needed to obtain an

Figure 2.3 (cont'd)

initial 200 pA EPSC in L2/3 in voltage-clamp at -94 mV, whereas short-term plasticity was tested at the cell's own 200 pA intensity. Values are represented as mean ± SEM.

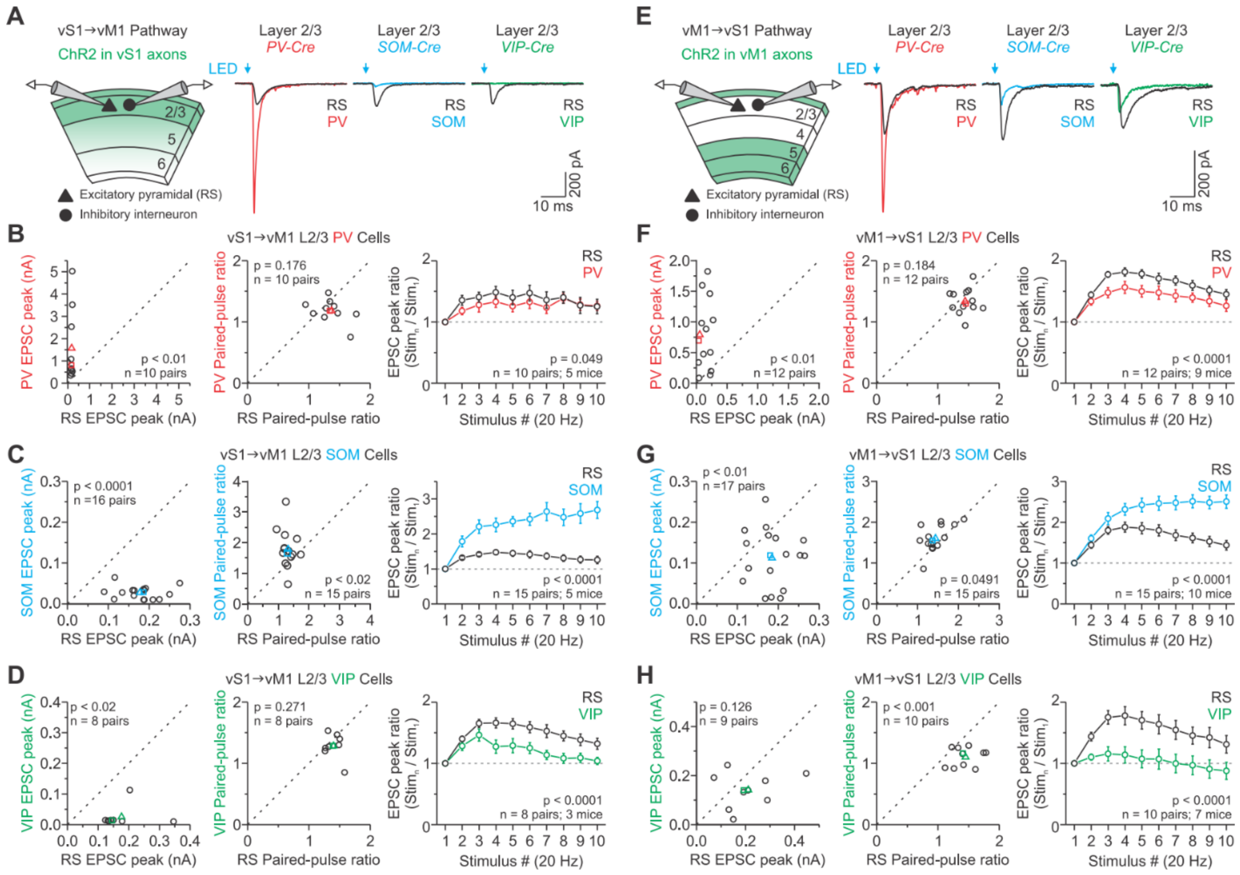

Figure 2.4. Comparison of ChR2-evoked CC responses across GABAergic interneurons in L2/3 of vM1 and vS1. (A) Left: Recording schematic for the vS1-vM1 pathway. We simultaneously recorded a specific L2/3 interneuron and a nearby excitatory neuron. Experiments utilized Cre-driver mice targeting three classes of GABAergic cells in the neocortex (see Methods). Right: Representative single EPSCs evoked optically in interneuron-RS pairs (average of 7-10 trials). (B-D) A comparison of the average vS1-vM1 optically evoked EPSC amplitude (left), the paired-pulse ratio at 20 Hz (middle), and EPSC amplitudes plotted as a function of stimulus number within 20 Hz trains for PV-RS (B), SOM-RS (C), and VIP-RS pairs (D). Colored triangles and squares represent means and median, respectively. n displayed on the plot. EPSCs were stronger in PV ($p < 0.01$, Wilcoxon paired signed-rank test) but weaker in both SOM and VIP as compared to those in L2/3 RS cells (SOM: $p < 0.0001$, Paired t-test; VIP: $p < 0.02$, Wilcoxon paired signed-rank test). Short-term dynamics of excitatory vS1-vM1 synapses onto L2/3 interneurons were significantly different during 20 Hz trains than RS cells ($p < 0.05$, Two-way ANOVA, stim. 2-10). (E) Left: The same experimental approach described in (A) for the vM1-vS1 pathway. Right: Representative single EPSCs evoked optically in interneuron-RS pairs (average of 8-10 trials). (F-H) A comparison of the average vM1-vS1 optically evoked EPSC amplitude (left), the paired-pulse ratio at 20 Hz (middle), and EPSC amplitudes plotted as a function of stimulus number within 20 Hz trains for PV-RS (F), SOM-RS (G), and VIP-RS pairs (H). Colored triangles and squares represent means and median, respectively. n displayed on the plot. EPSCs were stronger in PV ($p < 0.01$, Paired t-test),

Figure 2.4 (cont'd)

weaker in SOM ($p < 0.01$, Paired t-test), and similar in VIP as compared to those in L2/3 RS cells ($p = 0.126$, Paired t-test). Short-term dynamics of excitatory vS1-vM1 synapses onto L2/3 interneurons were significantly different during 20 Hz trains than RS cells ($p < 0.0001$, Two-way ANOVA, stim. 2-10). For single EPSCs, we tested pairs at the light intensity needed to obtain an initial 200 pA EPSC in the L2/3 excitatory neuron when recorded in voltage-clamp at -94 mV. We tested short-term plasticity at an intensity that evoked a reliable EPSC (typically 50-300 pA) for each cell. Values are represented as mean ± SEM.

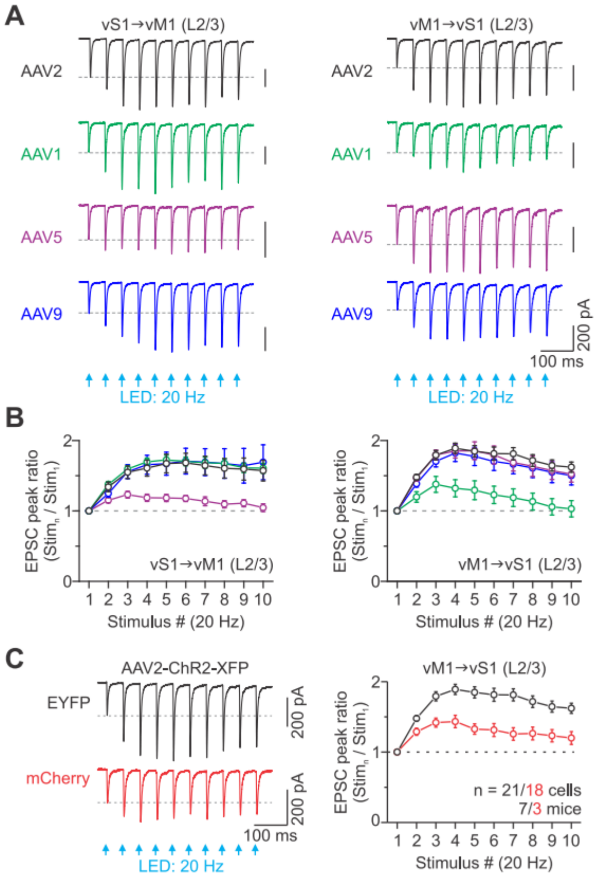

Figure 2.5. Effect of AAV serotype and ChR2 fusion protein on optically evoked facilitation at CC synapses. (A) For each serotype (AAV2, AAV1, AAV5, and AAV9), representative EPSCs evoked optically by 20 Hz trains for an excitatory L2/3 cell located in vM1 (left) or vS1 (right) (average of 3-17 trials). We used the same vector (AAV-hSyn-hChR2(H134R)-EFYP), titer (3.1 x 1012 viral genomes/ml), volume per injection site (~0.15 µl), and transduction time (21±1 days) for each serotype to keep expression levels similar. (B) Summary graphs show the average EPSC amplitudes plotted as a function of stimulus number within 20 Hz trains for each serotype tested in the vS1-vM1 (left) and vM1-vS1 pathway (right). Facilitation was significantly weaker than other serotypes when using AAV5 in the vS1-vM1 pathway ($p < 0.0001$) and AAV1 in the vM1-vS1 pathway ($p < 0.0001$, Two-way ANOVA, stim. 2-10, with Bonferroni's post-hoc test) (vS1-vM1: AAV1, n = 18 cells, 2 mice; AAV5, n = 16 cells, 3 mice; AAV9, n = 8 cells, 2 mice) (vM1-vS1: AAV1, n = 8 cells, 3 mice; AAV5, n = 8 cells, 3 mice; AAV9, n = 21 cells, 7 mice). AAV2 data same as shown in Figure 2.1D and 1F. (C) Left: Representative EPSCs evoked optically by 20 Hz trains for excitatory L2/3 cells in vS1 when using AAV2 to drive ChR2-EYFP or ChR2-mCherry expression in vM1 axons (average of 10 and 8 trials). For these experiments, we used the same titer and expression time. Right: Summary graph shows the average EPSC amplitudes plotted as a function of the stimulus number within 20 Hz trains for each vector. Short-term facilitation was blunted when using AAV2-ChR2-mCherry (n = 18 cells, 3 mice for mCherry; $p < 0.0001$, Two-way ANOVA, stim. 2-10). AAV2-ChR2-EYFP data same as shown in Figure 2.1F.

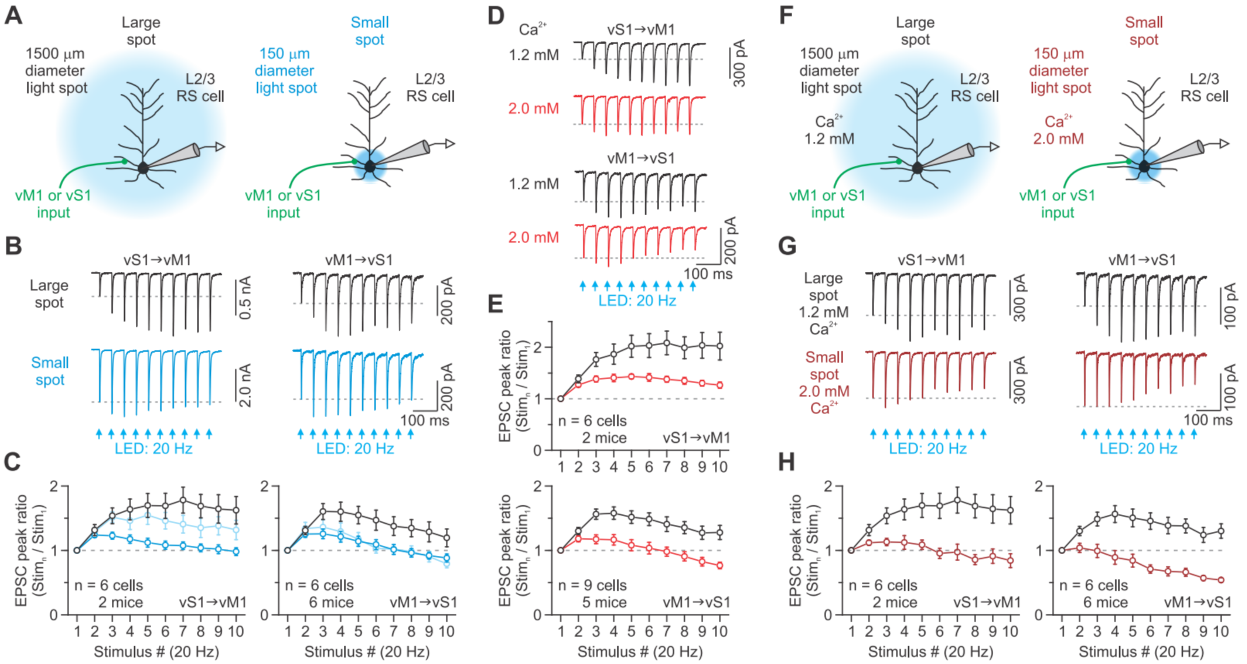

Figure 2.6. Effect of over-terminal stimulation and extracellular Ca2+ concentrations on optically evoked facilitation at CC synapses. (A) Recording schematic for (B-C) showing photostimulation of CC arbors using different light-spot sizes (blue circles). Restricting the excitation light to over the terminal ends of ChR2-expressing axons and keeping the total emitted light power the same will likely cause more terminal depolarization. (B) Representative EPSCs evoked by large- and small-field repetitive photostimulation at 20 Hz for an excitatory L2/3 cell in vM1 (left) or vS1 (right) (average of 5-11 trials). (C) Summary graphs show average EPSC amplitudes plotted as a function of stimulus number within 20 Hz trains for each condition. Restricting the excitation light significantly decreased the facilitation at both vS1-vM1 ($p < 0.0001$) and vM1-vS1 synapses ($p < 0.0001$, Two-way ANOVA, stim. 2-10; Average Power densities: vS1-vM1 = 0.71 and 71 mW/mm2; vS1-vM1 = 2.34 and 234 mW/mm2). Adjusting the power of the small spot to obtain an initial 200 pA EPSC also decreased facilitation (Light blue traces: vS1-vM1, $p < 0.006$; vM1-vS1, $p < 0.0001$; Two-way ANOVA, stim. 2-10; Average Power densities: vS1-vM1 = 21 mW/mm2; vS1-vM1 = 111 mW/mm2). (D) Representative EPSCs evoked optically by 20 Hz trains for an excitatory L2/3 cell located in vM1 (top) or vS1 (bottom) recorded in 1.2 and 2.0 mM external Ca2+ (average of 10-12 trials). (E) Summary graphs show average EPSC amplitudes plotted as a function of stimulus number within 20 Hz train for 1.2 and 2.0 mM external Ca2+. Raising Ca2+ significantly decreased facilitation at both vS1-vM1 ($p < 0.0001$) and vM1-vS1 synapses ($p < 0.0001$, Two-way ANOVA, stim. 2-10). (F) Recording schematic for (G-H) showing the same photostimulation approach described in (A). Large-field photostimulation was done in 1.2 mM external Ca2+, whereas small-field photostimulation was done in 2.0 mM external Ca2+. (G) Representative EPSCs evoked by large- and small-field repetitive photostimulation at 20 Hz recorded in 1.2 and 2.0 mM external Ca2+, respectively, for an excitatory L2/3 cell located in vM1 (left) or vS1 (right) (average of 10-12 trials). (H) Summary graphs show average EPSC amplitudes plotted as a function of stimulus

Figure 2.6 (cont'd)

number within 20 Hz train for the two conditions. Restricting the excitation light while in 2.0 mM external Ca2+ changed facilitation to depression (vS1-vM1, $p < 0.0001$; vM1-vS1, $p < 0.0001$, Two-way ANOVA, stim. 2-10). The light intensity was set to obtain an initial ~200 pA EPSC for C (light blue), D-E, and F-G. Right: Values are represented as mean ± SEM.

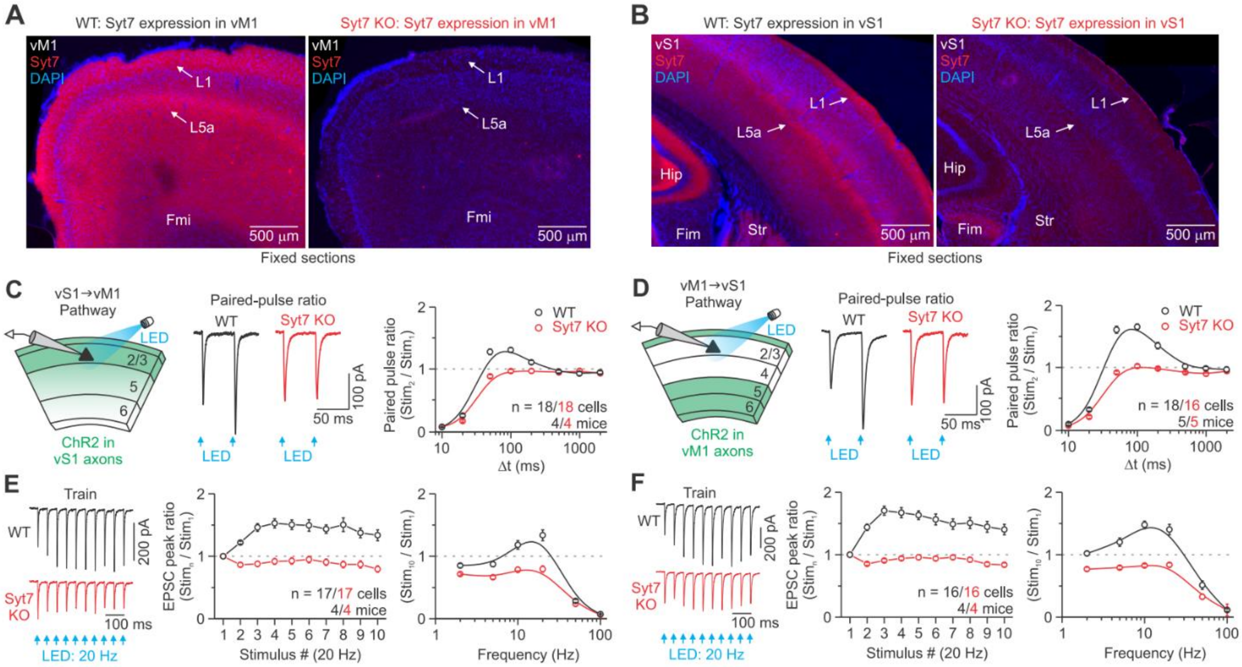

Figure 2.7. Facilitation at CC synapses is absent in Syt7 knockout mice. (A-B) Images of 60-µm-thick fixed coronal sections, centered on vM1 (A) and vS1 (B), from WT mice and Syt7 KO littermates (ages = P73 for A and P95 for B). Tissue was stained immunohistochemically for Syt7 and counterstained with DAPI. Syt7 expression was strong in L1 and L5a. Hip, hippocampus; Fim, fimbria of the hippocampus; Fmi, forceps minor of the corpus callosum, Str, striatum. (C-D) Left: Recording schematic for the vS1-vM1 (C) and vM1-vS1 CC pathway (D). The light intensity for each cell was set to obtain an initial 200 pA EPSC when held in voltage-clamp at -94 mV. Middle: Representative vS1-vM1 (C) and vM1-vS1 (D) EPSCs evoked in L2/3 RS cells by a pair of optical stimuli at 20 Hz, recorded from brain slices prepared from WT and Syt7 KO littermates (average of 9-17 trials). Right: Summary graphs show the average peak paired-pulse ratio at different interstimulus intervals (Δt) for vS1-vM1 (C) and vM1-vS1 synapses (D). n displayed on the plot. The peak paired-pulse ratio at 20 Hz was significantly different for WT and Syt7 KO at both synapses ($p < 0.0001$, Two-Sample t-test). (E-F) Left: vS1-vM1 (E) and vM1-vS1 (F) EPSCs evoked in the same pair of cells (shown in C and D) by a 20 Hz train of optical stimuli (average of 12-20 trials). Middle and Right: Summary graphs show EPSC amplitudes plotted as a function of stimulus number within 20 Hz trains, and the average normalized peak response to the tenth stimulus as a function of stimulus frequency for vS1-vM1 (E) and M1-vS1 synapses (F). In Syt7 KO mice, facilitation was eliminated at both synapses ($p < 0.0001$, Two-way ANOVA, stim. 2-10). Values are represented as mean ± SEM.

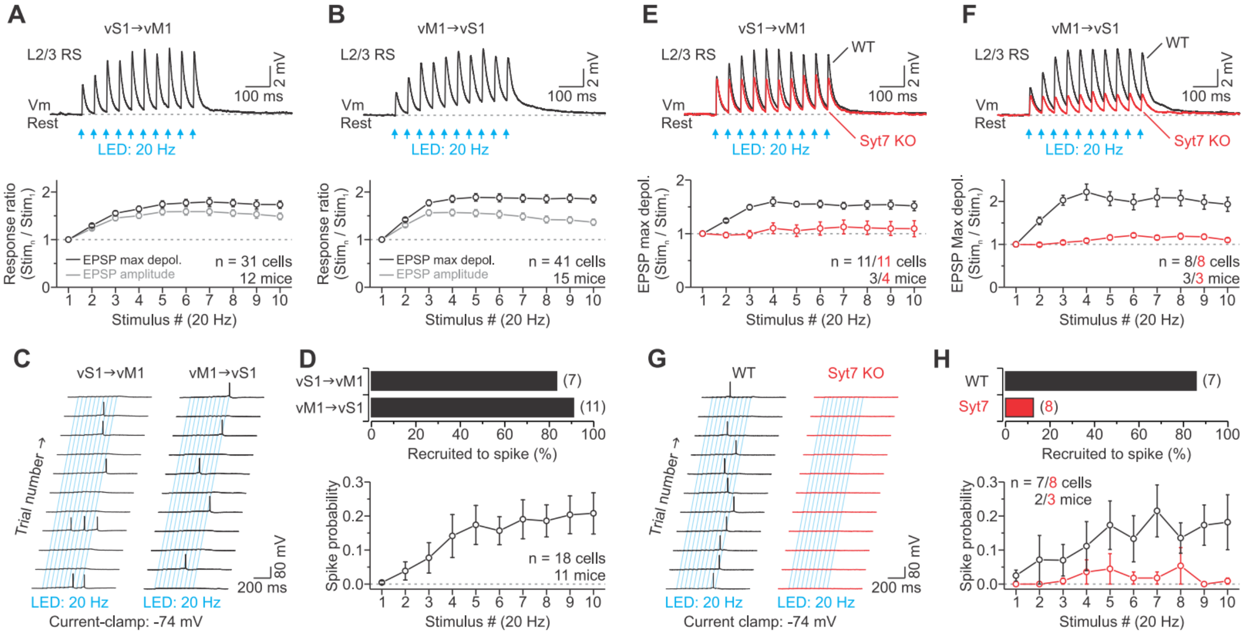

Figure 2.8. The functional role of short-term facilitation in the modulation of L2/3 excitability. (A-B) Top: Representative synaptic potentials evoked by low-intensity 20 Hz optical trains of CC arbors for an excitatory L2/3 cell at rest in vM1 (A) and vS1 (B) (average of 11 trials each). The light intensity for each cell was the same intensity needed to obtain an initial 200 pA EPSC when held in voltage-clamp at -94 mV. Bottom: Population data showing the average EPSPs' maximal depolarization and EPSPs' amplitude plotted as a function of stimulus number within 20 Hz trains for both vS1-vM1 (A) and vM1-vS1 (B) synapses. Short-term synaptic facilitation was apparent during 20 Hz trains. (C) Current-clamp recordings from an excitatory L2/3 cell in vM1 (left) and vS1 (right) in response to 20 Hz optical stimulation of CC axons/terminals. Same conditions as in (A-B), but neurons were held in current-clamp at a more depolarized membrane potential (-74 mV). A train of optical CC stimuli elicits action potentials in excitatory L2/3 cells in some but not all trials. (D) Top: Summary histogram showing the percentage of L2/3 RS cells recruited to spike by photostimulation of both CC pathways (n shown in parentheses). Bottom: Summary graph showing spike probability plotted against stimulus number for L2/3 RS cells in vM1 and vS1. (E-F) Top: Representative synaptic potentials evoked by low-intensity 20 Hz optical trains of CC arbors for an excitatory L2/3 neuron at rest in vM1 (A) and vS1 (B), recorded from brain slices prepared from WT and Syt7 KO mice (average of 11-12 trials). Bottom: Population data showing the average EPSPs' maximal depolarization and EPSPs' amplitude plotted as a function of stimulus number within the trains for both vS1-vM1 (E) and vM1-vS1 (F) synapses in WT and Syt7 KO mice. Short-term synaptic facilitation was absent in Syt7 KO mice ($p < 0.0001$, Two-way ANOVA, stim. 2-10). (G) Similar current-clamp recordings as described in (C) for excitatory L2/3 neurons recorded in brain tissue prepared from WT (left) and Syt7 KO (right) mice in response to 20 Hz optical stimulation of CC axons/terminals. A train of optical CC stimuli elicits action potentials in WT L2/3 cells in some but not all trials, whereas cells in KO mice rarely responded with action potentials. (H) Top: Summary histogram showing the percentage of L2/3 RS cells recruited to spike by photostimulation

Figure 2.8 (cont'd)

of CC afferents for both WT and Syt7 KO mice (n shown in parentheses). Bottom: Summary graph showing spike probability plotted against stimulus number for WT and Syt7 KO L2/3 RS cells. In Syt7 KO mice, spike probability was significantly reduced ($p < 0.0001$, Two-way ANOVA). Values are represented as mean ± SEM.

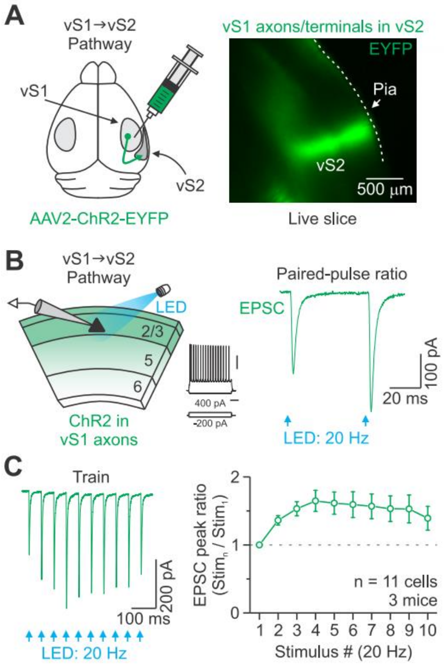

Figure 2.9. vS1 synapses in vS2 have similar short-term dynamics as vS1-vM1 and vM1-vS1 synapses. (A) Right: Injection schematic. AAV2-ChR2-EFYP was injected unilaterally into the right vS1. Left: Epifluorescence image of a live coronal brain slice (300 µm) centered on vS2, from a P43 mouse injected in vS1 16 days prior with AAV2-ChR2-EYFP. (B) The recording schematic shows photostimulation of ChR2-expressing vS1 terminal arbors (green) and whole-cell recording from a non-expressing L2/3 RS neuron. Middle: Responses of a L2/3 RS cell in vS2 to intracellular current steps (scale bars 40 mV/ 200 ms). Right: vS1 excitatory synaptic current evoked in the same neuron (middle) by a pair of optical stimuli at 20 Hz (blue arrow, 0.5 ms) (average 13 sweeps). (C) Left: vS1 excitatory synaptic currents evoked in the same neuron (shown in B, middle) by a 20 Hz train of optical stimuli (average of 30 trials). Right: Average short-term dynamics of EPSCs evoked in L2/3 RS cells of vS2 during 20 Hz trains (n = 11 cells from 3 mice). Overall, long-range vS1-vS2 (sensory-sensory) CC responses facilitate similar to those observed in the vS1-vM1 (sensory-motor).

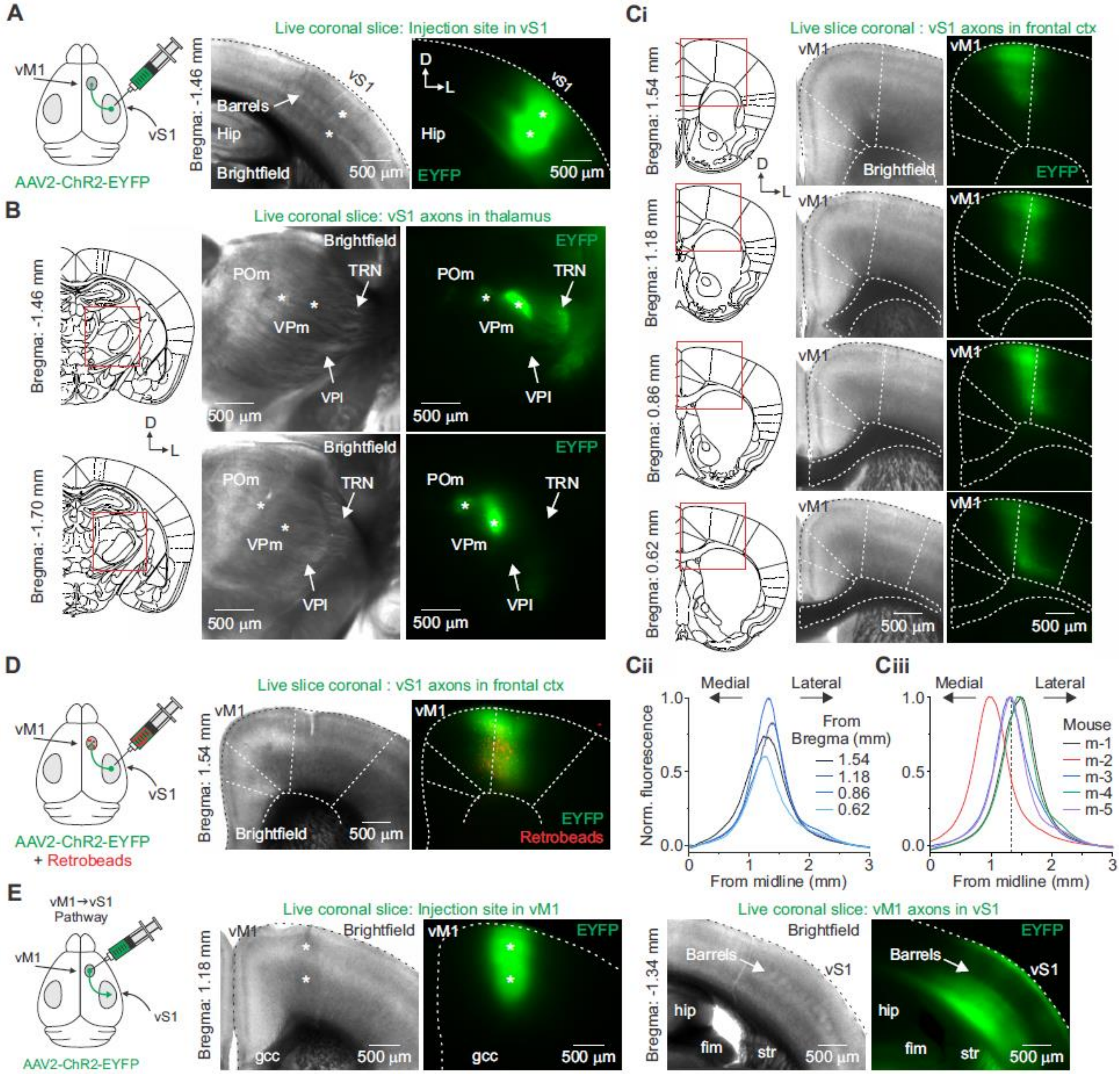

Figure 2.10. Mapping the region of the frontal cortex that mediates long-range reciprocal connections between vS1 and vM1. Related to Figure 2.1. (A) Left: AAV2-ChR2-EYFP was injected into vS1 of mice in vivo, and then live 300 mm-thick serial coronal sections were collected 20-22 days after for imaging. Right: Brightfield and epifluorescence images of a live coronal slice through vS1 of a P40 mouse. The presence of L4 barrels identified vS1. Asterisks indicate the viral injection sites. (B) Left and middle: Reference atlas drawings and brightfield images of consecutive coronal slices through somatosensory thalamus (same mouse as A). Right: Epifluorescence images show EYFP-expressing axons/terminals in the somatosensory thalamus, including the thalamic reticular nucleus (TRN), ventral posterior medial nucleus (VPm), and posterior medial nucleus (POm). No expression was observed in the ventral posterior lateral nucleus (VPl). (C) Top (Ci): Reference atlas drawings and serial slices through frontal cortex (same mouse as A). EYFP-expressing vS1 projections formed a narrow band just lateral to midline that was strongest between 0.5 and 2.0 mm anterior to bregma when compared

Figure 2.10 (cont'd)

to a reference atlas. (Cii), Fluorescence profile plot for each image shown in Ci, normalized to the strongest expressing slice. The anterior-posterior coordinate for vM1 was based on the approximate location of the strongest expressing slice. (Ciii), Normalized fluorescence profile plot of the strongest expressing slice for each mouse. The distance of the peak from the midline was used to calculate the medial-lateral coordinate for vM1. (Average vM1 coordinates: anterior-posterior location from bregma, 1.12 ± 0.13 mm; medial-lateral location from midline, 1.27 ± 0.07 mm; half-width of the normalized fluorescence plot, 0.65 ± 0.02 mm; n = 5 mice). (D) vM1 and vS1 are reciprocally connected. Left: AAV2-ChR2-EYFP and retrobeads were co-injected into vS1. Right: Brightfield and epifluorescence image of a live coronal slice through vM1 of a P39 mouse (23 days of expression). Shown is the overlap of retrograde cells (red) and vS1 anterograde axons/terminals (green) in vM1 (results were repeated in n = 4 mice). (E) vM1 axons terminate diffusely in vS1. Left: AAV2-ChR2-EYFP was injected unilaterally into vM1 using the coordinates above. The virus serotype, volume, and the location of each injection (see Methods) were chosen to best match the pattern of vS1 terminal arbors and to minimize spread into neighboring areas (compare the vM1 images in E with C and D). Right: Brightfield and epifluorescence images through vM1 and vS1 of a P39 mouse injected in vM1 21 days prior with AAV2-ChR2-EYFP. Genu of the corpus callosum (gcc). The vS1 images are used in Figure 2.1. Values are represented as mean ± SEM.

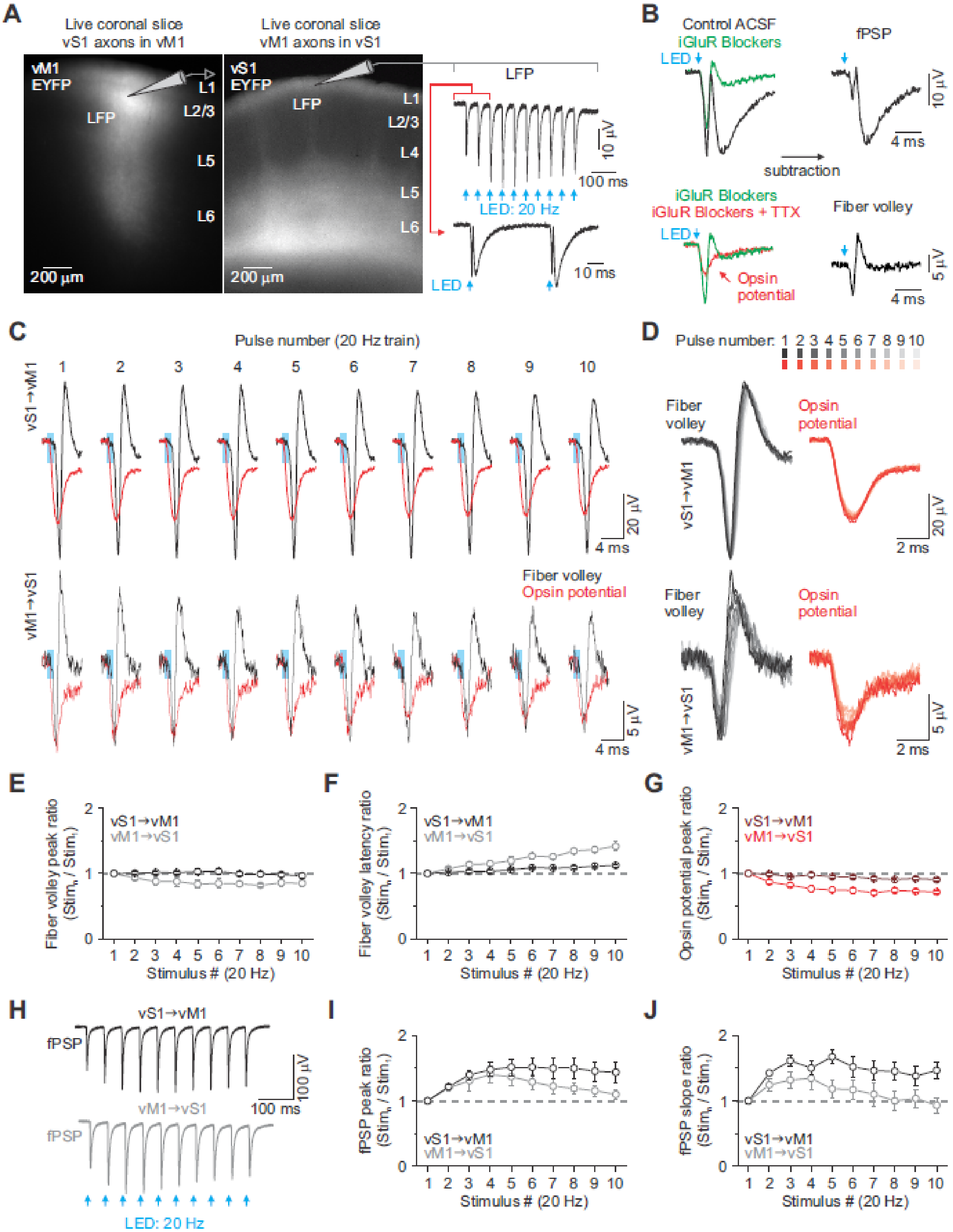

Figure 2.11. ChR2 can reliably drive action potentials in long-range CC axons. Related to Figure 2.1. (A) Left: Epifluorescence image of a live 300 mm coronal slice showing ChR2-EYFP expressing vS1 terminal arbors in vM1 of a P39 mouse (22 days after viral injection in vS1). Middle: Similar image showing ChR2-EYFP expressing vM1

Figure 2.11 (cont'd)

terminal arbors in vS1 of a P41 mouse (21 days after viral injection in vM1). Right: To test the effectiveness of ChR2 in driving presynaptic action potentials (APs), we recorded the local field potential (LFP) in response to a 20 Hz train (10 pulses, 0.5 ms pulse duration, every 10 sec). LFP recordings and optical stimulation were targeted to L2/3 and L1 for vM1 and vS1, respectively. Light intensities were adjusted for each slice to the power needed to evoke a 200 pA EPSC in a neighboring L2/3 RS cell when held near the inhibitory reversal potential (average LED power: 1.7 mW or 1.0 mW/mm2 for vS1 axons in vM1, 12.4 mW or 7.0 mW/mm2 for vM1 axons in vS1). (B) Example traces showing how the fiber volley was pharmacologically isolated from the recorded LFP (Hass and Glickfeld 2016). Ionotropic glutamate receptors (iGluRs) were first blocked by adding selective antagonists (DNQX, 20 mM; APV, 50 mM) to the control ACSF. Subtracting the resulting trace from the control produced the field postsynaptic potential (fPSP). Sodium channels were subsequently blocked by adding tetrodotoxin (TTX, 1 mM). The resulting TTX-insensitive potential was referred to as the opsin potential (Hass and Glickfeld 2016). Subtracting the opsin potential from the potential recording in iGluR blockers resulted in the isolated fiber volley (bottom right). (C) Repetitive activation of CC axons with ChR2 is reliable. Fiber volleys (black) and opsin potentials (red) evoked by a 20 Hz train of optical stimuli (blue boxes: 0.5 ms) for both the vS1- vM1 (top) and vM1-vS1 (bottom) pathways (average of ~200 trials each). (D) Overlay of the fiber volleys and opsin potentials from the recordings in (C). (E-G) Population data showing the normalized fiber volley amplitude (E), fiber volley latency (F), and opsin potential amplitude (G) during 20 Hz trains (n = 10 slices from 5 mice for the vS1-vM1 pathway; n = 7 slices from 4 mice for the vM1-vS1 pathway). Repetitive 20 Hz stimulation of ChR2- expressing vS1 axons/terminals resulted in a fiber volley amplitude decay of ~0% after the second pulse and 4% on the tenth pulse. The same stimulation of ChR2-expressing vM1 axons/terminals resulted in a modest fiber volley amplitude decay of ~7% after the second pulse and ~15% on the tenth pulse (E). (H) Isolated fPSPs evoked in vM1 and vS1 by a 20 Hz train of optical stimuli (average of 200 trials each). (I-J) Population data showing the normalized fPSP amplitude and fPSP slope during 20 Hz trains (n = 10 slices from 5 mice for the vS1-vM1 pathway; n = 7 slices from 4 mice for the vM1-vS1 pathway). Repetitive 20 Hz stimulation resulted in modest facilitation in fPSP amplitude and slope for both pathways. Values are represented as mean ± SEM.

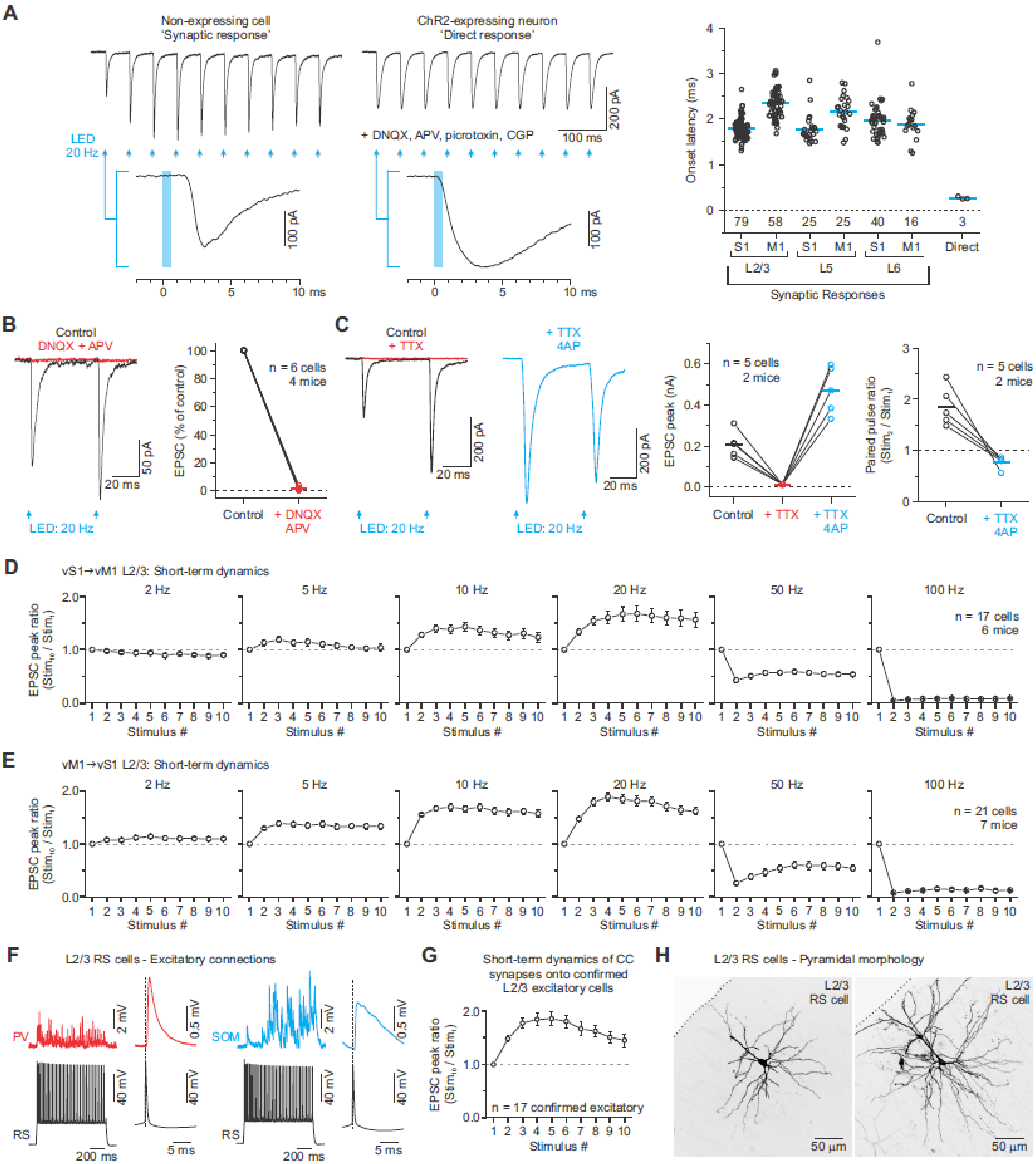

Figure 2.12. Quantification of onset latencies, glutamate sensitivity, action potential dependence, and frequency dependence of ChR2-evoked responses in L2/3 of the vS1-vM1 CC system. Related to Figure 2.1. (A) Optically evoked synaptic responses had delays consistent with the timing of neurotransmission at fast synapses. Left: Current responses of a non-expressing L2/3 RS cell and a ChR2-expressing L2/3 RS cell to brief widefield LED illumination (10 pulses, 20 Hz, 0.5 ms pulse duration). An expanded trace of the first response shows a 1.8 ms response delay from the non-expressing cell (synaptic response) and a 0.24 ms response delay for the expressing cell

Figure 2.12 (cont'd)

(direct response) (average of 10 and 13 trials). During the recordings of ChR2-expressing cells, glutamate and GABA receptor antagonists were bath applied to block synaptic transmission (DNQX, 20 mM; APV, 50 mM; picrotoxin, 50 mM; CGP-55845, 2 mM). Right: Population plot of the onset latencies for the vS1 and vM1 synaptic responses and ChR2-expressing cortical neurons (direct). Synaptic responses are divided according to the cortical and laminar location of the recorded cell. Cell counts are located below the zero line. Each point represents the average onset latency for an individual neuron, measured with a LED intensity adjusted to obtain a 200 pA EPSC. Blue lines indicate average latencies for each population. Note that the onset latencies of ChR2-expressing neurons were significantly faster than synaptic responses, consistent with previous reports (Cruikshank et al. 2010; Crandall et al. 2017). The average onset latency for the entire population (excluding L4 in vS1) was 1.99 ± 0.02 ms (n = 239 cells). (B) Optically evoked CC synaptic responses require fast glutamatergic transmission. Left: In control ACSF, synaptic currents evoked in an RS cell by a pair of 0.5 ms optical stimuli at 20 Hz (black trace) (average of 10 trials). Bath application of the glutamate receptor antagonists APV (50 mM) and DNQX (20 mM) for 10 min blocked >98% of the postsynaptic current (red trace) (average of 10 trials). Right: Population effects of glutamate receptor antagonists on LED-evoked CC responses (n = 6 cells from 4 mice). (C) Optically evoked CC synaptic responses require presynaptic APs and are monosynaptic. Left: In control ACSF, synaptic currents were evoked in an RS cell by a pair of 0.5 ms optical stimuli at 20 Hz (black trace) (average of 14 trials). Bath application of the sodium channel blocker TTX (1 mM) for 10 min blocked 100% of the postsynaptic current (red trace) (average of 14 trials) (similar results seen in n = 5 cells from 2 mice). Middle: For the same cell, subsequent bath application of the potassium channel blocker 4-AP (1 mM) for 10 min rescued the EPSC (blue trace) (average of 14 trials) (Petreanu et al. 2009). The currents evoked in TTX+4AP were larger, slower, and the dynamics switched from facilitating to depressing. Right: Population effects of TTX and TTX+4AP on optically evoked CC response amplitudes (n = 5 cells from 2 mice). Population effect of TTX+4AP on the paired-pulse ratio of CC responses (n = 5 cells from 2 mice). The horizontal bars are averages for each group. (D-E) Facilitation is present in long-range CC synapses at multiple frequencies. Population plots of the average normalized peak synaptic responses evoked by 2-100 Hz optical trains (10 stimuli; 0.5 ms pulse duration). Results for both the vS1-vM1 (D) and vM1-vS1 (E) pathways are shown. Synaptic enhancement during trains was present over a range of frequencies. Responses switched to depression during 50 and 100 Hz trains, most likely due to the properties of ChR2 (Lin et al. 2009). (F) Confirmation that RS neurons are excitatory. EPSPs recorded from PV and SOM cells, evoked by stimulation of presynaptic L2/3 RS cells. Inset shows a spike-triggered average EPSP. (G) Summary data of CC-evoked EPSC dynamics from RS cells confirmed to be excitatory (n = 17 cells from 15 mice). (H) Confocal image (Z projection) of two RS cells filled with neurobiotin. Their pyramidal shape confirms they were excitatory neurons. Values are represented as mean ± SEM.

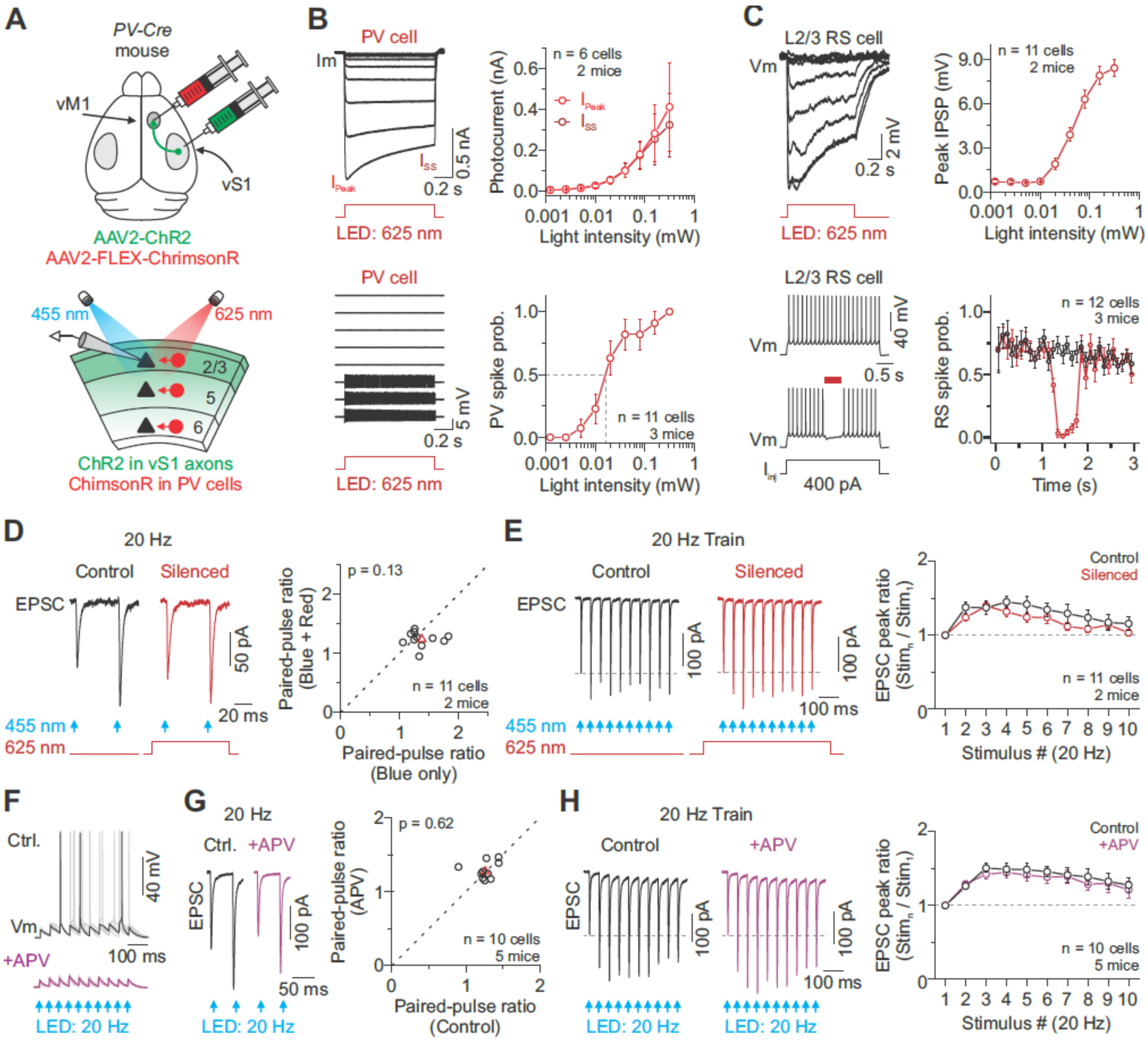

Figure 2.13. Optogenetically or pharmacologically silencing local excitatory connections reveals intracortical inputs do not confound long-range CC facilitation. Related to Figure 2.1. (A) Schematic illustration of cortical silencing experiments to determine if intracortical excitatory inputs confound long-range CC facilitation. Top: We injected AAV2-ChR2-EYFP and AAV2-Flex-ChrimsonR into the cortex of PV-Cre mice in vivo, and then live 300 mm-thick coronal brain sections were collected for in vitro recordings. Bottom: We optogenetically silenced local excitatory cells by activating ChrimsonR-expressing PV inhibitory interneurons (625 nm) to isolate long-range CC inputs (455 nm). (B) Top Left: Photocurrent responses of a ChrimsonR-expressing PV cell to large-field red light stimulation when recorded in voltage-clamp (-94 mV; 1000 ms pulse duration; tested with 9 LED intensities). Top Right: Summary graph shows light intensity and photocurrent response relationship measured for the peak and steady-state (SS) currents. Bottom Left: Loose-patch voltage recordings of a ChrimsonR-expressing PV cell while stimulating with 625 nm light (1000 ms pulse; tested with 9 LED intensities). Bottom

Figure 2.13 (cont’d)

Right: Summary graph shows light intensity and spike probability relationship measured for ChrimsonR-expressing PV cells. (C) Top Left: Voltage responses of a non-expressing L2/3 RS cell to large-field red light stimulation when recorded in current-clamp (-74 mV; 1000 ms pulse duration; tested with 9 LED intensities). Top Right: Summary graph shows light intensity and voltage response relationship measured for the peak hyperpolarization. Bottom Left: Voltage responses of a non-expressing L2/3 RS cell to intracellular positive current steps with (red) and without (black) PV cell photostimulation. Bottom Right: Summary graph showing spike rate with and without PV cell photostimulation (0.04 mW; 100 ms bins). (D) Left: Representative vS1-vM1 excitatory synaptic currents evoked by a pair of optical stimuli at 20 Hz (455 nm, blue arrow, 0.5 ms) delivered with and without PV cell photostimulation (1000 ms; average of 10 trials each). Summary graph showing the paired-pulse ratio of the optically evoked CC responses for each cell with and without photostimulation of PV cells (0.04 mW). The red triangle represents the mean. Optogenetically silencing local excitatory cells did not result in short-term depression. (E) Left: Representative vS1-vM1 excitatory synaptic currents evoked by a 20 Hz optical train (455 nm, blue arrow, 0.5 ms) delivered with and without PV cell photostimulation (1000 ms; average of 10 trials each). Summary graph showing EPSC amplitudes plotted as a function of stimulus number within 20 Hz trains. Optogenetically silencing local excitatory cells did not result in short-term depression. (F) In a subset of experiments, 50 mM APV was added to the bathing solution to reduce the responses of local excitatory cells by pharmacologically blocking non-linearities in the synaptic conductances associated with NMDA receptors. Current-clamp recording of a representative L2/3 RS cell during repetitive CC activation (20 Hz). Top: Control activity while holding the cell at a depolarized membrane potential (-74 mV). Note cells did not spike from their resting membrane potential with the LED intensities used for testing (Table S1). Bottom: the same cell and conditions except in the presence of 50 mM APV (overlay of 10 sweeps for each condition). The addition of APV suppressed excitatory cell excitability. (G) Left: Representative vM1-vS1 excitatory synaptic currents evoked by a pair of optical stimuli at 20 Hz delivered with and without APV (average of 10 trials each). Summary graph showing the paired-pulse ratio of the optically evoked responses for each cell with and without APV. The red triangle represents the mean. (H) Left: Representative vM1-vS1 excitatory synaptic currents evoked by a 20 Hz optical train delivered with and without APV (average of 10 trials each). Summary graph showing EPSC amplitudes plotted as a function of stimulus number within 20 Hz trains. Pharmacologically reducing local excitatory cell excitability did not result in short-term depression.

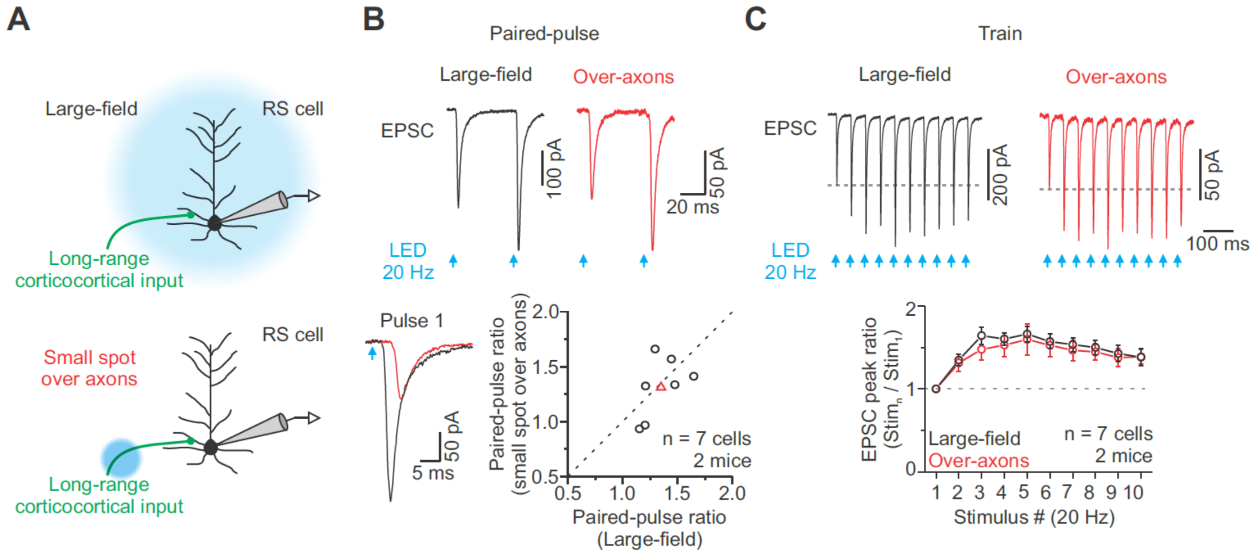

Figure 2.14. Large-field optically evoked short-term facilitation is similar to over-axon stimulation. Related to Figure 2.1. (A) Recording schematic to test the performance of large-field optical stimulation. We recorded light-evoked excitatory responses recorded from an excitatory L2/3 RS cell during large-field illumination (standard approach) and over-axon stimulation (20 Hz, 0.5 ms pulse duration). Optical stimulation over-axons was achieved by restricting the light spot size and directing the light over the axons near white matter (800-1000 mm away). (B) Top: vM1 excitatory synaptic currents evoked by a pair of optical stimuli at 20 Hz (blue arrow, 0.5 ms) delivered using our standard approach (large-field) or over-axons (average of 14 trials each). Bottom Left: Axonally induced EPSCs showed a longer synaptic delay, confirming that spikes were initiated far from the recording pipette (Large-field: 2.1 ± 0.1 ms; Over-axon: 4.7 ± 0.3 ms). Bottom Right: Population data showing no difference in the paired-pulse ratio (PPR) for large-field versus over-axon optical stimulation (n = 7 cells from 2 mice; $p = 0.71$, Paired t-test). The red triangle represents the mean. (C) Excitatory synaptic currents evoked in the same neuron (shown in B, left) by a 20 Hz optical train delivered by our standard approach (large-field) or over-axons (average of 14 trials each). Short-term plasticity was similar for large-field and axon stimulation with 20 Hz trains ($p = 0.24$, Two-way ANOVA, stim. 2-10).

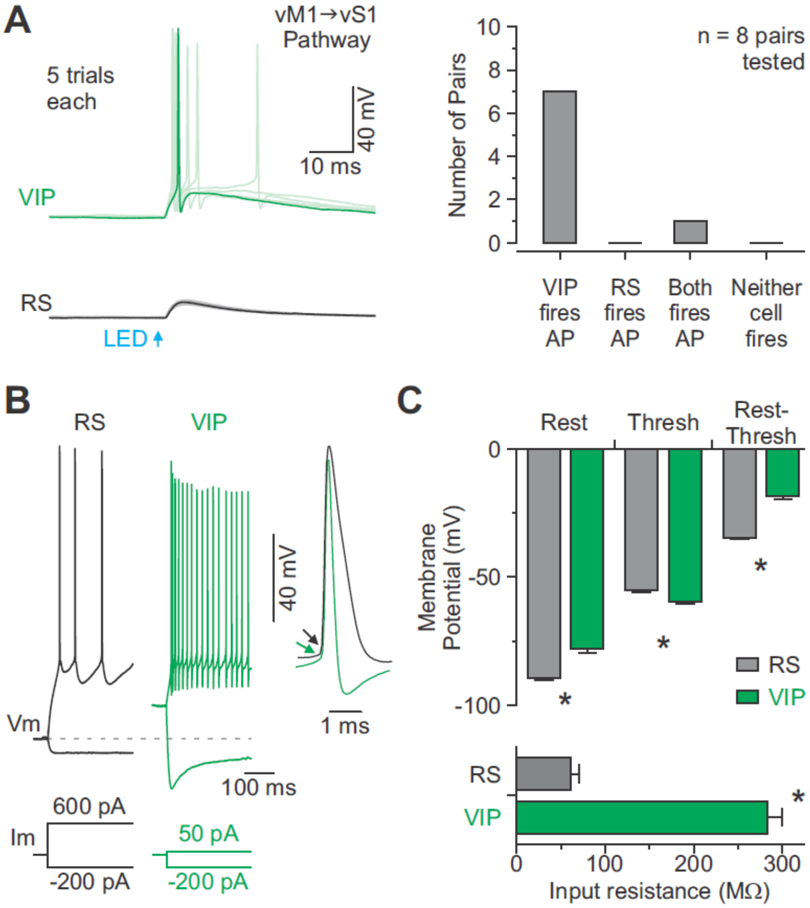

Figure 2.15. vM1-vS1 CC voltage responses were strongest in vS1 VIP cells despite similar synaptic current strengths in paired VIP-RS cell recordings due to their greater intrinsic excitability. Related to Figure 2.4. (A) Left: Paired VIP-RS cell recordings of CC responses in current-clamp at rest (5 trials shown). Action potentials can be seen ~3.5 ms after CC photostimulation. Right: Summary of 8 cell pairs exhibiting spike responses to CC input (all current-clamp recordings at rest; max stimulus 32 mW). In all pairs tested, the VIP cell fired an action potential. (B) Responses of VIP-RS cell pair to injected current from rest (same cells as A). VIP cells were more depolarized at rest than RS cells. Voltage response to negative current step was larger in VIP than RS cells, reflecting higher membrane input resistance. A larger positive current was required to reach spike threshold in the RS than VIP cell (+450 pA versus +50 pA). Voltage thresholds for spiking were slightly lower in the VIP than RS cells. (C) Top: mean resting potential (Rest: $p < 0.0001$, Two-sample t-test), spike threshold (Thresh: $p < 0.001$, Two-sample t-test), and the differences between them (Rest-Thresh: $p < 0.0001$, Two-sample t-test; $n = 10$ pairs). Bottom: mean membrane input resistance ($p < 0.001$, Mann-Whitney U test; $n = 10$ pairs).

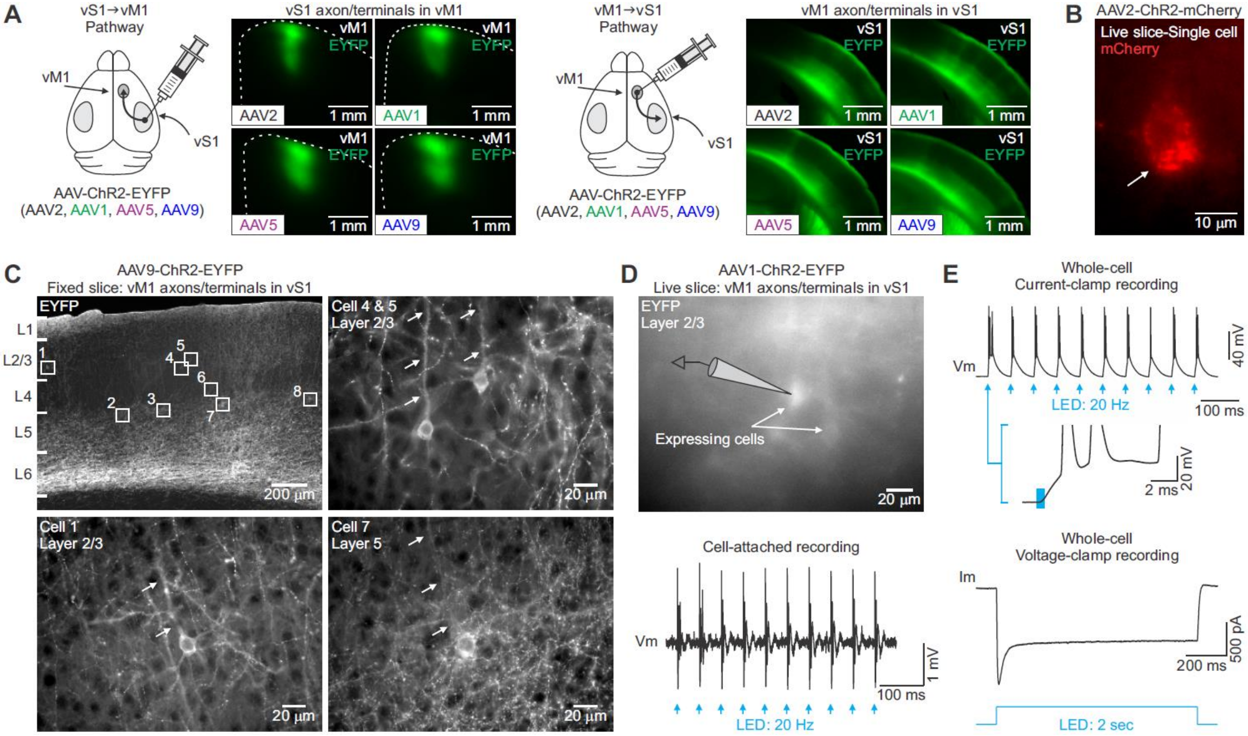

Figure 2.16. Retrograde viral transduction of CC circuits with certain AAVs and aggregation of ChR2-mCherry. Related to Figure 2.5. (A) Schematic showing virus injected into the vS1 (left) or vM1 (right) of mice in vivo (AAV2, AAV1, AAV5, or AAV9). We used the same vector and titer for each viral serotype (AAV-hsyn-ChR2(H134R)-EYFP). Live slice (300 mm) images showing vS1 (left) and vM1 (right) axon/terminal arbors expressing ChR2- EYFP after injection of each AAV. Expression levels were similar for all serotypes in both pathways (vS1-vM1: $p = 0.81$; AAV2, $n = 6$ mice; AAV1, $n= 2$ mice, AAV5, $n = 3$ mice; AAV9, $n = 2$ mice; vM1-vS1: $p = 0.82$; AAV2, $n = 7$ mice; AAV1, $n= 5$ mice, AAV5, $n = 3$ mice; AAV9, $n = 7$ mice, One-way ANOVA). (B) A high-magnification fluorescence image of a live 300 mm thick slice showing a representative ChR2-mCherry expressing neuron in vS1 (23 days after viral injection in vS1). Notice that ChR2-mCherry appears to be aggregated within the membrane or cytoplasm of the cell (white arrow). Similar results were observed in 3 mice. (C) Top left: Low-magnification fluorescence image of a 30-mm-thick section showing AAV9-driven expression of ChR2-EYFP in vM1 axons terminating in vS1 (20 days after virus injection in vM1), as well as retrograde viral expression in cortical neurons (boxes). High-magnification images from the same section show cortical cells in vS1 with EYFP-labeled somata and apical dendrites (arrows). We routinely observed signs of retrograde viral transduction of cortical neurons using AAV1, AAV5, and AAV9, but not AAV2 ($n = 3$ mice each). Most expressing cells had a pyramidal shape, characteristic RS physiology, and concentrated in L2/3 and L5a, where many CC cells populate (Harris and Shepherd 2015). (D) Top: Epifluorescence image of EYFP-expressing neurons in L2/3 of vS1 (live 300-µm-thick slice), 20 days after virus injection in vM1. Bottom: From the same cell shown above, voltage recordings of light-evoked responses in cell-attached mode (0.5 ms pulse

Figure 2.16 (cont'd)

duration, 10 pulses, 20 Hz, 32 mW or 18.0 mW/mm2). Spikes were evoked on each flash. (E) During whole-cell recording, responses of the same cell (shown in B) to a 20 Hz optical train of 0.5 ms light flashes (32 m or 18.0 mW/mm2W; blue arrows). Again, spikes were evoked on each flash. Membrane depolarization began almost immediately at flash onset (<0.5 ms). Bottom: Current recording of the same ChR2-expressing L2/3 cell to a 2 s LED stimulus (1.7 mW or 1.0 mW/mm2). The inward current initially peaked, then decreased to a sustained level within 100 ms. We obtained similar results in all 7 cells recorded after AAV1, AAV5, or AAV9 viral injections. Consistent with the anatomical work, less than 2% of all cells recorded after AAV2 injections showed signs of retrograde viral transduction (n = 8/527 cells).

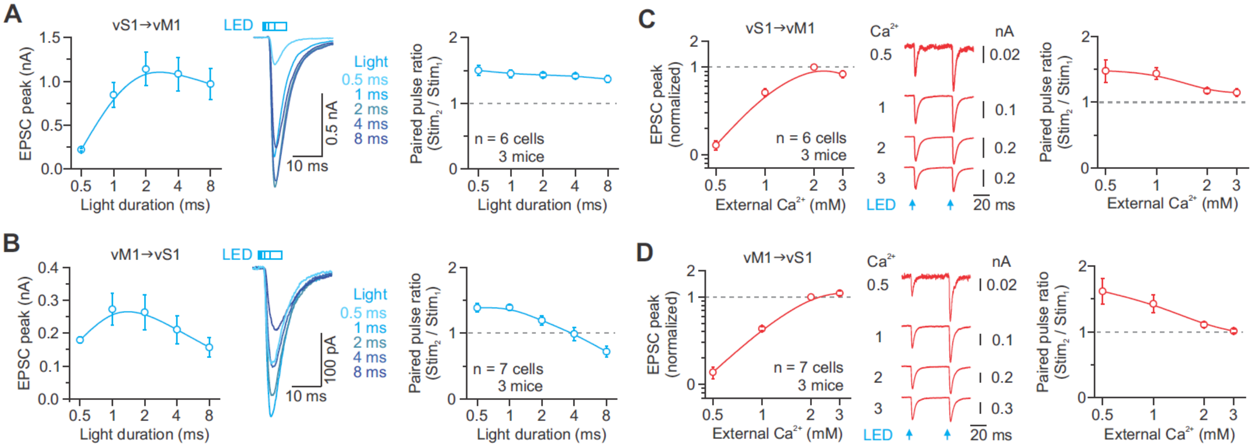

Figure 2.17. Effect of light duration and extracellular calcium on optically evoked short-term plasticity at CC synapses. Related to Figure 2.6. (A-B) Left: Population data showing the average EPSC amplitude of vS1-vM1 (A) and vM1-vS1 (B) synapses on L2/3 RS cells recorded in response to increasing LED pulse duration (different shades of blue: 0.5 – 8.0 ms). Middle: Representative EPSCs evoked with different LED pulse durations (average of 10-12 trials). Right: Population plot showing the peak paired-pulse ratio recorded in response to different LED pulse durations (50 ms interstimulus interval) (vS1-vM1: n = 6 cells from 3 mice; vM1-vS1: n = 7 cells from 3 mice). Increasing the LED pulse duration from 0.5 to 4 and 8 ms resulted in a significant decrease in paired-pulse facilitation for the vM1-vS1 pathway ($p < 0.01$, One-way ANOVA, with Bonferroni's post-hoc test). Duration did not influence the peak paired-pulse ratio for the vS1-vM1 pathway ($p = 0.53$, One-way ANOVA). (C-D) Left: Population data showing the average normalized EPSC amplitude for vS1-vM1 (C) and vM1-vS1 (D) synapses on L2/3 RS cells recorded in different external Ca2+ concentrations. Data were normalized to the amplitude in 2 mM Ca2+. Middle: A pair of optically evoked EPSCs recorded in different external Ca2+ (50 ms interstimulus interval; average of 9-19 trials each). Right: Population plot showing the peak paired-pulse ratio recorded in different external Ca2+ (50 ms interstimulus interval) (vS1-vM1: n = 6 cells from 3 mice; vM1-vS1: n = 7 cells from 3 mice). Raising Ca2+ increased EPSC size and decreased paired-pulse facilitation.

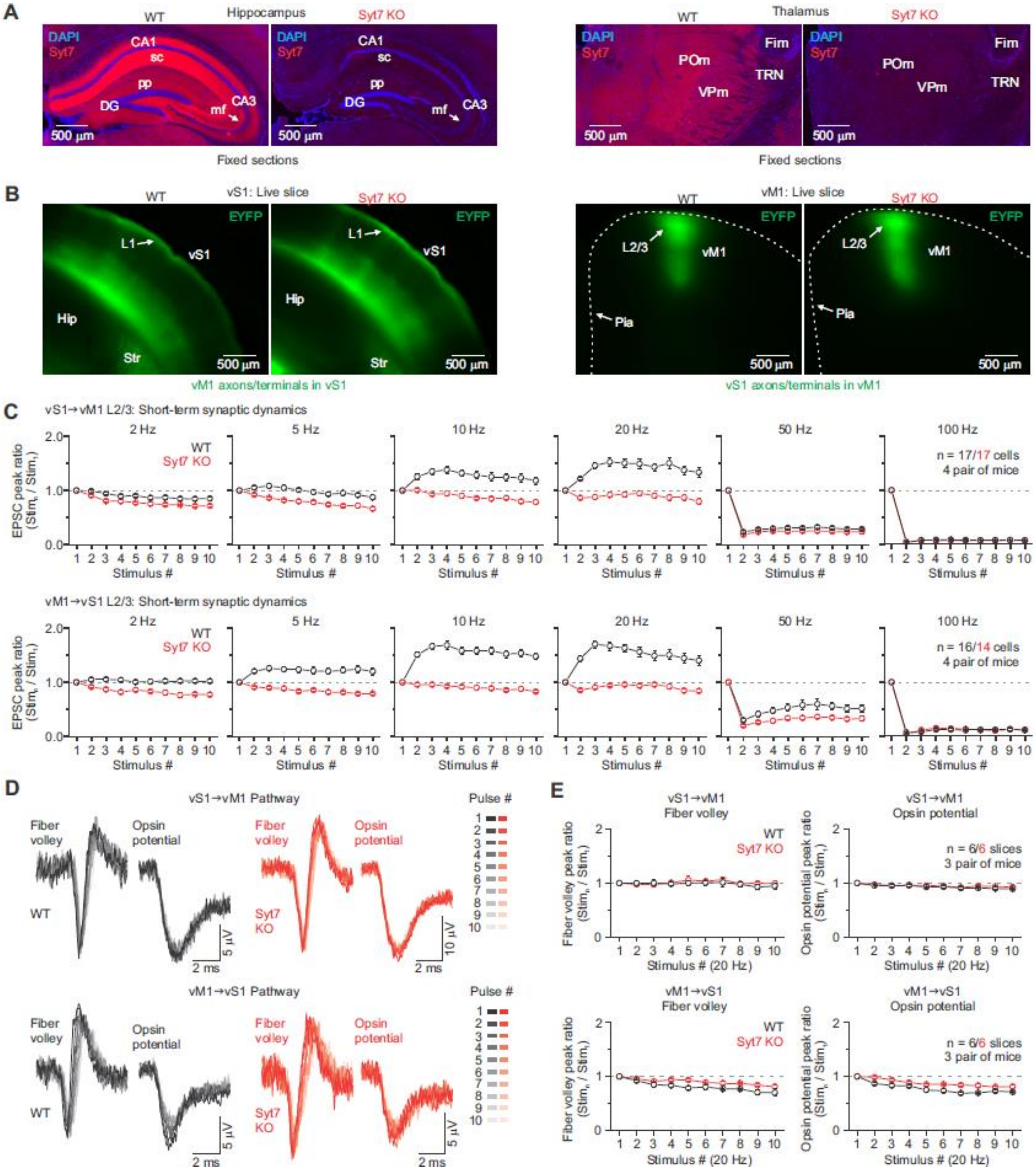

Figure 2.18. Facilitation is absent in Syt7 KO mice at multiple frequencies. Related to Figure 2.7. (A) Fluorescence images of the hippocampus (left) and thalamus (right) in a P116 WT and a Syt7 KO littermate mouse immunostained for Syt7 and counterstained with DAPI. In WT mice, Syt7 labeling is present in hippocampal and thalamic regions containing synapses known to facilitate, such as the Schaffer collateral synapses (sc), the mossy fiber synapses (mf), perforant path synapses (pp), thalamic reticular nucleus (TRN), ventral posterior medial nucleus (VPm), and posterior medial nucleus (POm).

Figure 2.18 (cont’d)

Thalamic regions are known to receive dense input from L6 corticothalamic cells, which facilitate. All regions lacked Syt7 expression in the KO animal. (B) Left: Epifluorescence images of live coronal slices (300 mm) showing ChR2-EYFP-expressing vM1 terminal arbors in vS1 of a P65 WT mouse and a P64 Syt7 KO littermate (23 and 22 days of expression). Right: Epifluorescence images of live coronal slices (300 mm) showing ChR2/EYFP-expressing vS1 terminal arbors in vM1 of a P44 WT mouse and a P43 Syt7 KO littermate (22 and 21 days of expression). Notice that the overall pattern of EYFP labeling in regions containing long-range vM1 or vS1 terminal arbors is similar in both WT and KO mice (n = 5 WT/KO pairs for vM1 synapses; n = 4 WT/KO pairs for vS1 synapses). This anatomical data suggests that the absence of Syt7 does not alter the structural organization of CC projections. (C) Population plots of the average normalized peak synaptic responses evoked by 2-100 Hz optical trains (10 stimuli; 0.5 ms pulse duration) at the vS1-vM1 (top) and vM1-vS1 (bottom) synapses in slices prepared from WT and Syt7 KO littermates. In Syt7 KO mice, synaptic facilitation during trains was absent for both synapses at all frequencies tested. (D) ChR2 can reliably drive action potentials (APs) in CC axons from both WT and Syt7 KO animals. Overlay of the fiber volleys and opsin potentials recorded from the activation of the vS1-vM1 (top) and vM1-vS1 pathway (bottom) for both WT (black) and Syt7 KO mice (red). Responses were evoked by a 20 Hz train of optical stimuli (10 stimuli, 0.5 ms pulse duration, an average of ~200 trials each). See Figure 2.11 for a description of how presynaptic APs (i.e., fiber volley) and opsin potentials were isolated from the recorded LFP. Light intensities were adjusted for each slice to the power needed to evoke a 200 pA EPSC in a neighboring L2/3 RS cell (average WT/KO LED powers: 1.4/1.1 mW or 0.8/0.6 mW/mm2 for vS1 axons in vM1, 12.7/6.1 mW or 7.2/3.2 mW/mm2 for vM1 axons in vS1). (E) Population data showing the normalized fiber volley amplitude and opsin potential amplitude during 20 Hz trains (n = 6/6 slices from 3 pairs of WT/KO mice vS1-vM1 pathway; n = 6/6 slices from 3 pairs of WT/KO mice vM1-vS1 pathway). Repetitive optical stimulation of ChR2-expressing axons/terminals resulted in similar fiber volley decay in both WT and KO animals. Overall, the decays were minimal for both animals in each pathway. Thus, the loss of short-term facilitation observed in the Syt7 KO animal (Figure 7) is not due to unreliable action potential generation (i.e., the number of axons recruited) during high-frequency stimulation. Values are represented as mean ± SEM.

		EPSP Amplitude		Full-field LED Power		
Cortex	Layer	EPSP peak (mv)	n cells	Total Power (mW)	Power Density (mW*mm^2)	n cells
vS1	L2/3	3.0 ± 0.3	41	12.8 ± 1.3	7.2 ± 0.7	61
vS1	L4	0.6 ± 0.2	2	-	-	-
vS1	L5	2.1 ± 0.4	17	19.3 ± 3.0	10.9 ± 1.7	22
vS1	L6	5.1 ± 0.3	35	4.8 ± 0.7	2.7 ± 0.4	18
vM1	L2/3	3.0 ± 0.2	31	1.7 ± 0.3	1.0 ± 0.2	54
vM1	L5	2.9 ± 0.4	19	2.9 ± 0.5	1.6 ± 0.4	24
vM1	L6	4.1 ± 0.6	15	10.8 ± 3.7	6.1 ± 2.1	13

- EPSP data collected using the intensity needed to evoke a 200 pA EPSC in voltage-clamp, which was the intensity used for testing
- EPSP data measured from rest
- Full-field LED power is the average light intensity measured at the focal plane needed to evoke a 200 pA EPSC
- Max power at focal plane ~32 mW (~18 mW*mm^2)
- Values represent mean ± SEM

Table 2.1. vM1 and vS1 synaptic responses in current-clamp and LED power information.

			Top boundaries		Bottom boundaries		
Cortex	Layer	Cre line	Relative depth	Absolute depth (μm)	Relative depth	Absolute depth (μm)	*n* slices/mice
vS1	L4	*Scnn1-Tg3-Cre*	0.32 ± 0.01	409.3 ± 14.6	0.47 ± 0.01	608.5 ± 17.8	6/4
vS1	L5	*Rbp4-Cre*	0.48 ± 0.01	636.9 ± 15.2	0.72 ± 0.00	942.2 ± 16.5	13/7
vS1	L6	*Ntsr1-Cre*	0.69 ± 0.01	956.7 ± 12.2	0.97 ± 0.00	1343.2 ± 16.9	9/5
vM1	L4	*Scnn1-Tg3-Cre*	-	-	-	-	3/3
vM1	L5	*Rbp4-Cre*	0.30 ± 0.01	430.5 ± 15.2	0.54 ± 0.01	785.3 ± 16.5	10/5
vM1	L6	*Ntsr1-Cre*	0.70 ± 0.01	1053.6 ± 14.7	0.92 ± 0.01	1376.6 ± 17.3	8/4

- To characterize the pattern of Cre expression in each driver mouse we bred to the Ai14 tdTomato reporter line (Jackson 007908)
- All measurements were based on live slice images
- Relative depth is normalized to pia (0) and white matter (1)
- No Cre expression was observed in vM1 of the *Scnn1-Tg3-Cre* mouse line

Table 2.2. Layer boundaries based on layer specific Cre mouse lines. Related to Figure 2.3.

	WT L2/3 RS cells		Syt7 KO L2/3 RS cells			
	Mean ± s.e.m.	*n* cells / *n* mice	Mean ± s.e.m.	*n* cells / *n* mice	*P*	Test
RMP (mV)	-89.7 ± 0.8	14 / 3	-89.0 ± 0.9	15 / 3	0.643	Mann-Whitney *U* -test
R_m (MΩ)	48.1 ± 2.6	14 / 3	46.4 ± 2.4	15 / 3	0.371	Mann-Whitney *U* -test
τ_m (ms)	12.7 ± 0.5	14 / 3	12.1 ± 0.5	15 / 3	0.369	two-sample *t*- test
C_m (pF)	273.7 ± 17.0	14 / 3	263.9 ± 8.1	15 / 3	0.599	two-sample *t*- test
Rheobase (pA)	292.5 ± 16.0	12 / 3	298.3 ± 23.3	12 / 3	0.838	two-sample *t*- test
Spike threshold (mV)	-57.1 ± 0.4	12 / 3	-57.1 ± 1.1	12 / 3	0.993	two-sample *t*- test
Spike amplitude (mV)	91.8 ± 0.9	12 / 3	92.6 ± 1.1	12 / 3	0.470	Mann-Whitney *U* -test
Spike half-width (ms)	0.72 ± 0.01	12 / 3	0.67 ± 0.01	12 / 3	0.012*	two-sample *t*- test
AHP amplitude (mV)	-14.5 ± 0.6	12 / 3	-13.7 ± 1.0	12 / 3	0.458	two-sample *t*- test
Max rate of rise (mV*ms)	586.5 ± 15.6	12 / 3	621.8 ± 20.3	12 / 3	0.181	two-sample *t*- test
Max rate of decay (mV*ms)	-99.9 ± 2.5	12 / 3	-106.4 ± 2.7	12 / 3	0.091	two-sample *t*- test

- See methods for an explanation of how the electrophysiological parameters were defined/measured.
- All membrane potentials were corrected for a -14 mV liquid junction potential
- All statistical tests were two-tailed

Table 2.3. Electrophysiological properties of wild type (WT) and Syt7 knockout (KO) neurons in layer 2/3 of vS1. Related to Figure 2.7.

CHAPTER 3: MOTOR CONTROL OF LAYER 6 CORTICOTHALAMIC CIRCUITS

Author contributions*:* L.E.M. and S.R.C. designed the experiments and supervised the study; L.E.M. performed the surgeries and electrophysiological experiments; D.M.A. performed the histological experiments; D.M.A. and L.E.M. performed the microscopy experiments; L.E.M. analyzed the data; L.E.M. prepared and wrote the manuscript.

3.1 – Abstract

Active sensation involves a dynamic interplay between sensory and motor systems, enabling behavioral adaptation to real-time demands. In the rodent somatomotor system, communication between the vibrissae representation of primary somatosensory (vS1) and motor (vM1) cortices plays a pivotal role in this process. The dense projections from vM1 to layer 6a (L6a) of vS1 potentially engage corticothalamic (CT) neurons, which modulate thalamic activity to shape sensory throughput into the cortex. However, direct influence of vM1 on the two main classes of L6a CT cells in S1 has been understudied, likely due to technical challenges in their identification. Using retrograde tracing, in vitro electrophysiological recordings, and optogenetic control strategies in mice, we investigated the synaptic effects of vM1 input on the two main classes of L6a CT neurons. Our results reveal selective engagement by vM1 of CT neurons projecting to both the ventral posteromedial (VPm) and posteromedial (POm) nuclei in the thalamus (referred to as Dual CT neurons hereinafter), but not in those who solely project to the VPm (referred to as VPm CT neurons hereinafter). Dual CT, but not VPm CT neurons exhibited spiking activity exclusively when held at a depolarized membrane potential simulating an “active state”, with multiple possible mechanisms being involved in this difference. One such mechanism is possibly a difference in intrinsic membrane physiology, making Dual CT neurons more excitable. Our results also show a

synaptic mechanism, where Dual CT neurons get stronger monosynaptic excitatory and di-synaptic inhibitory inputs observed upon vM1 axon/terminal stimulation. Furthermore, this study provides a detailed view of the anatomical organization of L6a CT circuits in vS1, shedding light on the cellular and synaptic mechanisms underlying vM1 recruitment of L6a CT circuits.

3.2 – Introduction

Active sensation is a dynamic process that involves a close interplay between sensory and motor systems, allowing us to adapt behaviorally to satisfy momentary demands (Harris et al., 1999; Kleinfeld et al., 2006; Diamond et al., 2008). In the rodent whisker system, a major player of this process is the communication between the heavily interconnected vibrissal representation of the primary somatosensory (vS1) and motor (vM1) cortices (Harris et al., 1999; Lee et al., 2008). vM1 projects densely to layer 6a (L6a) of vS1 (Miyashita et al., 1994; Zhang and Deschênes, 1998) and can modulate the activity of corticothalamic (CT) cells, which can in turn heavily modulate thalamic activity to modify sensory throughput into the cortex (Cudeiro and Sillito, 2006; Briggs and Usrey, 2008; Lee et al., 2008; Crandall et al., 2015; Clayton et al., 2021), allowing for a dynamic interplay between incoming sensory information and behavioral output.

L6a CT neurons can have dramatic effects in the thalamus, as they provide massive glutamatergic, highly dense and convergent projections that outnumber the afferent thalamocortical axons by 10:1 (Sherman and Koch, 1986; Deschênes et al., 1998). Yet, most in vivo studies report that most L6a CT neurons are silent, lack suprathreshold responses to sensory input (Tsumoto and Suda, 1980; Landry and Dykes, 1985; Sirota et al., 2005; Briggs and Usrey, 2009; Kwegyir-Afful and Simons, 2009; Vélez-

Fort et al., 2014), and their activity is highly context-and-state-dependent (Steriade, 2001; Lee et al., 2008; Vélez-Fort et al., 2018). Given that L6a CT activity is highly selective (Vélez-Fort et al., 2014) and sparse, the question that arises is: who engages L6a CT neurons, and when are they active? A recent study focused on the latter and established that a proportion of these cells are highly active when mice are actively whisking or modulated during motor behaviors (Dash et al., 2022). vM1 activity is highly elevated during whisking (Carvell et al., 1996), and although L6a of vS1 receives inputs from other cortical and thalamic areas, vM1 provides the densest and strongest projections to L6a (Zhang and Deschênes, 1998; Kinnischtzke et al., 2014, 2016). Interestingly, vM1 can influence thalamic throughput via its activation of L6a CT neurons in vS1 (Lee et al., 2008), providing further evidence that the interactions between vM1 and L6a CT circuits should be more thoroughly studied.

Despite the prominence of experimental efforts to study L6a CT circuits, (Cudeiro and Sillito, 2006; Briggs and Usrey, 2008; Crandall et al., 2017; Chevée et al., 2018; Briggs, 2020; Whilden et al., 2021) no study has established a direct, functional role between the activity vM1 and L6a CT neurons in sensory processing. The lack of a thorough understanding of CT functions is still elusive, possibly due to the technical challenges of selectively manipulating and recording L6a CT cells. The introduction of the Ntsr1- Cre mouse line (expresses Cre-recombinase in most L6a CT cells; Gong et al., 2007) and optogenetic tools have made studying the functions L6a CT neurons more attainable. Although these techniques have greatly improved our understanding of L6a CT functions, they illuminate the need to parse out these highly intertwined circuits as these tools don’t define CT subtypes.

In the rodent vS1, L6a CT neurons can be broadly divided in two classes based on their thalamic projection targets; those with cell bodies biased to the upper portion of L6a (L6aU) and project solely to the ventral posteromedial nucleus (VPm; VPm CT neurons), and those with cell bodies biased to the lower portion L6a (L6aL) that project to the posteromedial nucleus (POm) and collateralize in the VPm (Dual CT neurons) (Bourassa et al., 1995; Killackey and Sherman, 2003; Chevée et al., 2018; Whilden et al., 2021). Furthermore, these cells also have distinct intracortical projection patterns: VPm CT neurons project to the center of the layer 4 (L4) “barrel”, whereas Dual CT neurons project to layers 1 (L1) and 5a (L5a). This is interesting because these projections mirror those of the thalamic areas to which they are projecting (i.e., VPm targets L4 and POm targets L1 and L5; Zhang and Deschênes, 1997). The location and projection patterns of these two CT classes makes them able to strategically influence thalamic sensory throughput and cortical responsiveness very distinctly (Olsen et al., 2012; Bortone et al., 2014; Kim et al., 2014; Frandolig et al., 2019; Voigts et al., 2020). Despite the prominence of anatomical studies parsing L6a CT classes, a thorough understanding of how discrete these CT projections are remains elusive. Moreover, an open question is if vM1 engages these circuits distinctly. A recent anatomical study showed that “Dual CT” neurons receive drastically more inputs from vM1 than “VPm CT” neurons (Whilden et al., 2021), suggesting selectivity of CT class recruitment by vM1.

To investigate the influence of vM1 on these two main classes of L6a CT neurons in vS1, we performed a triple-injection strategy in mice where both CT cell classes were labeled by injecting retrograde tracers in the thalamus, and vM1 neurons expressed Channelrhodopsin-2 (ChR2) via an injection of a viral construct, allowing us to selectively and optically activate vM1 terminals in vS1 (Martinetti et al., 2022). Consistent with previous anatomical studies in the rodent vS1 (Bourassa et al., 1995; Killackey and Sherman, 2003; Chevée et al., 2018; Whilden et al., 2021), we report that VPm CT cells bias towards L6aU, whereas Dual CT neurons bias towards L6aL. Furthermore, by performing in vitro paired whole-cell recordings in acute brain slices containing vS1, we report that vM1 can selectively recruit Dual CT neurons to spike when their membrane potential is depolarized and resembles that of and "awake and active" state. This dichotomy in recruitment is perhaps due to stronger vM1-evoked monosynaptic excitation and di-synaptic inhibition in Dual CT neurons as compared to VPm CT neurons, in addition to a higher membrane excitability of the Dual CT population. Together, our findings demonstrate a dichotomy in the recruitment of L6a CT circuits by vM1, showing how synaptic and intrinsic mechanisms combine to determine the postsynaptic effects to motor inputs.

3.3 – Materials and Methods

Animals. All procedures were performed in accordance with the National Institutes of Health (NIH) Guidelines *for the Care and Use of Laboratory Animals*, and approved by the Institutional Animal Care and Use Committee (IACUC) at Michigan State University.

We used the following mouse lines in this study: Ntsr1-Cre (catalog # 017266-UCD, Mutant Mice Research & Resource Center; RRID: MMRC_017266-UCD); (Gong et al., 2007), Ai14 (catalog #007908, The Jackson Laboratory; (Madisen et al., 2010), and Crl:CD1 (ICR) (catalog #022, Charles River Laboratories). The Ntsr1-Cre mouse line had ICR genetic background and was bred by crossing it with a homozygous Ai14 reporter line, resulting in experimental mice that were homozygous for the indicated genes. The following Cre lines had ICR genetic backgrounds were not used for their genetic labeling: PV-Cre (catalog# 008069, The Jackson Laboratory: 008069; Hippenmeyer et al. 2005), and Grp-Cre (catalog # 031183, Mutant Mice Regional Resource Center; RRID:MMRRC_031183-UCD). All animals were group housed with combined sex litters in a dedicated animal care facility maintained on a 12:12 h light–dark cycle. Food and water were available ad libitum. We used both male and female mice in this study.

Stereotaxic virus injections and surgical procedures. For stereotaxic injections, mice of either sex, ~3 weeks old were used. All surgeries were performed as previously described (Crandall et al., 2017; Martinetti et al., 2022). Briefly, mice were first deeply anesthetized with a Dexdomitor-Ketamine cocktail diluted in sterile saline (Dexdomitor, 0.25 mg/kg; KetaVed, 100 mg/kg; intraperitoneally). Mice were then placed into a stereotaxic frame with an integrated warm base that maintained constant core body temperature (Stoelting). A layer of eye ointment was placed to prevent damage or drying of the eyes (Patterson Veterinary Artificial Tears). An incision was then made by fine surgical scissors to expose the skull after retracting the scalp and superficial fascia. Next, a small craniotomy was performed, a glass micropipette was loaded with either virus or tracer and lowered slowly into the brain. A small volume of virus or tracer was then pressure-ejected (Picospritzer pressure system) over 5-10 min, then held in place for an additional 5-10 min before slowly being withdrawn from the brain. Following the injection(s), the incision was closed with a surgical adhesive (GLUture), and the analgesic Bupivacaine (2 mg/kg) and anti-sedative (Antisedan; 2.5 mg/kg) were administered to all animals postoperatively. All mice were allowed to recover on a heating pad for ~1 hr before returning to their home cage.

To functionally characterize the properties of vM1 synapses onto L6 CT cells (*Ntsr1x Ai14* mouse cross) in vS1, we injected an adeno-associated virus (volume: 150 nL/ injection site, 4 sites; titer= 3.1 – 3.5 x 10^{12} viral particles/mL) that encoded genes for hChR2 (H134R)-EYFP fusion proteins (rAAV2/hSyn-hChR2[H134R]-eYFP-WPREpA; lot #AV4384H, University of North Carolina Viral Vector Core) into vM1 (vM1 coordinates: +0.9 and +1.3 mm anterior, +1.25 mm lateral, -0.4 and -1.0 mm ventral, from Bregma). Animals were humanely sacrificed after ~3 weeks for sufficient expression of viral construct (Mean injection age for all mice: 25.51 ± 0.57 days, range 17 – 35 days; Mean viral expression time: 20.85 ± 0.31 days, range 13 – 29 days; n = 61 mice).

For the anatomical characterization of L6 CT circuits by projection class (VPm, POm, or both), we injected both the POm and VPm simultaneously with Choleratoxin-B conjugated to either Alexa 647 (CTB 647, ThermoFisher C34778) or Alexa 555 (CTB 555, ThermoFisher C34776). Both CTBs were prepared by mixing 0.5 ul of saline and 0.5 ul of CTB (2 ug/ul) and injected in either VPm or POm (volume: 100 – 150 nL/site; concentration: 1 ug/ul). In a subset of mice, 150 nl of a saline-retrobead mixture (1:40 dilution; red latex retro-beads, Lumafluor, Cat# R180) was injected solely into the VPm. (Most commonly used VPm coordinates: -1.25 mm posterior, +1.8 mm lateral, and -3.10 mm ventral, from Bregma; most commonly used POm coordinates: -1.35 mm posterior, +1.4 mm lateral, and -2.87 mm ventral, from Bregma). Animals were sacrificed after 2-3 weeks to allow sufficient retrograde transport of the tracer, and to match the timing of expression from the viral injection mentioned above.

To functionally characterize vM1 inputs onto retrogradely labeled L6 CT cells, we performed a triple injection strategy where we injected vM1 with an AAV-ChR2-EYFP (as described above), and both POm and VPm simultaneously with two different CTBs ipsilaterally (as described above). Animals were sacrificed after ~3 weeks to allow for sufficient viral expression in vM1 neurons, as well as retrograde transport into L6a CT cells.

Acute brain slice preparation. After ~3 weeks of viral and tracer expression, mice of either sex were deeply anesthetized using isoflurane and decapitated. The brains were rapidly extracted and placed in a cold (~4 °C) and oxygenated (5% CO_2, 95% O_2) slicing solution containing the following (in mM): 3 KCl, 1.25 NaH_2PO_4, 10 $MgSO_4$, 0.5 $CaCl_2$, 26 NaHCO3, 10 glucose, and 234 sucrose. The brain was then hemisected along the midline, and the injected side was mounted on a flat platform. Acute coronal brain slices (300 µm thick) containing the vS1 were then sectioned (VT-1200s, Leica) using the same slicing solution, and transferred to a holding chamber in warm (32 °C) oxygenated artificial cerebrospinal fluid (ACSF) containing the following (in mM): 126 NaCl, 3 KCl, 1.25 NaH_2PO_4, 2 $MgSO_4$, 2 $CaCl_2$, 26 $NaHCO_3$, and 10 glucose. Slices were incubated at 32 °C for 20 minutes, then at room temperature for at least 40 minutes before recording. Slices containing injection sites (vM1, POm, and VPm) were always collected for imaging to assess injection target accuracy and tissue health. We only considered mice in which there were no obvious signs of off-target injections or tissue damage.

In vitro electrophysiological recordings and data acquisition. Brain slices were transferred to a submersion chamber on an upright microscope (Zeiss Axio Examiner.A1) and were continually superfused with warm (32 ± 1 °C) oxygenated ACSF containing (in mM): 126 NaCl, 3 KCl, 1.25 NaH_2PO_4, 1 $MgSO_4$, 1.2 $CaCl_2$, 26 $NaHCO_3$, and 10 glucose. Neurons were visualized using infrared differential interference contrast (IR-DIC) and fluorescence microscopy using a 40x water-immersion objective (Zeiss, W Plan-Apo 40x/1.0 NA) and a video camera (Olympus, XM10-IR). vS1 was identified based on the visible cytoarchitecture of the barrels in layer 4 (L4).

Whole-cell recordings were obtained by using patch pipettes (4-6 MΩ) pulled (Sutter P-1000, Sutter Instruments) from filamented borosilicate capillary glass (Sutter Instruments) and back-filled with a potassium-based internal solution containing (in mM): 130 K-gluconate, 4 KCl, 2 NaCl, 10 HEPES, 0.2 EGTA, 4 ATP-Mg, 0.3 GTP-Tris, and 14 phosphocreatine-K (pH 7.25, 290-300 mOsm). Voltages were corrected for a -14 mV liquid junction potential. In a subset of experiments, to isolate pure excitatory and inhibitory currents we used a cesium-based internal solution containing the following (in mM): 130 Cs-gluconate, 4 CsCl, 2 NaCl, 10 HEPES, 0.2 EGTA, 4 ATP-Mg, 0.3 GTP-Tris, and 14 phosphocreatine-K (pH 7.25, 290-300 mOsm). The calculated reversal potential for $GABA_A$ receptor-mediated inhibitory responses was -79 mV.

L6 CT cells were identified and targeted for recording in two ways: first, by their expression of the red fluorescent protein (tdTomato) in the Ntsr1-Cre;Ai14 or second, by their retrograde labeling from POm, VPm, or both. CT neurons that projected solely to the VPm were targeted for recording and exclusively located in the upper portion of L6a (L6aU; 70 – 84% depth from pia), and CT neurons that projected to both POm and VPm were targeted for recording and exclusively located in the lower portion of L6a (L6aL; 84 – 97% depth from pia). CT neurons whose soma were not located at the specified depths were excluded from further analysis.

Electrophysiological data were acquired and digitized at 20 kHz (50 kHz when assessing intrinsic membrane properties; MultliClamp 700B amplified, Digidata 1550B4, pClamp 11), and low-pass filtered at 3 kHz (voltage-clamp) or 10 kHz (current-clamp) prior to digitizing. The pipette capacitances were neutralized, and the series resistances (typically 10-25 MΩ) were compensated online (70 – 80% for voltage-clamp and 100% for current-clamp). Series resistances were continually monitored and adjusted online to ensure accurate compensation.

Photostimulation of ChR2 expressing axons/terminals. ChR2 was stimulated optically using a high-power white light-emitting diode (LED; Mightex, LCS-5500-03-22) manipulated by an LED controller (Mightex, BLS-1000-2). LED on/off times were fast (<50 µs) and had constant amplitude and duration, verified by a fast photodiode (Thorlabs, DET36A). The light was collimated an reflected through a dichroic beam-splitter (Semrock, FF660-FDi02) and a high-magnification water-immersion objective (Zeiss, W Plan-Apo 40x/1.0 NA), with an estimated spot diameter of ~1500 µm, and maximum LED power of 60 mW. Light flashes were delivered as 0.5 ms pulses and centered directly over ChR2-expressing axons/terminals and the recorded cell.

For the experiments using the Ntsr1;Ai14 mice, the LED intensity was adjusted to evoke an EPSP threshold response (defined by having an EPSP at least 50% of trials) of each recorded neuron when held at their preferred resting membrane potential (RMP; ~ -84 mV) in current-clamp (also see Fig. 3.5 for intrinsic membrane properties). This response was strictly subthreshold for the recorded cell (< 3mV). For experiments where L6 CT cells were identified by retrograde tracer expression, the LED intensity was adjusted to evoke an EPSP or EPSC threshold response specifically in Dual CT neurons when held at their RMP in current clamp or held near the calculated reversal for inhibition when held in voltage clamp, respectively. For experiments where an LED intensity series was applied, the intensity necessary to elicit an EPSP/EPSC threshold response was multiplied by 1-6 times, respectively.

Electrophysiological data analysis. Analysis of electrophysiological data was performed in Molecular Devices Clampfit 11 and Microsoft Excel. Post-synaptic responses to optical stimulation were recorded in L6 CT neurons in whole-cell current-clamp and voltage-clamp. Excitatory and inhibitory post-synaptic currents (EPSC/IPSC) were measured in voltage-clamp and using a cesium-based internal solution. EPSCs were recorded when the membrane potential was held at the calculated reversal potential for inhibition (-79 mV). IPSCs were recorded when the membrane potential was held at the recorded reversal potential for excitation (0 mV). The amplitude of an evoked EPSP or EPSC was measured relative to a pre-stimulus baseline of 5 ms. The EPSP/EPSC peak amplitude was measured over the 10 ms post-stimulus. The amplitude of an evoked IPSC was measured relative to a pre-stimulus baseline of 5 ms. The IPSC peak amplitude was measured over the 20 ms post-stimulus. Reported values were based on average responses to 2-10 stimuli per intensity (typically 5).

Intrinsic properties. All intrinsic properties were measured in current-clamp, at each neuron's preferred resting membrane potential (RMP). RMPs were measured immediately after break-in, with no current applied. Membrane input resistance (R_{in}, in MΩ) was determined by using Ohm's law with a voltage response to a small negative current injection (~1.5 mV response; 5-20 pA; 600 ms duration; 20-137 sweeps). Membrane time constant (τ_m, in ms) was measured from the average voltage response (see R_{in} above) by fitting a single exponential to the initial falling phase of the response (50 – 100 ms, omitting the 1st ms). Membrane capacitance (C_{in}, in pF) was calculated as

τ_m / R_{in}. Rheobase current (in pA) was measured from the voltage response to a minimum positive current to elicit an action potential (AP) from a resting potential, typically -84 mV (1 sec pulse duration; 5 pA steps).

The following AP properties were measured from the same AP elicited by the rheobase current described above: AP latency (in ms) was determined by measuring the time from the start of the rheobase current step until the peak of the first AP. AP threshold was determined when the membrane potential of the rising phase (*dV/dt*) of the AP exceeded 10 mV/ms. AP amplitude (in mV) was determined by measuring the difference between the threshold and the peak amplitude of the AP. AP half-width (in ms) was determined by measuring the half height between threshold and the peak amplitude of the AP. The max rate of rise (in mV/ms) was defined as the maximal *dV/dt* during the rising phase of the first AP, and the max rate of decay (in mV/ms) was defined as the maximal negative *dV/dt* during the falling phase of the same AP.

To measure the spike rate output of the cell (F/I plot), defined as the spike frequency (F) in response to different current intensities (I), cells were injected with increasing 1 s, +25 pA steps from a resting potential, typically -84 mV. The following analyses were performed on responses in which the firing frequency at the beginning of the train (first interspike interval) was near 50 Hz. AP frequency adaptation was determined by calculating the adaptation ratio, which is the firing frequency of the second or last inter-spike interval divided by the firing frequency of the first inter-spike interval.

Tissue processing for analysis of CT neuron distribution in L6a. All tissues collected for analyzing the distribution of L6a CT neurons by projection target were prepared from acute coronal brain slices, as described previously (Martinetti & Bonekamp et al., 2022). Briefly, acute brain slices (300 µm thick) containing vS1 were placed in a 4% paraformaldehyde in 0.1 M phosphate buffered saline (PBS) overnight at 4 °C. Slices were then transferred to a 30% sucrose in 0.1 M PBS solution and stored at 4 °C until re-sectioning (~2 – 3 days). Tissue was placed flat on a freezing microtome platform (Leica, SM2010 R) and re-sectioned at 50 µm. Next, sections were immunostained for NeuN as described previously (Crandall et al., 2017). Sections were washed twice in 0.1 M PBS followed by 3 washes in 0.1 M PBS with 0.15 M NaCl (5 min/wash). After washing, the sections were incubated at room temperature for 1 hr in a blocking solution containing 0.1% Tween, 0.25% Triton X-100, 10% normal goat serum in PBS. Then the sections were incubated with primary antibody for 3-4 days in a rotating platform at 4 °C. Following primary incubation, the tissue was washed 5 times in PBS (5 min/wash), then pre-blocked in a blocking solution (same as above; 45 min) and incubated with secondary antibody for 2 hours at room temperature and washed 3 times in PBS (10 min/wash). All sections were placed on a glass slide and cover slipped using Vectashield with DAPI (Vector laboratories H-1200). The primary antibody used was mouse monoclonal anti-NeuN (1:1000; Millipore MAB377), and secondary antibody used was goat anti-mouse IgG (H+L) Alexa Fluor 488 (1:500; Fisher A11029).

Microscopy and Analysis of CT neuron distribution by projection target in L6a. Sections processed for immunohistochemistry were initially visualized using an epifluorescent microscope (Zeiss Axio Imager.D2) and Zen software to identify representative samples for cell counting. Section selection criteria were: at least 3 adjacent L4 barrels were anterogradely filled by VPm terminals (due to CTB anterograde properties), L5a exhibited "cupping" by POm terminals (also due to CTB anterograde properties), and the same columns corresponding to the filled barrels also expressed retrogradely filled CT cells in L6a. Selected sections were then visualized on a confocal microscope (Nikon A1 Laser Scanning Confocal Microscope) using a 40x (1.0 N.A.) or 100x (1.2 N.A.; example cells in Fig. 3.3*C*). Z-stacks were obtained of the full depth of the section, at 0.8 µm/plane.

The vertical extent from the middle of L4 to the bottom of white matter were imaged to set boundaries for depth normalization. The transition between L4 and L5a were used as the superficial boundary, and the white matter was used as the lower boundary, allowing to normalize somatic location along the vertical depth of L6a across preparation. The upper and lower borders of L6a were determined by measuring the CTB fluorescence representing retrogradely filled- VPm CT neurons, for a 120 µm region through the middle column. The analyzed area consisted of a 20 µm stack of images centered on the middle barrel to capture the center of the column, with an attempt to exclude septa from the analyses. Colocalization of both NeuN and retrograde tracers was quantified using the Cell counter plugin in Fiji (Schindelin et al., 2012).

Previous literature has shown that CTB can be taken up by fibers of passage (Chen and Aston-Jones, 1995), and that the fibers of CT cells projecting into POm travel through the VPm (Bourassa and Deschênes, 1995). This suggests that the tracer injected into the VPm could possibly be taken up by axons belonging to POm CT neurons that, giving a false labeling as “Dual CT”. Although we did not observe this effect in our preparation (note lack of retrogradely labeled cells with tracer targeted to VPm in Layer 5; Fig. 3.3*B*), we injected a saline-retrobead mixture into the VPm in a subset of animals (3 mice). The tissue was processed as mentioned above with a few key differences. A single thalamic injection was performed (rather than multiple), and the secondary antibody used to label the NeuN primary antibody was goat anti-mouse igG (H+L) Alexa Fluor 647 (1:500; Fisher A21236). Analysis of somatic position along the vertical depth was performed as mentioned above, and the counts resulted similar as those using CTB.

Experimental design and statistical analyses. No formal method of randomization was used in this study, nor were the experimenters blind to experimental groups. No statistical methods were used to identify sample size, but our sample size is similar to those previously reported (Crandall et al., 2017; Martinetti et al., 2022). Statistical analyses were performed using the Origin Pro 2023 software. To test whether the data were drawn from a normally distributed population, we used a Shapiro-Wilk test. Parametric tests were used for normally distributed populations, whereas non-parametric tests were used if a normality assumption was not valid. Significance was assessed using the appropriate parametric (Paired t-test or two-sample t-test) or non-parametric test (Wilcoxon paired sign-rank test or Mann-Whitney U test) as indicated in the results. All tests were two-tailed. Statistical significance was defined as $p < 0.05$, and the data are represented as mean ± SEM.

3.4 – Results

vM1 preferentially targets corticothalamic circuits in the lower portion of layer 6a of vS1. To investigate the synaptic organization and influence of vM1 on CT circuits in L6a of vS1, we used an optogenetic strategy in the mouse (Crandall et al., 2017)(Martinetti et al., 2022) to selectively express a Channelrhodopsin-2/enhanced yellow fluorescent protein (ChR2-EYFP) in vM1 neurons (Fig. 3.1*A*, top). To identify and target L6a CT cells, we used a transgenic approach by crossing the *Ntsr1-Cre* mouse line to a fluorescent tdTomato reporter line (*Ai14;* Madisen et al., 2010) that selectively labels L6a CT cells in sensory cortices (Olsen et al., 2012; Bortone et al., 2014; Crandall et al., 2015, 2017; Whilden et al., 2021; Martinetti et al., 2022)*.* Previous studies have identified differences in the cytoarchitectonic organization along the depth of L6 (Bourassa and Deschênes, 1995; Bourassa et al., 1995; Killackey and Sherman, 2003; Crandall et al., 2017; Frandolig et al., 2019; Whilden et al., 2021) of both excitatory (Kumar and Ohana, 2008; Crandall et al., 2017; Chevée et al., 2018; Gouwens et al., 2019; Whilden et al., 2021) and inhibitory neurons (Frandolig et al., 2019; Gouwens et al., 2020) suggesting that L6a can be subdivided into an upper (L6a$_U$) and a lower (L6a$_L$) section with a transition zone between 40-60% of the vertical extent of L6a.

To understand vM1 axon/terminal patterns in L6a, we first obtained acute brain slices of vS1 to examine the fluorescence of vM1 axons/terminals expressing ChR2/EYFP (Fig. 3.1*A*, bottom; asterisk indicates example column for the rest of Fig.1). We observed a larger and uniform density of vM1 axons/terminals in the lower portion of L6a (L6a$_L$), whereas terminals in the upper part of L6a (L6a$_U$) were more diffuse in the central “infrabarrel” section (Crandall et al., 2017), but dense along the septa (Fig. 3.1*B*). Analysis of the spatial pattern of fluorescence intensity along the vertical extent of L6a showed that EYFP is significantly stronger in L6a$_L$ than L6a$_U$ (Fig. 3*.1C;* mean fluorescence values: L6a$_U$: 0.782 ± 0.017 a.u., L6a$_L$: 0.950 ± 0.004 a.u.; $P=0.00195$, Wilcoxon sign-ranks test) with a strong transition of fluorescence at the 50% depth of L6a (84% depth from pia; Fig. 3.1*D*), suggesting a stronger targeting by vM1 to circuits located deep within L6a. These results support that L6a can be divided into two sublayers (L6a$_U$

and L6a$_L$), and that vM1 axons/terminals are well positioned in a L6a$_L$ to target a subpopulation of CT neurons.

Since the optogenetic strategy used does not allow us to distinguish between axons and terminals, we performed whole-cell electrophysiological recordings of tdTomato+ CT cells in vS1 spanning the vertical length of L6 while stimulating vM1 terminals to measure the strength of inputs. The inputs from vM1 to excitatory cells in vS1 have been well described (Petreanu et al., 2009; Kinnischtzke et al., 2014, 2016; Zolnik et al., 2020; Martinetti et al., 2022) and show that L6 receives the strongest inputs out of all layers.

Previous literature has demonstrated that the activity patterns of CT cells is highly correlated to the behavioral state of the animal (Dash et al., 2022; Reinhold et al., 2023), having an increased activity profile when the animal is in an awake state – engaging in sensorimotor behaviors. Interestingly, it has been described in rats that motor commands (from vM1) enhance sensory transmission in the thalamus, possibly via recruitment of L6 CT circuits in vS1 (Lee et al., 2008). Therefore, we asked, are CT cells recruited differently based on their location within L6s? To determine the impact of vM1 input in CT cell excitability, we measured the spiking behavior in response to a single stimulus (0.5 ms, wide-field light pulse) while holding the cell at their preferred resting membrane potential, and at a depolarized membrane potential (-74 mV), closer to the potential during active wakefulness to simulate an “active state”.

When we optically stimulated vM1 terminals and held the cells at RMP (~ -84 mV), we observed that CT cells in L6a$_L$ received much stronger sub-threshold EPSPs than those in L6a$_U$ (traces in Fig. 3.2*B*). Interestingly, when we held their membrane potential at -74 mV, we observed that the only cells recruited to spike were located under the 50% depth mark of L6 (L6a$_{L}$) (Fig. 3.2 *A*-*C*). All the cells that spiked had a peak time under 10 ms, correlated with mono-synaptic drive from vM1 stimulation (Fig. 3.2*D*). Together, these results indicate that vM1 targets CT circuits of vS1 that reside in the lower portion of L6a.

Anatomical layout of L6a CT neurons. Previous studies have shown that the L6a CT population is heterogenous in sensory cortices based on their projection targets (Bourassa et al., 1995; Killackey and Sherman, 2003; Crandall et al., 2017; Chevée et al., 2018; Whilden et al., 2021; Breuer and Krieger, 2022). In the rodent somatosensory cortex, CT cells in L6a$_{U}$ project primarily to the VPm, whereas those in L6a$_{L}$ are suggested to project to the POm and send collaterals to VPm (Bourassa et al. 1995). Previous studies have identified these circuits by injecting retrograde tracers in either the VPm or POm. However, a caveat exists as these projection patterns have not been assessed in the same preparation. This limitation may be attributed to the difficulty in targeting these closely apposed thalamic nuclei, making it challenging to accomplish multiple injections in the same animal without any spillover.

To explore the cellular organization of CT cells along the vertical depth of L6a, we analyzed their spatial distribution based on their projection target, either the VPm, POm, or both. To label each CT cell class based on projection, we injected the retrograde tracer Choleratoxin subunit-B (CTB) conjugated to either Alexa-647 (CTB 647) or Alexa-555 (CTB 555). Each tracer was injected in either the VPm or POm simultaneously to label both classes of CT cells in the same animal (Fig. 3.3*A*). No overlap of fluorescence was visible in the thalamic injections (data not shown), and we achieved good retrograde labeling of CT cells in L6 (Fig. 3.3*B*). Subjects with tracer overlap in the thalamus were not considered for these analyses. We next analyzed the spatial distribution of CT neurons along the vertical depth of L6a of single columns (Fig. 3.3*C*, left). To examine this distribution, we counted CT and non-CT neurons using the tissue samples from the injected mice, and immunolabeled for NeuN, a neuron-specific marker (Fig. 3.3*B, C*). CT neurons that projected to the VPm (VPm CT; Fig. 3.3*C*; box 1) were identified by their cytosolic expression of the fluorophore injected into the VPm, those who projected to the POm (POm CT; Fig. 3.3*C*; box 2) were labeled by the fluorophore injected into the POm, and those who projected to both areas (Dual CT; Fig. 3.3*C*; box 3) were labeled by both fluorophores.

CTB can label injected cells in an anterograde fashion (Wan et al., 1982; Dederen et al., 1994; Abbott et al., 2013), therefore we also observed VPm and POm thalamocortical (TC) patterns in vS1: stereotypical terminal patterns from VPm filling the L4 barrels, and "cupping" in L5a from POm terminals (Fig. 3.3*B*). We used the (TC) anterograde fluorescence in the border of L4/5 and white matter to normalize the depth of each neuron (see the Experimental Procedures).

We identified two major classes of neurons that make up a major fraction of the CT population within L6a: the VPm-only projecting and Dual CT neurons (VPm only CTs = 0.511 ± 0.05, Dual CTs = 0.421 ± 0.05; mean ± SEM fraction of total CT population; n= 7 barrel columns, 5 mice, 1263 cells). Moreover, we observed that most cells projecting to the POm also sent collaterals into the VPm (0.837 ± 0.04 of L6 CT population), with only a minimal fraction projecting solely to the POm (0.068 ± 0.01 of total L6a CT population). In line with previous work (Zhang and Deschênes, 1997; Olsen et al., 2012;

Kim et al., 2014), we found that CT cells make up the largest neuronal population in L6a (0.569 ± 0.01; mean ± SEM). Also see Table 1 for more detailed quantification.

Interestingly, analysis of the vertical distribution on CT cells in L6a revealed that both major CT cell classes had a stark segregation along the sublayers of L6a; L6a$_{U}$ is mainly populated by VPm-only CT neurons (0.781 ± 0.05 of L6aU CT population; light gray box in Fig. 3.3*D*), whereas L6a$_{L}$ was predominantly populated by Dual CT neurons (0.722 ± 0.07 of L6aL CT population; dark gray box in Fig. 3.3*D*). These data indicate that L6a$_{U}$ and L6a$_{L}$ are primarily composed of two different populations of CT cells, defined by their distinct projection patterns.

Previous literature has shown that CTB can be taken up by fibers of passage (Chen and Aston-Jones, 1995; Vercelli et al., 2000), whereas others have reported evidence that CTB doesn’t get taken up by fibers of passage (Conte et al., 2009; Abbott et al., 2013). One study identified that CTB has the ability to enter damaged fibers of passage, while sparing intact ones (Luppi et al., 1990). Our results would be confounded if CTB would enter axons of passage since L6a CT neurons projecting to the POm traverse through the VPm (Bourassa et al., 1995). Although we did not observe any CTB taken up by axons of passage (note the lack of L5 CT cells labeled by CTB-555 in Fig. 3.*3B*), we injected latex retrobeads into the VPm of a subset of animals to confirm our results (Fig. 3.3*E*). Previous literature has established that retrobeads are not taken up by fibers of passage (Vercelli et al., 2000; Saleeba et al., 2019).

In summary, our results show that CT neuron populations tend to cluster in specific areas of L6a based on their somatic depth; CT neurons in L6a$_{U}$ preferentially project to the VPm, whereas CT neurons in L6a$_{L}$ mainly project to the POm, with the vast majority of those also sending collaterals to the VPm. We conclude that L6a can be subdivided into distinct sublayers based on the CT circuits residing in them.

vM1-evoked synaptic inputs are stronger in Dual CT than in VPm CT neurons. Previous anatomical studies focusing on CT neurons in vS1 indicate that vM1 has a biased connectivity towards “Dual CT neurons” and sends fewer projections to VPm CTs (Whilden et al., 2021), which could explain stronger inputs in CT cells in L6aL (Figs. 2 and 3). Although the genetic and transcriptional identity of CT cells in vS1 have been described (Chevée et al., 2018), there is currently a lack of animal model or viral vector that we can use to genetically label these cells. Therefore, we next used a triple intracranial injection strategy (Fig. 3.4*A*, left; also see Experimental Methods) where we injected CTB conjugated with different fluorophores (also see Fig. 3.3) simultaneously into both the VPm and POm to label CT neurons, and injected ChR2-EYFP in vM1 to photoactivate vM1 terminals and assess their inputs onto L6a CT neurons (Fig. 3.4*A,* right).

To investigate the influence of vM1 inputs onto both VPm CT and Dual CT neurons, we obtained acute brain slices of vS1 and optically stimulated the vM1 terminals expressing ChR2 while recording from pairs of both classes of CT neurons simultaneously (Fig. 3.4*A*, right). This strategy allows us to control for the variability of ChR2 expression levels across mice. We photo-stimulated vM1 axons/terminals with a brief wide-field light pulse (0.5 ms) while recording in current clamp using a potassium-based internal solution to measure post-synaptic potentials (PSPs) (Martinetti et al., 2022).

When we stimulated vM1 axons while holding the membrane potential of cells at their preferred resting potential (RMP), Dual CT neurons received ~3X stronger EPSPs than VPm CT neurons (Fig. 3.4*B*; Dual CT = 7.07 ± 0.85 mV; VPm CT = 2.43 ± 0.92 mV; n= 21 pairs from 13 mice; p = 0.00137, Wilcoxon paired sign-ranked test). We also stimulated vM1 axons with a range of intensities to investigate if the peak of the EPSPs scaled similarly in both CT cells (Fig. 3.4*C*, left) and observed that Dual CTs always responded more strongly than VPm CTs (Fig. 3.4C, right; P= 2.46 x 10-8, two-way ANOVA, multiples 3-6). Only one Dual CT neuron spiked when held at RMP (data not shown).

Knowing that vM1 can selectively elicit spiking behavior of CT cells in L6a$_L$ of the *Ntsr1:Ai14* mouse (Figs. 1 and 2), and that these cells are very likely Dual CT neurons (Fig. 3.3), we next wanted to know if vM1 selectively drives Dual CT cell spiking behavior when their membrane potential is depolarized (-74 mV) to simulate an “active” state. When we stimulated vM1 terminals while holding the neurons’ membrane potentials at -74 mV. We observed that a large proportion of Dual CT neurons were recruited to spike whereas VPm CT neurons were rarely recruited (Fig. 3.*4D,E;* 4X threshold, VPm CT= 5.8 ± 0.06 %; Dual CT= 35 ± 0.11 %; mean ± SEM) across a range of intensities (Fig. 3.4*F*; P= 8.09 x 10-8, two-way ANOVA). Next, analysis of the spike peak time showed that all spikes happened within 10ms after the light stimulation (Fig. 3.4*D*, left, and 4E). Together, these results clearly indicate that vM1 has a stronger influence in Dual CT than VPm CT neurons, showing a dichotomy in the recruitment and possible functions of these two CT circuits.

Dual CT neurons are more intrinsically excitable than the VPm CT population. We next turned to measure the intrinsic membrane physiology of VPm CT and Dual CT neurons to start assessing the possible mechanisms leading to the dichotomy in recruitment of L6a CT circuits by vM1. Previous literature has suggested different intrinsic properties of CT cells in L6 of the rodent (Breuer and Krieger, 2022), but no general consensus has been reached.

Current-clamp recordings from VPm CT and Dual CT neurons held at their resting membrane potential showed different responses to both depolarizing and hyperpolarizing current injections (Fig.5). Although both cell types could be driven to fire action potentials (AP), Dual CT neurons were significantly more excitable than VPm CT neurons and exhibited distinct initial frequency AP patterns (see example traces in Fig. 3.1*A*). Analysis of the maximum AP frequency to 1s depolarizing square steps starting from 0pA and increasing by +25pA steps revealed that the Dual CT neurons exhibit spiking behavior before VPm CT neurons, although the slope of both neuron types was similar (Fig. 3.5*B, C*). These observed differences in spiking behavior were possibly due to the lower rheobase current that Dual CTs than VPm CT neurons, but not due to the resting membrane potentials since there both classes of cell's membranes rested at the similar potentials (average= ~ -84 mV) (Fig. 3.5C).

Furthermore, assessing passive membrane properties can also shed light into the possible mechanisms responsible for dichotomy observed by differential recruitment by vM1. Analysis of the cell's membrane response to a 500 ms negative step current showed that the input resistance and input capacitance of Dual CT neurons was significantly higher than VPm CT neurons (Fig. 3.5*D*), and that the time membrane time constant was briefer in VPm CT neurons (Fig. 3.5*E*). These data demonstrate that Dual CT neurons are better equipped to be more responsive, to obtain and hold larger charges for longer than VPm CT neurons. See more detailed quantification of active and passive membrane properties in Table 2.

Together, these data show that VPm and Dual CT neurons have distinct intrinsic physiological properties. These data also revealed that Dual CT neurons are intrinsically more excitable than VPm CT neurons, which supports that an intrinsic membrane mechanism could partly explain the dichotomy of L6a CT recruitment by vM1.

vM1-evoked monosynaptic excitation is stronger in Dual CT neurons. To isolate vM1 responses, we recorded pairs of both VPm and Dual CT cells in voltage clamp using a cesium-based internal solution to measure direct currents while stimulating vM1 terminals, similarly to Fig. 3.4 (also see experimental procedures). When we stimulated vM1 terminals and recorded neurons while holding their membrane potential at the reversal potential for inhibition (-79 mV), we observed that Dual CT neurons received ~2.5X stronger excitatory post-synaptic currents (EPSCs) than VPm CT neurons (Fig. 3.5*B*, left). The vM1-evoked EPSC onset and peak latencies were similar for both cell classes (data not shown), suggesting that the main difference in their responses is purely by magnitude, rather than distinct response kinetics. Previous literature has identified that vM1 also provides strong inputs to inhibitory interneurons in vS1, therefore we wanted to assess if vM1 engages distinct feedforward di-synaptic inhibitory mechanisms depending on the CT cell class. When we stimulated vM1 terminals and recorded at the reversal potential for excitation (0 mV), we observed that Dual CT neurons also received ~2X stronger di-synaptic inhibitory post-synaptic currents (IPSCs) than VPm CT neurons (Fig.

3.5*B*, right).

These data indicate that a possible synaptic mechanism can be at play, where vM1 stimulation results in larger responses in Dual CT neurons, but their net conductance could be equal. Since pyramidal cell activity depends on integrating both EPSCs and IPSCs, we wanted to know if the ratio of excitation to inhibition (E/I ratio) was distinct for these CT cells. Analysis of the E/I ratio of both Dual CT and VPm CT neurons revealed that both CT classes received similar ratios of excitatory and inhibitory inputs (Dual CT= 0.34 ± 0.07; VPm CT= 0.18 ± 0.04; p = 0.03906 Wilcoxon signed-ranks test; n= 9 pairs from 6 mice).

3.5 – Discussion

The role of vM1 in modulating sensory CT circuits has long been a subject of scientific interest. However, unraveling this intricate relationship has been a major challenge due to the complexity of the CT circuitry in L6a of vS1. In this study, we overcome this obstacle by thoroughly dissecting the anatomical layout of VPm CT and Dual CT neurons within L6a, allowing us to assess their independent responsiveness to vM1 inputs. We characterized the inputs from vM1 onto the two main classes of CT neurons *in vitro*, making several novel observations. First, using the *Ntsr1 x Ai14* mouse we found that vM1 provides much stronger inputs to CT neurons located in L6aL vS1. Second, the majority of CT neurons in $L6a_L$ target both the VPm and POm. Third, vM1 preferentially targets Dual CT neurons and can elicit spiking behavior when their membrane potential is depolarized, simulating an “active state”. Finally, the differences in the membrane properties of both CT classes and synaptic inputs from vM1 can explain the dichotomy in recruitment of these two classes of CT neurons. Together, our results demonstrate that vM1 selectively targets CT circuits that provide inputs to the two main somatosensory thalamic areas, the VPm and POm, shedding new light on the intricate interplay between motor and sensory cortices during sensory processing.

vM1 preferentially targets L6aL in vS1. To assess the functional impact of vM1 inputs onto the two main CT cell classes in L6a of vS1, we recorded the responses of CT neurons at different resting membrane potentials while stimulating vM1. Many *in vivo* studies have reported that L6 CT neurons are silent (Tsumoto and Suda, 1980; Landry and Dykes, 1985; Swadlow and Weyand, 1987; Swadlow and Hicks, 1996; Sirota et al., 2005; Kwegyir-Afful and Simons, 2009; Vélez-Fort et al., 2014), but others have recently reported that a significant proportion of L6a CT neurons are active during active-motor behaviors (Clayton et al., 2021; Dash et al., 2022), most likely coordinated by vM1. In the rodent, vM1 contributes to the initiation of whisking behaviors (Carvell et al., 1996), and sends the most abundant projections to L6a of vS1 (Zhang and Deschênes, 1998).

The vM1 – vS1 connection is thought to communicate motor preparatory signals to L6 CT neurons, providing context-dependent control of afferent sensory processing in the somatosensory thalamus during active sensation (Lee et al., 2008). We observed that vM1 provides ~10-fold stronger inputs to CT cells residing in L6aL, but this input was not strong enough to engage spiking behavior while the cells were at RMP (-84 mV). This was expected since the behavioral state of the animal influences the membrane potential and activity of cortical neurons (Steriade et al., 2001; Crochet and Petersen, 2006), with profound effects in L6 CT neurons (Steriade, 2001; Reinhold et al., 2023). Therefore, we wanted to know if vM1 input is strong enough to engage spiking of CT cells while their membrane potentials simulate that of an “active state”. Interestingly, only CT neurons residing in L6a$_L$ exhibited vM1-evoked spiking behavior, showing a dichotomy in the recruitment of CT circuits in sensory cortices. These results align with recent findings in the mouse showing that CT neurons in L6a$_L$ receive more direct anatomical inputs from vM1 than those in L6a$_U$ (Whilden et al., 2021).

Anatomical characterization of L6a CT circuits. The two major CT neuron types in L6a are mainly segregated along its vertical axis: VPm CT neurons populate L6a$_U$ whereas Dual CT neurons populate L6a$_L$ (Bourassa et al., 1995; Killackey and Sherman, 2003; Chevée et al., 2018; Whilden et al., 2021). Although multiple studies have done a thorough characterization of the proportions of CT neurons projecting to either VPm or POm in each sublayer, a caveat arises from the lack of testing both projections simultaneously. This is most likely due to the challenge in targeting the closely apposed VPm and POm to inject retrograde tracers. Here, we add to the growing evidence of CT circuits by reporting the proportions of neurons that project to the VPm, POm, or both. The predominant output of L6a$_U$ CT circuits is the VPm, whereas L6a$_L$ predominantly targets both areas, with the VPm projection being a collateral (Bourassa et al., 1995). These results are similar to those previously reported (Chevée et al., 2018; Whilden et al., 2021) and provide a discrete anatomical characterization of L6a CT circuits in vS1.

Preferential activation of Dual CT neurons by motor cortex. The simultaneous CT labeling performed here allowed us to assess the responsiveness to motor input in both CT cell classes with higher resolution. Here, we confirm that Dual CT neurons receive much stronger synaptic input by vM1 than those who project solely to the VPm, supporting previous anatomical results. Interestingly, only the Dual CT cell class exhibits spiking behavior evoked by vM1 inputs, suggesting a different role in the activity of L6a CT circuits during sensorimotor behaviors (e.g., active sensation; (Petersen, 2019; Briggs, 2020). Furthermore, we identified two possible mechanisms that could explain the selective recruitment of Dual CT neurons by vM1.

First, we found that the increased intrinsic membrane excitability of Dual CT neurons would allow them to respond stronger to vM1 input; previously suggested by (Breuer and Krieger, 2022). When we stimulated both cells with the with the same current injections in increasing steps, the Dual CT population started spiking earlier, but both cell classes exhibited similar slope suggesting an effect of a lower rheobase (Fig. 3.5*B).* Although both cell classes' membrane potential rests relatively similar to each other, indeed Dual CT neurons have a higher input resistance and a lower rheobase current, allowing them to integrate inputs more reliably.

Second, we found that the monosynaptic EPSCs elicited upon vM1 stimulation are ~2.5X stronger in Dual CT neurons. Previous studies have shown that vM1 can engage parvalbumin-expressing interneurons (PV) in L6a of vS1 (Kinnischtzke et al., 2014) and that they are highly connected to CT cells in both L6a sublayers (PV – CT connection rate: 54% in L6aU, 37% in L6aL; (Frandolig et al., 2019). Therefore, we wanted to test for differences in the strength of M1-evoked di-synaptic IPSCs in VPm CT and Dual CT neurons and found that Dual CT neurons also receive stronger inhibitory inputs. Ultimately, the net synaptic influence is dictated by the integration of both excitatory and inhibitory inputs. Interestingly, the E/I ratio was similar in both CT classes, supporting that the synaptic mechanism involved in the dichotomy of recruitment of CT neurons by vM1 is purely by the strength of excitatory inputs. Together, these results show both an intrinsic and a synaptic mechanism that can explain the dichotomy in recruitment of CT circuits in

L6a by M1.

Functional implications of vM1 selective engagement of Dual CT neurons. Our results contribute to the expanding body of evidence showing differential roles in sensory processing by different L6a CT circuits. Although intermingled, VPm CT and Dual CT neurons are thought to have distinct roles in sensory processing, as they are different in both their inputs and outputs. Since VPm CT neurons receive both sensory, and to a lesser extent, motor input, they could serve as coincidence detectors (Larkum et al., 1999; Ledergerber and Larkum, 2010; Bastos et al., 2012). This mechanism could serve to integrate both motor input at the basal dendrites and sensory input at their distal dendrites residing in L4 (Bourassa et al., 1995; Crandall et al., 2017), the thalamocortical recipient layer. Ultimately, this integration can alter the gain by modulating the temporal properties of VPm CT neurons projecting to the same whisker column.

Conversely, Dual CT neurons receive minimal input from thalamus (Audette et al., 2018) and get the majority of their inputs from vM1 and S2 (Whilden et al., 2021). Perhaps these neurons could represent the CT population that exhibit motor modulation and are active in vivo during whisking (Dash et al., 2022). Dual CT neurons could act primarily as temporal integrators by receiving facilitating vM1 input (Martinetti et al., 2022). Interestingly, Dual CT neurons contact the areas in the thalamic reticular nucleus (TRN) that are reciprocally connected to the POm, but not the VPm (Bourassa et al., 1995; Martinez-Garcia et al., 2020). Although much less is known about the behavioral and functional impacts that CT neurons might have on the POm, this pathway can enhance sensory-evoked responses in the VPm in a frequency-dependent manner (Lee et al., 2008; Crandall et al., 2015).

Acknowledgements. This work was supported by NIH grants K99-NS096108 (to S.R.C), R00-NS096108 (to S.R.C), R00-NS096108-S1 (to S.R.C and L.E.M), and F31-NS124244-01 (to L.E.M.). We thank Suryadeep Dash (Crandall Lab), Charles “Lee” Cox (Michigan State University), and Scott Cruikshank (The University of Alabama at Birmingham) for helpful and insightful discussions. Barry Connors for generously providing the *Ntsr1-Cre* mice. Charles Lee Cox (Michigan State University) for imaging support. Melinda Frame and the MSU Center for Advanced Microscopy (CAM) for their support in the acquisition of the confocal laser microscopy images for this project.

BIBLIOGRAPHY

Abbott CJ, Choe TE, Lusardi TA, Burgoyne CF, Wang L, Fortune B (2013) Imaging axonal transport in the rat visual pathway. Biomed Opt Express 4:364–386.

Audette NJ, Urban-Ciecko J, Matsushita M, Barth AL (2018) POm Thalamocortical Input Drives Layer-Specific Microcircuits in Somatosensory Cortex. Cereb Cortex 28:1312–1328.

Bastos AM, Usrey WM, Adams RA, Mangun GR, Fries P, Friston KJ (2012) Canonical microcircuits for predictive coding. Neuron 76:695–711.

Bortone DS, Olsen SR, Scanziani M (2014) Translaminar inhibitory cells recruited by layer 6 corticothalamic neurons suppress visual cortex. Neuron 82:474–485.

Bourassa J, Deschênes M (1995) Corticothalamic projections from the primary visual cortex in rats: a single fiber study using biocytin as an anterograde tracer. Neuroscience 66:253–263.

Bourassa J, Pinault D, Deschênes M (1995) Corticothalamic projections from the cortical barrel field to the somatosensory thalamus in rats: a single-fibre study using biocytin as an anterograde tracer. Eur J Neurosci 7:19–30.

Breuer TM, Krieger P (2022) Sensory deprivation leads to subpopulation-specific changes in layer 6 corticothalamic cells. Eur J Neurosci 55:566–588.

Briggs F, Usrey WM (2008) Emerging views of corticothalamic function. Curr Opin Neurobiol 18:403–407.

Briggs F, Usrey WM (2009) Parallel processing in the corticogeniculate pathway of the macaque monkey. Neuron 62:135–146.

Briggs F (2020) Role of feedback connections in central visual processing. Annu Rev Vis Sci 6:313–334.

Carvell GE, Miller SA, Simons DJ (1996) The relationship of vibrissal motor cortex unit activity to whisking in the awake rat. Somatosens Mot Res 13:115–127.

Chen S, Aston-Jones G (1995) Evidence that cholera toxin B subunit (CTb) can be avidly taken up and transported by fibers of passage. Brain Res 674:107–111.

Chevée M, Robertson JDJ, Cannon GH, Brown SP, Goff LA (2018) Variation in activity state, axonal projection, and position define the transcriptional identity of individual neocortical projection neurons. Cell Rep 22:441–455.

Clayton KK, Williamson RS, Hancock KE, Tasaka G-I, Mizrahi A, Hackett TA, Polley DB (2021) Auditory corticothalamic neurons are recruited by motor preparatory inputs. Curr Biol 31:310-321.e5.

Conte WL, Kamishina H, Reep RL (2009) Multiple neuroanatomical tract-tracing using fluorescent Alexa Fluor conjugates of cholera toxin subunit B in rats. Nat Protoc 4:1157–1166.

Crandall SR, Cruikshank SJ, Connors BW (2015) A corticothalamic switch: controlling the thalamus with dynamic synapses. Neuron 86:768–782.

Crandall SR, Patrick SL, Cruikshank SJ, Connors BW (2017) Infrabarrels Are Layer 6 Circuit Modules in the Barrel Cortex that Link Long-Range Inputs and Outputs. Cell Rep 21:3065–3078.

Crochet S, Petersen CCH (2006) Correlating whisker behavior with membrane potential in barrel cortex of awake mice. Nat Neurosci 9:608–610.

Cudeiro J, Sillito AM (2006) Looking back: corticothalamic feedback and early visual processing. Trends Neurosci 29:298–306.

Dash S, Autio DM, Crandall SR (2022) State-dependent modulation of activity in distinct layer 6 corticothalamic neurons in barrel cortex of awake mice. J Neurosci 42:6551–6565.

Dederen PJ, Gribnau AA, Curfs MH (1994) Retrograde neuronal tracing with cholera toxin B subunit: comparison of three different visualization methods. Histochem J 26:856–862.

Deschênes M, Veinante P, Zhang ZW (1998) The organization of corticothalamic projections: reciprocity versus parity. Brain Res Brain Res Rev 28:286–308.

Diamond ME, von Heimendahl M, Knutsen PM, Kleinfeld D, Ahissar E (2008) “Where” and “what” in the whisker sensorimotor system. Nat Rev Neurosci 9:601–612.

Frandolig JE, Matney CJ, Lee K, Kim J, Chevée M, Kim S-J, Bickert AA, Brown SP (2019) The synaptic organization of layer 6 circuits reveals inhibition as a major output of a neocortical sublamina. Cell Rep 28:3131-3143.e5.

Gong S, Doughty M, Harbaugh CR, Cummins A, Hatten ME, Heintz N, Gerfen CR (2007) Targeting Cre recombinase to specific neuron populations with bacterial artificial chromosome constructs. J Neurosci 27:9817–9823.

Gouwens NW et al. (2019) Classification of electrophysiological and morphological neuron types in the mouse visual cortex. Nat Neurosci 22:1182–1195.

Gouwens NW et al. (2020) Integrated morphoelectric and transcriptomic classification of cortical gabaergic cells. Cell 183:935-953.e19.

Harris JA, Petersen RS, Diamond ME (1999) Distribution of tactile learning and its neural basis. Proc Natl Acad Sci USA 96:7587–7591.

Killackey HP, Sherman SM (2003) Corticothalamic projections from the rat primary somatosensory cortex. J Neurosci 23:7381–7384.

Kim J, Matney CJ, Blankenship A, Hestrin S, Brown SP (2014) Layer 6 corticothalamic neurons activate a cortical output layer, layer 5a. J Neurosci 34:9656–9664.

Kinnischtzke AK, Fanselow EE, Simons DJ (2016) Target-specific M1 inputs to infragranular S1 pyramidal neurons. J Neurophysiol 116:1261–1274.

Kinnischtzke AK, Simons DJ, Fanselow EE (2014) Motor cortex broadly engages excitatory and inhibitory neurons in somatosensory barrel cortex. Cereb Cortex 24:2237–2248.

Kleinfeld D, Ahissar E, Diamond ME (2006) Active sensation: insights from the rodent vibrissa sensorimotor system. Curr Opin Neurobiol 16:435–444.

Kumar P, Ohana O (2008) Inter- and intralaminar subcircuits of excitatory and inhibitory neurons in layer 6a of the rat barrel cortex. J Neurophysiol 100:1909–1922.

Kwegyir-Afful EE, Simons DJ (2009) Subthreshold receptive field properties distinguish different classes of corticothalamic neurons in the somatosensory system. J Neurosci 29:964–972.

Landry P, Dykes RW (1985) Identification of two populations of corticothalamic neurons in cat primary somatosensory cortex. Exp Brain Res 60:289–298.

Larkum ME, Zhu JJ, Sakmann B (1999) A new cellular mechanism for coupling inputs arriving at different cortical layers. Nature 398:338–341.

Ledergerber D, Larkum ME (2010) Properties of layer 6 pyramidal neuron apical dendrites. J Neurosci 30:13031–13044.

Lee S, Carvell GE, Simons DJ (2008) Motor modulation of afferent somatosensory circuits. Nat Neurosci 11:1430–1438.

Luppi PH, Fort P, Jouvet M (1990) Iontophoretic application of unconjugated cholera toxin B subunit (CTb) combined with immunohistochemistry of neurochemical substances: a method for transmitter identification of retrogradely labeled neurons. Brain Res 534:209–224.

Madisen L, Zwingman TA, Sunkin SM, Oh SW, Zariwala HA, Gu H, Ng LL, Palmiter RD, Hawrylycz MJ, Jones AR, Lein ES, Zeng H (2010) A robust and high-throughput Cre reporting and characterization system for the whole mouse brain. Nat Neurosci 13:133–140.

Martinetti LE, Bonekamp KE, Autio DM, Kim H-H, Crandall SR (2022) Short-Term Facilitation of Long-Range Corticocortical Synapses Revealed by Selective Optical Stimulation. Cereb Cortex 32:1932–1949.

Martinez-Garcia RI, Voelcker B, Zaltsman JB, Patrick SL, Stevens TR, Connors BW, Cruikshank SJ (2020) Two dynamically distinct circuits drive inhibition in the sensory thalamus. Nature 583:813–818.

Miyashita E, Keller A, Asanuma H (1994) Input-output organization of the rat vibrissal motor cortex. Exp Brain Res 99:223–232.

Olsen SR, Bortone DS, Adesnik H, Scanziani M (2012) Gain control by layer six in cortical circuits of vision. Nature 483:47–52.

Petersen CCH (2019) Sensorimotor processing in the rodent barrel cortex. Nat Rev Neurosci 20:533–546.

Petreanu L, Mao T, Sternson SM, Svoboda K (2009) The subcellular organization of neocortical excitatory connections. Nature 457:1142–1145.

Reinhold K, Resulaj A, Scanziani M (2023) Brain State-Dependent Modulation of Thalamic Visual Processing by Cortico-Thalamic Feedback. J Neurosci 43:1540–1554.

Saleeba C, Dempsey B, Le S, Goodchild A, McMullan S (2019) A student’s guide to neural circuit tracing. Front Neurosci 13:897.

Schindelin J, Arganda-Carreras I, Frise E, Kaynig V, Longair M, Pietzsch T, Preibisch S, Rueden C, Saalfeld S, Schmid B, Tinevez J-Y, White DJ, Hartenstein V, Eliceiri K, Tomancak P, Cardona A (2012) Fiji: an open-source platform for biological-image analysis. Nat Methods 9:676–682.

Sherman SM, Koch C (1986) The control of retinogeniculate transmission in the mammalian lateral geniculate nucleus. Exp Brain Res 63:1–20.

Sirota MG, Swadlow HA, Beloozerova IN (2005) Three channels of corticothalamic communication during locomotion. J Neurosci 25:5915–5925.

Steriade M, Timofeev I, Grenier F (2001) Natural waking and sleep states: a view from inside neocortical neurons. J Neurophysiol 85:1969–1985.

Steriade M (2001) Impact of network activities on neuronal properties in corticothalamic systems. J Neurophysiol 86:1–39.

Swadlow HA, Hicks TP (1996) Somatosensory cortical efferent neurons of the awake rabbit: latencies to activation via supra--and subthreshold receptive fields. J Neurophysiol 75:1753–1759.

Swadlow HA, Weyand TG (1987) Corticogeniculate neurons, corticotectal neurons, and suspected interneurons in visual cortex of awake rabbits: receptive-field properties, axonal properties, and effects of EEG arousal. J Neurophysiol 57:977–1001.

Tsumoto T, Suda K (1980) Three groups of cortico-geniculate neurons and their distribution in binocular and monocular segments of cat striate cortex. J Comp Neurol 193:223–236.

Vélez-Fort M, Bracey EF, Keshavarzi S, Rousseau CV, Cossell L, Lenzi SC, Strom M, Margrie TW (2018) A Circuit for Integration of Head- and Visual-Motion Signals in Layer 6 of Mouse Primary Visual Cortex. Neuron 98:179-191.e6.

Vélez-Fort M, Rousseau CV, Niedworok CJ, Wickersham IR, Rancz EA, Brown APY, Strom M, Margrie TW (2014) The stimulus selectivity and connectivity of layer six principal cells reveals cortical microcircuits underlying visual processing. Neuron 83:1431–1443.

Vercelli A, Repici M, Garbossa D, Grimaldi A (2000) Recent techniques for tracing pathways in the central nervous system of developing and adult mammals. Brain Res Bull 51:11–28.

Voigts J, Deister CA, Moore CI (2020) Layer 6 ensembles can selectively regulate the behavioral impact and layer-specific representation of sensory deviants. eLife 9.

Wan XC, Trojanowski JQ, Gonatas JO (1982) Cholera toxin and wheat germ agglutinin conjugates as neuroanatomical probes: their uptake and clearance, transganglionic and retrograde transport and sensitivity. Brain Res 243:215–224.

Whilden CM, Chevée M, An SY, Brown SP (2021) The synaptic inputs and thalamic projections of two classes of layer 6 corticothalamic neurons in primary somatosensory cortex of the mouse. J Comp Neurol 529:3751–3771.

Zhang ZW, Deschênes M (1997) Intracortical axonal projections of lamina VI cells of the primary somatosensory cortex in the rat: a single-cell labeling study. J Neurosci 17:6365–6379.

Zhang ZW, Deschênes M (1998) Projections to layer VI of the posteromedial barrel field in the rat: a reappraisal of the role of corticothalamic pathways. Cereb Cortex 8:428–436.

Zolnik TA, Ledderose J, Toumazou M, Trimbuch T, Oram T, Rosenmund C, Eickholt BJ, Sachdev RNS, Larkum ME (2020) Layer 6b Is Driven by Intracortical Long-Range Projection Neurons. Cell Rep 30:3492-3505.e5.

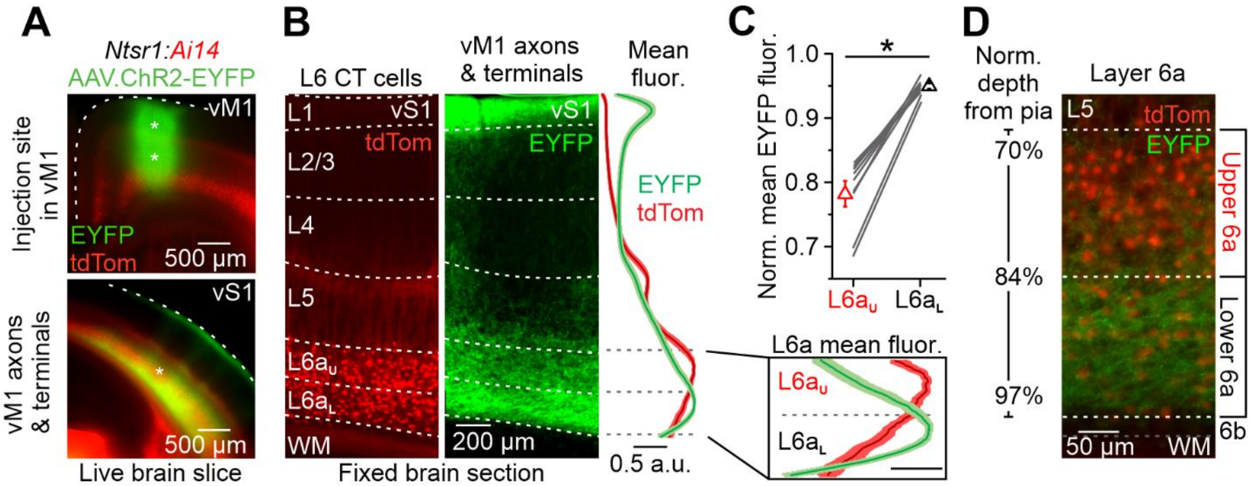

Figure 3.1. vM1 axon and terminal expression in denser in L6aL than in L6aU of vS1. A, Top, Fluorescent image of a live coronal slice (300 µm) from an Ntsr1-Cre x tdTomato reporter mouse (Ai14; fluorescently labels layer 6 corticothalamic cells in red) injected in the vibrissal primary motor cortex (vM1) with an adeno-associated virus (AAV; green). Asterisks indicate viral injection sites. Bottom, Image of EYFP-labeled vM1 axons/terminals in the vibrissal primary somatosensory cortex (vS1) from the same mouse. Asterisk indicates example column from panel B, B, Left, Higher magnification, fluorescent image of a 50-µm-thick section obtained from the same vS1 slice shows the distribution of layer 6 (L6) corticothalamic cells (CT). Right, same section showing the EYFP labeled vM1 axons/terminals densely innervating layers 1 and 6. Fluorescence intensity profiles (L6 CT cells, tdTomato; vM1 axons/terminals, EYFP) are shown as a function of normalized depth from pia to white matter (WM). EYFP fluorescence is strongest in L6aL than in L6aU, showing a higher density of vM1 axons/terminals in L6aL (scale bar for enlarged L6a mean fluorescence: 0.25 a.u.). C, Summary of normalized vM1 axon/terminal EYFP fluorescence in L6aU and L6aL of vS1 in the same slice (n=10 sections from ten mice; P= 0.00592, Wilcoxon signed ranks test) D, High-magnification fluorescent image of the same slice shown in (A). To define L6a into distinct sublayers, we established the normalized depths (from pia) of L6aU and L6aL (L6aU from 70 to 83%; L6aL from 84 to 97%). Clear stronger EYFP fluorescence is seen in L6aL.

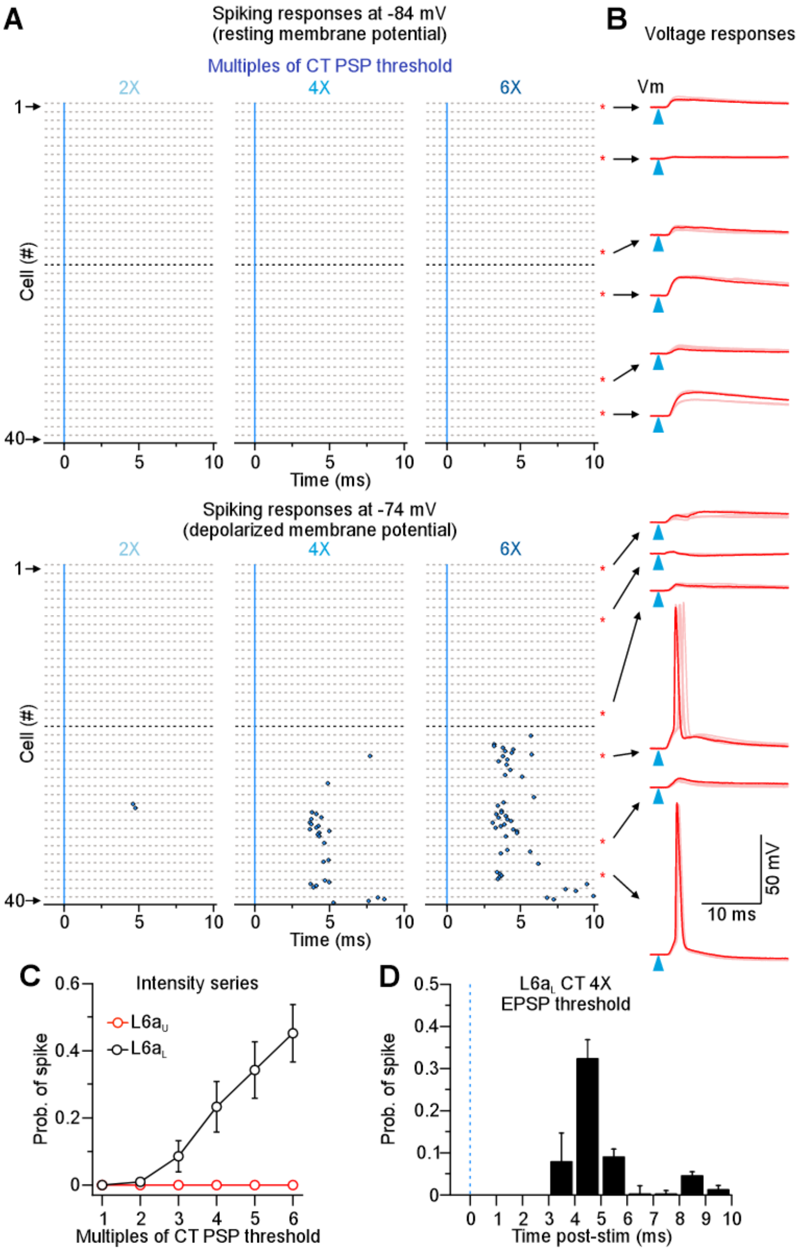

Figure 3.2. vM1 axons/terminals selectively recruit lower 6a CT neurons to spike in the Ntsr1-Cre driver mouse line. A, Raster plots of vM1-evoked spiking (black+blue circles) of 40 CT cells, ordered by depth within L6a of vS1 (5 trials/cell; each row between broken lines represents 1 cell and each circle represents one trial/spike). Brief LED stimulation (0.5 ms) was applied at different intensities, based on the cell's EPSP threshold intensity at their resting membrane potential (RMP)(2X, 4X, and 6X, respectively). Black dashed lines indicate the border between L6aU and L6aL (n= L6aU: 19 cells, L6aL: 21 cells, 5 mice). Top, Cells were recorded at their resting membrane potential (RMP; -84 mV). Bottom, same cells were held at a depolarized membrane potential (-74 mV) with a constant current injection. Notice the only cells spiking are located in L6aL. B, Example voltage responses of 6 different CT cells in response to activation of vM1 axons/terminals (current clamp RMP mean = -84 mV; 0.5-ms-light pulse

Figure 3.2 (cont’d)

duration; overlay of 5 sweeps; traces represent the response at 6X intensity threshold). Asterisks and arrows indicate the cell from the example traces, ordered by depth, respectively. Blue triangles indicate single LED pulse. Top, sub-threshold voltage responses evoked at RMP. Notice the differences in magnitude. Bottom, voltage responses evoked at -74 mV (depolarized). C, Summary of population spike probability by sublayer across an intensity series (n= L6aU: 19 cells, L6aL: 21 cells, 5 mice) (P= 3.30 x 10-8, two-way ANOVA), D, Population peristimulus time histogram (PSTH, 1-ms bins) plotting the spike timing for those L6aL CT cells that spiked upon vM1 stimulation held at -74mV (n = 9 cells from 4 mice). Blue dashed line indicates light pulse.

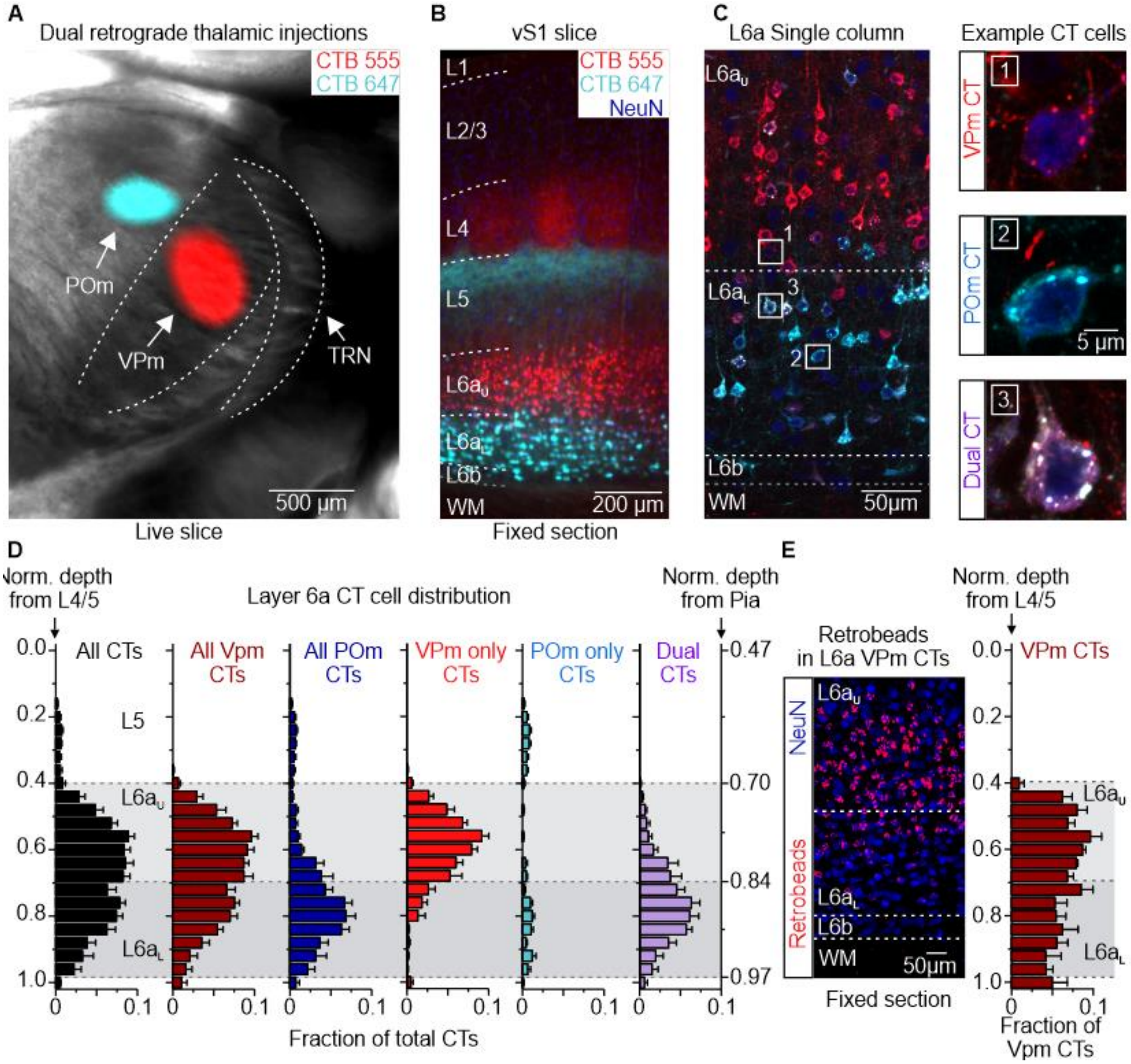

Figure 3.3. Retrograde labeling of CT neurons reveals a relationship between cell depth across L6a and target thalamic area. A, Live slice (300 µm) image showing an overlay of brightfield and two different CTB molecules conjugated to two distinct fluorophores (Alexa-555 or Alexa-647) injected into VPm (CTB-555, red) and POm (CTB-647, cyan) in vivo to retrogradely label L6a CT neurons in vS1. B, Low-magnification fluorescent image of a 50-µm-thick section from the same live slice. More neurons are labeled by CTB-555 in the upper part of L6aU, whereas more neurons are labeled by CTB-647 in L6aL. C, Left, high-magnification confocal image of a single column from the same section, used for counting CT cells that project to the VPm, POm, both, and non-CT neurons. Right, three example CT neurons surrounded by white squares; top, VPm-projecting CT neuron, middle, POm- projecting CT neuron, bottom, a CT neuron that projects to both VPm and POm (called Dual CT neurons for clarity). D, Normalized distribution histograms of L6a CT cells (n= 1,236 cells, 7 barrel columns, 5 mice). CT cells

Figure 3.3 (cont'd)

that were retrogradely filled via an injection into the VPm, POm, or both were counted to determine their distribution along the depth of L6a. L6aU depth is from 0.417 ± 0.01 to 0.691 ± 0.01 (light gray area), and L6aL depth is from 0.691 ± 0.01 to 0.966 ± 0.02 (darker gray area) Note: depth for cell counts was normalized from the L4/5 border. The normalized – relative depth from Pia can be found on the right side of plot for reference. This figure is complementary to Table 1. Bin size is 20 µm. Data are represented as mean ± SEM. E, CT cells were retrogradely filled via an injection of red Retrobeads in VPm to determine their distribution along the depth of L6a. Left, high-magnification confocal image of a L6a section, used for counting cells expressing red Retrobeads. Right, Normalized distribution histogram of L6a VPm CT cells (n= 490 cells, 3 barrel columns, 2 mice.

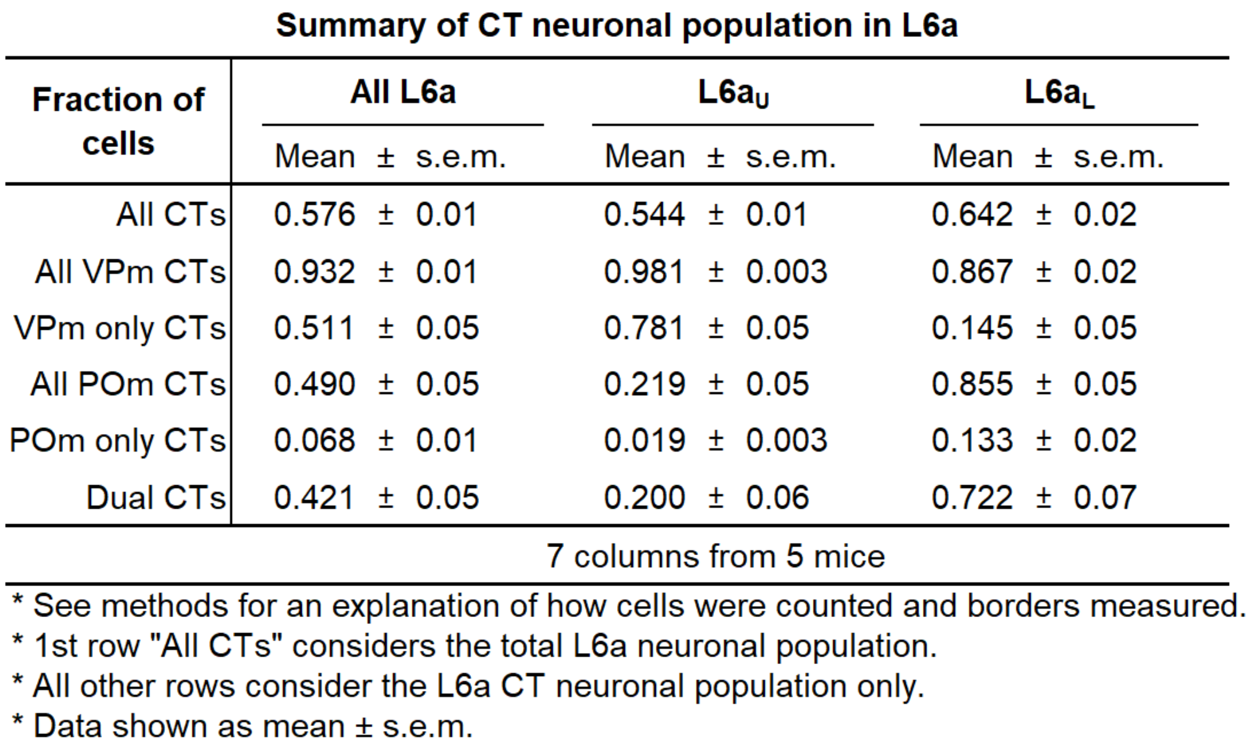

Summary of CT neuronal population in L6a

Fraction of cells	**All L6a**	**$L6a_U$**	**$L6a_L$**
	Mean ± s.e.m.	Mean ± s.e.m.	Mean ± s.e.m.
All CTs	0.576 ± 0.01	0.544 ± 0.01	0.642 ± 0.02
All VPm CTs	0.932 ± 0.01	0.981 ± 0.003	0.867 ± 0.02
VPm only CTs	0.511 ± 0.05	0.781 ± 0.05	0.145 ± 0.05
All POm CTs	0.490 ± 0.05	0.219 ± 0.05	0.855 ± 0.05
POm only CTs	0.068 ± 0.01	0.019 ± 0.003	0.133 ± 0.02
Dual CTs	0.421 ± 0.05	0.200 ± 0.06	0.722 ± 0.07
	7 columns from 5 mice		

* See methods for an explanation of how cells were counted and borders measured.
* 1st row "All CTs" considers the total L6a neuronal population.
* All other rows consider the L6a CT neuronal population only.
* Data shown as mean ± s.e.m.

Table 3.1. Summary of CT neuronal population in L6a. The results presented in Fig. 3.3 are quantified here.

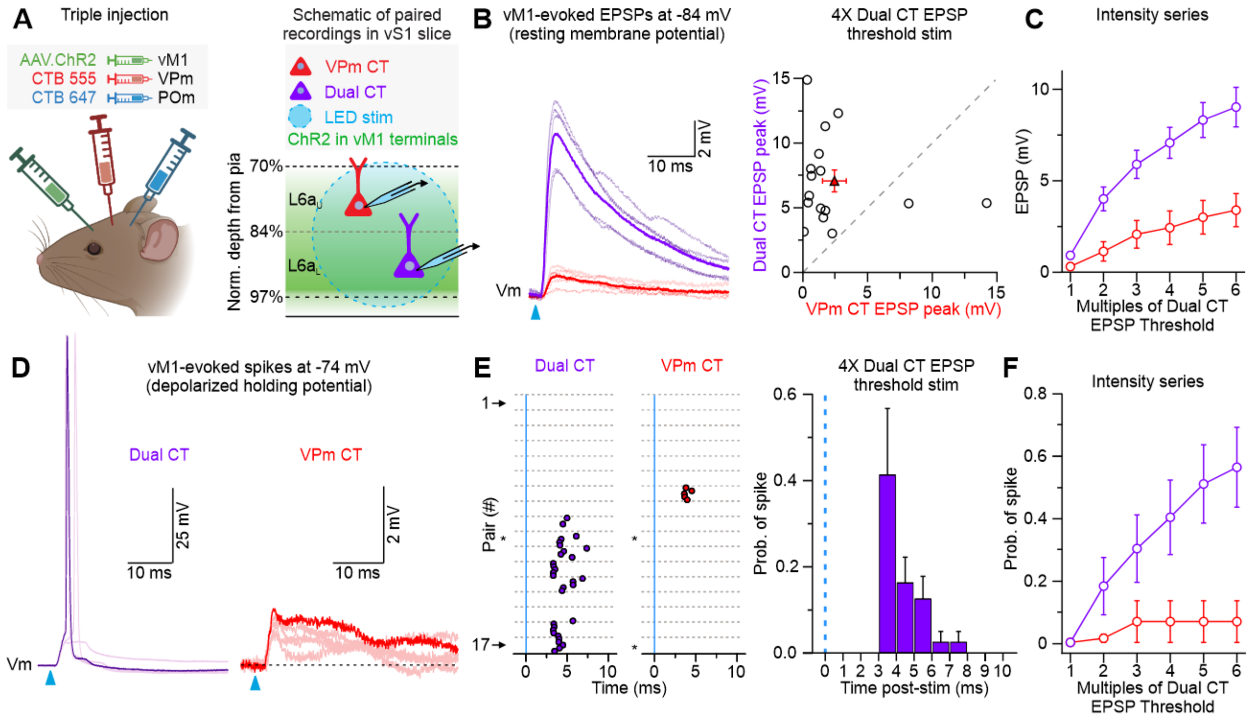

Figure 3.4. vM1 axons/terminals recruit Dual CT neurons more strongly than VPm CTs. A, Left, schematic of surgical procedure in vivo; Both the VPm and POm were targeted and injected simultaneously with two different CTB molecules with different fluorescent spectra to fluorescently label L6a CT neurons, and vM1 was injected with an AAV2-ChR2-EYFP to transfect vM1 neurons and photo-activate their terminals. Created with BioRender.com. Three weeks post-surgery, acute brain slices are obtained for electrophysiological experiments. Right, schematic of recording configuration in vitro; VPm- and Dual CT neurons were targeted simultaneously to record their responses to vM1 axon/terminal optical stimulation. VPm CT neurons were identified by their expression of the fluorescent CTB that was injected into VPm, and they were only targeted for recording in L6aU. Dual CT neurons were identified by their dual expression of both fluorescent CTBs that were injected in both VPm and POm, and they were only targeted in L6aL. Blue dashed circle indicates full-field LED stimulation. B, Left, Example voltage responses in paired recordings of Dual CT (purple) and VPm CT (Red) neurons, held at their resting membrane potential (-84mV), in response to activation of vM1 axons/terminals (current clamp RMP mean = -84 mV; 0.5-ms-light pulse duration; overlay of 5 sweeps; traces represent the response at 4X intensity threshold; Bold trace indicates average response, lighter traces are multiple trials within session). Average. Blue triangle indicates single LED pulse (0.5-ms duration). Right, a summary comparison of the average peak EPSP amplitude responses of Dual- and VPm CT neurons in response to 4X the light intensity needed to elicit a threshold EPSP in Dual CT neurons. Red triangle represents mean. Dual CT neurons responses were significantly stronger (P=0.00774, Wilcoxon paired signed-ranks test; n= 16 pairs, 11 mice). C, summary of vM1-evoked EPSPs over a range of light intensities. Dual CT neurons always responded stronger than VPm CT neurons (n= 16 pairs, 11 mice) (P= 2.46 x 10-8, two-way ANOVA, multiples 3-6). D, Left, representative example traces of both CT cell classes when stimulated at 4X EPSP Dual CT threshold intensity (asterisks next to raster indicate the cell from the example traces). The cell's membrane potentials were depolarized and held at -74mV, and vM1 axons/terminals were photo-activated. All traces are different trials within

Figure 3.4 (cont'd)

session, the bold trace emphasizes a representative response. E, Left, Raster plots of CT cell spikes to light-evoked vM1 activity, (Dual CT cells= purple circles, VPm CT cells= red circles; 17 pairs from 10 mice) (5 trials/cell; each row between broken lines represents 1 cell, each circle is one trial). Right, Summary of responses at 4X Dual CT EPSP threshold. Population peristimulus time histograms (PSTH, 1-ms bins) plotting the vM1-evoked spike timing for the responsive CT neurons when held at a depolarized membrane potential of -74mV. VPm-CT data was not plotted since only one cell spiked (all spikes were within 3-4 ms post-stimulation). F, vM1-evoked spiking is more prominent in the Dual CT than VPm CT population across a range of light intensities (P= 8.09 x 10-8, two-way ANOVA) Data are represented as mean ± SEM.

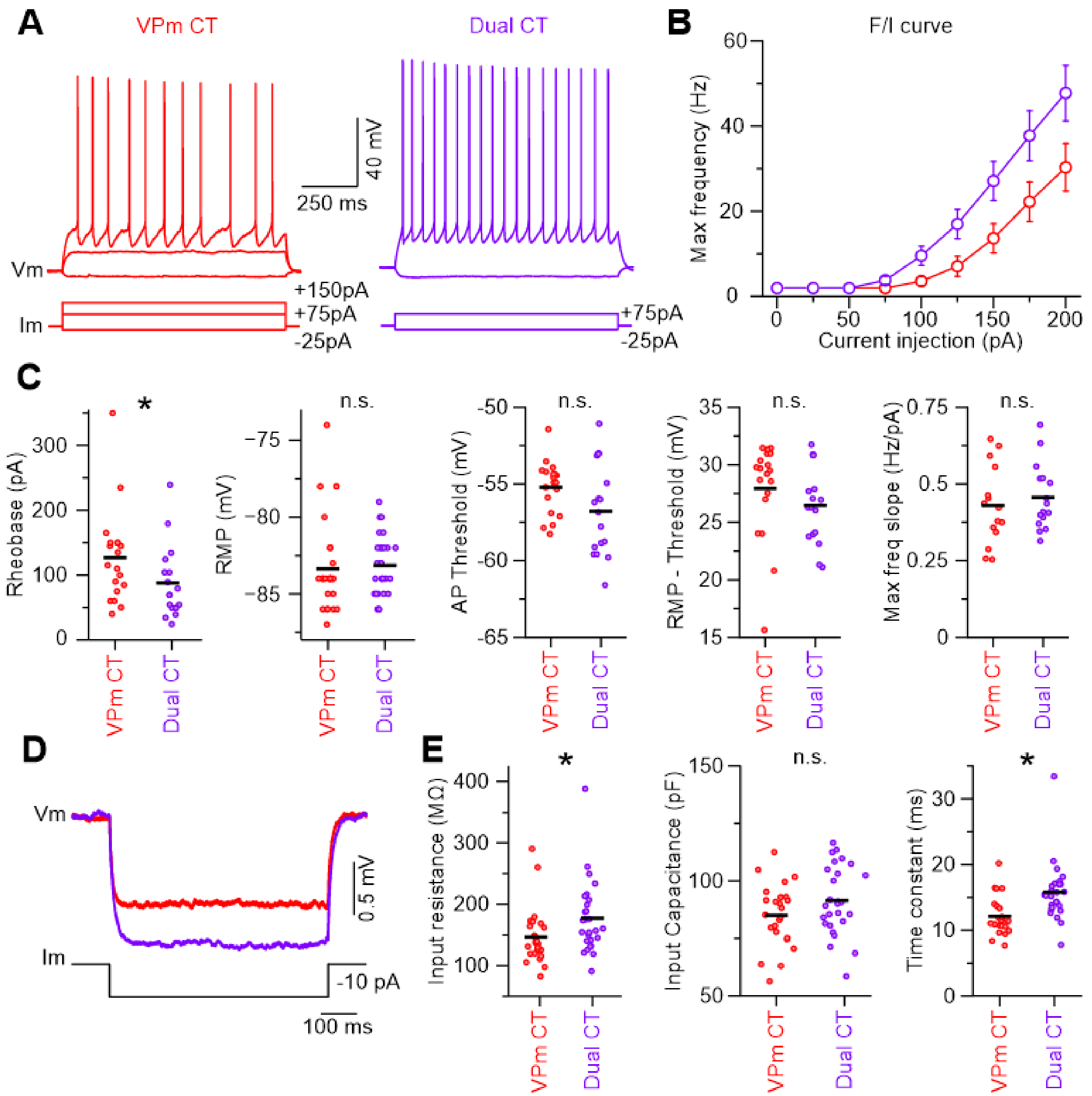

Figure 3.5. Dual CT neurons are more intrinsically excitable than VPm CT neurons. A, Voltage responses of representative VPm CT (red) and Dual CT (purple) neurons at resting potential to hyperpolarizing and depolarizing current steps. The VPm CT cells response to a +75 pA shows weaker/subthreshold output whereas Dual CT cells spike. B, Current-frequency plot (F/I plot) showing average maximum AP frequency fired at different current strengths. Both VPm CT and Dual CT cells exhibit a regular spiking pattern depending on the stimulus strength, but Dual CT neurons respond more strongly to the same stimulus. See Table 2 for a statistical summary of all intrinsic properties measured. C, From left to right, the minimal current necessary to elicit an action potential (AP) (rheobase) is lower in Dual CT than in VPm CT neurons (VPm CT= 126.84 ± 16.63 pA; Dual CT= 83.825 ± 13.64 pA). The resting membrane potential of both cell classes is

Figure 3.5 (cont'd)

similar (VPm CT= 83.36 ± 0.60 mV; Dual CT= 83.15 ± 0.38 mV). The action potential/spike threshold of both cell classes is similar (VPm CT= -55.32 ± 0.39 mV; Dual CT= -56.88 ± 0.72 mV). The difference between the resting potential and spike threshold is similar in both CT classes (VPm CT= 27.94 ± 0.95; Dual CT= 26.47 ± 0.80). The slope of the max frequency to increasing current steps (from panel B) between cell classes is similar (VPm CT= 0.43 ± 0.03 Hz/pA; Dual CT= 0.46 ± 0.03 Hz/pA). Black horizontal lines indicate mean. D, Left, Average responses to a -10 pA current injection from both CT cell classes. The same current elicited a stronger hyperpolarization in Dual CTs, suggesting a higher membrane resistance than VPm CT neurons. E, Scatter plots showing the population distribution and means for key passive properties. From left to right, input resistance is higher in Dual CT neurons, indicating stronger responses to same inputs (VPm CT= 146.56 ± 9.22 MΩ; Dual CT= 177.53 ± 11.41 MΩ) The input capacitance is similar between both CT cell classes (VPm CT= 85.04 ± 2.69 pF; Dual CT= 91.46 ± 2.89 pF). The time constant is faster in VPm CT than in Dual CT neurons (VPm CT= 12.12 ± 0.57 ms; Dual CT= 15.80 ± 0.85 ms). Horizontal black lines mean. Asterisks indicate statistical significance.

	L6a$_U$ VPm CT		L6a$_L$ Dual CT		L6a$_L$ POm CT		VPm vs Dual CT		Dual vs POm CT	
	Mean ± s.e.m.	*n* cells / mice	Mean ± s.e.m.	*n* cells / mice	Mean ± s.e.m.	*n* cells / mice	*P*	Test	*P*	Test
Resting membrane potential (mV)	-83.4 ± 0.6	25 / 13	-83.1 ± 0.4	27 / 15	-83.6 ± 0.4	24 / 17	0.305	Mann-Whitney	0.375	*t*-test
Membrane resistance (MΩ)	146.6 ± 9.2	25 / 13	177.5 ± 11.4	27 / 15	171.8 ± 11.3	24 / 17	0.012	Mann-Whitney	0.698	Mann-Whitney
Membrane time constant (ms)	12.1 ± 0.6	25 / 13	15.8 ± 0.8	27 / 15	15.7 ± 0.7	24 / 17	1.03×10^{-4}	Mann-Whitney	0.992	Mann-Whitney
Membrane capacitance (pF)	85.0 ± 2.7	25 / 13	91.5 ± 2.9	27 / 15	95.6 ± 3.8	24 / 17	0.111	*t*-test	0.386	*t*-test
Rheobase (pA)	126.8 ± 16.6	19 / 11	83.8 ± 13.6	17 / 10	75.3 ± 10.3	18 / 14	0.029	Mann-Whitney	0.920	Mann-Whitney
Spike threshold (mV)	-55.3 ± 0.4	19 / 11	-56.9 ± 0.7	17 / 10	-55.9 ± 0.7	18 / 14	0.058	Mann-Whitney	0.314	*t*-test
Delay to spike (ms)	335.2 ± 64.0	19 / 11	226.8 ± 44.0	17 / 10	158.3 ± 26.2	18 / 14	0.056	Mann-Whitney	0.241	Mann-Whitney
Spike amplitude (mV)	85.0 ± 1.0	19 / 11	92.1 ± 1.7	17 / 10	90.0 ± 1.3	18 / 14	6.16×10^{-4}	*t*-test	0.336	*t*-test
Spike half-width (ms)	0.58 ± 0.01	19 / 11	0.66 ± 0.01	17 / 10	0.64 ± 0.01	18 / 14	1.08×10^{-4}	*t*-test	0.249	*t*-test
Max rate of rise (mV*ms)	521.1 ± 15.4	19 / 11	569.6 ± 24.7	17 / 10	558.8 ± 22.9	18 / 14	0.096	*t*-test	0.750	*t*-test
Max rate of decay (mV*ms)	-146.1 ± 5.7	19 / 11	-129.5 ± 4.3	17 / 10	-137.1 ± 3.4	18 / 14	0.039	Mann-Whitney	0.170	*t*-test
Resting potential - spike threshold (mV)	27.9 ± 0.95	19 / 11	26.5 ± 0.80	17 / 10	27.7 ± 0.80	18 / 14	0.093	Mann-Whitney	0.275	*t*-test
1st frequency F/I slope (Hz/pA)	0.46 ± 0.03	15 / 9	0.46 ± 0.02	16 / 11	0.44 ± 0.03	9 / 8	0.736	Mann-Whitney	-	-
Max frequency F/I slope (Hz/pA)	0.43 ± 0.03	15 / 9	0.46 ± 0.03	16 / 11	0.44 ± 0.03	9 / 8	0.797	Mann-Whitney	-	-
Spike frequency adaptation ratio (2nd/1st)	0.82 ± 0.02	13 / 7	0.73 ± 0.01	16 / 11	0.72 ± 0.02	9 / 8	0.001	*t*-test	-	-
Spike frequency adaptation ratio (last/1st)	0.64 ± 0.03	13 / 7	0.54 ± 0.02	16 / 11	0.52 ± 0.02	9 / 8	0.013	Mann-Whitney	-	-

* See methods for an explanation of how the electrophysiological parameters were defined/measured. Data shown as mean ± s.e.m.

* All membrane potentials were corrected for a -14 mV liquid junction potential.

Table 3.2. Electrophysiological properties of retrogradely labeled CT neurons in L6a of vS1. The results presented in Fig 3.5 are quantified in this table.

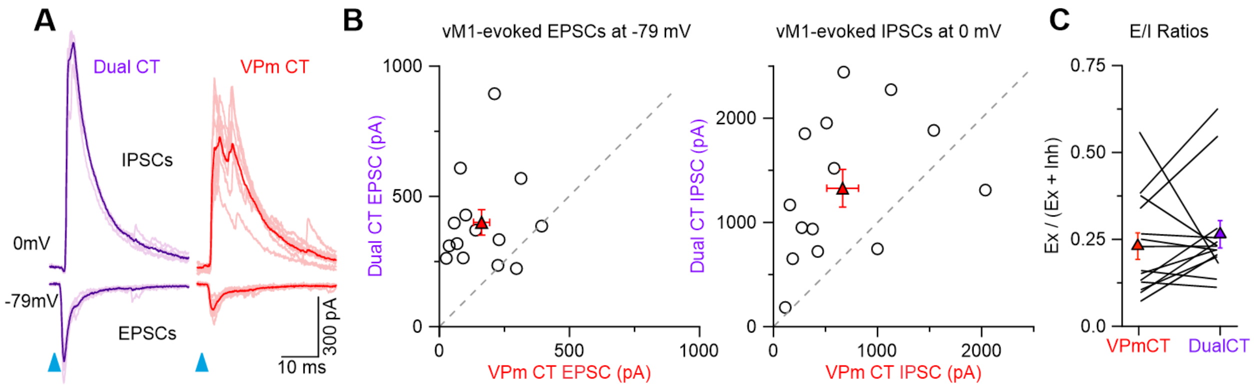

Figure 3.6. vM1 inputs evoke stronger excitation in Dual CT neurons. A, Left, example traces of light-evoked vM1 monosynaptic EPSCs and di-synaptic IPSCs in Dual CT (left) and VPm CT (right) neurons, held at their measured reversal potential for excitation and inhibition, respectively. Blue arrow indicates light pulse (0.5ms). Bold trace indicates average response, lighter traces are multiple trials within session. B, Left, unity plot summarizing vM1-evoked EPSC peak amplitude of Dual and VPm CT neurons held at their reversal potential for inhibition (-80mV) and stimulated at 4X Dual CT EPSC threshold; Dual CT neurons always received stronger excitation (VPm CT= 162.92 ± 31.11 pA; Dual CT= 400.17 ± 48.77 pA; P=0.0026, Wilcoxon paired signed-ranks test; n= 14 pairs from 9 mice). Right, unity plot summarizing IPSC peak amplitude while holding cells at their reversal potential for excitation (0mV); Dual CT neurons always received stronger inhibition as (VPm CT= -664.77 ± 152.32 pA; Dual CT= -1328.32 ± 180.65 pA; P=0.0008, paired sample t-test; n=9 pairs from 6 mice). C, Pair-wise comparison of excitation-to-inhibition ratios (ex /(ex-in)) in VPm CT and Dual CT neurons (VPm CT= 0.23 ± 0.04; Dual CT= 0.26 ± 0.04; P=0.346, Wilcoxon signed-ranks test; n=14 pairs from 9 mice).

CHAPTER 4: PRELIMINARY DATA AND FUTURE DIRECTIONS

4.1 - Introduction

The highly dynamic interplay between the somatosensory and motor systems allows us to adapt our behavior to satisfy behavioral demands (Gilbert and Li 2013). Therefore, studies regarding this topic have been of high interest since the early days of neuroscience. We have further progressed our understanding of this highly complex system due to the rapid advancement of technology allowing us to dissect the specific circuits involved in sensory processing at distinct levels. The cortical L6 corticothalamic (CT) pathway is of particular interest due to the highly specific and powerful influence that it has in modulating thalamic sensory processing (Briggs 2020).

In chapter 3, I introduced a highly specific anatomical layout of the distribution of CT neurons along the vertical depth of L6a, supported by much previous literature (Bourassa et al., 1995; Killackey and Sherman, 2003; Chevée et al., 2018; Whilden et al., 2021). The purpose of this study is to take advantage of our knowledge of L6a CT circuitry and use genetic methods to study the individual influence that the two major L6a CT subcircuits have in the thalamus. Specifically, we know that most L6aU CT neurons belong to the "VPm CT" class (84%), whereas the majority of those in L6aL are considered "Dual CT" neurons (70%). Historically, it has been difficult to parse out these cell classes due to the complexity of these intermingled circuits, but the combination of recent technological advancements has made this possible. The detailed understanding of L6a CT circuits allows us to ask highly specific questions about the influence of distinct L6a CT circuits on sensory processing in the thalamus.

The role of the L6 CT system on sensory processing in the thalamus has been previously studied, but with multiple caveats. Firstly, many studies have used electrical stimulation using the thalamocortical slice (Agmon and Connors, 1991), which does not provide specific stimulation to a pre-defined cell class, rather than bulk activation. Fortunately, the recent advancement in optogenetic tools and mouse genetic models (i.e., Ntsr1-Cre line) has provided us with the ability to selectively manipulate the L6a CT system (Gong et al., 2007; Olsen et al., 2012; Crandall et al., 2015). Although this is a good approach, the viral injections necessary to selectively activate distinct neurons tend to be broad and ignore CT neuron subtypes. In fact, most studies using these genetic tools tend to perform bulk activation of this pathway, and do not account for the differential effects that each CT subtype might have in the thalamus.

Here, I present preliminary studies taking advantage of a previously described approach involving highly spatially restricted viral stereotaxic injections (Frandolig et al., 2019; Whilden et al., 2021) to selectively manipulate the different L6a CT microcircuits. First, I performed a plethora of spatially restricted injections along the depth of vS1 deep layers (L5a – WM) to test if selective expression of ChR2 expression to either L6a sublayer was possible. Furthermore, I performed whole-cell electrophysiological recordings in the thalamic areas while optically activating L6aL (Dual CTs) terminals in the TRN, VPm, and POm, respectively. These novel preliminary findings allow us to selectively study the effects that activating CT neurons from both L6a sub-layers has in the somatosensory thalamus, offering new insights into thalamic circuitry dynamics.

4.2 – Materials and Methods

Animals. All procedures were performed in accordance with the National Institutes of Health (NIH) Guidelines for the Care and Use of Laboratory Animals and approved by the Institutional Animal Care and Use Committee (IACUC) at Michigan State University.

We used the following mouse lines in this study: Ntsr1-Cre (catalog # 017266-UCD, Mutant Mice Research & Resource Center; RRID: MMRC_017266-UCD); Gong et al. 2007), and Ai14 (catalog #007908, The Jackson Laboratory; Madisen et al. 2010). The Ntsr1-Cre mouse line had ICR genetic background and was bred by crossing it with a homozygous Ai14 reporter line, resulting in experimental mice that were homozygous for the indicated genes. All animals were group housed with combined sex littermates in a dedicated animal care facility maintained on a 12:12 h light–dark cycle. Food and water were available ad libitum. I used both male and female mice in this preliminary study.

Stereotaxic injections and surgical procedures. For stereotaxic injections, mice of either sex, ~ 3 weeks old were used. All surgeries were performed as previously described (Crandall et al. 2017; Martinetti et al. 2022; Frandolig et al. 2019; Whilden et al. 2021). To test whether I could selectively express ChR2 in CT neurons located in either L6aU or L6aL of vS1, I injected a bi-lateral single small bolus of adeno-associated virus (volume: ~10-50 nL; titer= 3.5 x 1012 viral particles/mL) that encoded genes to selectively express hChR2 (H134R)-EYFP fusion proteins in a cre-dependent manner (rAAV2/Ef1α-DIO-hChR2[H134R]-eYFP; Batch #AV4378J, University of North Carolina Viral Vector Core) into L6a, in addition to Choleratoxin-B conjugated to Alexa 647 (CTB 647, ThermoFisher C34778) to locate the center of the injection. CTB was diluted using 0.1 M phosphate buffered saline and this was used to dilute the virus to the preferred titer. L6aU coordinates (bi-lateral) were: -0.8 mm posterior, +/- 3.0 mm lateral, -1.0 mm ventral, from Bregma), and L6aL coordinates (bi-lateral) were: -0.8 mm posterior, +/- 3.0 mm lateral, -1.5 mm ventral, from Bregma). Animals were humanely sacrificed after ~3 weeks to allow for sufficient expression of viral construct.

Acute brain slice preparation. After ~3 weeks of viral and tracer expression, mice of either sex were deeply anesthetized using isoflurane and decapitated. The brains were rapidly extracted and placed in a cold (~4 °C) and oxygenated (5% CO2, 95% O2) slicing solution containing the following (in mM): 3 KCl, 1.25 NaH2PO4, 10 MgSO4, 0.5 CaCl2, 26 NaHCO3, 10 glucose, and 234 sucrose. Acute somatosensory thalamocortical slices (300 µm thick) of both hemispheres were collected as previously reported (Agmon and Connors 1991; Crandall et al. 2015). Shortly, the brain slices containing the vS1 and somatosensory thalamus were sectioned (VT-1200s, Leica) using the same slicing solution, and transferred to a holding chamber in warm (32 °C) oxygenated artificial cerebrospinal fluid (ACSF) containing the following (in mM): 126 NaCl, 3 KCl, 1.25 NaH2PO4, 2 MgSO4, 2 CaCl2, 26 NaHCO3, and 10 glucose. Slices were incubated at 32 °C for 20 minutes, then at room temperature for at least 40 minutes before recording. Slices containing injection sites (vS1) and terminal sites (TRN, VPm, and POm) were always collected for imaging to assess accuracy and tissue health. We only considered mice in which there were no obvious signs of off-target injections or tissue damage.

In vitro electrophysiological recordings and data acquisition. Brain slices were transferred to a submersion chamber on an upright microscope (Zeiss Axio Examiner.A1) and were continually superfused with warm (32 ± 1 °C) oxygenated ACSF containing (in mM): 126 NaCl, 3 KCl, 1.25 NaH2PO4, 1 MgSO4, 1.2 CaCl2, 26 NaHCO3, and 10 glucose. Neurons were visualized using infrared differential interference contrast (IR-DIC) and fluorescence microscopy using a 40x water-immersion objective (Zeiss, W Plan-Apo 40x/1.0 NA) and a video camera (Olympus, XM10-IR). vS1 was identified based on the visible cytoarchitecture of the barrels in layer 4 (L4) in addition to the strong expression of EYFP.

Whole-cell recordings were obtained by using patch pipettes (4-6 MΩ) pulled (Sutter P-1000, Sutter Instruments) from filamented borosilicate capillary glass (Sutter Instruments) and back-filled with a potassium-based internal solution containing (in mM): 130 K-gluconate, 4 KCl, 2 NaCl, 10 HEPES, 0.2 EGTA, 4 ATP-Mg, 0.3 GTP-Tris, and 14 phosphocreatine-K (pH 7.25, 290-300 mOsm). Voltages were corrected for a -14 mV liquid junction potential. Thalamic cells were identified and targeted for recording by their location within the thalamus and the co-localization of EYFP.

Electrophysiological data were acquired and digitized at 20 kHz (50 kHz when assessing intrinsic membrane properties; MultliClamp 700B amplified, Digidata 1550B4, pClamp 11), and low-pass filtered at 10 kHz (current-clamp) prior to digitizing. The pipette capacitances were neutralized, and the series resistances (typically 10-25 MΩ) were compensated online (100% for current-clamp). Series resistances were continually monitored and adjusted online to ensure accurate compensation.

Photostimulation of ChR2 expressing axons/terminals. ChR2 was stimulated optically using a high-power white light-emitting diode (LED; Mightex, LCS-5500-03-22) manipulated by an LED controller (Mightex, BLS-1000-2). LED on/off times were fast (<50 µs) and had constant amplitude and duration, verified by a fast photodiode (Thorlabs, DET36A). The light was collimated and reflected through a dichroic beam-splitter (Semrock, FF660-FDi02) and a high-magnification water-immersion objective (Zeiss, W Plan-Apo 40x/1.0 NA), with an estimated spot diameter of ~1500 µm, and maximum LED power of 60 mW (~X mW/mm2). Light flashes were delivered as 0.5 ms pulses and centered directly over ChR2-expressing axons/terminals and the recorded cell.

The LED intensity was adjusted to evoke an EPSP threshold response (defined by having an EPSP at least 50% of trials) of each recorded neuron when held at their preferred resting membrane potential (RMP; ~ 70 mV) in current-clamp, or an intensity in which I recorded the maximum response (i.e., no stronger mono-synaptic responses with higher intensities).

Microscopy. Sections processed for immunohistochemistry were initially visualized using an epifluorescent microscope (Zeiss Axio Imager.D2) and Zen software to identify representative samples. Section selection criteria were as follows: cell bodies expressing ChR2 were contained in either L6aU or L6aL, and thalamic pattern had to be appropriate for the cells injected (i.e., injection in L6aU only showed EYFP expression in TRN and VPm, whereas L6aL expressed EYFP in TRN, VPm, and POm). Selected sections were then visualized on a confocal microscope (Nikon A1 Laser Scanning Confocal Microscope) using a 40x (1.0 N.A.) or 100x (xx N.A.; example cells in Fig. 4.3C-D). Z-stacks were obtained of the full depth of the section, at 0.8 µm/plane.

4.3 – Results

Selective expression of ChR2 in both L6a sublayers using minimal injection techniques. To investigate the influence of CT neurons originating from distinct L6a sub-layers on the thalamus, I used an optogenetic strategy in the mouse (Crandall et al. 2017; Martinetti & Bonekamp et al. 2022) to selectively express a Channelrhodopsin-2/enhanced yellow fluorescent protein (ChR2-EYFP) in a cre-dependent manner in either L6aU or L6aL CT neurons (Figs. 4.1 & 4.2) of vS1.

I used a transgenic and viral approach to selectively express ChR2 in either L6aU or L6aL CT neurons. I first crossed the Ntsr1 x Ai14 mouse that selectively labels L6a CT cells in sensory cortices (Bortone et al. 2014; Crandall et al. 2015; Crandall et al. 2017; Olsen et al. 2012; Martinetti et al. 2022; Whilden et al. 2021). I then performed a intracranial viral injection of a cre-dependent virus encoding ChR2 in either L6aU or L6aL CT neurons. In addition to the anatomical characterization that I performed in Chapter 3, previous studies have identified differences in the cytoarchitectonic organization of CT neurons along the depth of L6a (Bourassa et al. 1995; Bourassa and Deschênes 1995; Killackey and Sherman 2003), showing that L6a can be subdivided into an upper and a lower section.

To choose the correct injection coordinates to restrain viral expression in a single L6a sublayer, I performed a series of injections that varied in depth (L6aU: -0.8 mm, -1.0 mm, and -1.2 mm deep; L6aL: -1.2 mm and -1.5 mm deep) (Fig. 4.1 A-D). The most successful injection depth to keep viral expression in L6aU was -1.0 mm (Figs. 4.1B, 2A; N= 5 hemispheres from 3 mice), which we confirmed by observing "stereotypical" morphological patterns expressed by VPm CT neurons (see Chapter 3). Analysis of the spatial pattern of fluorescence intensity along the vertical extent from Pia to WM showed strong EYFP fluorescence within the lower part of L4 and L6aU, consistent with previous studies (Zhang and Deschênes 1997; Crandall et al. 2017; Whilden et al. 2021; Kim et al. 2014). Additionally, the most successful injection depth to restrain viral expression in L6aL was -1.5 mm (Figs. 4.1D, 4.2B; N= 3 hemispheres from 3 mice), which we confirmed by observing "stereotypical" morphological patterns expressed by VPm CT neurons (also see Chapter 3). Analysis of the spatial pattern of fluorescence intensity along the vertical extent from Pia to WM showed strong EYFP fluorescence in the border between L4 and L5a, and L6aL, consistent with previous studies.

The cortical neurite patterns of L6a CT neurons provide a good indication that we correctly transfected our cell of interest but does not indicate anything about their thalamic projection patterns. Therefore, I next looked at the L6a CT neuron terminal patterns in the thalamus. I observed axon/terminal patterns solely in the core of the TRN and in the VPm when I targeted L6aU (Fig. 4.2C). Furthermore, I observed axon/terminal patterns in the edge of the TRN, weak expression in the VPm, and strong expression in the POm when I targeted L6aL (Fig. 4.2D). These results suggest that getting ahold of putative VPm CT neurons (by restraining viral expression in L6aU) or Dual CT neurons (by restraining viral expression in L6aL) is possible, as seen in the cortical and thalamic axon/terminal patterns, and in previous studies (Bourassa et al. 1995; Zhang and Deschênes 1997; Martinez-Garcia et al. 2020).

Studying the specific effects of L6aL “Dual CT” neurons in the thalamus is possible. Building on Chapter 3's findings, I explored the unique effects of selectively activating L6aL axons/terminals in the thalamus, focusing on "Dual CT" neurons. Briefly, we identified that most CT neurons in L6aL belong to the “Dual CT” type, and that vM1 has an affinity to selectively recruit these cells, but not the “VPm CT” type from L6aU (Fig. 3.4) Therefore, I decided to explore the effects of selective activation of L6aL axons/terminals in the thalamus.

As previously mentioned, a viral injection targeted specifically to the L6aL CT neurons yields dendritic/axonal patterns that match those of the “Dual CT” type, but it doesn’t necessarily indicate a lack of ChR2 expression of L6aU CT neurons. Therefore, I decided to take a closer look into the somatic expression of ChR2 along the depth of L6a of a section where the virus was targeted to L6aL (Fig. 4.3; N=1). I did not observe any

L6aU (from 70 – 84% norm. depth from pia) CT neurons expressing somatic ChR2 (Fig. 4.3 B, C), whereas a number of neurons in L6aL (from 84 – 97% norm. depth from pia) expressed ChR2 in their cell bodies (Fig. 4.3 B, D not quantified). These findings suggest that I can effectively and selectively express ChR2 in the “Dual CT” neuron type via highly spatially restrained injections in L6aL, although more investigation is necessary to confirm these findings.

These restricted viral injections give us a chance to express ChR2 in L6aL CT neurons, but due to the nature of the injection (i.e., small volumes) we were unsure if the expression would be enough to elicit reliable photoactivation in the thalamus. Therefore, I next investigated the thalamus (Fig. 4.4A) to assess whether this technique was viable to reliably study the specific influence that L6aL CT neurons have in the TRN, VPm, and POm (Fig. 4.4 A – B). Indeed, when I recorded cells held at their preferred resting membrane potential (RMP) and stimulated L6aL CT terminals with a single light pulse (0.5 ms), I observed robust responses (Fig. 4.4C) using relatively low light intensities (data not shown). Together, these data strongly suggest that highly spatially restricted injections to selectively target “VPm CTs” or “Dual CT” neurons are viable to study the distinct post-synaptic effects in the thalamus. Due to time constraints of this project, these experiments were largely exploratory and thus there is no formal analysis of this data at this point.

4.4 – Discussion

In this preliminary study, I take advantage of a spatially restricted viral method to selectively express ChR2 in CT neurons from distinct L6a sub-layers of vS1, allowing for precise investigation of their individual effects on thalamic post-synaptic sites. This contrasts with previous approaches using global electrical stimulation or bulk optogenetic activation via the Ntsr1-Cre line, which lacked specificity. By injecting minimal volumes of cre-dependent virus into each L6a sub-layer, I determined that this previously described approach allows us to investigate the effects that "VPm CT" and "Dual CT" neurons have on the on the VPm, TRN, and POm, providing novel insights into the influence of fine L6a CT microcircuitry functions.

Selective expression and thalamic projection patterns of L6aU and L6aL CT Neurons. The integration of genetic mouse models and viral techniques has significantly advanced the study of circuits neuroscience, particularly within the corticothalamic system (Olsen et al. 2012; Bortone et al. 2014; Kim et al. 2014; Crandall et al. 2015; Crandall et al. 2017; Chevée et al. 2018; Frandolig et al. 2019; Born et al. 2021; Whilden et al. 2021; Gu et al. 2023). To explore the distinct impacts of distinct L6a CT circuits, such as “VPm CT” and “Dual CT” neuronal projections on the thalamus, I initially considered using a retrograde virus (retroAAV; Tervo et al. 2016) injection in Ntsr1 mice targeting VPm and POm. However, these attempts did not result in retrograde expression in L6a CT neurons, perhaps due to specific tropisms exhibited by certain AAVs (Yizhar et al. 2011). Subsequently, I investigated the possible retrograde-traveling properties of certain serotypes seen in other anterograde AAVs (see Martinetti et al. 2022 for review), but found no retrograde expression with AAV1, AAV5, AAV6, or AAV9, presenting a challenge to this approach.

Despite initial challenges with retrograde viral approaches, I achieved selective ChR2 expression in L6aU and L6aL by leveraging spatially restricted injections of a cre-dependent virus in the Ntsr-line (Frandolig et al. 2019; Whilden et al. 2021). Due to our detailed anatomical understanding of L6a CT neuron distribution (see Chapter 3 for review; Chevée et al. 2018; Whilden et al. 2021), I had confidence that we could achieve restricted control of distinct L6a sub-circuits by injecting minimal volumes of AAV2. This method allows us to precisely study the effects of L6aU "VPm CT" and L6aL "Dual CT" neurons in the thalamus and/or cortex (Kim et al. 2014). This approach underscores the potential of targeted viral techniques for dissecting complex neural circuits.

The possible influences of the L6a Dual CT pathway in thalamic processing. Having a technique that allows us to study fine CT circuitry opens the possibilities to ask detailed questions about its functions in the thalamus and cortex in vitro and in vivo. Extensive research has shown that L6a CT circuits significantly influence thalamic information processing (Olsen et al., 2021; Crandall et al., 2015). However, these studies primarily relied on “bulk” or non-selective activation techniques, limiting the precision in understanding specific microcircuit effects. Specifically, having the ability to selectively stimulate the "VPm CT" and "Dual CT" microcircuits in the thalamus allows for finely targeted investigations. For the future of this project, I would foresee studying the circuit mechanisms that underlie corticothalamic surround suppression in the sensory thalamus (Murphy and Sillito 1987; Jones et al. 2012; Born et al. 2021; Temereanca and Simons 2004). Surround suppression refers to a neuronal pathway phenomenon where the response to a stimulus presented in the center of a neuron's receptive field is suppressed by simultaneous stimulation of a surrounding area. If I were to continue leading this project, I would have liked to probe the engagement of the Dual CT pathway in the following areas:

1. At the level of the TRN; particularly the engagement of “edge” or “shell” cells, where

this pathway targets (Figs. 4.2 – 4.4; Whilden et al. 2021). Interestingly, this area is reciprocally connected to the POm, but not the VPm (Martinez-Garcia et al. 2020) having the ability to modify the activity of inhibitory circuits that target the POm (Landisman and Connors 2007).

2. At the level of the POm; particularly the dynamic interplay between the direct excitatory corticothalamic input (Landisman and Connors 2007) and the possible inhibition from the TRN. Looking into the precise temporal integration of both mono-synaptic excitatory input from cortex, and di-synaptic inhibitory input from the TRN in POm neurons could shed light in understanding the corticothalamic mechanisms involved in the generation of surround suppression, specifically the spatial and temporal activity patterns elicited by CT activation in aligned barreloids vs surrounding ones (Landisman and Connors 2007; Jones et al. 2012), and how this affects the temporal processing properties of ascending sensory inputs seen in the POm (Ahissar et al. 2000; Sosnik et al. 2001; Diamond et al. 1992).

3. At the level of the VPm; the thalamic terminal patterns of this pathway pose an interesting view of its role in VPm processing. This pathway does not target the area in the TRN that provides inhibitory inputs to the VPm, therefore its influence is strictly excitatory (Figs 4.2 – 4.4; (Martinez-Garcia et al. 2020; Whilden et al. 2021). Although these inputs are numerous, they are considered axonal collaterals (Bourassa et al. 1995; Deschênes et al. 1998), which are thought to provide weak inputs (see Fig. 4.4). Interestingly, their terminal fields are somatotopically aligned (Temereanca and Simons 2004), which gives them an anatomical advantage to provide excitation to VPm circuits involved in processing sensory information from the same whisker. Perhaps this weak-

but-selective excitation could slightly enhance excitability in VPm relay neurons.

In conclusion, in this chapter I harness advanced genetic and viral tools to unravel the intricate roles of L6a CT microcircuits in the modulation of thalamic processes, offering fresh perspectives on optogenetic applications. Here, I have shown the feasibility of isolating specific L6a CT microcircuits to precisely control their temporal and spatial activity, enabling a detailed examination of their impact on thalamic function. These findings move us a step closer to deciphering the complex interactions between the motor and somatosensory systems, leading to a deeper understanding of sensorimotor processing mechanisms.

BIBLIOGRAPHY

Agmon A, Connors BW (1991) Thalamocortical responses of mouse somatosensory (barrel) cortex in vitro. Neuroscience 41:365–379.

Ahissar E, Sosnik R, Haidarliu S (2000) Transformation from temporal to rate coding in a somatosensory thalamocortical pathway. Nature 406:302–306.

Born G, Schneider-Soupiadis FA, Erisken S, Vaiceliunaite A, Lao CL, Mobarhan MH, Spacek MA, Einevoll GT, Busse L (2021) Corticothalamic feedback sculpts visual spatial integration in mouse thalamus. Nat Neurosci 24:1711–1720.

Bortone DS, Olsen SR, Scanziani M (2014) Translaminar inhibitory cells recruited by layer 6 corticothalamic neurons suppress visual cortex. Neuron 82:474–485.

Bourassa J, Pinault D, Deschênes M (1995) Corticothalamic projections from the cortical barrel field to the somatosensory thalamus in rats: a single-fibre study using biocytin as an anterograde tracer. Eur J Neurosci 7:19–30.

Briggs F, Usrey WM (2008) Emerging views of corticothalamic function. Curr Opin Neurobiol 18:403–407.

Chevée M, Robertson JDJ, Cannon GH, Brown SP, Goff LA (2018) Variation in activity state, axonal projection, and position define the transcriptional identity of individual neocortical projection neurons. Cell Rep 22:441–455.

Clayton KK, Williamson RS, Hancock KE, Tasaka G-I, Mizrahi A, Hackett TA, Polley DB (2021) Auditory corticothalamic neurons are recruited by motor preparatory inputs. Curr Biol 31:310-321.e5.

Crandall SR, Cruikshank SJ, Connors BW (2015) A corticothalamic switch: controlling the thalamus with dynamic synapses. Neuron 86:768–782.

Crandall SR, Patrick SL, Cruikshank SJ, Connors BW (2017) Infrabarrels Are Layer 6 Circuit Modules in the Barrel Cortex that Link Long-Range Inputs and Outputs. Cell Rep 21:3065–3078.

Cudeiro J, Sillito AM (2006) Looking back: corticothalamic feedback and early visual processing. Trends Neurosci 29:298–306.

Deschênes M, Veinante P, Zhang ZW (1998) The organization of corticothalamic projections: reciprocity versus parity. Brain Res Brain Res Rev 28:286–308.

Diamond ME, Armstrong-James M, Budway MJ, Ebner FF (1992) Somatic sensory responses in the rostral sector of the posterior group (POm) and in the ventral posterior medial nucleus (VPM) of the rat thalamus: dependence on the barrel field cortex. J Comp Neurol 319:66–84.

Frandolig JE, Matney CJ, Lee K, Kim J, Chevée M, Kim S-J, Bickert AA, Brown SP (2019) The synaptic organization of layer 6 circuits reveals inhibition as a major output of a neocortical sublamina. Cell Rep 28:3131-3143.e5.

Gong S, Doughty M, Harbaugh CR, Cummins A, Hatten ME, Heintz N, Gerfen CR (2007) Targeting Cre recombinase to specific neuron populations with bacterial artificial chromosome constructs. J Neurosci 27:9817–9823.

Gu M, Li X, Liang S, Zhu J, Sun P, He Y, Yu H, Li R, Zhou Z, Lyu J, Li SC, Budinger E, Zhou Y, Jia H, Zhang J, Chen X (2023) Rabies virus-based labeling of layer 6 corticothalamic neurons for two-photon imaging in vivo. iScience 26:106625.

Jones HE, Andolina IM, Ahmed B, Shipp SD, Clements JTC, Grieve KL, Cudeiro J, Salt TE, Sillito AM (2012) Differential feedback modulation of center and surround mechanisms in parvocellular cells in the visual thalamus. J Neurosci 32:15946–15951.

Killackey HP, Sherman SM (2003) Corticothalamic projections from the rat primary somatosensory cortex. J Neurosci 23:7381–7384.

Kim J, Matney CJ, Blankenship A, Hestrin S, Brown SP (2014) Layer 6 corticothalamic neurons activate a cortical output layer, layer 5a. J Neurosci 34:9656–9664.

Landisman CE, Connors BW (2007) VPM and PoM nuclei of the rat somatosensory thalamus: intrinsic neuronal properties and corticothalamic feedback. Cereb Cortex 17:2853–2865.

Lee S, Carvell GE, Simons DJ (2008) Motor modulation of afferent somatosensory circuits. Nat Neurosci 11:1430–1438.

Madisen L, Zwingman TA, Sunkin SM, Oh SW, Zariwala HA, Gu H, Ng LL, Palmiter RD, Hawrylycz MJ, Jones AR, Lein ES, Zeng H (2010) A robust and high-throughput Cre reporting and characterization system for the whole mouse brain. Nat Neurosci 13:133–140.

Martinetti LE, Bonekamp KE, Autio DM, Kim H-H, Crandall SR (2022) Short-Term Facilitation of Long-Range Corticocortical Synapses Revealed by Selective Optical Stimulation. Cereb Cortex 32:1932–1949.

Martinez-Garcia RI, Voelcker B, Zaltsman JB, Patrick SL, Stevens TR, Connors BW, Cruikshank SJ (2020) Two dynamically distinct circuits drive inhibition in the sensory thalamus. Nature 583:813–818.

Murphy PC, Sillito AM (1987) Corticofugal feedback influences the generation of length tuning in the visual pathway. Nature 329:727–729.

Olsen SR, Bortone DS, Adesnik H, Scanziani M (2012) Gain control by layer six in cortical circuits of vision. Nature 483:47–52.

Sosnik R, Haidarliu S, Ahissar E (2001) Temporal frequency of whisker movement. I. Representations in brain stem and thalamus. J Neurophysiol 86:339–353.

Temereanca S, Simons DJ (2004) Functional topography of corticothalamic feedback enhances thalamic spatial response tuning in the somatosensory whisker/barrel system. Neuron 41:639–651.

APPENDIX C: CHAPTER 4 FIGURES AND TABLES

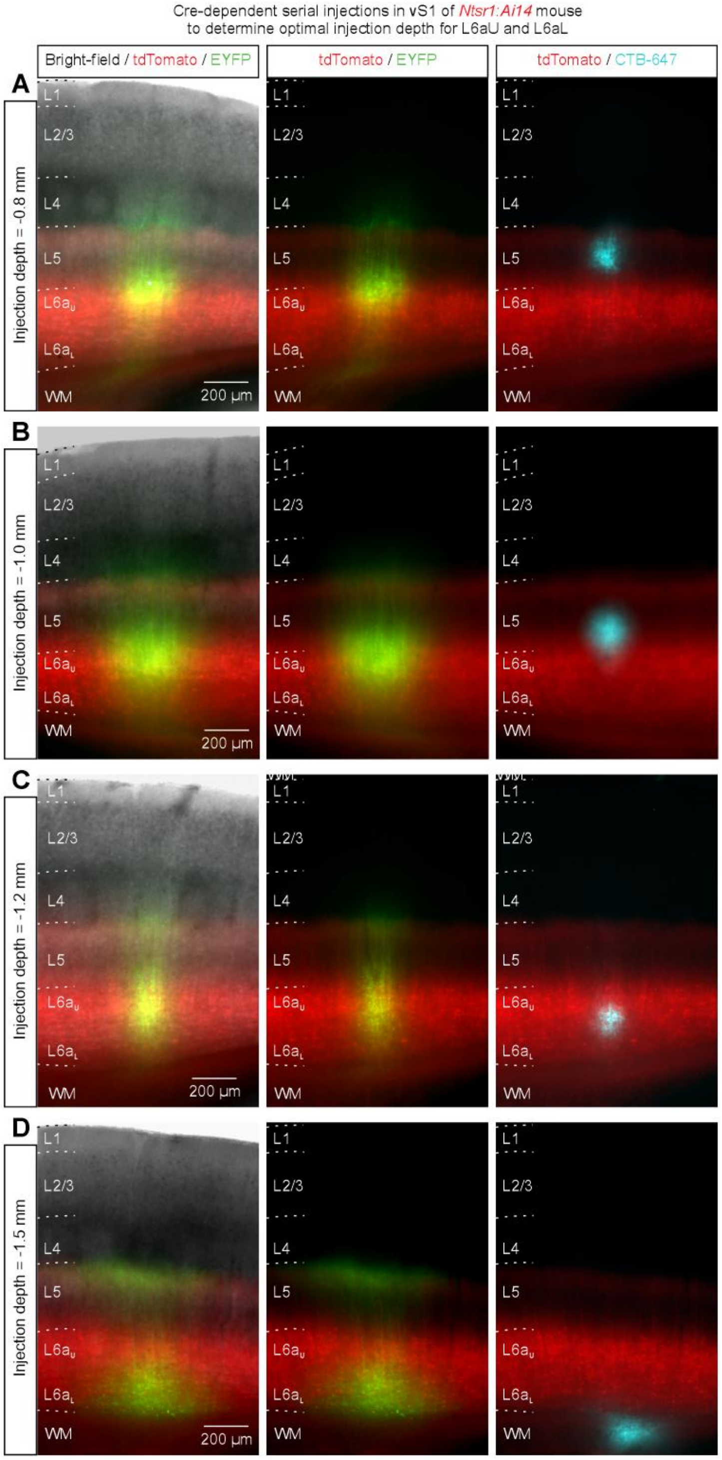

Figure 4.1. Serial depth injections of cre-dependent virus in Ntsr1 mouse reveal precise coordinates to selectively express ChR2 in either L6a sub-layer. Serial injections of cre-dependent virus encoding for ChR2/EYFP in different *Ntsr1-Cre* x *Ai14* mice. ***A,*** Fluorescent images of a live vS1 slice in the thalamocortical plane (300 µm).

Figure 4.1 (cont’d)

The injection depth was -0.8 mm deep. Left, a bright-field illuminated image of an injection site targeting L5a showing weak ChR2/EYFP expression (green) in L6a$_U$ CT neurons (tdTomato/red). Middle, same injection without the bright- field illumination to enhance visualization of fluorescent patterns. Right, shows center of the injection with CTB-647 (cyan) located in L5a. ***B,*** Injection was -1.0 mm deep. Same organization as in *A*, but the injection targets L5b and shows robust ChR2/EYFP expression restricted to L6a$_U$ CT neurons. ***C,*** Injection was -1.2 mm deep. Same organization, but the injection targets the middle of L6a and shows unrestricted ChR2/EYFP expression in both L6a$_U$ and L6a$_L$ CT neurons. ***D,*** Injection was -1.5 mm deep. Same organization, but the injection targets the white matter under L6, and shows ChR2/EYFP restricted to L6a$_L$ CT neurons.

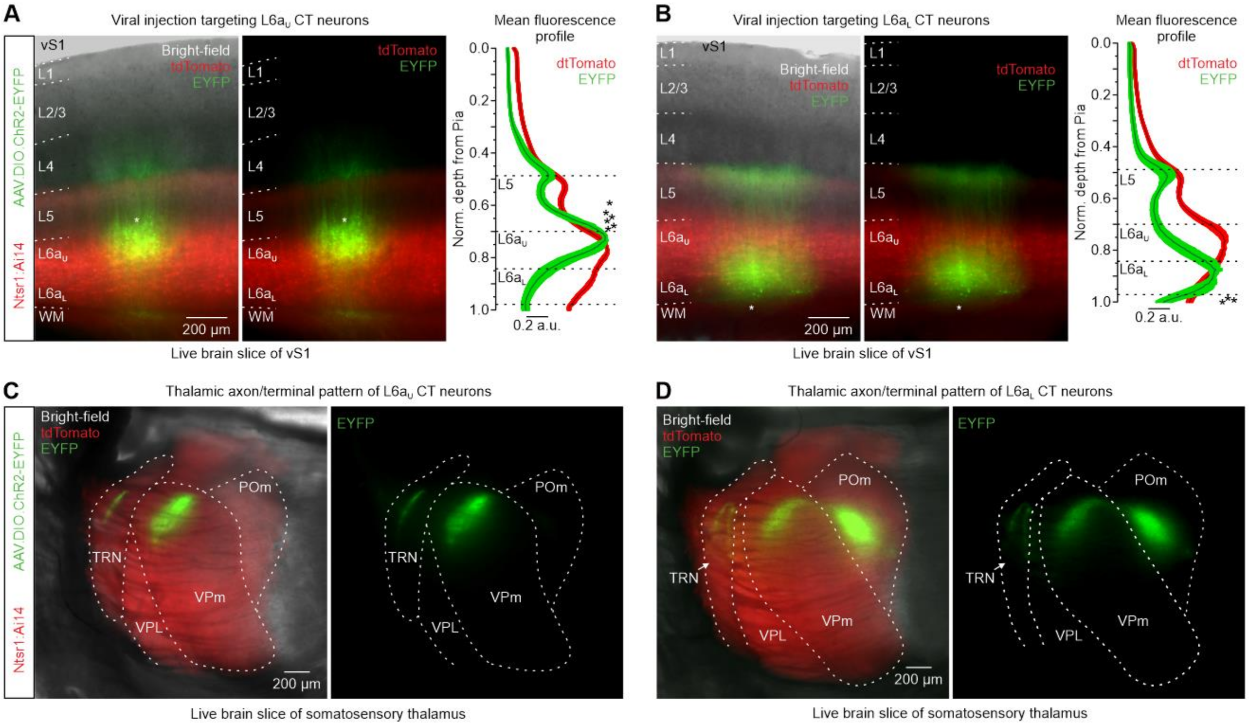

Figure 4.2. Selective expression of ChR2 in L6aU or L6aL shows stereotypical VPm CT or Dual CT cortical and thalamic terminal patterns, respectively. A, Fluorescent images of a live slice in the thalamocortical plane (300 µm) from an Ntsr1-Cre x Ai14 mouse cross injected in vS1 with a cre-dependent adeno-associated virus (AAV/ef1α.DIO). Left, image of an injection targeting L6aU to selectively express ChR2 in putative VPm CT neurons. Middle, same section without the bright-field illumination to enhance fluorescent pattern. Right, mean fluorescence intensity profiles (L6 CT cells, tdTomato/red; L6aU CT neurons, EYFP/green) are shown as a function of normalized depth from pia to white matter (WM). Asterisks indicate injection site centers. B, Same organization as in A, but the injection targets L6aL to selectively express ChR2 in putative Dual CT neurons. C, Fluorescent images of the same live slice shown in A, showing putative VPm CT neuron axon/terminal patterns in the thalamus. Note that the only visible EYFP fluorescence is located in the core of the TRN and in the VPm. D, Fluorescent images of the same live slice shown in B, showing putative Dual CT neuron axon/terminal patterns in the thalamus. Note that visible EYFP fluorescence is located in the edges of the TRN, the VPm, and in the POm.

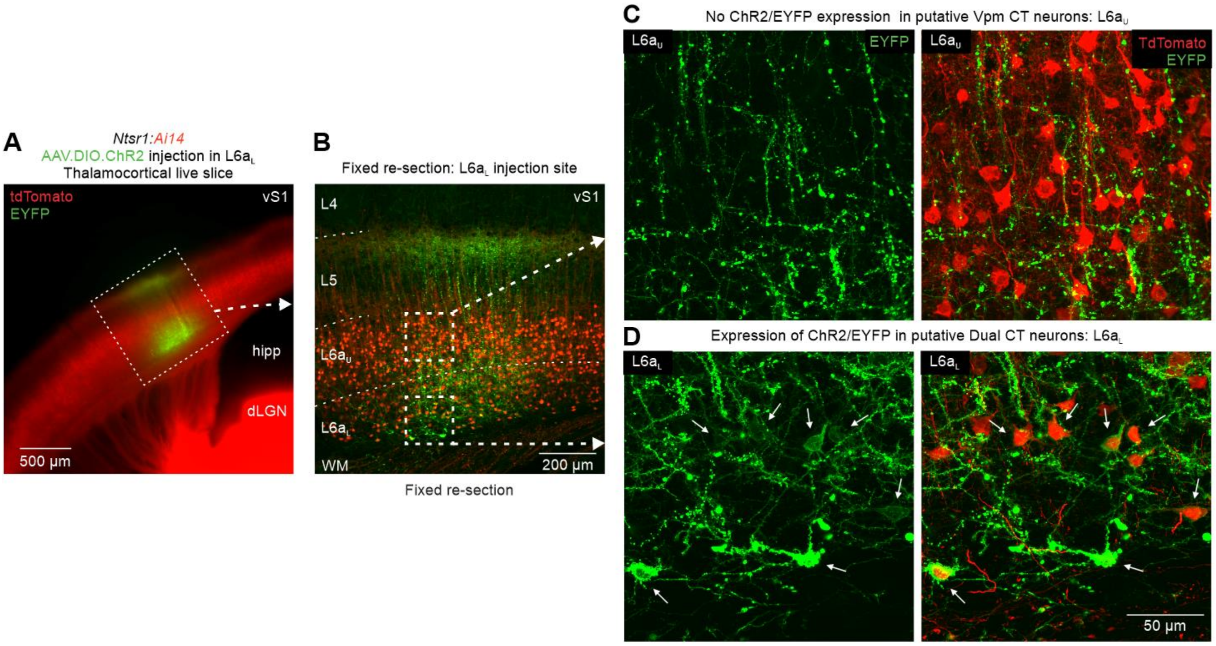

Figure 4.3. Targeted expression of ChR2/EYFP in L6aL CT neurons. ***A,*** Fluorescent image of a live slice in the thalamocortical plane from an *Ntsr1-Cre* x *Ai14* mouse cross injected in vS1 with a floxed adeno-associated virus (AAV.DIO) targeted towards L6aL (L6 CT cells, tdTomato/red; L6aL CT neurons, EYFP/green). ***B,*** High-magnification fluorescent image of a fixed re-section (50-µm-thick) from the slice shown in *A*. Only cell bodies in L6aL express ChR2-EYFP, whereas no cells expressing ChR2 are visible in L6aU. ***C,*** Magnified view of the upper white dashed square in *B* showing no EYFP and tdTomato co-localization in L6aU. Left, only EYFP is visible to provide a clearer picture of L6aU ChR2 expression. Right, same image but also showing cell bodies in tdTomato. Note that there are no cell bodies expressing ChR2. ***D,*** Magnified view of the lower white dashed square in *B* showing EYFP and tdTomato co-localization in L6aL. Left, only EYFP is visible to provide a clearer picture of L6aL ChR2 expression. Right, same image but also showing cell bodies in tdTomato. Note the multiple cell bodies expressing ChR2.

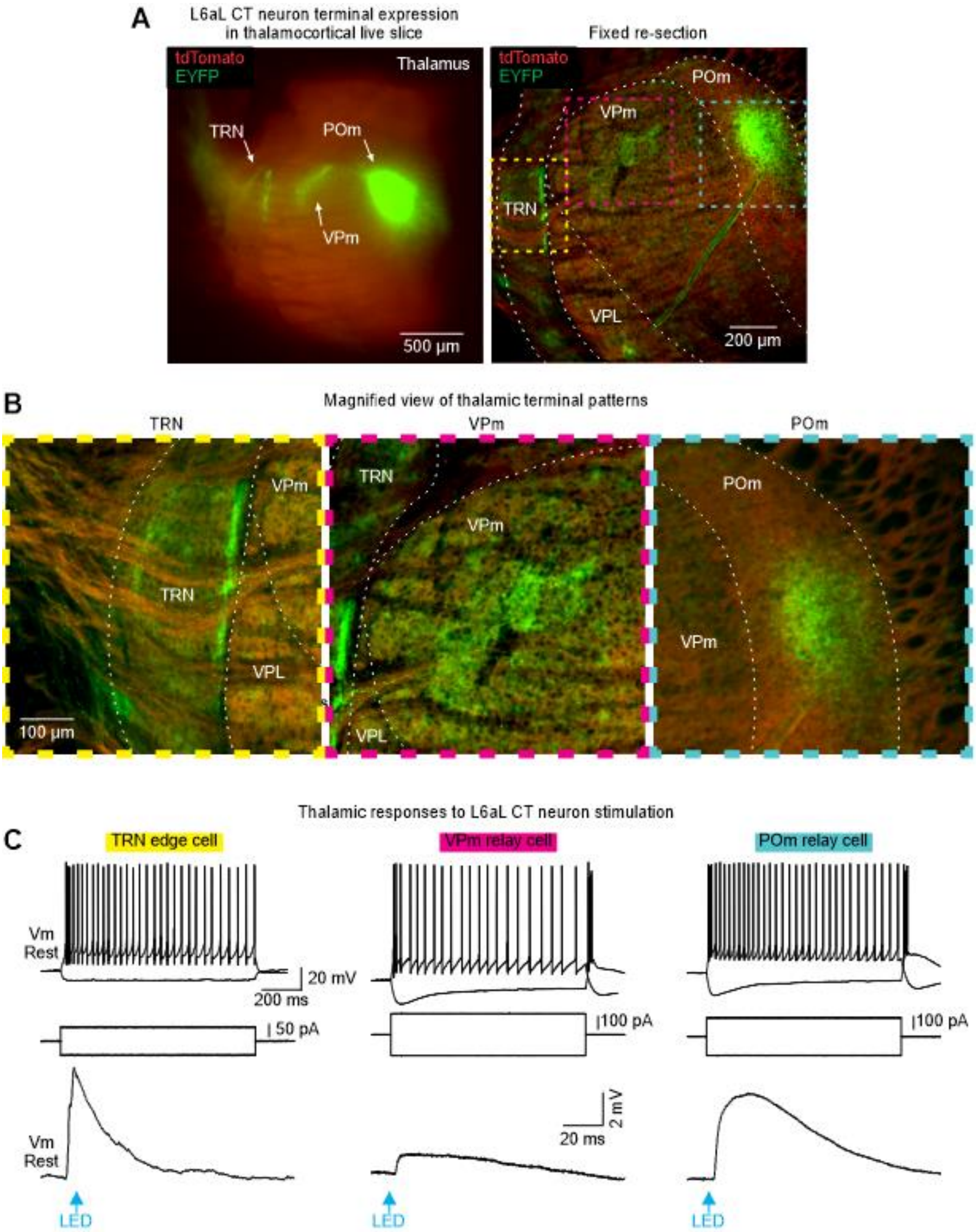

Figure 4.4. L6aL CT neuron thalamic terminals mirror those of "Dual CT" neurons and can be activated to study effects in TRN, VPm and POm neurons. A, Left, Fluorescent image of a live slice in the thalamocortical plane from the same section as Fig. 4.2, focusing on the thalamic terminal patterns from CT neurons expressing ChR2 (green) from L6aL (all L6a CT terminals shown in red). Right, high-magnification fluorescent image of a fixed re-section (50-µm-thick) of the same slice. Note that the

Figure 4.4 (cont'd)

EYFP terminal patterns follow the same patterns reported in Dual CT neurons; edge TRN, VPm, and POm. B, Left, high-magnification of the TRN (yellow dashed square shown in A, right). Middle, high magnification of the VPm (pink dashed square). Right, high magnification of the POm (Blue dashed square). C, Example recordings from the same slice. Top traces show a stereotypical physiological response of distinct thalamic cell types. Bottom traces show L6aL CT-evoked responses. Left, responses of a TRN edge cell when held at their preferred RMP. Middle, responses of a VPm relay neuron, right, responses of a POm relay neuron.

CHAPTER 5: GENERAL CONCLUSIONS

5.1 – Summary of key findings

The primary objective of this PhD dissertation was to investigate the impact of vM1 activity on the somatosensory cortex, in the context of sensory processing. In the first two chapters, we made significant strides toward understanding the synaptic and circuit mechanisms facilitating sensorimotor processing in the cortex by studying the reciprocally connected vM1 – vS1 pathways. Initially, we conducted a comprehensive analysis of the synaptic properties of both pathways, revealing synaptic properties not previously reported, and a pronounced response from L6a excitatory cells to vM1 inputs (Chapter 2). Secondly, I demonstrated that vM1 preferentially engages activity in $L6a_L$ “Dual CT’ neurons, but not $L6a_U$ “VPm CT” neurons (Chapter 3). Lastly, I illustrated our ability to target these specific L6a microcircuits by employing viral techniques with minimal volumes to ensure spatially restricted viral expression (Chapter 4). Collectively, these findings present a new perspective on the involvement of vM1 and vS1 in sensory-motor behaviors.

5.2 – Overall discussion

In Chapter 2, we examined the synaptic communication between the highly interconnected vM1 and vS1, two areas whose interactions are essential for active sensation. Interestingly, initial findings from our laboratory revealed that the vM1 – vS1 pathway exhibited short-term facilitation, a result that contradicted the existing literature which typically describes this pathway as exhibiting short-term depression. Upon further examination of the literature, we identified significant discrepancies in the methodologies used to investigate these synapses. Notably, we found that different aspects of using optogenetic tools could markedly influence the studied neuronal responses.

Consequently, to gain a clearer understanding of the interactions between these two areas, we decided to investigate the vS1 – vM1 reciprocal pathways using optogenetic techniques. This approach allowed us to establish a standardized experimental method for examining long-range intracortical pathways.

First, under our experimental conditions, we found that stimulation of the vS1 – vM1 reciprocal pathways led to short-term facilitation, in contrast to local connections, as demonstrated in Chapter 2 (Figs. 2.1-3 A significant distinction between these pathways is the unique synaptic dynamics observed in excitatory cells based on the target layer and area, along with different L2/3 GABAergic interneurons. These distinct synaptic features are crucial as they underscore the roles of different cortical neurons in the integration and distribution of information It is believed that intracortical pathways showing synaptic facilitation convey information regarding ongoing activity and enable flexible control over the post-synaptic site in a manner dependent on current activity, as suggested by (Zagha et al., 2013) and further supported by supplemental figures in (Martinetti and Bonekamp et al., 2022).

An obvious question that arises is: how do we see facilitation whereas others report depression? This discrepancy prompted us to collect and analyze experimental data from all studies indicating depression. In the following, I will outline a few recurring aspects that we identified.

1: The viral serotype used by different studies varied widely. Previous studies have shown that the choice of viral serotype used (e.g., AAV-1, -2, -5, -9) to express ChR2 can significantly impact the synaptic dynamics of intracortical synapses (Jackman et al., 2014). Aware of this, we conducted extensive experiments to identify a serotype that more accurately mirrors the natural dynamics of intracortical synapses (Martinetti & Bonekamp et al., 2022). We found AAV2 to be the most reliable serotype for studying these pathways, based on assessments of fiber volleys and retrograde expression properties.

2: The fusion protein mCherry was the reporter most commonly used, but our experiments showed that it significantly impairs synaptic plasticity. This issue may arise from the aggregation of the fusion protein within virally transfected neurons (Asrican et al., 2013).

3: The strategy for optical stimulation and the concentration of extracellular Ca2+ can influence the extent of synaptic facilitation observed. Most studies used a high-power density light stimulation over terminals with long pulse durations (3–10 ms), which we showed significantly impacts the recorded dynamics, perhaps due to de-sensitization and reduced conductance by ChR2. Furthermore, we show that the extracellular Ca2+ concentration used by most studies (2.0 mM) contributes to synaptic depression, as compared to (1.2 mM) extracellular C12+ concentration that we used. Higher Ca2+ concentration affects synaptic dynamics by increasing Ca2+ influx, thus enhancing the probability of initial neurotransmitter release and leading to early terminal depletion in a train, resulting in apparent synaptic depression.

Modifying these parameters increased our confidence that the synaptic facilitation we observed represents a natural phenomenon, rather than a consequence of experimental conditions leading to synaptic depression. Fine-tuning the experimental optical approach to study long-range intracortical synapses allowed us to perform a comprehensive study of these reciprocally connected areas. While these data support my specific hypothesis stating that the vM1 – vS1 pathway exhibits short-term facilitation, they also contradict my specific hypothesis stating that the vS1 – vM1 pathway exhibits short-term depression. While previous literature suggests a “clean-cut” definition for feedforward and feedback pathways as “drivers” and “modulators, these results indicate a revision of this naming convention (Sherman and Guillery 2011). Furthermore, the transient/rapid nature of the S1-M1 pathway (Yamashita et al. 2013) doesn’t necessarily suggest depression because this is the intact animal and inhibitory systems are engaged, possibly suppressing further firing instead of depressive synapses.

Next, I will focus on the findings that are important to the following sections of this dissertation.

One of the key findings of this study is that vM1 delivers the strongest inputs to excitatory neurons in L6a of vS1. L6a is particularly important because it is considered an “output” layer via its CT neurons and can modulate thalamocortical, and cortical activity (i.e., sensory processing; Olsen et al., 2012; Bortone et al., 2014; Kim et al., 2014; Crandall et al., 2015; Frandolig et al., 2019). The CT neurons in L6a are important as they are targeted by vM1 (Zhang and Deschênes, 1998; Kinnischtzke et al., 2014, 2016) and can control the firing properties of specific relay neurons in the thalamus, shown to be important for normal sensory processing.

The role of M1 in modulating afferent/efferent sensory information has long been a subject of interest. A growing body of evidence shows that the vM1 – L6a CT pathway is important due to the L6a CT neuron’s ability to heavily modulate thalamic processing (Cudeiro and Sillito, 2006; Briggs and Usrey, 2008; Lee et al., 2008; Crandall et al., 2015 ; Clayton et al., 2021). However, this work's specificity is limited due to the complex and intertwined circuitry of L6a CT. In Chapter 3, I focused on detailing the anatomical layout of L6a CT neurons and how vM1 specifically targets different CT populations *in vitro*.

When we were testing the vM1 – L6a pathway using the Ntsr1-cre mouse in chapter 2, I consistently observed stronger vM1 axon/terminal patterns in the lower half of L6a. Interestingly, prior research has identified two primary types of CT cells: those projecting solely to the VPm (VPm CT neurons, present in L6a$_U$) and those projecting to both the VPm and POm (Dual CT neurons, present in L6a$_L$).. These studies have speculated on the location and distribution of both types, but no consensus had been reached.

In Chapter 3 I performed experiments to understand the specific engagement of L6a CT circuits by vM1. Initially, I replicated earlier experiments by selectively inducing ChR2 expression in vM1 through viral injection and confirmed that L6aL (defined by its normalized depth from pia to white matter, from 84 to 97% depth). The fluorescence observed contains both axons and terminals, which could confound my interpretation of terminal density, therefore I used whole-cell electrophysiology to record the responses of the genetically labeled L6a CT neurons (Ntsr1x Ai14 mouse) to vM1 optical stimulation. I showed that there is a selective engagement of CT neurons in L6aL when their membrane potential was depolarized (-74 mV), simulating that of an “active” state. This finding is intriguing as previous studies have shown a depth-dependent separation of the two principal L6a CT circuits.

Others have shown that VPm CT neurons predominantly occupy L6a$_U$ (defined by its normalized depth from pia to WM; 70 – 84% depth), while Dual CT neurons are primarily found in L6aL. However, these studies often lacked direct comparisons within the same preparation, leaving uncertainty about the exact proportions of projection classes within each sub-layer.

Here, I performed dual thalamic injections of the retrograde tracer CTB into both the VPm and POm to label and quantify L6a CT neurons along the vertical depth of vS1. My findings confirmed that L6aU mainly consists of VPm CT neurons (84%), and L6aL predominantly houses Dual CT neurons (70%), providing a detailed anatomical map of the L6a CT circuitry.

Since I have a good understanding of the architecture of L6a CT neurons, I investigated the specific inputs that vM1 provides to both CT types. To do this, I performed a triple injection strategy where I retrogradely labeled both CT classes as described above, and I also injected ChR2 into vM1. These results validated my initial observations: vM1 preferentially targets Dual CT neurons, not VPm CT neurons, and engages spiking behavior when their membrane potential is depolarized.

Next, to understand the mechanisms potentially mediating this difference, we first measured the intrinsic physiology of both CT types. We found that, overall, Dual CT neurons exhibit increased responsiveness to injected currents, possibly due to their higher membrane resistance and lower rheobase current. Subsequently, we explored potential synaptic mechanisms. By measuring direct currents in voltage-clamp mode, we demonstrated that Dual CT neurons exhibit stronger vM1-evoked excitation compared to their counterparts, albeit with similar disynaptic inhibition, resulting in a higher E/I ratio in Dual CT neurons. These mechanisms provide a preliminary understanding of why Dual CT neurons are more engaged by vM1 inputs, warranting further investigation.

Specifically, although I identified two potential mechanisms leading to this difference in evoked activity, experiments altering these properties need to be performed to dictate the contribution of each mechanism to this effect. One technique that could facilitate this is dynamic clamp mode, which would allow for a data-driven simulation of synaptic conductances and membrane properties of CT neuron types, enabling selective manipulation of certain parameters to decipher the specific cellular mechanisms by which Dual CT neurons respond more prominently to vM1 inputs. Furthermore, these results support my specific hypotheses that vM1 preferentially targets L6a neurons in the lower part of L6a, and these inputs are strong enough to alter their excitability.

The results presented in Chapter 3 reveal, for the first time, a specific L6a CT circuit activated by vM1 activity. Therefore, in chapter 4 I wanted to know if I could gain genetic access to the L6a sub-circuits separately, to evaluate their impact in the sensory thalamus. I showed that we could achieve separate genetic and spatially restricted access to either VPm or Dual CT circuits by injecting minimal volumes (10 – 50 µL) of cre-dependent virus into L6aU or L6aL, respectively. Interested in the CT population engaged by vM1 (Dual CT neurons), I began by assessing the effectiveness of this method for activating this pathway in the thalamus. However, a potential limitation of this approach could be insufficient ChR2 expression in Dual CT neurons due to the minimal viral volumes used, combined with the reportedly weak synapses that L6 CT neurons form in the thalamus.

To address the efficacy of this technique to study synaptic communication, I recorded neurons in the thalamic areas receiving L6aL inputs. As anticipated, I found that ChR2/EYFP expression in L6aL resulted in a thalamic terminal pattern characteristic of “Dual CT neurons” (encompassing shell TRN, VPm, and POm). Subsequently, I activated L6aL terminals expressing ChR2 while using whole-cell electrophysiology to record neurons in each of these three thalamic regions. Overall, my recordings show that this technique is viable to study specific L6a CT microcircuit influence in the thalamus, and perhaps in the cortex. The future directions of this project would be to look at the specific strength and synaptic dynamics of this pathway into all thalamic areas it contacts, and ultimately probe this pathway *in vivo*.

BIBLIOGRAPHY

Asrican B et al. (2013) Next-generation transgenic mice for optogenetic analysis of neural circuits. Front Neural Circuits 7:160.

Bortone DS, Olsen SR, Scanziani M (2014) Translaminar inhibitory cells recruited by layer 6 corticothalamic neurons suppress visual cortex. Neuron 82:474–485.

Briggs F, Usrey WM (2008) Emerging views of corticothalamic function. Curr Opin Neurobiol 18:403–407.

Clayton KK, Williamson RS, Hancock KE, Tasaka G-I, Mizrahi A, Hackett TA, Polley DB (2021) Auditory corticothalamic neurons are recruited by motor preparatory inputs. Curr Biol 31:310-321.e5.

Crandall SR, Cruikshank SJ, Connors BW (2015) A corticothalamic switch: controlling the thalamus with dynamic synapses. Neuron 86:768–782.

Cudeiro J, Sillito AM (2006) Looking back: corticothalamic feedback and early visual processing. Trends Neurosci 29:298–306.

Frandolig JE, Matney CJ, Lee K, Kim J, Chevée M, Kim S-J, Bickert AA, Brown SP (2019) The synaptic organization of layer 6 circuits reveals inhibition as a major output of a neocortical sublamina. Cell Rep 28:3131-3143.e5.

Jackman SL, Beneduce BM, Drew IR, Regehr WG (2014) Achieving high-frequency optical control of synaptic transmission. J Neurosci 34:7704–7714.

Kim J, Matney CJ, Blankenship A, Hestrin S, Brown SP (2014) Layer 6 corticothalamic neurons activate a cortical output layer, layer 5a. J Neurosci 34:9656–9664.

Kinnischtzke AK, Fanselow EE, Simons DJ (2016) Target-specific M1 inputs to infragranular S1 pyramidal neurons. J Neurophysiol 116:1261–1274.

Kinnischtzke AK, Simons DJ, Fanselow EE (2014) Motor cortex broadly engages excitatory and inhibitory neurons in somatosensory barrel cortex. Cereb Cortex 24:2237–2248.

Lee S, Carvell GE, Simons DJ (2008) Motor modulation of afferent somatosensory circuits. Nat Neurosci 11:1430–1438.

Martinetti LE, Bonekamp KE, Autio DM, Kim H-H, Crandall SR (2022) Short-Term Facilitation of Long-Range Corticocortical Synapses Revealed by Selective Optical Stimulation. Cereb Cortex 32:1932–1949.

Olsen SR, Bortone DS, Adesnik H, Scanziani M (2012) Gain control by layer six in cortical circuits of vision. Nature 483:47–52.

Zagha E, Casale AE, Sachdev RNS, McGinley MJ, McCormick DA (2013) Motor cortex feedback influences sensory processing by modulating network state. Neuron 79:567–578.

Zhang ZW, Deschênes M (1998) Projections to layer VI of the posteromedial barrel field in the rat: a reappraisal of the role of corticothalamic pathways. Cereb Cortex 8:428–436.